Geochemical consequences of subduction zone metamorphism: Case studies of metamorphic rocks from Palaeozoic subduction zone complexes in Tianshan and Qilian Orogenic Belts, NW China

XIAO, YUANYUAN

Geochemical consequences of subduction zone metamorphism: Case studies of metamorphic rocks from Palaeozoic subduction zone complexes in Tianshan and Qilian Orogenic Belts, NW China

Yuanyuan Xiao

Subduction-zone metamorphism (SZM) is considered to be a major geochemical process on Earth of both petrological and geodynamic significance that triggers the subduction-zone magmatism and contributes to the mantle compositional heterogeneity. To understand SZM and elemental responses to SZM, detailed petrological and geochemical studies were conducted on metamorphic rocks of basaltic and sedimentary protoliths from two orogenic belts, i.e., Western Tianshan and North Qilian Mountain, in NW China.

Based on the bulk-rock geochemistry of rocks from ultrahigh pressure metamorphic belt of Western Tianshan, different elemental mobility/immobility has been identified using the inter-elemental correlations.

Mineral compositions have also been analyzed for the same rocks. The significant elemental hosts are phengitic muscovite, paragonite, garnet, epidote group minerals, rutile and titanite. Together with detailed petrography and considering a series of plausible metamorphic reactions, we conclude that it is the presence and stability of these minerals that largely controls the geochemical behaviors of chemical elements during SZM.

In terms of both bulk-rock composition and mineral geochemistry for rocks from North Qilian Mountain, we conclude the same except the mobility of U, which may be attributed to the seafloor alteration rather than SZM.

The consistent immobility of U, Th and light rare earth elements (LREEs), like high field strength elements (HFSEs), during SZM indicates that the enrichment of these elements in arc magmas is not caused by simple dehydrated aqueous fluids. Therefore, the traditionally accepted fluid flux induced-melting needs reconsideration in order to explain the arc signature in melts produced through subduction-zone magmatism. In addition, the lack of Rb/Sr-Sm/Nd (or Lu/Hf) correlation in these and other metabasites world-wide is inconsistent with the observed first-order Sr-Nd (or Hf) isotope correlation in oceanic basalts. Hence, the subducted residual ocean crust cannot be the major source materials for oceanic basalts although it can contribute to mantle compositional heterogeneity.

Geochemical consequences of subduction zone metamorphism: Case studies of metamorphic rocks from Palaeozoic subduction zone complexes in Tianshan and Qilian Orogenic Belts, NW China

Yuanyuan Xiao

A thesis submitted in partial fulfillment of the requirements for the degree of Doctor of Philosophy at Durham University

Department of Earth Sciences, Durham University

April 2012

Table of Contents

List of Figures

Abbreviation List

A	
Ab	albite
Act	actinolite
Aeg	aegirine
Alm	almandine
Aln	allanite
Amp	amphibole
AMP	amphibolite
And	andalusite
AOC	altered oceanic crust
Ap	apatite
Arg	aragonite
Atg	antigorite
Aug	augite
AYCF	Ablation Yield Correction Factor
B	
Brs	barroisite
BS	blueschist
C	
-c	mineral core
Ca	carbonate mineral
Car	carpholite
CC	Continental crust
Chl	chlorite
Cld	chloritoid
CNQ	North Qaidam continental-type UHP Metamorphic Belt
Coe	coesite
Cpx	clinopyroxene
CTP	Central Tianshan Plate
CTT	Central Tianshan Terrane
Czs	(clino)zoisite
D	
D	radiogenic daughter
Di	diopside
Dia	diamond
DM	depleted mantle
Dol	dolomite
E	
EA	epidote amphibolite
EC	eclogite
EDS	Energy Dispersive Spectrometer
EM	enriched mantle
E-MORB	enriched-type mid-oceanic ridge basalts
Ep	epidote group minerals
EPAW	early Palaeozoic accretionary wedge
EPMA	Electron Probe Micro-analyzer
F	
FMQ	fayalite-magnetite-quartz
G	
Gln	glaucophane
GLOSS	global oceanic subducted sediments
GR	granulite
Gr	graphite
Grs	grossular
Grt	garnet
GS	greenschist
H	
Hbl	hornblende
HFSEs	high field strength elements
HGB	high-grade blueschist/eclogite metamorphic belt
HGR	high pressure granulite
HIMU	high μ; $\mu = {}^{238}U/{}^{204}Pb$
HP	high pressure
HPM	high pressure metamorphism
HREEs	heavy rare earth elements
HT	high temperature
I	
IAB	island arc basalts
ICP OES	Inductively Coupled Plasma Optical Emission Spectrometer
ICPMS	Inductively Coupled Plasma Mass Spectrometry
incl.	inclusion
J	
Jd	jadeite
JP	Junggar Plate
K	
Ky	Kyanite
L	
LA-ICP MS	Laser ablation-Inductively Coupled Plasma Mass Spectrometry
LGB	low-grade blueschist metamorphic belt
LILEs	large ion lithophile elements
LOI	loss on ignition
LP	low pressure

(Continued)

Abbreviation List (continued)

L	
LREEs	light rare earth elements
LT	low temperature
Lws	lawsonite
M	
-m	mineral mantle
Mgs	magnesite
Mhb	magnesiohornblende
Mica	white micas
MORB	mid-oceanic ridge basalts
MREEs	middle rare earth elements
Ms	muscovite
N	
n.d.	not detected
NCC	North China Craton
N-MORB	normal-type mid-oceanic ridge basalts
NMT	Northern Margin of Tarim Plate
NTBO	North Tianshan Back-arc Ocean
NTIA	North Tianshan Island Arc
O	
OC	oceanic crust
OIB	ocean island basalts
Omp	omphacite
ONQ	North Qilian oceanic-type Suture Zone; North Qilian Mountain
Opq	opaque mineral
org.	orogen
P	
P	radioactive parent
P/D	the ratio of radioactive parent/radiogenic daughter
Pg	paragonite
Ph	phengite
PJO	Palaeo-Junggar Ocean
PM	primitive mantle
PPL	plane polarized light
ppm	parts per million
Prp	pyrope
PSTO	Palaeo-South Tianshan Ocean
Q	
QL	North Qilian Mountain
QQB	Qilian–Qaidam block
Qz	quartz

R	
-r	mineral rim
RE	relative error
REEs	rare earth elements
Retro.	retrograde
rm	reference material
RSD	relative standard deviation
Rt	rutile
S	
sam	sample
sedi	sediment
SEM	Scanning Electron Microscope
SHRIMP	sensitive high-resolution ion microprobe
SSPM	surface processed materials
SZM	subduction-zone metamorphism
T	
TAS	total alkali vs. silica
Tlc	talc
TP	Tarim Plate
Tr	tremolite
TS	Western Tianshan
Ttn	titanite
Tur	tourmaline
U	
UHP	ultrahigh pressure
UHPM	ultrahigh pressure metamorphism
USGS	United States Geological Survey
V	
VAB	volcanic arc basalts
vol.	volume
W	
WEF	wollastonite + enstatite + ferrosilite
WPA	within-plate alkali basalts
WPT	within-plate tholeiites
wt.	weight percent
X	
XPL	crossed polarized light
XRF	X-ray fluorescence spectrometry
Y	
YB	Yili Block
YCTP	Yili-Central Tianshan Plate

Declaration

I declare that this thesis, which I submit for the degree of Doctor of Philosophy at Durham University, is my own work and not substantially the same as any which has previously been submitted at this or any other university.

Yuanyuan Xiao

Durham University

April 2012

Acknowledgements

The foremost I would like to thank both of my supervisors: Yaoling Niu, and Jon Davidson. Without their patience and strong supports, I cannot make such big improvements. Especially for the first paper, within the first two years for preparation and revision, they put lots of their time and efforts although their busy schedule; otherwise, it cannot be accepted finally. They have different ways to teach and train me, not only on my English but also on my academic thinking during these years.

Most of the analytical work was performed at the State Key Laboratory of Continental Dynamics of Northwest University in Xi'an and State Key Laboratory of Geological Processes and Mineral Resources, China University of Geosciences in Wuhan, China. Shan Gao, my previous supervisor for master degree, Xiaoming Liu, Honglin Yuan, Ming Li, Jianqi Wang, Ye Liu, Keqing Zong, Mengning Dai, and Kaiyun Chen are thanked for their arrangements of the experiments, as well as their great helps in the adjustment of the instruments for obtaining the best possible data. Shuguang Song is thanked for the comprehensive information in the field work of North Qilian Mountain, and the subsequent discussions on the geology of Qilian. Lavis Shaun, Colin Macpherson and Lifei Zhang are also thanked for the constructive discussion on related problems. Jonny, Karen, Paula, Janice, Gary, Dave, Stacey and Allan are thanked for their great helps for solving all those academic-related issues. All the colleagues, particularly Jude, Izzy, Kathy, Claire, Niamh, Sarah Porter, Sarah Collins, Bansri, Amelie, Jinxiu, Hongliang, Hui, Sabina, Alex and Scott, thank you all for your friendship with me in these invaluable years, especially your motivation when I felt upset, tired and depressed, and your tolerance for a non-English native speaker like me as well as everything you did for me. You made me feel not lonely in a foreign country and your warmest hugs made me feel not so cold. My family and all my friends in China, thank you for the endless love, support and your understandings. I am really proud to be part of it all.

Last but not least, I would like to thank Durham University who supplied the main funding for this project.

Dedicate to my parents; my supervisors for PhD research, Professor Yaoling Niu, Professor Jon Davidson; my supervisors for previous studies, Professor Shan Gao, Professor Zhanli Ren

CHAPTER 1:

INTRODUCTION

1.1 THE GEOLOGICAL SIGNIFICANCE OF SUBDUCTION ZONES AND THE PROBLEM

Subduction zones are the most important tectonic setting on Earth in terms of the extent, magnitude, and diversity of mass exchange between the Earth's exterior and the deep mantle. Subduction zones provide a highly selective physical and chemical filter, conceptualized as the "subduction factory" (e.g., Tatsumi & Kogiso, 2003). The main processing in the subduction factory is metamorphism. In fact, it is subduction-zone metamorphism (SZM) that is considered to trigger subduction-zone magmatism (e.g., Tatsumi, 1986; Peacock, 1990; McCulloch & Gamble, 1991) and result in mantle chemical and isotopic heterogeneity.

1.1.1 For Arc Magmatism

1.1.1.1 Arc magmatism formation and "characteristic arc signatures"

There are three mechanisms widely accepted to induce melting of a solid rock via passing through the solidus: heating, decompression and volatile addition (note that the fourth mechanism, compression, is also theoretically possible, Niu, 2005). Since mid-oceanic ridge basalts (MORB) are produced by the melting of depleted upper mantle as a result of decompression, and if island arc basalts (IAB) are also produced by partial melting of mantle wedge without other process involved, it is expected that both MORB and IAB should be compositionally similar. However, IAB differ from MORB in having the characteristic "arc signature", i.e., relatively enriched in large ion lithophile elements (LILEs) and depleted high field strength elements (HFSEs) (McCulloch & Gamble, 1991; Stopler & Newman, 1994), which has led to the understanding that the petrogenesis of IAB differs from that of MORB.

The characteristic arc signature plus the abundant water in IAB (~ 6 – 8 wt.% H_2O in parental melt prior to significant degassing; Wallace, 2005) has led to the general acceptance that IAB result from subducting slab-dehydration which lowers the melting temperature of the mantle wedge peridotite and produces the IAB melt. This IAB formation process is also termed "flux melting" (e.g., Vidal *et al.*, 1989; Arculus, 1994; Tatsumi & Kogiso, 1997; Kelley *et al.*, 2006). Specifically, seafloor materials, experienced different extents of hydrothermal alteration (Xiao *et al.*, 2012; Chapter 4) and weathering, would become altered oceanic crust (AOC; Staudigel *et al.*, 1995; Kelley *et al.*, 2003). Owing to abundant fluids carried, it is most likely that AOC undergoes dehydration in subduction zones, which will lead to the melting of overlying mantle

wedge as a result of volatile addition and consequent lowering of the solidus (e.g., Davies & Stevenson, 1992). The released fluids can selectively carry fluid soluble/mobile elements (e.g., LILEs) into the overlying mantle wedge (McCulloch & Gamble, 1991; Keppler, 1996), while leave behind water insoluble/immobile elements (e.g., HFSEs) in the "residual" subducting ocean crust (Keppler, 1996; Kogiso *et al.*, 1997; Tropper & Manning, 2005; Audétat & Keppler, 2005). Melting of the so-enriched mantle wedge, thus, produce basaltic magmas with the characteristic arc signature (e.g., Tatsumi *et al.*, 1986).

1.1.1.2 Across-arc variations and tracers for subducting/subducted components

Spatial variations across arc. IAB, with tholeiitic and calc-alkaline compositions, show some systematic geochemical variations across the arc, although there are exceptions. The most distinctive feature of major element composition is the *K-h* (K_2O content vs. depth of subducting slab) correlation, i.e., K_2O contents in lavas across arc increase with the depth of the top of the subducting slab, which was first recognized by Kuno (1959) and defined by Dickinson and co-authors (Dickinson & Hartherton, 1967; Dickinson, 1968 for Japanese arcs). In addition, LILE contents are higher in arc-front volcanoes compared with those in rear-arc volcanoes; the opposite is true for light rare earth elements (LREEs) contents (e.g., Tamura *et al.*, 2007). Along with elemental abundance variations are also variations of element ratios and ratios of radiogenic isotopes (e.g., see Figs. 19 and 20 in Tamura *et al.*, 2007). These across-arc systematic variations were thought to be caused by the decreasing degrees of partial melting away from the volcanic front (e.g., Tatsumi & Eggins, 1995). Alternatively, especially after the introduction of hydrous melting/supercritical fluids (see section 1.3.4) during the breakdown/dissolution of phengite at great depths as advocated in recent studies (e.g., Schmidt *et al.*, 2004a), different fluid components at different depths are considered to have led to the *K-h* relationship and other associated variations across the arc volcanoes (e.g., Tamura *et al.*, 2007).

Tracers of subducting/subducted slab rocks. Except the mantle wedge as major source materials for IAB considering the dominated basalts in bulk of arc rocks, the contribution of subducting/subducted slab rocks to the generation of IAB and characteristic arc signatures is crucial. Therefore, different methods are used to trace the slab component in IAB (e.g., Ryan *et al.*, 1995; Morris & Ryan, 2003) and distinguish the varying entities, i.e., subducting ocean crust, overlying sediments, possible effects of subducting ocean lithospheric mantle (Scambelluri *et al.*, 2004; Stern *et al.*, 2006; van der Straaten *et al.*, 2008; Kendrick *et al.*, 2011; John *et al.*, 2011)

over the recent 30 years.

Considering different solubility in hydrous fluids but the similar incompatibility during basaltic magmatism, elemental ratios like U/Th and Ba/Th were used to constrain the nature and component of subducted-slab-derived fluids for IAB magmatism (Morris & Hart, 1983; Ben Othman *et al.*, 1989; Gill & Williams, 1990; Hawkesworth *et al.*, 1997). Co-variation diagrams, e.g., Ba/La vs. Th/Yb, La/Yb vs. Sr/Nd and Ba/Th vs. La/Sm, are widely used to identify the effects of ''slab fluids'' vs. ''hydrous melts'' (see Woodhead *et al.*, 2001; Wallace, 2005; Martin *et al.*, 2011). However, Ba/La ratio of the hydrous melts in recent experimental studies (Hermann & Rubatto, 2009) has been reported to be highly variable by a factor of four from 750°C at 2.5 GPa to 900°C at 4.5 GPa, suggesting that caution is required when use this tracer.

Compared with Sr, Nd and Hf isotopic systems, $^{206}Pb/^{204}Pb$, $^{208}Pb/^{204}Pb$ and $^{207}Pb/^{204}Pb$ isotopic systems are robust radiogenic isotopic tracers for sediments. As early used by Armstrong (1971) for New Zealand and Lesser Antilles volcanic arc magmas and by Kay *et al.* (1978) for Aleutian arc rocks, lead isotopic compositions in IAB show higher values (overlapped with Pb isotope composition of sediments) than those in MORB (e.g., Hawkesworth *et al.*, 1993; Ishikawa & Nakamura, 1994; Elliott *et al.*, 1997; Plank & Langmuir, 1993, 1998; You *et al.*, 1996; Turner & Hawkesworth, 1997; Turner & Foden, 2001; Currie *et al.*, 2007).

The most indisputable tracer of recycled sedimentary component in IAB is ^{10}Be isotope (Tera *et al.*, 1986; Edwards *et al.*, 1993). This is because ^{10}Be can only be produced by cosmic ray spallation reactions on oxygen and nitrogen in the atmosphere (Tera *et al.*, 1986), and thus it is strongly enriched in upper layers of the earth's surface including seafloor sediments, i.e., 10^9 atom/gram in pelagic sediments vs. $< 10^6$ atom/gram in MORB and oceanic island basalts (OIB) (Tanaka & Inoue, 1980). Considering its relatively short half-life (only 1.5 ± 0.3 Ma, Yiou & Raisbeck, 1972), ^{10}Be is especially helpful for tracing those recycled youngest sediments (< 10 Ma; Morris & Ryan, 2003; Dreyer *et al.*, 2010). Boron, because of its high mobility in fluids (Bebout *et al.*, 1993) as well as its higher content in sediments and AOC (~ 100 ppm) than fresh MORB or the mantle (~ 0.1 ppm) (Ryan & Langmuir, 1993), is also taken as one important tracer for the recycled oceanic sediments and/or AOC (Tatsumi & Eggins, 1995; Martin *et al.*, 2011). During subduction-zone metamorphism, B will be carried by those aqueous fluids from the subducting slab rocks into mantle wedge, and result in higher ratios of B/Be in IAB (ca. 4 – 10) than those produced in magmatic process (< 4 in MORB and OIB) (Ryan & Langmuir, 1993; Ryan *et al.*, 1995; Dreyer *et al.*, 2010). However, because of the strong conservation of

tourmaline for B, the tourmaline saturation/solubility in fluids is the important control for the geochemical behavior of B (Nakano & Nakamura, 2001; Bebout & Nakamura, 2003). Lithium has high mobility in fluids and higher contents in sediments (~ 60 ppm) compared with that in MORB, like B, thus may also be used as a tracer of subducting/subducted component in IAB (You *et al.*, 1996; Moriguti & Nakamura, 1998; Zacker *et al.*, 2003; Marschall *et al.*, 2007).

1.1.2 Heterogeneous Mantle Compositions

One of the major advances in the field of solid earth geochemistry over the past ~ 40 years is the recognition of mantle chemical and isotopic heterogeneity through studies of oceanic basalts, including MORB and basalts erupted on intra-plate volcanic islands or OIB. OIB are particularly variable in composition such that several isotopically distinct end-members, e.g., enriched mantle I (EMI), enriched mantle II (EMII), high μ (HIMU; $\mu = {}^{238}U/{}^{204}Pb$) are required to explain the variability (e.g., White, 1985; Zindler & Hart, 1986). The depleted MORB mantle (DMM) is thought to have resulted from the extraction of continental crust from the primitive mantle early in Earth's history (Gast, 1968; O'Nions *et al.*, 1979; Allègre *et al.*, 1983), but the origin of OIB end-members remains enigmatic. Isotopic ratio differences among these end-members reflect the differences in ratios of radioactive parent (P) over radiogenic daughter (D) elements (i.e., P/D) (e.g., Rb/Sr, Sm/Nd, U/Pb and Th/Pb) (Zindler & Hart, 1986) in their ultimate mantle sources, which, with time, evolve to distinctive fields in isotopic ratio spaces (see Niu & O'Hara, 2003). Significant P-D element fractionation in the solid state is considered unlikely in the deep mantle due to extremely slow diffusion rates (Hofmann & Hart, 1978; Van Orman *et al.*, 2002, 2006; Holzapfel *et al.*, 2005) , hence processes known to occur in the upper mantle and crust (e.g., partial melting, magma evolution, metamorphism, weathering, transportation and sedimentation) are possible causes of P-D fractionations (Niu & O'Hara, 2003). Among other processes, mantle metasomatism can effectively cause mantle compositional heterogeneity (Sun & McDonough, 1989; Halliday *et al.*, 1995; Donnelly *et al.*, 2004), and may take place at the base of the growing oceanic lithosphere (e.g., Niu & O'Hara, 2003; Pilet *et al.*, 2008) or in the mantle wedge above subduction zones (Schiano *et al.*, 1995; Ferrari *et al.*, 2001; Donnelly *et al.*, 2004; Currie *et al.*, 2007).

As an inevitable consequence of plate tectonics, subduction of shallow and surface processed materials (SSPM) must volumetrically be the major agent that causes mantle compositional heterogeneity (see the compositional features of representative mantle end-members in Table A.1). This has led to the contention that mantle heterogeneity can be related to specific

subducting/subducted components. For example, (1) altered ocean crust with high U/Pb ratio and appropriate values for other P/D ratios (e.g., Weaver, 1991; Noll Jr *et al.*, 1996; Eiler *et al.*, 1997; Hofmann, 1997) could produce mantle sources with HIMU characteristics, (2) land-derived sediments or upper continental crust materials (e.g., Weaver, 1991; Hofmann, 1997; Willbold & Stracke, 2006) may contribute to EMII type lavas; and (3) pelagic sediments (e.g., Weaver, 1991) or lower continental crust (Willbold & Stracke, 2006) may contribute to EMI type lavas. While these interpretations are apparently reasonable, they cannot be validated without understanding the geochemical effects of SZM and, importantly, metamorphic dehydration has been widely accepted to cause mantle wedge melting for arc magmatism (Armstrong, 1971; Kay *et al.*, 1978; Gill, 1981; Peacock, 1990; McCullough & Gamble, 1991; White *et al.*, 1985; Tatsumi, 1986; Tatsumi *et al.*, 1986; Plank & Langmuir, 1993, 1998; Stolper & Newman, 1994).

1.1.3 The Significance of SZM

As illustrated in Fig. 1.1, the subducted component entering the trench (i.e., $[P/D]_{in}$) must have been modified as it passes through the "subduction factory" (e.g., Tatsumi & Kogiso, 2003) (i.e., $[P/D]_{out}$), so the process mentioned above needs to be accounted for in any realistic mass balance models. We cannot indiscriminately treat the compositions of subducted/subducting sediments (of various types) or AOC as source materials for oceanic basalts without understanding the effects of SZM, because it is the geochemical properties of $[P/D]_{out}$ that contribute to mantle compositional heterogeneity with P/D and isotopic imprints. Essentially, it is the SZM and related geochemical consequences of SZM that can effectively lead to P-D fractionation, which further contributes to the arc magmatism and the deep mantle compositional heterogeneity.

Therefore, a genuine understanding of SZM and behaviors of chemical elements in response to SZM is a major aspect of the chemical geodynamics.

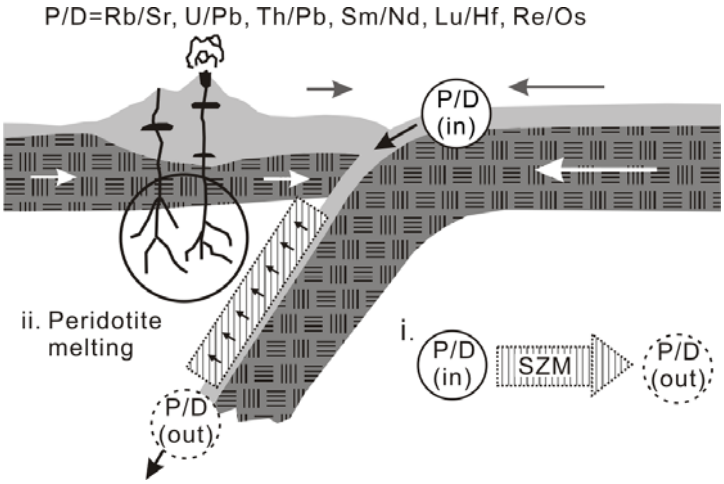

Figure 1.1 Schematic diagram showing the geochemical consequences of subduction-zone metamorphism (SZM), including the likely changes of the subducting materials and the possible effects on elemental ratios of radioactive over radiogenic isotopes (P/D) by dehydration dominated SZM (i), which is also widely accepted to cause the mantle wedge melting for arc magmatism (ii). Conceptually, it is P/D ratios of the residual materials passing through SZM that determine mantle chemical and, with time, isotopic heterogeneities recognized in oceanic basalts (after Niu, 2009).

1.2 THE INTRA-OCEANIC-TYPE SZM

Among other types of metamorphism in different tectonic settings (e.g., contact metamorphism, dynamic metamorphism), subduction-zone metamorphism is characterized by its low temperature at high pressures, which is especially the case for intra-oceanic-type (Fig. 1.2; also see Table A.2 in Appendix A for comparison with continental-type subduction-zone metamorphism). The world-wide distribution of intra-oceanic subduction zones ('cold' subduction zones) with lawsonite-eclogite assemblages is shown in Fig. 1.3. Considering the significant relationship between oceanic-type subduction and continental-type subduction, Fig. 1.3 also shows the distribution of recognized ultrahigh pressure (UHP) metamorphic belts in the world (Liou *et al.*, 2004) although the UHP metamorphism is more likely related to continental-type subduction. The UHP metamorphic conditions can be evidenced by the occurrence of UHP minerals, such as diamond and coesite (see summary in Table 1 of Liou *et al.*, 2004). The peak P-T metamorphic conditions for representative high pressure (HP) – UHP metamorphic belts in the world are given in Fig. 1.4, normally from lawsonite blueschist to (epidote) eclogite facies. The blueschist and eclogite facies rocks are dominant metamorphic rocks from intra-oceanic subduction zones (Table A.2 in Appendix A). Although their protoliths can be highly variable, MORB and sedimentary rocks are the most common lithologies for their protoliths.

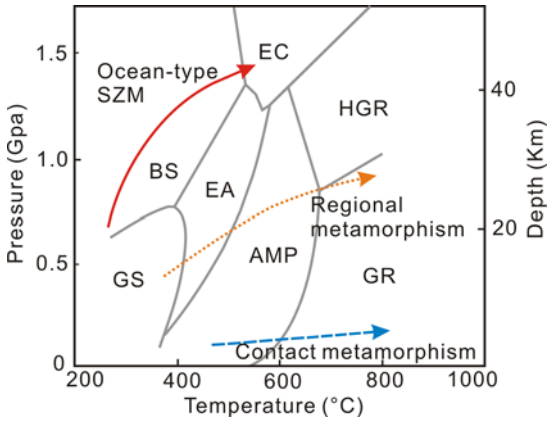

Figure 1.2 P-T diagram for different geothermal gradients (modified after Maruyama *et al.*, 2010). The metamorphic facies boundaries are after Liou *et al.* (2004), as we used in Fig. 2.3 and Fig. 2.6. The red solid curve – the schematic P-T path of ocean-type subduction-zone metamorphism; the orange dotted curve – the P-T path of regional metamorphism in continental orogenic belts; the blue dash curve – the P-T path of contact metamorphism. See Abbreviation List for all the abbreviations used.

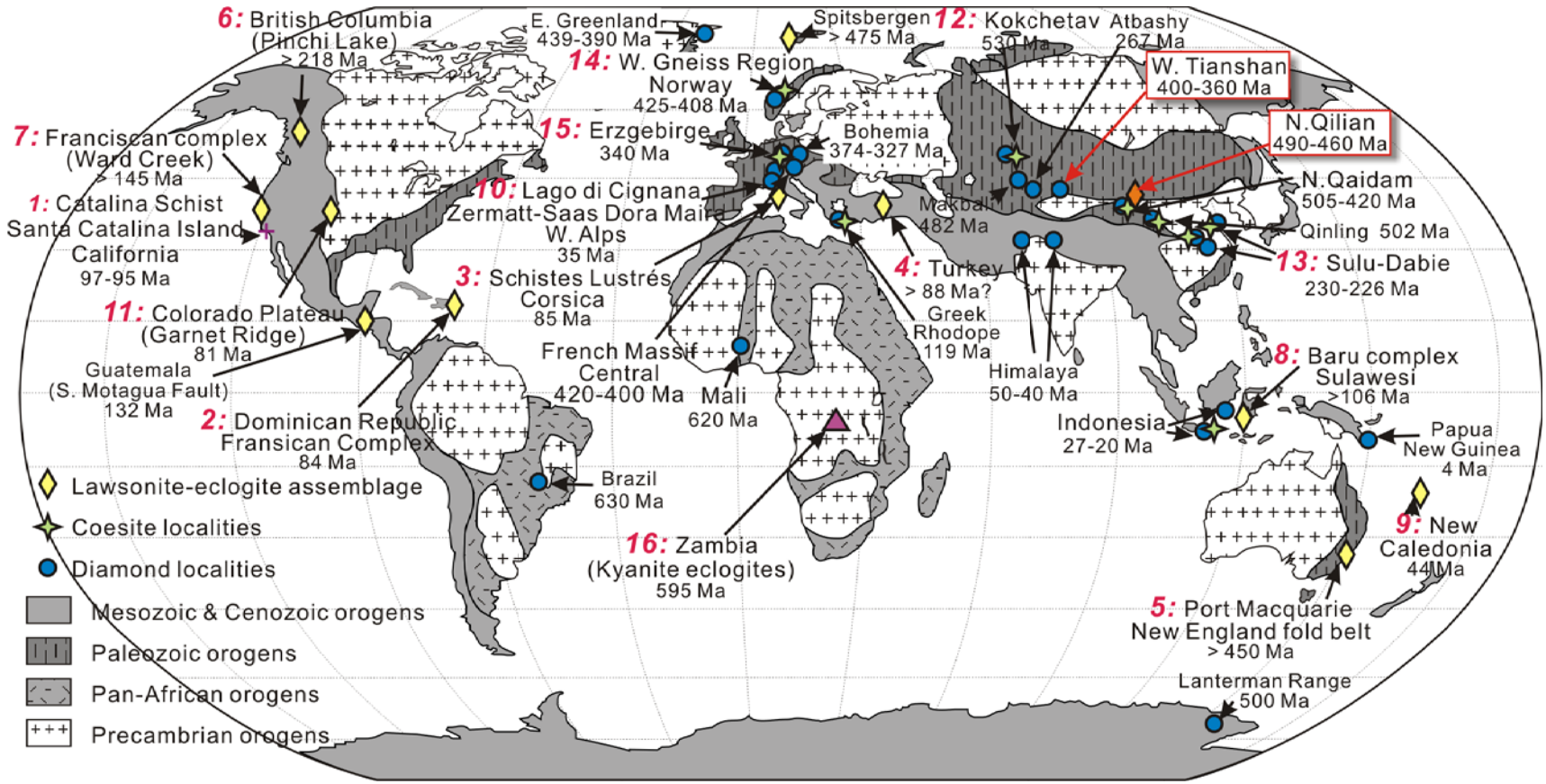

Figure 1.3 Distribution and peak metamorphic age of HP-UHP metamorphic rocks in the world (modified from Liou *et al.*, 2004; Tsujimori *et al.*, 2006). The occurrence of lawsonite-eclogite assemblage marks intra-oceanic subduction zones, while those localities with coesite- and diamond-bearing UHP metamorphic rocks (referred to Liou *et al.*, 2004) are more likely represent those continental-type subduction zones. The location of North Qilian Mountain, one of our study areas, has been added with the age data of Zhang *et al.* (2007) and Song *et al.* (2009), and together with Tianshan, has been highlighted. Kyanite eclogite from Zambia (Location 16) with the Sm-Nd isochron age of 595 Ma (John *et al.*, 2003)and Catalina Schist in Santa Catalina Island from California (Location 1) with the age of 97-95 Ma (Grove *et al.*, 2008), have also been plotted. All the numbers in front for each locality are as used in Fig. 1.4.

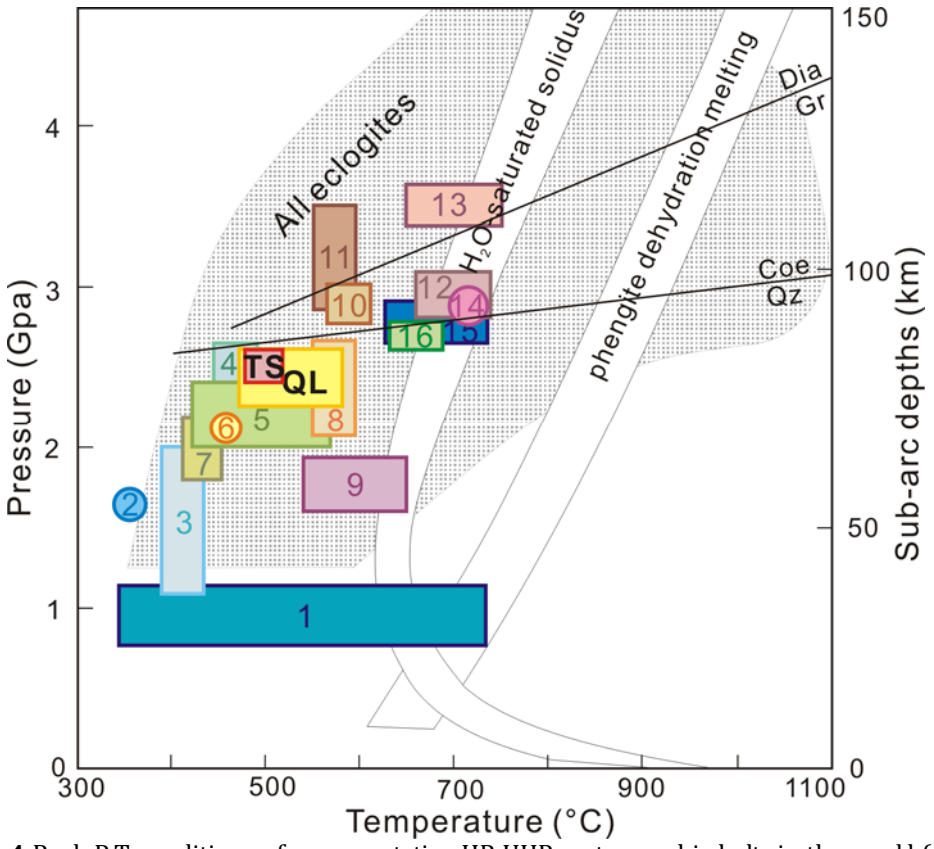

Figure 1.4 Peak P-T conditions of representative HP-UHP metamorphic belts in the world (modified from Tsujimori *et al.*, 2006 and Bebout, 2007). Each number in rectangles or circles points to the specific HP-UHP metamorphic locality in Fig. 1.3. Our two study areas, North Qilian Mountain and Western Tianshan, have been highlighted, TS – Western Tianshan (Lü *et al.*, 2009), QL – North Qilian Mountain (Song *et al.*., 2009).

1.3 MODELS OF GEOCHEMICAL PROCESSES DURING SZM

1.3.1 Previous Models, Limitations and General Progresses

A common point in previous models is that the breakdown of amphibole in subducting oceanic crust during the transition from blueschist to eclogite facies, which is the major dehydration process (Peacock, 1993; Pawley & Holloway, 1993; Liu *et al.*, 1996), was thought to trigger partial melting of mantle wedge directly or indirectly (see details summarized in Ringwood, 1979 and Arculus, 1994). For example, Tatusmi and co-workers (Tatusmi, 1986; Tatsumi *et al.*, 1986; Tatsumi & Eggins, 1995; Tatsumi & Kogiso, 1997) proposed that the subducted slab rocks may have released all its fluids beneath the forearc as the result of amphibole breakdown (most likely glaucophane; Tatsumi & Eggins, 1995; Liu *et al.*, 1996) and will hydrate peridotite at the base of the mantle wedge. They further explained that when this hydrous peridotite was dragged

down by coupling to the subducting slab, it would experience the dehydration as a result of the breakdown of amphibole at 3.5 GPa and phlogopite at 6.0 GPa respectively. Therefore, the dehydration processes were considered as a series of discontinuous reactions (a sudden change in mineral assemblages as a result of the facies change) strictly controlled by the metamorphic conditions, and the mantle wedge melting to generate IAB is thus a response to such dehydration reactions (Tatsumi, 1986; Tatsumi *et al.*, 1986, 1995; Wyllie, 1988).

Glaucophane is the volumetrically most important hydrous mineral responsible for the dehydration reactions from blueschist to eclogite facies (Tatsumi & Kogiso, 1997; Peacock, 1990, 1993; Liu *et al.*, 1996). However, in recent studies, other HP hydrous metamorphic minerals and even UHP hydrous minerals beyond the stability of amphibole (> ~ 2.5 GPa; e.g., phengite, lawsonite, zoisite and allanite) have been recognized in natural rocks under subduction-zone metamorphic conditions (see Table A.3 in Appendix A; Sorensen, 1991; Thompson, 1992; Liu *et al.*, 1996; Sorensen *et al.*, 1997; Hermann, 2002). This has also been verified experimentally on the stability of different metamorphic minerals under SZM conditions (Pawley & Holloway, 1993; Pawley, 1994; Schmidt, 1995; Poli & Schmidt, 1995, 1998, 2002; Schmidt & Poli, 1994, 1998, 2003; Domanik & Holloway, 1996, 2000). All these indicated that the breakdown of amphibole cannot liberate all the fluids in the subducting slab rocks completely (e.g., Forneris & Holloway, 2003), and even the apparently "dry eclogite" can carry ~ 1 – 2 vol.% fluids hosted in lawsonite and phengite to up to 150 km depth (Poli & Schmidt, 1995; Mibe *et al.*, 2003). Recent studies revealed that even if there are no hydrous minerals present in eclogites, nominally anhydrous minerals can be responsible for transporting trace amounts of water, even down to the lower mantle, especially through those 'coldest' subduction zones, e.g., up to 870 ppm H_2O in omphacite, 130 ppm in garnet, 740 ppm in rutile at ~ 6.0 GPa and ~ 1000°C (Katayama *et al.*, 2006), and up to 3010 ± 300 ppm H_2O in Al-bearing stishovite at 20 GPa and 1400°C (Litasov *et al.*, 2007).

SZM itself is much more complex than previous thought and controlled by many factors. (1) Varied geothermal conditions in different subduction zones (Pawley & Holloway, 1993; Peacock & Wang, 1999; also see Figure 5 in Bebout, 2007). (2) Heterogeneous geothermal structure within a given subducting slab (Peacock, 1993). (3) Reaction kinetics, including: I. element diffusion rate that will also affect trace element partitioning (Carlson, 1989, 2002; Schmidt & Poli, 2003; King *et al.*, 2004; Lucassen *et al.*, 2010); II. the chemical gradient between interacted fluids and rocks (van der Straaten *et al.*, 2008; Beinlich *et al.*, 2010); III. the relative rate of an older phase breakdown and a new one precipitation, also element transport

rates and complexation (Zack & John, 2007; John *et al.*, 2008; van der Straaten *et al.*, 2008; Beinlich *et al.*, 2010). (4) Varying bulk-rock compositions and lithologies within the subducting slab (Spandler *et al.*, 2004). (5) Fluid compositions, abundances and flow mechanisms (Zack *et al.*, 2001; Manning, 2004; Zack & John, 2007; John *et al.*, 2008). (6) Oxidation state (Rebay *et al.*, 2010). The contribution of continuous reactions (minor phase changes and solid-solution adjustment) to partial melting of mantle wedge has also been largely emphasized by recent studies (e.g., Schmidt & Poli, 1998, 2003), although the mobilization of trace elements may be still controlled by pulses released from their hosts. Schmidt & Poli (2003) proposed a model combining both stepwise and continuous reactions happening simultaneously in different parts of the subducting slab, instead of simple discontinuous dehydrations in previous models (e.g., Tatsumi, 1986; Tatsumi & Eggins, 1995; Tatsumi & Kogiso, 1997).

More importantly, detailed analyses of trace element contents of metamorphic minerals revealed that some of these HP-UHP metamorphic minerals have a strong capacity for hosting trace elements (Nagasaki & Enami, 1998; Zack *et al.*, 2001; Feineman *et al.*, 2007; Bebout *et al.*, 2007; Tamura *et al.*, 2007; El Korh *et al.*, 2009), including those "highly mobile elements" considered in previous studies (e.g., McCulloch & Gamble, 1991). This indicates that metamorphic minerals are not only capable of accommodating fluids in the form of hydroxyl or H_2O but can also sequester fluid-soluble elements after the breakdown of amphibole. Therefore, element mobility is controlled by both dehydration reactions and the stability of newly formed hydrous phases. Retention of these elements may result in a complicated element transfer process during SZM, even obvious decoupling between element mobility and dehydration associated with the transition from blueschist to eclogite facies (Hermann, 2002; Spandler *et al.*, 2003). Klimm *et al.* (2008) and Hermann & Rubatto (2009) proposed that even accessory minerals can significantly conserve their preferential elements, e.g., LREEs and Th (U to a lesser extent) can be largely conserved in allanite after the breakdown of zoisite (Hermann, 2002). It follows that the fluids and the otherwise mobile elements can be carried in the subducting ocean crust (and sediments) for as long and deep as the host hydrous minerals remain stable.

All the discussions above indicate that careful studies on the stability of mineral assemblages, reactions among minerals, and the trace element (re)distributions in response to specific metamorphic histories are crucial for understanding the mass transfer from subducting slab rocks to the magma source of IAB.

1.3.2 Trace Element in Different Mineral Phases

Recent studies, especially micro-analytical techniques (e.g., Laser Ablation-Inductively Coupled Plasma Mass Spectrometry, LA-ICP-MS; Secondary-ion Mass Spectrometry, SIMS) allow for *in situ* mineral analyses with high precision and accuracy. This largely improved our understanding of highly heterogeneous compositions of metamorphic minerals (e.g., Tribuzio *et al.*, 1996; Zack *et al.*, 2001; Spandler *et al.*, 2003; King *et al.*, 2004; van der Straaten *et al.*, 2008; El Korh *et al.*, 2009; Schmidt *et al.*, 2009; Beinlich *et al.*, 2010).

Garnet is commonly enriched in middle-heavy rare earth elements (M-HREEs; Tribuzio *et al.*, 1996; Spandler *et al.*, 2003; King *et al.*, 2004; El Korh *et al.*, 2009; Beinlich *et al.*, 2010). Normally, it shows a chondrite-normalized pattern with higher HREE/MREE ratios, but crystals with MREE > HREE patterns have also been reported (Spandler *et al.*, 2003; Konrad-Schmolke *et al.*, 2008). Phengite has been found to be the major host of K, Ba, Rb and Cs in the whole rock (Sorensen *et al.*, 1997; Becker *et al.*, 2000; Melzer & Wunder, 2000; Zack *et al.*, 2001; El Korh *et al.*, 2009; Beinlich *et al.*, 2010). Epidote group minerals, including epidote, (clino)zoisite, and allanite along with lawsonite, can host most Sr, Pb, U, Th and REEs to varying extents (Sorensen, 1991; Tribuzio *et al.*, 1996; Nagasaki & Enami, 1998; Brunsmann *et al.*, 2001; Hermann, 2002; Spandler *et al.*, 2003; van der Straaten *et al.*, 2008; El Korh *et al.*, 2009). Apatite can also host REEs and Sr (Zack *et al.*, 2001; van der Straaten *et al.*, 2008; El Korh *et al.*, 2009; Beinlich *et al.*, 2010). Experimental studies show variably high partition coefficients for REEs between epidote group minerals and fluids (Brunsmann *et al.*, 2001; Feineman *et al.*, 2007; Martin *et al.*, 2011). Rutile and titanite host essentially all the Ti, Nb and Ta in the bulk rock (e.g., Stalder *et al.*, 1998; Hermann, 2002; El Korh *et al.*, 2009), and titanite may also have high contents of REEs (Tribuzio *et al.*, 1996; van der Straaten *et al.*, 2008; El Korh *et al.*, 2009; Beinlich *et al.*, 2010), while zircon is responsible for almost all Zr and Hf in the bulk rock (e.g., Hermann, 2002; Rubatto & Hermann, 2003). Carbonate can host some Sr (van der Straaten *et al.*, 2008; Beinlich *et al.*, 2010). Volumetrically, major metamorphic minerals like glaucophane and omphacite, on the other hand, contribute little to the bulk-rock trace element budgets (e.g., El Korh *et al.*, 2009).

1.3.3 Stability of HP-UHP Metamorphic Minerals

Other hydrous minerals carrying fluids and otherwise mobile elements can remain stable far deeper than the stability of amphibole (2 – 2.6 GPa at 700°C, Pawley & Holloway, 1993; up to 3

GPa at 625°C for glaucophane, Forneris & Holloway, 2003). A large body of experimental studies in the recent literature have provided important constraints on the stability of HP-UHP metamorphic minerals.

Lawsonite is stable up to 12 GPa at 960°C (~ 360 km; Schmidt & Poli, 1994; Schmidt, 1995). Clinozoisite (and zoisite) is reported to be stable at 3.2 GPa (~ 100 km; Pawley & Holloway, 1993), but others show this mineral can be stable up to 6.5 – 6.8 GPa at 800 – 1200°C (Schmidt & Poli, 1994; Poli & Schmidt, 1998). Furthermore, Forneris & Holloway (2003) pointed out that at the pressures above the stability field of amphibole, lawsonite should be stable at temperatures below 645°C, above which (clino)zoisite becomes stable. Comparing with previous studies (Schmidt & Poli, 1998), a small difference of 35°C of the estimated temperature for the stability of lawsonite and (clino)zoisite (i.e., the replacement from lawsonite to zoisite) can result in a big difference in the estimated dehydration depth (e.g., 90 – 100 km vs. > 150 km deep reported by Schmidt & Poli [1998]). In addition, Hermann (2002) reported that at the expense of zoisite at > 700°C and 2.0 GPa, allanite will be formed and can incorporate LREEs stable up to 1050°C (900°C and 1000°C for meta-basalts and meta-sediments respectively) at pressures no less than 4.5 GPa.

Phengite can be stable up to 10 GPa (~ 300 km; Sorensen *et al.*, 1997; Domanik & Holloway, 1996, 2000; Poli & Schmidt, 2002). Based on the experimental study on meta-pelite from Dabie Mountain, Domanik & Holloway (2000) reported that phengite will be melted at 1075-1150°C and 7 – 8 GPa, or 1000 – 1050°C and 10 GPa. At 800°C and 10 – 11 GPa, phengitic muscovite will be replaced by octahedral-cation-deficient muscovite and K-hollandite (Domanik & Holloway, 1996, 2000), the latter of which can be subducted to the deep mantle, i.e., > 16 – 23 GPa (as the important host for LILEs, Pb, Th, U and LREEs; Rapp *et al.*, 2008).

Therefore, to understand dehydration processes and the behaviors of commonly perceived fluid-mobile elements during SZM, it is necessary to understand the stability of the above discussed hydrous metamorphic minerals and the related metamorphic reactions. The identification and the estimation of modal abundances of these minerals in the rocks are also necessary.

1.3.4 About Fluids During SZM

Although the fluids release from the subducting ocean crust (with the overlying sediments) is well known, the fluid composition has been hotly debated. Considering the strong control of

fluid compositions on elemental behaviors, the knowledge of fluid composition is important for understanding element transfer during SZM (Philippot & Selverstone, 1991; Manning *et al.*, 2004).

The most direct way to assess the fluid composition is to study fluid inclusions in SZM minerals (Philippot, 1993; Sisson & Layne, 1993; Scambelluri *et al.*, 1997; Gao & Klemd, 2001). The HP dehydration veins and/or transport veins formed during the transition from blueschist to eclogite facies have also been used to study fluid compositions. For example, Philippot & Selverstone (1991) studied eclogitic veins from the Monviso ophiolitic complex in Western Alps. Others have studied similar veins from Western Tianshan and the reaction relationship with the wall-rock (Gao & Klemd, 2001; John *et al.*, 2008; Zack & John, 2007). The dehydration vein is argued to be surrounded by a reaction zone, while the transport vein has a sharp boundary with the wall-rock and taken as the pathway for an external fluid. These two types of veins may actually represent different evolution stages of a SZM vein (John *et al.*, 2008).

Several potential fluid compositions in subduction zones proposed in recent literature are given below. (1) Aqueous fluids: H_2O-rich or CO_2-rich fluids (with total amount of dissolved solids < 30 wt.%; Walker *et al.*, 2003; Gao & Klemd, 2001; Philippot, 1993) vs. saline brines (Philippot, 1993; Keppler, 1996; Scambelluri *et al.*, 1997; Manning, 2004), which are also identified as non-wetting fluids and wetting fluids respectively by Selverstone *et al.* (1992). Furthermore, Mannning (2004) emphasized the presence of dissolved alkali-aluminosilicate in fluids. (2) Hydrous melts (or SiO_2-rich fluids, H_2O < 35 wt.%): e.g., Hermann, 2002; Hermann *et al.*, 2006; Hermann & Rubatto, 2009. And (3) supercritical fluids (e.g., Schmidt *et al.*, 2004a; Kessel *et al.*, 2005; Stern *et al.*, 2006; Mibe *et al.*, 2011). As experimental works showed that the solubility of both water in silicate melts and silicate in aqueous fluids increases with increasing pressure, at and above a certain critical condition (for subduction zones, it is the second critical endpoint, where the closure of the fluid-melt solvus intersected with the fluid-saturated solidus, Schmidt *et al.*, 2004a), aqueous fluids and hydrous silicate melts will be indistinguishable and become a single fluid phase, which is termed as supercritical fluids. It is also defined as transitional fluids with solute-rich component by Hermann *et al.* (2006), and defined as supercritical melts by Schmidt *et al.* (2004a) to distinguish it from the "supercritical fluids", which is produced as a result of the closure of the liquid-gas curve.

The latter two concepts, supercritical fluids and hydrous melts derived from subducting sediments at deeper depths of subduction zones or along the relatively hot slab-mantle wedge

interface, are widely invoked in recent studies (Ryan *et al.*, 1995; Spandler *et al.*, 2003; Stern *et al.*, 2006; Tamura *et al.*, 2007; Herman, 2002; Hermann *et al.*, 2006; Hermann & Rubatto, 2009; Regelous *et al.*, 2010; Mibe *et al.*, 2011). The pressure for the occurrence of supercritical fluids is closely associated with bulk-rock compositions (Schmidt *et al.*, 2004a). Based on the recent experiments, supercritical fluids derived from the subducting ocean crust appear to form beyond 3.4 GPa at 770°C (as shown in Fig. 3 of Mibe *et al.*, 2011) and 5 – 6 GPa at 800 – 1200°C (Schmidt *et al.*, 2004a; Kessel *et al.*, 2005). The experimental study of Kessel *et al.* (2005) on supercritical fluids from rutile-bearing eclogite modeled the element partitioning between the eclogitic residues and the supercritical fluids, the composition of which resembles the characteristic arc signature (also see Mibe *et al.*, 2011). Considering the strong conservation of LILEs in phengite, the breakdown/dissolution of phengite in supercritical fluids (e.g., Schmidt *et al.*, 2004a) may be responsible for the enriched LILEs in arc lavas. Furthermore, the breakdown/dissolution of phengite in a supercritical fluid has also been used to explain the across-arc K-h relationship (e.g., Tamura *et al.*, 2007). Considering the strong conservation of LREEs, Th and less U in allanite that can only be dissolved in a hydrous melt at high temperature rather than fluids, it has also been argued that hydrous melting of subducting sediments may be responsible for the enrichment of LREEs, Th and U in arc magmas (Hermann, 2002; Hermann *et al.*, 2006; Hermann & Rubatto, 2009).

In addition to the effect of fluid compositions, the importance of fluid content (e.g., higher content in permeable mélange zones) and the fluid flow mechanism (channels/veins vs. porous fluids) have also been emphasized as important controls on the fluid-rock interactions during SZM (Zack *et al.*, 2001; Manning, 2004; Zack & John, 2007; John *et al.*, 2008). It is argued that the high fluid/rock ratios can generally enhance the mobility of trace elements, and even REEs and HFSEs can be moderately mobilized in a high fluid flux system (Zack & John, 2007; John *et al.*, 2008; Bebout, 2007).

1.3.5 Response of Chemical Elements to SZM

The 'traditional' method (reverse model) to deduce the possible contributions of subducting/subducted slab rocks to arc magmas is based on the geochemistry of IAB (e.g., Tatsumi & Kogiso, 1997; Churikova *et al.*, 2001; Tamura *et al.*, 2007; Regelous *et al.*, 2010) or melt inclusions in IAB phenocrysts (e.g., Cervantes & Wallace, 2003; Walker *et al.*, 2003). On the other hand, in terms of subducting slab rocks there are generally two more methods to estimate the mobilization of trace elements in response to SZM (forward model).

One is to directly measure the composition of HP veins/segregations formed during eclogitisation (Becker *et al.*, 1999; Brunsmann *et al.*, 2000; Spandler & Hermann, 2006; Gao *et al.*, 2007; John *et al.*, 2008), and/or to compare the composition of selvages and unaltered host rock using mass balance calculations (e.g., van der Straaten *et al.*, 2008; Beinlich *et al.*, 2010) or that of the unaltered equivalent protoliths (Spandler *et al.*, 2004; John *et al.*, 2004; Breeding *et al.*, 2004). The advantage of this method is that it can identify and quantitatively evaluate the specific chemical changes during the SZM (also retrograde metamorphism during exhumation). However, because metamorphic rocks have highly heterogeneous bulk-rock compositions (Spandler *et al.*, 2004) and mineral distributions, the representative composition of the protoliths of altered metamorphic rocks is not always easily found. Therefore, this method may include the effects of bulk-rock compositional heterogeneity (Bebout, 2007).

The other method is to analyze the composition of each of the constituent mineral phases to evaluate the budget of different elements. Together with the detailed petrography and the study of potential metamorphic reactions during SZM, possible geochemical changes can be theoretically estimated (e.g., Tribuzio *et al.*, 1996; Becker *et al.*, 2000; Zack *et al.*, 2001; Spandler *et al.*, 2003; El Korh *et al.*, 2009). This method is also important for understanding the mass transfer in subduction zones. Note that the element mobility discussed in this thesis refers to the mobility in aqueous fluids, not hydrous melts or supercritical fluids.

1.3.5.1 LILEs (including Ba, Rb, Cs, K), Pb, Sr mobility/immobility

Because of the relative enrichment of LILEs and the relative depletion of HFSEs in IAB (i.e., the characteristic “arc signature”) compared with oceanic basalts, the composition of IAB can be used to deduce the composition and contribution of slab-derived fluids (see section 1.1.1.2; e.g., Arculus, 1994). Such comparison has led to the perception that LILEs have been mobilized during the SZM if IAB magmatism is indeed triggered by flux melting (e.g., Kay *et al.*, 1978; McCulloch *et al.*, 1991; Cervantes & Wallace, 2003; Regelous *et al.*, 2010). On the other hand, the strong conservation of LILEs and the wide stability range of phengite seem to result in the immobility of LILEs (Spandler *et al.*, 2003), which contradicts the earlier general inference (also see Breeding *et al.*, 2004). Spandler *et al.* (2003) proposed that even those assumed highly mobile elements would not show their mobility except in relatively hot zones in the slab, e.g., along the subducting slab-mantle wedge interface. However, most studies on natural SZM HP-UHP rocks seem to show a first-order LILEs mobility (e.g., Beck *et al.*, 2000; Breeding *et al.*, 2004; Beinlich *et al.*, 2010; Xiao *et al.*, 2012 or Chapter 4).

1.3.5.2 Ambiguous mobility/immobility of LREEs

Although we also observed relatively enriched LREEs in IAB compared with MORB, the geochemical behavior of LREEs in response to SZM is hotly debated, and different conclusions are reached based on different experiments and studies on natural rocks. Comparing eclogites of gabbroic protolith with their precursor, i.e., unaltered gabbros, from Zambia, John *et al.* (2004) suggested that LREEs were mobilized during this eclogitization process. Based on decreasing modal amounts of LREE-rich epidote and decreasing LREE contents in epidote towards segregation veins, Brunsmann *et al.* (2000) also pointed out the mobility of LREEs, which is further supported by their subsequent experimental work on partition coefficients between zoisite and fluids (Brunsmann *et al.*, 2001). Different fluid compositions have different influences on elemental behaviors (see Section 1.3.4). Supercritical fluids (Kessel *et al.*, 2005) and hydrous melts (Hermann, 2002; Hermann *et al.*, 2006; Hermann & Rubatto, 2009) are proposed to have strong ability to carry LREEs, which may be the primary control on LREE-enrichment in arc magmas. Studies on dehydration/transport veins in Western Tianshan (Zack & John, 2007; John *et al.*, 2008) suggest that given an aqueous fluid, reaction kinetics (e.g., chemical gradient, high temperature in the slab, Zack & John, 2007) and high fluid/rock ratios (Bebout, 2007) may be crucial for mobility of LREEs.

In contrast, Feineman *et al.* (2007) have shown experimentally that LREEs are preferentially incorporated into zoisite, which differs from the conclusion by of Brunsmann *et al.* (2001). In addition, because of the strong controls on REE budgets by lawsonite and epidote, Tribuzio *et al.* (1996) proposed that REEs would be redistributed into newly-formed epidote group minerals without significant liberation during SZM and carried into the deep mantle. Others have also show immobility of LREEs during SZM (e.g., Becker *et al.*, 1999, 2000; Spandler *et al.*, 2003; Usui *et al.*, 2007). More importantly, Hermann (2002) showed experimentally that allanite, the most important high temperature LREE-carrier (also for Th and less U), can host these preferential elements after the breakdown of zoisite. Therefore, LREEs will be redistributed between lawsonite, epidote, (clino)zoisite, and allanite covering much of the SZM temperature range.

1.3.5.3 Th and U

On the mobility/immobility of Th and U, it seems complex and also critical for understanding the petrogenesis of IAB (e.g., Gill & Williams, 1990; Hawkesworth *et al.*, 1993, 1997). U is

considered highly mobile in its U^{6+} form (vs. U^{4+}) while Th is water insoluble (Bailey & Ragnarsdottir, 1994). Therefore, the elevated U/Th ratios observed in IAB (0.44 for average value of U/Th ratio in highly depleted arc lavas) compared with those in the bulk Earth (0.26) and the depleted upper mantle (0.39) (Hawkesworth *et al.*, 1997), is most likely caused by fluid addition of U into the IAB source region as the result of subducting slab dehydration (Gill & Williams, 1990; Bailey & Ragnarsdottir, 1994; Brenan *et al.*, 1995). John *et al.* (2008) and Zack & John (2007) argued that Th and other 'immobile' elements could be mobile and carried by aqueous fluids, depending on many factors (including dissolution rates, elemental solubility of the fluid, subduction-zone thermal structures).

In contrast, based on the global HP-UHP metamorphic rocks, Becker *et al.* (2000) demonstrated the immobility of Th and moderate mobility of U during SZM. However, they attributed the mobility of U to the addition of U during seafloor alterations with limited or negligible loss during SZM (also see Chapter 6). Beinlich *et al.* (2010) pointed out that U and Th showed similar behavior to LREEs because they are largely hosted by the same carriers (epidote group minerals), resulting in significant correlations among them in SZM rocks, also relatively constant U/Th ratios (ranging from 0.25 in the blueschist host to 0.23 in the eclogitic selvage around the vein). The constant U/Th ratio is also reported by Xiao *et al.* (2012; see Chapter 4). The immobility of Th and U may also be controlled by the presence of allanite at higher temperatures beyond the stability of zoisite, as is the case for LREEs (Hermann, 2002).

1.3.5.4 HFSEs immobility and Nb/Ta ratios

Although HFSEs were widely considered to be immobile/insoluble during SZM (Kogiso *et al.*, 1997; Tropper & Manning, 2005; Audétat & Keppler, 2005), the mobility of HFSEs has also been reported in some studies (e.g., the presence of Ti-bearing minerals in eclogitic veins, Philippot & Selverstone, 1991; Gao *et al.*, 2001; Woodhead *et al.*, 2001 for Hf mobility). Ayers & Watson (1993) proposed that supercritical fluids can increase the solubility of rutile and the mobility of Ti, which is dissolved as the neutrally-charged $Ti(OH)_4$ in the fluids. Manning and his co-workers (Manning *et al.*, 2008; Antignano & Manning, 2008; Hayden & Manning. 2011) emphasized that the significance of dissolved Na-Al silicates, which increased the solubility of rutile through polymerization/complexation with alkali aluminosilicate components (also see Gao *et al.*, 2007; Tropper & Manning, 2005), but limited the stability field and the function of supercritical fluids. Rapp *et al.* (2010) emphasized the importance of halogen, especially F^- than chloride in fluids (also see Bright & Readey, 1987) in controlling the solubility of rutile and the

mobility of Nb-Ta-Ti. However, all these studies agree that the pure H_2O fluids have insignificant solubility of rutile. Alternatively, Zack & John (2007) and John *et al.* (2008) emphasized the effect of reaction kinetics and high fluid/rock ratios (van Baalen, 1993) in controlling the rutile solubility, and may allow HFSEs to be carried by aqueous fluids. Comparing the eclogitic selvage around the vein, as the product of alteration by fluid-blueschist interaction during the infiltration of external Ca-rich fluids, with the unaltered blueschist host in Western Tianshan, Beinlich *et al.* (2010) also reported the mobility of Nb and Ta (depleted by ~ 30%), which were decoupled from Zr and Hf (only ~ 10%).

If rutile (or Ti) indeed has high solubility and HFSEs are actually mobilized as discussed above, the depletion of HFSEs observed in arc magmas thus cannot be attributed to the depletion of these elements in the fluids released from the subducting slab. In that case, other processes and mechanism are required for the depletion of HFSEs in arc magmas (Rapp *et al.*, 2010; also see summary in Audétat & Keppler, 2005), e.g., changes in fluid composition and the re-precipitation of rutile along the passage from the subducting slab to the mantle wedge (Gao *et al.*, 2007). Alternatively, the mobility of HFSEs may be only a local phenomenon, and in most cases of subduction zones, HFSEs remain immobile.

Nb and Ta, sharing same ionic charge (+ 5) and similar atomic radii (Ta is about 0.015 Å smaller; Shannon, 1976), are expected to have similar behaviors without significant fractionation during geological processes. However, the Nb/Ta ratios of major silicate reservoirs, e.g., continental crust (~ 12; Barth *et al.*, 2000), MORB (14.2 ± 0.8; Münker *et al.*, 2003) and OIB (15.8 ± 1.6; Pfänder *et al.*, 2007) are all subchondritic ($[Nb/Ta]_{chondrite}$ = 17.4 ± 0.5 from Jochum *et al.*, 2000). By accepting the assumption that the primordial Earth has chondritic Nb/Ta, there should be a missing reservoir with superchondritic Nb/Ta in the bulk silicate Earth (BSE), which might be caused by the subduction of rutile-bearing eclogites into the deep mantle during the Archean (Rudnick *et al.*, 2000). In addition, Niu and co-authors (Niu & Batiza, 1997; Niu *et al.*, 2002; Niu, 2004) found that Nb/Ta is correlated with Zr/Hf and other ratios with elements more incompatible in the numerator than in the denominator (e.g., Th/U, La/Sm), as well as radiogenic isotopic ratios, indicating Nb – Ta (also Zr – Hf) fractionation is of magmatic origin, as suggested by recent experimental work (Kalfoun *et al.*, 2002; Schmidt *et al.*, 2004b; Klemme *et al.*, 2005). In this context, it is important to constrain the distribution and fractionation of Nb and Ta in Ti-rich minerals (e.g., rutile and titanite) through SZM (see Chapter 6).

1.4 THESIS AIMS AND OUTLINE

In this study, based on the HP-UHP metamorphic rocks from Western Tianshan and North Qilian Mountain in Northwest China (Fig. 1.5), we reported the analytical results of both bulk-rock compositions and the constituent mineral compositions.

The primary purposes of this thesis are:

(1) to identify and characterize the geochemical behaviors (e.g., mobility/immobility) of some petrologically important "incompatible" elements during SZM;
(2) to reconstruct trace element budgets in mineral assemblages and bulk-rock samples using analytical results of mineral compositions and mineral modal abundances;
(3) to understand the controls on element behaviors during SZM and possible elemental responses to mineral stability at different metamorphic stages along a specific P-T path;
(4) to access possible contributions of SZM to subduction-zone magmatism and mantle compositional heterogeneity using SZM rock samples from two orogenic belts.

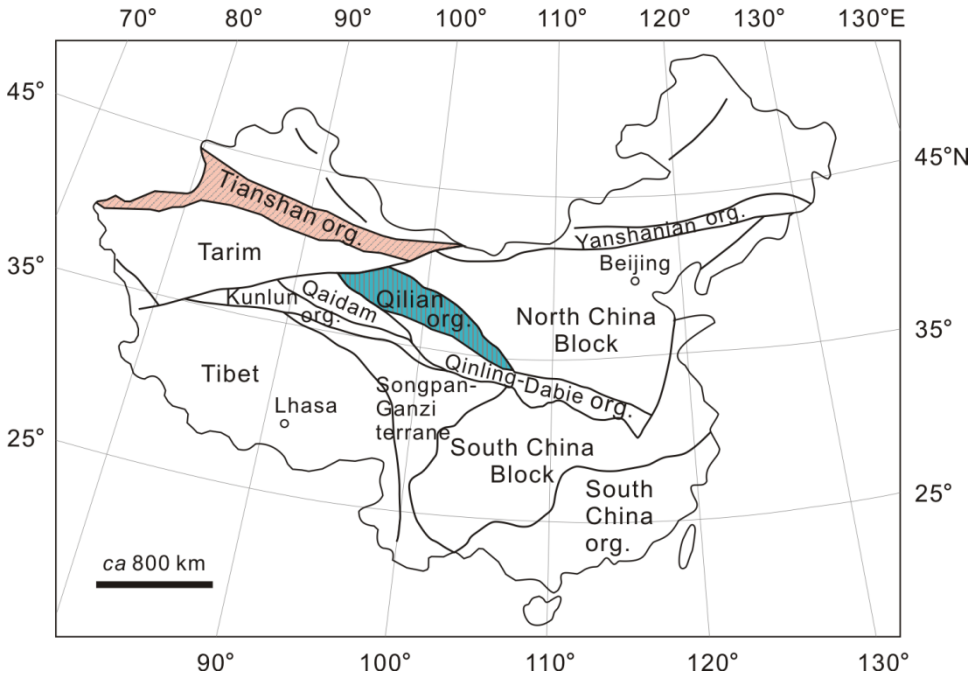

Figure 1.5 Simplified tectonic map of China, showing positions of the two study areas, i.e., Tianshan and Qilian Mountain in NW of China (modified from Meng *et al.*, 2000). Org.: orogen.

The outline of this thesis is:

Chapter 2: Introduces the brief geology of the two study areas, i.e., Western Tianshan and North

Qilian Mountain in Northwest China through critically summarizing the relevant literature, including the tectonic units, the tectonic evolution and metamorphic history. The updated conclusions on chronological and metamorphic conditions are also discussed.

Chapter 3: Briefly introduces the analytical techniques/instruments and methods used for both bulk-rock and mineral compositions.

Chapter 4: Discusses the petrology and the bulk-rock geochemistry of metamorphic rocks from UHP metamorphic belt of Western Tianshan, including rock classification and protolith discrimination. The mobility/immobility of trace elements during SZM on bulk-rock scales is also discussed. The contribution of SZM to subduction-zone magmatism and mantle compositional heterogeneity is also discussed.

Chapter 5: Reports the analytical results of mineral compositions from rocks discussed in ***Chapter 4*** from Western Tianshan. Together with the mineral modal data, trace element budgets are evaluated, and elemental (re)distribution/transportation and their controls during SZM are also discussed in some detail.

Chapter 6: Reports the results on samples from North Qilian Mountain, as for Western Tianshan in Chapters 4 and 5, and compares the two cases in terms of SZM and its effects on elemental behaviors.

Chapter 7: Combines the conclusions from Western Tianshan and North Qilian Mountain, generalizes the assumptions and conclusions from these studies to discuss the effect of SZM on subduction-zone related magmatism.

Chapter 8: Gives, in this final chapter, a brief summary of the major conclusions of this PhD thesis on the geochemical consequences of subduction-zone metamorphism.

All the abbreviations used in this thesis are given in the Abbreviation List.

1.5 AUTHORS CONTRIBUTIONS

1.5.1 Chapter 4

This has been accepted by the ***Geological Society of America Bulletin*** and is currently in press.

Yuanyuan Xiao (*Department of Earth Sciences, Durham University, Durham, DH1 3LE, UK*): I did point counting for mineral phases in each sample and detailed petrological study. I wrote the manuscript then passed it on for feedback from co-authors, whose comments improved the flow of the paper, but did not alter the interpretations or conclusions drawn.

Shaun Lavis (*School of Earth and Ocean Sciences, Cardiff University, Cardiff, CF10 3YE, UK):* SL participated in the sampling program and carried analytical work on bulk-rock compositions using Inductively Coupled Plasma-Optical Emission Spectrometer (ICP-OES) and Inductively Coupled Plasma-Mass Spectrometer (ICP-MS), along with valuable discussion of data interpretation.

Yaoling Niu (*Department of Earth Sciences, Durham University, Durham, DH1 3LE, UK; School of Earth Sciences, Lanzhou University, Lanzhou, 730000, China*): As my primary supervisor, YN conceived the scientific project, chose the study areas, planned and carried out the sampling program and provided useful assistance and direction throughout. As the second correspondence author, YN assisted greatly with discussion of the results and the publication of this paper.

Julian A. Pearce (*School of Earth and Ocean Sciences, Cardiff University, Cardiff, CF10 3YE, UK):* JP provided constructive and professional feedbacks on protoliths discrimination and elemental correlations.

Huaikun Li (*Tianjin Institute of Geology and Mineral Resources, Tianjin 300170, China):* HL was one of the major members who planned and carried out the field work and compiled the GPS data for all these samples.

Huichu Wang (*Tianjin Institute of Geology and Mineral Resources, Tianjin 300170, China):* HW was one of the major members for the field work.

Jon Davidson (*Department of Earth Sciences, Durham University, Durham, DH1 3LE, UK*): JD,

as my second supervisor, he provided guidance and suggestion on the interpretation of analytical results especially with how to best convey to the readers, as well as corrections on language problems throughout the manuscript.

1.5.2 Chapter 5

This has been submitted to ***Chemical Geology*** and is currently under reviews.

Yuanyuan Xiao (*Department of Earth Sciences, Durham University, Durham, DH1 3LE, UK):* I carried out all the analytical work, using several methods, including electron probe micro-analyzer (EPMA) and LA-ICPMS for mineral compositions from the same samples discussed in ***Chapter 4***. I wrote the manuscript in and then passed it onto the co-authors for feedback, which improved the flow and organization of the manuscript but not change the interpretation or the conclusions that were drawn.

Yaoling Niu (*Department of Earth Sciences, Durham University, Durham, DH1 3LE, UK; School of Earth Sciences, Lanzhou University, Lanzhou, 730000, China):* YN provided the great support and guidance throughout as well as useful feedback and discussion, which improved to clarify the arguments presented.

Huaikun Li (*Tianjin Institute of Geology and Mineral Resources, Tianjin 300170, China):* was one of the major members for the field work.

Huichu Wang (*Tianjin Institute of Geology and Mineral Resources, Tianjin 300170, China):* was one of the major members for the field work.

Jon Davidson (*Department of Earth Sciences, Durham University, Durham, DH1 3LE, UK):* JD provided guidance and suggestion on the data interpretation. He also gave the constructive suggestion to make the figures more clearly and efficiently, as well as corrections on language problems throughout the manuscript.

Xiaoming Liu (*State Key Laboratory of Continental Dynamics, Department of Geology, Northwest University, Xi'an 710069, China):* XL arranged the analytical work at Northwest University and gave guidance during ICPMS analyses. He also provided the valuable discussion and feedback on data quality and processing.

1.5.3 Chapter 6

This has been submitted to ***Lithos*** and is currently in revision.

Yuanyuan Xiao (*Department of Earth Sciences, Durham University, Durham, DH1 3LE, UK):* I carried out the field work and analytical work, using several methods, including XRF and ICPMS for whole rock compositions and EPMA and LA-ICPMS for mineral compositions. I wrote the manuscript in its entirety and then passed it onto the other authors for feedback, which improved the flow and organization of the manuscript but not change the interpretation or the conclusions that were drawn.

Yaoling Niu (*Department of Earth Sciences, Durham University, Durham, DH1 3LE, UK; School of Earth Sciences, Lanzhou University, Lanzhou, 730000, China):* YN planned and organized the fieldwork, provided the great support and guidance throughout as well as useful feedback and discussion which improved to clarify the arguments presented.

Shuguang Song (*MOE Key Laboratory of Orogenic Belts and Crustal Evolution, School of Earth and Space Sciences, Peking University, Beijing 100871, China*): SS also carried out the field work, and gave the valuable guidance in the geology. He also provided the discussion and feedback for the manuscript in terms of geology.

Jon Davidson (*Department of Earth Sciences, Durham University, Durham, DH1 3LE, UK):* JD provided guidance and suggestion on the data interpretation, and also how to best convey to the readers, including corrections on language problems throughout the manuscript.

Xiaoming Liu (*State Key Laboratory of Continental Dynamics, Department of Geology, Northwest University, Xi'an 710069, China):* XL arranged the analytical work at Northwest University and gave guidance during ICPMS analyses. He also provided the valuable discussion and feedback on data quality and processing.

1.5.4 Chapter 7

This will be submitted to ***Geology*** when it is ready.

Yuanyuan Xiao (*Department of Earth Sciences, Durham University, Durham, DH1 3LE, UK):* I wrote the manuscript in its entirety and then passed it onto the other authors for feedback, on the

basis of which, I will also correct the manuscript.

Yaoling Niu (*Department of Earth Sciences, Durham University, Durham, DH1 3LE, UK; School of Earth Sciences, Lanzhou University, Lanzhou, 730000, China):* YN provided the original idea and the summarized data. He also provided great support and guidance throughout as well as useful feedback and discussion which improved to clarify the arguments presented.

Jon Davidson (*Department of Earth Sciences, Durham University, Durham, DH1 3LE, UK):* JD will provide guidance and suggestion on the data interpretation, as well as how to best convey to the readers.

CHAPTER 2:

GEOLOGICAL SETTINGS

2.1 WESTERN TIANSHAN

2.1.1 The Geography and Geology of Tianshan

Tianshan ('Tian' means sky, 'shan' means mountain in Chinese; also named as Tien Shan or Tienshan, e.g., Liou *et al.*, 1989; Allen *et al.*, 1993), is an important intra-continental mountain belt in the Central Asian Orogenic Belt (also known as Altaid Tectonic Collage, Fig. 2.1a; Şengör *et al.*, 1993; Yakubchuk, 2004; Gao *et al.*, 2009). Thus, the study of its tectonic evolution is important for understanding the amalgamation of Eurasia and also for the continental growth of Central Asian Orogenic Belt in the Phanerozoic (e.g., Gao *et al.*, 2009; Long *et al.*, 2011). It extends E-W for more than 2,500 km with the peak height of > 7,400 m above sea level. The ~ 1500 km portion of Tianshan in Xinjiang Autonomous Region of NW China include a ~ 200 km long high pressure (HP) – ultrahigh pressure (UHP) metamorphic belt (Liou *et al.*, 1989; Gao *et al.*, 1995; Figs. 1.5&2.1c).

Because sutures mark the zones of seafloor subduction and continental collision in the geological history, they are used to divide tectonic units of Chinese Tianshan. From north to south, the Chinese Tianshan has been divided into Junggar Plate, North-Central-Tianshan Suture, Yili Block, Central Tianshan Plate, South-Central-Tianshan Suture and Tarim Plate with Precambrian basement and Meso-Cenozoic deposited covers (Fig. 2.1b,c; Gao *et al.*, 1998; Qian *et al.*, 2009). The North-Central-Tianshan Suture defines the southward collision between an active margin on the north side of the Yili-Central Tianshan Plate (YCTP) and the Junggar Plate upon closure of the Palaeo-Junggar Ocean during the Late Carboniferous (Gao *et al.*, 1998; Long *et al.*, 2011), while the South-Central-Tianshan Suture defines the convergent margin associated with northward subduction of the South Tianshan palaeo-seafloor beneath the YCTP, followed by the northward collision of the Tarim Plate upon closure of the South Tianshan Ocean probably during Late Palaeozoic (e.g., Gao *et al.*, 1995; despite the closure time remains debatable, see discussions below). Recently, the North Nalati Fault (or Adengbulake-Lardun Fault, e.g., Qian *et al.*, 2009) between Yili Block and Central Tianshan Plate in China (Fig.2.1b)

is taken as an independent Early Palaeozoic suture zone rather than a secondary fault (e.g., Qian *et al.*, 2009 and reference therein), and is considered as the eastward extension of Nikolaev Line in Kyrgyzstan and Kazakhstan (Qian *et al.*, 2009; Gao *et al.*, 2009; Fig. 2.1b). The North Nalati Fault - Nikolaev Line represents the remnant of the Palaeo Kyrgyz-Terskey Ocean (Qian *et al.*, 2009; Gao *et al.*, 2009), separating the North Tianshan Plate (or Kazakhstan-Yili Plate, e.g., Gao *et al.*, 2009) and the Central Tianshan (Arc) Terrane (Fig. 2.1b).

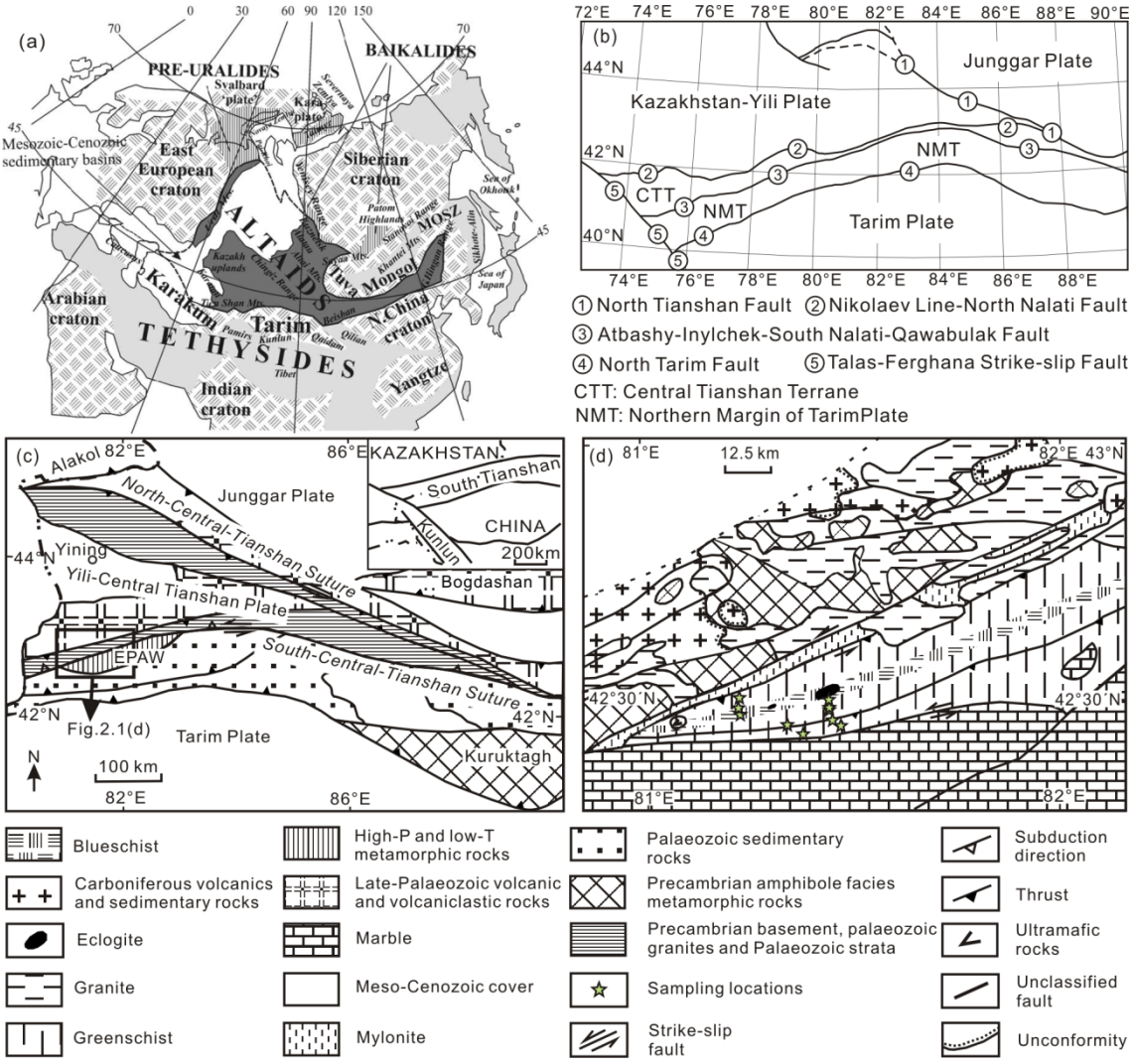

Figure 2.1 a. Altaid orogenic collage and adjacent tectonic units (after Şengör *et al.*, 1993; Yakubchuk, 2004). b. Distributions of different tectonic units in the Tianshan Orogenic belt (modified after Gao *et al.*, 2009). c. A geological map for the location of the Chinese Western Tianshan; d. Our sampling locations (c and d are after Gao & Klemd, 2003; Zhang *et al.*, 2003a).

The South-Central-Tianshan Suture in China (also known as the Qinbulak-Qawabulak or South

Nalati Fault), connected with the Atbashi-Inyl'chek Fault in Kyrgyzstan (Fig. 2.1b) define the South Tianshan terrane (also known as Western Tianshan) in China and Atbashy terrane in Kyrgyzstan (Gao *et al.*, 2009). The South-Central-Tianshan Suture with a great variety of mylonite is a large scale ductile shear zone (Volkova & Budanov, 1999), made up of a 7.5 km wide ductile zone and a ~ 0.5 km wide sinistral strike-slip shear zone (Fig. 2.1d; Gao *et al.*, 1995; Gao & Klemd, 2000). Along with the Palaeozoic ophiolitic mélange, a HP-UHP metamorphic belt (one of our study areas) is located within an early Palaeozoic accretionary wedge (EPAW; Gao *et al.*, 1995; Gao & Klemd, 2003) along the southern margin of the South-Central-Tianshan Suture (Fig. 2.1c), and thought to continue to the west in Kazakhstan (e.g., Liou *et al.*, 1989; Gao *et al.*, 1995; Volkova & Budanov, 1999; Zhang *et al.*, 2002a). It is the longest metamorphic belt produced during the closure of Palaeo-Asian ocean domain (Gao *et al.*, 1995).

2.1.2 Tectonic Evolution of the Chinese Western Tianshan

Thanks to more recent fieldwork and age data, our understanding on the tectonic evolution of the Chinese Western Tianshan has been improved. However, several problems remain debatable, such as: (1) the opening time of the South Tianshan Ocean: Late Precambrian-Early Palaeozoic (Gao *et al.*, 2006) vs. Cambrian-Ordovician (Shi *et al.*, 1994; Chen *et al.*, 1999) or late Ordovician (Gao *et al.*, 1998; Long *et al.*, 2011); (2) the closure time of the South Tianshan Ocean and the time of collision between the Tarim Plate and the YCTP: Triassic (233 ± 4 Ma – 226 ± 4.6 Ma in Zhang *et al.* [2007a], but this age has been interpreted to be the age of zircon produced by fluid-mediated recrystallization, see de Jong *et al.* [2008]) vs. Late Carboniferous (e.g., Gao *et al.*, 1998, 2006; 346 – 344 Ma eclogites from Gao & Klemd [2003]; 480 – 275 Ma arc-type granitoid rocks from Gao *et al.* [2009]; 319.5 ± 2.9 Ma and 318.7 ± 3.3 Ma eclogites from Su *et al.* [2010]; 319 ± 4 Ma eclogite from Hegner *et al.* [2010]; 284.8 ± 2.0 Ma granite dike, constraining the age upper limit of HP – low temperature [LT] metamorphism from Gao *et al.* [2011]; Long *et al.*, 2011).

Following the regional geology studies by Gao and co-authors (Gao *et al.*, 1995, 1998, 2009; Long *et al.*, 2011), the tectonic evolution of Chinese Tianshan Orogenic Belt may be summarized in terms of several stages (Fig. 2.2):

(a) Early Cambrian: A Palaeo-Junggar Ocean existed as evidenced by the occurrence of Tangbale ophiolites (508 ± 20 Ma; Feng *et al.*, 1989), which is separated from the southern margin of the Junggar Plate. The Early Palaeozoic Terskey Ocean may exist between the Yili Block and the Central Tianshan Plate as evidenced by the presence of MORB-type basalts on the southern margin of the Yili Plate (zircon U-Pb age of 516.3 ± 7.4 Ma; Qian *et al.*, 2009).

(b) Early Cambrian – Middle Ordovician*:* The age of arc-type rocks along the Terskey oceanic ophiolitic belt indicates the Terskey Ocean began to subduct (470 ± 12 Ma for a dioritic pluton with adakitic affinity, Qian *et al.*, 2009). As a result of the subduction of the Terskey Oceanic lithosphere, the Central Tianshan Terrane separated from the Tarim Plate, which further led to the formation of Palaeo-South Tianshan Ocean as evidenced by the presence of ~ 425 Ma MORB-type basalts (Long *et al.*, 2006) and ~ 450 Ma OIB-type basalts (Wang *et al.*, 2007; Gao *et al.*, 2009).

(c) Late Ordovician – Late Silurian: Palaeo-Junggar oceanic lithosphere subducted southward, leading to the formation of Early Palaeozoic island-arc-type volcanic rocks, granitoids, high temperature (HT) – low pressure (LP) metamorphic rocks in the north margin of Yili Block and blueschists within North-Central-Tianshan Suture. The closure of the Terskey Ocean is most likely represented by the North Nalati Fault – Nikolaev Line, which marked the amalgamation of Central Tianshan Plate with Yili Plate (Yili-Central Tianshan Plate, YCTP) in the Late Ordovician (Gao *et al.*, 2009; Qian *et al.*, 2009). The Palaeo-South Tianshan Ocean, which had separated the Tarim Plate from the YCTP, subducted northward, resulting in the formation of island-arc-type volcanic rocks, palaeozoic granitoid plutons, as well as HT-LP and HP-LT metamorphic rocks along the south-margin of the YCTP (Gao *et al.*, 1995).

(d) Late Silurian – Early Carboniferous: The further subduction of Palaeo-Junggar oceanic lithosphere in the Late Devonian may have led to the formation of the back arc and North Tianshan Island Arc (NTIA; Gao *et al.*, 1998). The Palaeo-South Tianshan oceanic seafloor continued to subduct into deeper depths, probably reaching the UHP metamorphic condition during this period (see discussions on the occurrence of UHP metamorphism [UHPM] in section 2.1.3.2).

(e) End of Early Carboniferous – Late Carboniferous: It is most likely that the Junggar Plate, the YCTP and the Tarim Plate were amalgamated with Eurasia during this time, resulting in the disappearance of back-arc basin and Palaeo-Junggar Ocean, and also leading to the collision of the NTIA with the YCTP (evidenced by the presence of unconformably overlaid Middle Carboniferous clastic rocks, Gao *et al.*, 1998). To the south, YCTP collided with the Tarim Plate, constrained by the occurrence of Permian post-collisional granitoids resulted from the delamination caused by the slab breakoff (e.g., Long *et al.*, 2011). As a result, the HP-UHP metamorphic rocks were exhumed during this collision.

(f) Early Permian: The Palaeo-Tianshan range began to uplift (Gao *et al.*, 1995).

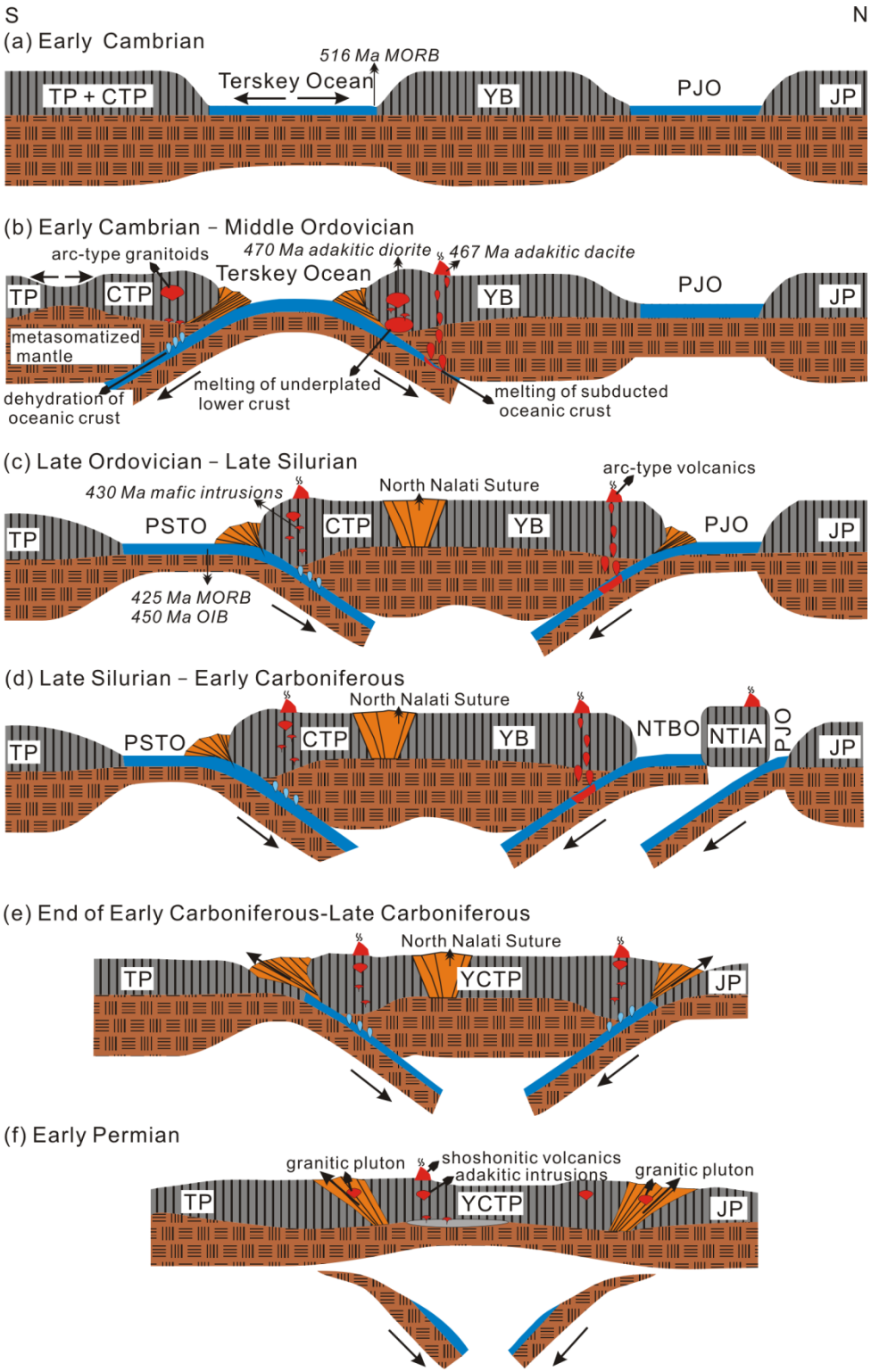

Figure 2.2 Model for Palaeozoic tectonic evolution of the Chinese Tianshan Orogenic Belt (modified after Gao *et al.* [1998] and Long *et al.* [2011]). CTP = Central Tianshan Plate; NTBO = North Tianshan Back-arc Ocean; JP = Junggar Plate; NTIA = North Tianshan Island Arc; PJO = Paleo-Junggar Ocean; PSTO = Paleo-South Tianshan Ocean; TP = Tarim Plate; YB = Yili Block; YCTP = Yili-Central-Tianshan Plate.

2.1.3 UHP Metamorphic Belt in the Chinese Western Tianshan

2.1.3.1 The recognition of the HP-UHP metamorphic belt

The HP-UHP metamorphic belt occurs along the south margin of the South-Central-Tianshan Suture, bounded by ductile shear zones and brittle reverse or strike slip faults (e.g., Gao & Klemd, 2000). At first, owing to the poor natural conditions of this remote study area, only blueschists were found to, occur as discrete blocks (2 km^2), lenses and thin layers (2 – 50 cm in size) or thick beds (~ 50 m in size) intercalated with the greenschist facies layers (e.g., Liou *et al.*, 1989; Gao *et al.*, 1995). Therefore, it was recognized as a metamorphic belt with only up to blueschist facies (450°C at 0.9 – 1.0 GPa). The blueschists are, intermingled with terrigenous sediments and volcaniclastic rocks, thought to constitute a metamorphosed subduction complex belt (mélange belt; Gao *et al.*, 1995).

More recent studies have led to the recognition of eclogite facies rocks (Gao, 1997), occurring as pods, boundins, thin layers or as massive blocks within bodies of blueschists with intimate contacts. The estimated peak metamorphic conditions were T = ~ 500 – 600°C and P = ~ 1.4 – 2.1 GPa (Gao & Klemd, 2000). The gradual transition between blueschists and eclogites was thought to indicate that they experienced the same metamorphic P-T conditions, but suffered from varying effects of fluid flow or possessed different protolith compositions (Gao & Klemd, 2000, 2003).

Not until the early 21th century, did Zhang *et al.* (2002a,b) propose that the peak metamorphic condition in the Chinese Western Tianshan should be ultra-high pressure (i.e., > 2.5 GPa), as indicated by the presence of coesite pseudomorphs in garnet, quartz exsolution lamellae in omphacite of eclogites, as well as the mineral assemblage of calcite pseudomorphs (after aragonite) + magnesite in meta-pelites that coexist with eclogites. Since then, the peak metamorphic condition in the Chinese Western Tianshan has attracted hot debate (represented by Klemd, 2003).

2.1.3.2 About the UHPM in Chinese Western Tianshan

The discovery of coesite from Western Tianshan eclogites (Lü *et al.*, 2008, 2009) has ended the ~ 10 year debate on the peak P-T conditions (e.g., Zhang *et al.*, 2002a-b, 2003b; Klemd, 2003), and offered smoking gun evidence in support of UHPM with peak pressures in excess of 2.5 GPa (Smith, 1984; Chopin, 1984).

Nevertheless, it is worthwhile to go over briefly the history with the aim of correctly informing the international community of the nature of the dispute. Prior to the discovery of coesite, applications of geothermobarometer to Tianshan eclogite samples (including our samples) led some authors (e.g., Klemd, 2003; Lavis, 2005) to argue against the UHPM. One reason to accept the calculated low pressures against the observation of coesite (pseudomorphs) in these rocks (Zhang *et al.*, 2005) is that these authors did not find coesite in samples they studied. Coesite is volumetrically rare, and it can be widespread throughout an UHP metamorphic belt, but is not necessarily present in every random sample. For example, if we make 10 thin sections from a single hand specimen, we may not find coesite at all or may find coesite only in one of the 10 thin sections. This is also the reason why it may take a long time to confirm one UHP metamorphic belt. It is thus incorrect to argue that the thin section that contains coesite had subducted to depth > 80 km whereas other 9 thin sections of the same hand specimen without coesite had not subducted to that depth. Furthermore, because of the rapid subduction and exhumation, the rock may not stay at peak P-T conditions long enough relative to the quartz-coesite transformation, which results in even rarer occurrence of coesite. In addition, because of the widespread retrograde metamorphism and overprints, it is also likely that coesite crystals may have completely reverted to quartz during re-equilibrium at low pressures.

Although not observed in samples we studied, previous studies afford additional lines of evidence for UHPM in the Chinese Western Tianshan:

(1). Presence of quartz and coesite exsolution lamellae in omphacite of Tianshan eclogite

(Zhang *et al.*, 2002a, 2005). These lamellae are considered as resulting from decompression of a super silicic clinopyroxene with a Ca-Eskola component, which can only be stable at pressures in excess of 3.0 GPa: 2 $Ca_{0.5\square 0.5}AlSi_2O_6 \rightarrow CaAl_2SiO_6 + 3\ SiO_2$ (Smyth, 1980; Katayama *et al.*, 2000; Konzett *et al.*, 2008).

(2). Coexistence of dolomite, magnesite and calcite (aragonite pseudomorph) in rocks of sedimentary protolith within Tianshan eclogite bodies (e.g., present between eclogitized basaltic flows and pillows; Zhang *et al.*, 2002b, 2003a,b). It has been demonstrated experimentally that the decomposition reaction, dolomite = magnesite + aragonite, takes place at pressure of no less than 5.0 GPa (Biellmann *et al.*, 1993; Sato & Katsura, 2001; Luth, 2001). Zhang *et al.* (2002b) interpreted the coexisting dolomite + magnesite + calcite assemblage representing a snapshot of this reaction. With estimated T = 560 – 600°C, the minimum peak pressure reflected by this reaction would be about 4.95 to 5.07 GPa (Zhang *et al.*, 2003a).

The latter two arguments, however, are not exclusive evidence for UHPM. For example, Ca-Eskola could be stable in the quartz (vs. coesite) stability field (Page *et al.*, 2005) and the decomposition of dolomite may take place at lower pressures (e.g., 2.3 – 2.8 GPa; Smit *et al.*, 2008). Nevertheless, the presence of coesite, together with the arguments considering Ca-Eskola component and dolomite decomposition, ~ 2.5 GPa is likely the minimum for peak metamorphic pressure. Hence, there should be no dispute on the nature of the UHPM in the Chinese Western Tianshan.

2.1.3.3 UHP metamorphic rocks

The HP-UHP metamorphic belt in the Western Tianshan is mainly made up of eclogite, omphacitite, epidosite and blueschist. Based on geochemical studies, blueschists and eclogites are thought to have normal/enriched (N/E)-MORB and OIB-like protoliths (Gao *et al.*, 1995; Gao & Klemd, 2003; Volkova & Budanov, 1999), as well as volcanic arc basalts (VAB)-like protoliths (Ai *et al.*, 2006). The highly variable compositions of meta-basaltic rocks are

consistent with the geochemistry of seamounts like those near the East Pacific Rise (see Niu & Batiza, 1997), juxtaposed with some arc-type rocks as well as eroded sediments in the trench (Ai *et al.*, 2006).

Existing work has argued that HP-UHP metamorphic rocks from Western Tianshan have experienced subduction and ultimate exhumation of ocean crust in response to a continental collision event, with a clockwise P-T path on a regional scale (Fig. 2.3) and nearly isothermal decompression from peak eclogite facies to epidote-amphibolite facies (Gao & Klemd, 2003). Both prograde and retrograde blueschists are present (Gao & Klemd, 2003).

Much effort has been expended to date the peak metamorphic event using a variety of techniques including the Ar-Ar plateau method and the Sm-Nd and Rb-Sr isochron methods (Gao & Klemd, 2003), the latter of which gave an age of ~ 350 – 345 Ma (Carboniferous) for peak metamorphism and ~ 311 – 310 Ma for exhumation (i.e., cooling age, details are given in Gao *et al.*, 2006). Much younger ages of 233 ± 4 to 226 ± 4.6 Ma (Triassic) have been obtained using the sensitive high-resolution ion microprobe (SHRIMP) U-Pb method on metamorphic zircons extracted from both blueschist and UHP eclogite (Zhang *et al.*, 2007a; also see discussions in section 2.1.2 above). However, based on the zircon SHRIMP U-Pb ages most recently reported by Gao *et al.* (2009) and Su *et al.* (2010), together with the constraints of the cooling age (~ 311 Ma; personal communication with Lifei Zhang, 2010), it is clear that the peak metamorphism happened in the Carboniferous (vs. Triassic) Period in the Western Tianshan, and this is also consistent with the tectonic evolutionary history of Chinese Western Tianshan as discussed in section 2.1.2 above (Fig. 2.2d,e).

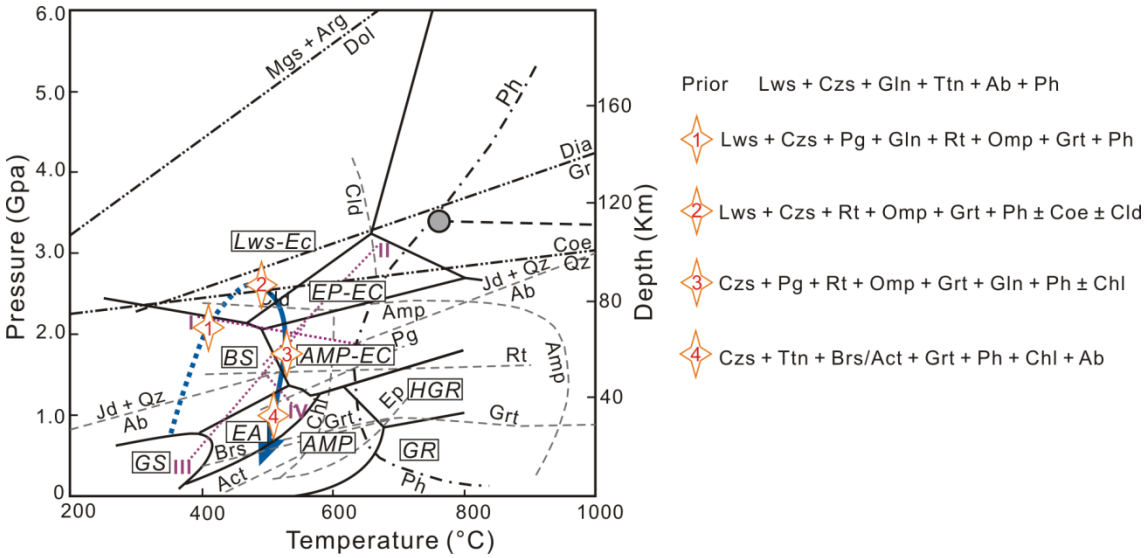

Figure 2.3 Schematic phase diagram (after Xiao *et al.*, 2012; Schmidt & Poli, 1998; Poli & Schmidt, 2002; Zhang *et al.*, 2002a, 2003a) and mineral assemblages for each metamorphic stage for rocks of basaltic protoliths from Western Tianshan, China. Metamorphic facies boundaries are from Liou *et al.* (2004). The dark blue curve with four diamonds is a schematic P-T path for our rocks of basaltic protoliths based on the detailed petrography, both the mineral assemblages and the textural relationship (see Fig. 4.1 and related discussions in section 4.2). Each diamond represents a metamorphic stage, including prograde blueschist facies, UHP eclogite facies, retrograde eclogite facies and epidote amphibolite facies, and the related typical mineral assemblage is detailed on the right. The estimated second critical endpoint and the position of the critical curve are also given (Mibe *et al.*, 2011), represented by the grey solid circle and the horizontal dash line respectively. See Abbreviation List for all the abbreviations, including most of the mineral abbreviations referred to Whitney & Evans (2010). Dotted lines labelled as I – IV represent four metamorphic reactions: reaction I – Pg = Ky + Jd_{50} + H_2O ; II - Lws + Grt 1 = Czs + Di + Grt 2 +H_2O (Poli & Schmidt, 1997); III - Lws + Jd = 2 Czs + Pg + Qz + 6 H_2O or 4 Lws + Ab = 2 Czs + Pg + 2 Qz + 6 H_2O (Gao *et al.*, 1999); IV - 26 Jd + 12 Di + 9 Prp + 19 Qz + 15 H_2O = 13 Gln + 6 Czs (Zhang *et al.*, 2002a).

The estimated peak metamorphic condition defined by Lü *et al.* (2009) is used in this study as the stage 2. During prograde metamorphism, as evidenced by the occurrence of the box-shaped lawsonite pseudomorphs and the glaucophane and omphacite inclusions in garnet, it indicates that the rocks have experienced prograde blueschist facies metamorphism, stage 1. During retrograde metamorphism, lawsonite may have replaced by clinozoisite and paragonite through reaction II or reaction III, which we define as the stage 3, although other works also proposed that the breakdown of lawsonite may happen during prograde metamorphism (e.g., Gao *et al.*, 1999; Gao & Klemd, 2003). As evidenced by the occurrence of omphacite relict in glaucophane porphyroblast and the replacement of glaucophane by barroisite, it may indicate reaction IV and 25 Gln + 6 Czs + 7 Qz + 14 H_2O = 50 Ab + 6 Tr + 9 Chl (Maruyama *et al.*, 1986), shown as the stage 4. The replacement of rutile by titanite may also happen at this stage and may indicate the reactions of Rt + Qz + Ca = Ttn + CO_2 (Niu & Lesher, 1991) and 3 Di + 2 Jd + H_2O + Qz + 3 Rt = 3 Ttn + Gln (van der Straaten *et al.*, 2008).

2.2 NORTH QILIAN MOUNTAIN

2.2.1 Geological Settings of North Qilian Mountain

The name of Qilian Mountain is originated from Ancient Hun, in whose language it also means sky or celestial (Song, 2009). North Qilian oceanic-type Suture Zone (ONQ, or North Qilian Mountain) is about 80 to 100 km wide, and extends NW-SE for over 800 km along the northern margin of the Tibetan Plateau in NW China (Fig. 2.4a; Song *et al.*, 2006, 2009). The recognition of lawsonite-bearing eclogite (e.g., Wu *et al.*, 1993; Zhang & Meng, 2006; Zhang *et al.*, 2007b; Song *et al.*, 2007) and Mg-carpholite-bearing metamorphic rocks of pelitic protolith (Song *et al.*, 2007) indicates that the ONQ is one of the oldest orogenic belts (560 – 440 Ma) preserving rock assemblages of a cold intra-oceanic-type subduction (see Song *et al.*, 2007, 2009; Zhang *et al.*, 2007b).

The ONQ, together with other sub-parallel tectonic units (Qilian Block, North Qaidam continental-type UHP Metamorphic Belt [CNQ] and Qaidam Block) forms the northern margin of the Greater Tibetan Plateau (Qilian-Qaidam Mountain, e.g., Song *et al.*, 2006; Fig. 2.4a). These units are offset to the west by the Altyn Tagh Fault (the largest sinistral fault system in Western China). The ONQ was taken as one part of the Caledonian Fold Belt along the Qinling-Qilian-Kunlun Tectonic Belt (e.g., Wu *et al.*, 1993), but has been emphasized to be an independent orogenic collage in the Palaeozoic and was connected with the West Kunlun afterwards by transform or accretionary tectonics, which now lies somewhere along the Altyn Tagh fault zone (Xiao *et al.*, 2009). The ONQ comprises an ophiolite complex, island-arc volcanic rocks, HP blueschists and eclogites, Silurian flysch formation, Devonian molasse, and Post Devonian sedimentary cover sequences (e.g., Wu *et al.*, 1993; Feng & He, 1995; Xia *et al.*, 2003; Song *et al.*, 2006; Song *et al.*, 2012; Fig. 2.4b).

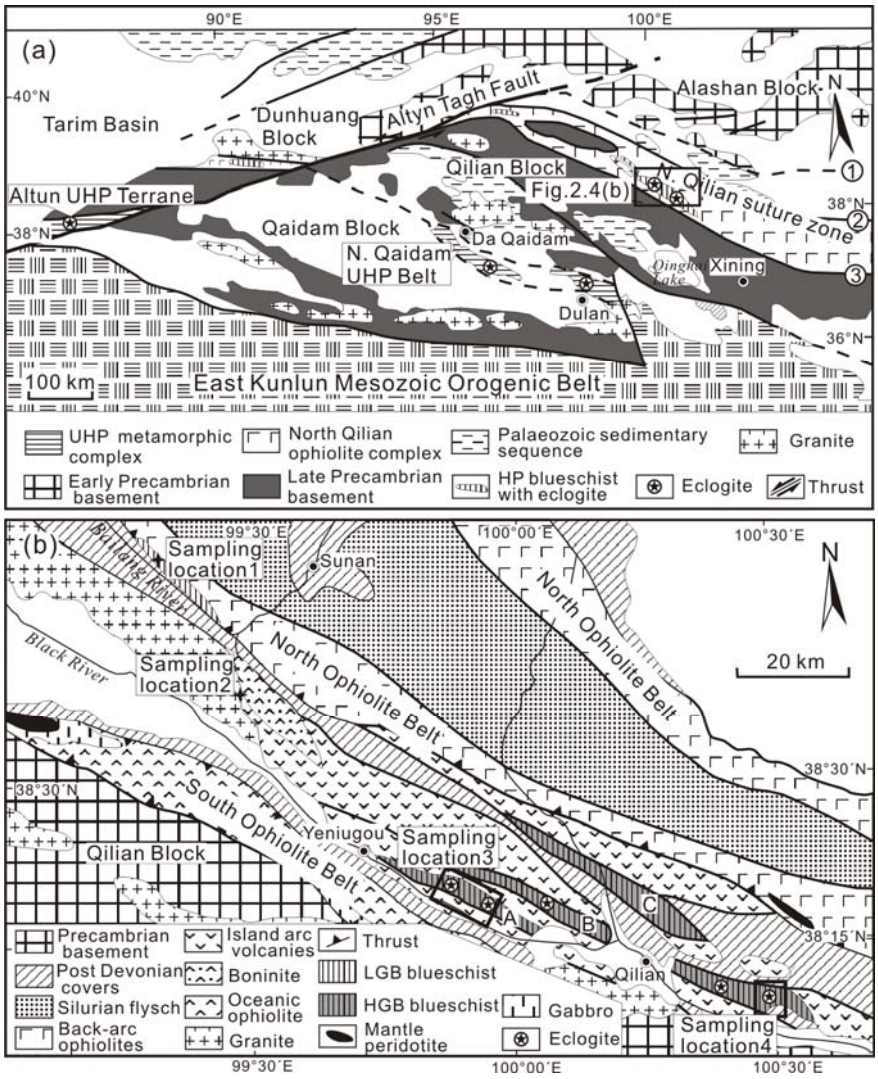

Figure 2.4 (a) Simplified geological map of Qilian-Qaidam Mountain region in NW China. ①-Longshoushan Fault; ②, ③-northern and southern boundary faults of North Qilian Suture Zone. (b) Outcrop of North Qilian Suture Zone including sampling locations (after Wu *et al.*, 1993; Song *et al.*, 2007, 2009; Xia & Song, 2010). Sampling location 1 in Sunan is along the low grade blueschist metamorphic belt (LGB), while sampling location 3 and sampling location 4 near Qilian County are within slices (slice A and slice B) of high grade blueschist/eclogite metamorphic belt (HGB). Sampling location 2 is for boninite, which is not of our interest in this thesis.

Two sub-parallel NW-SE trending metamorphic sub-belts are present (Fig. 2.4b): one is a high-grade blueschist/eclogite metamorphic belt (HGB) with higher metamorphic temperature and pressure up to 460 – 510°C at 1.8 – 2.6 GPa (using Grt – Omp – Ph geothermobarometer, Song *et al.*, 2006, 2007); the other is a low grade blueschist metamorphic belt (LGB) with only 320 – 375°C at 0.75 – 0.95 GPa (Zhang *et al.*, 2009; Lin *et al.*, 2010) or 250 – 350°C at 0.6 – 1.1 GPa (Song *et al.*, 2009a).

The HGB is made up of three slices within the arc-type volcanic rocks around Qilian County, Qinghai Province (Fig. 2.4b). It is composed of blueschist to eclogite facies metamorphic rocks of limestone and Cambrian ophiolitic fragments including serpentinite, basalt (depleted normal [N-] to enriched [E-] basalts of near-ridge seamounts or OIB like), pelite and pelagic chert within a blueschist-facies meta-greywacke matrix, which dominates more than half of the HGB (Wu *et al.*, 1993; Song *et al.*, 2009a). The eclogitization has been constrained to be 490 – 460 Ma (Wu *et al.*, 1993; Zhang *et al.*, 2007b; Song *et al.*, 2009a; Table D.1 of Appendix D), and the formation of HGB may be attributed to the subduction of the mature ocean seafloor (Wu *et al.*, 1993; Song *et al.*, 2009a). On the other hand, the LGB is a belt of lawsonite-bearing blueschists along Bailang River in Sunan County, Gansu Province (Wu *et al.*, 1993; Song *et al.*, 2004). The recent published laser ^{40}Ar-^{39}Ar isochron age on glaucophane and phengite constrained the lower limit age of the transition from lawsonite blueschist to epidote blueschist facies around 413 – 415 Ma (Lin *et al.*, 2010; Table D.1 of Appendix D). The formation of LGB is interpreted to be resulted from the subduction of the late evolved back-arc basin seafloor, and basaltic rocks are the dominant protolith rock type (Wu *et al.*, 1993; Song *et al.*, 2009a; Zhang *et al.*, 2009).

The further geological details of LGB and HGB and the related representative mineral assemblages are summarized in Table D.1 and Table D.2 of Appendix D. All these differences between LGB and HGB allow a better understanding of the elemental behaviors during subduction-zone metamorphism as a function of metamorphic conditions and protolith compositions.

2.2.2 Tectonic Evolution of North Qilian Mountain

As shown in Fig. 2.5, the ONQ ophiolite complex is of Early Palaeozoic age (e.g., 568 – 495 Ma; Yang *et al.*, 2002; Shi *et al.*, 2004; Tseng *et al.*, 2007; Zhang *et al.*, 2007b; Song *et al.*, 2012), and the ancient Qilian Ocean already existed in early Cambrian and may have opened in the Late Proterozoic at ~ 710 Ma (Song *et al.*, 2009a; Song *et al.*, 2012). The timing of subsequent eclogitization (i.e., ~ 490 – 460 Ma, e.g., Zhang *et al.*, 2007b; Song *et al.*, 2009a) is

consistent with the age of island-arc volcanic rocks (~ 486 – 445 Ma; Wu *et al.*, 1993; Xia *et al.*, 2003; Wang *et al.*, 2005; Liu *et al.*, 2006) and the spreading history of the back-arc basin (490 ± 5 Ma, Xia & Song, 2010; Xia *et al.*, 2012; Song *et al.*, 2012). The back-arc basin spreading and eclogitization have been interpreted as resulting from northward subduction of Qilian Ocean floor, the dehydration of which further led to the formation of arc volcanic rocks in the Ordovician time (e.g., Xia *et al.*, 2003; Song *et al.*, 2006). The Ar–Ar dating of glaucophane and phengite from retrograde blueschist (i.e., ~ 462 to 440 Ma, cooling ages; Wu *et al.*, 1993; Liou *et al.*, 1989; Zhang *et al.*, 1997; Song *et al.*, 2007, 2009) and meta-pelite (454 – 442 Ma, Liu *et al.*, 2006) in HGB, together with the occurrence of Silurian flysch formation and Devonian molasse, mark the end of oceanic seafloor subduction at ~ 440 Ma (e.g., Song *et al.*, 2006; Song *et al.*, 2012). Together with the inferred progressive P-T-t path (Fig. 2.6), the thermal gradient during the subduction is estimated to be 6 – 7°C/km (Zhang *et al.*, 2007b; Song *et al.*, 2009a).

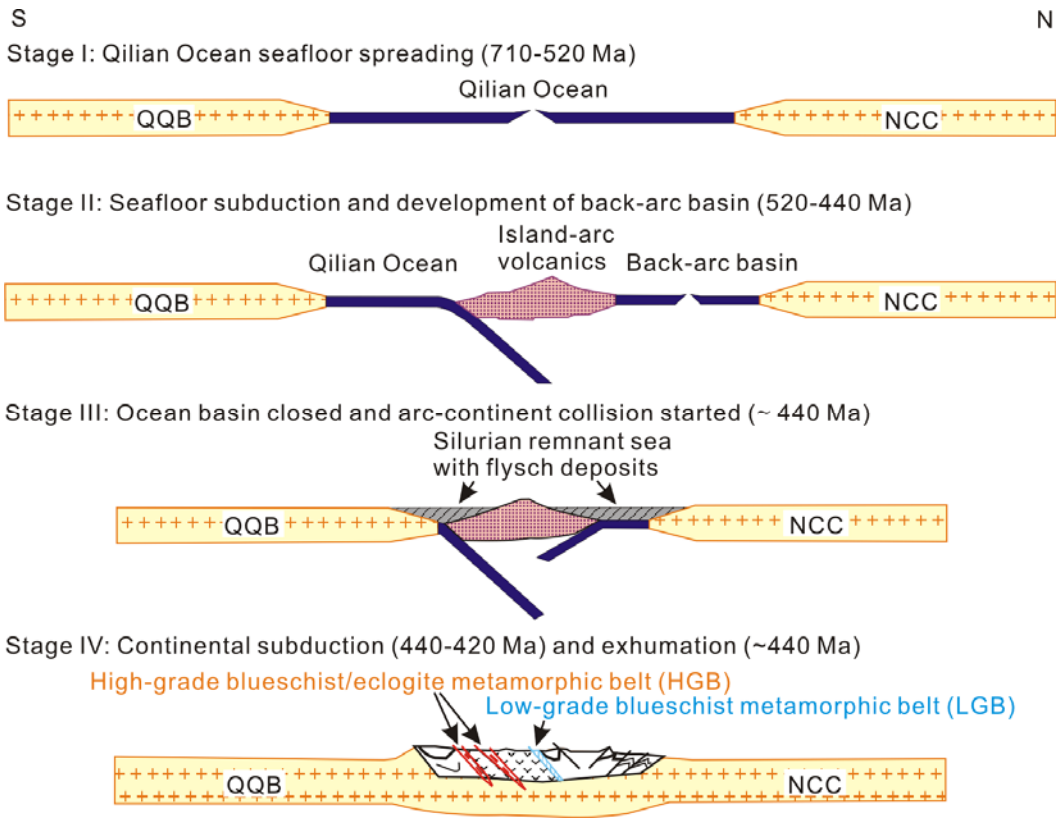

Figure 2.5 Model for Early Palaeozoic tectonic evolution of the North Qilian oceanic-type Suture Zone (after Song *et al.*, 2009a, 2012). NCC – North China Craton, QQB – Qilian – Qaidam block.

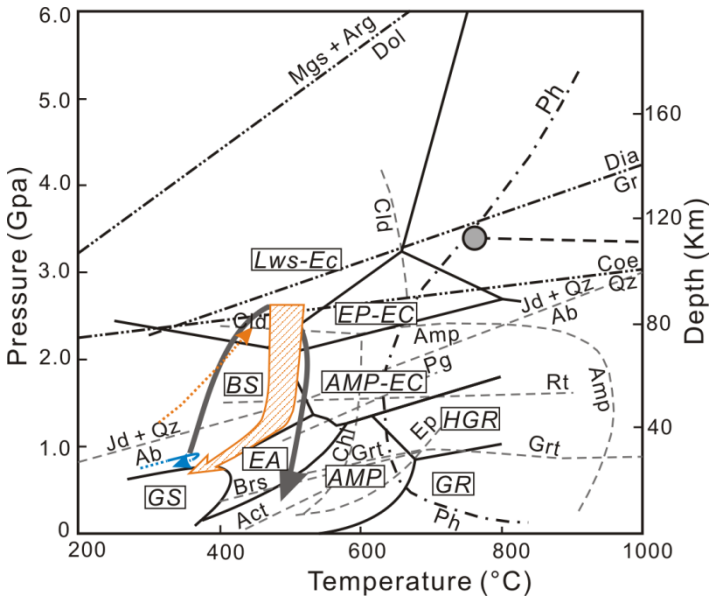

Figure 2.6 Estimated P-T paths for rocks of basaltic protoliths from HGB and LGB of North Qilian Mountain (metamorphic facies boundaries are as used in Fig. 2.3, referred to Liou *et al.* [2004]). The dotted and the wide hatched orange arrow for HGB is referred to Song *et al.* (2007), while the small blue arrow for LGB is referred to Zhang *et al.* (2009). The grey curve is the schematic P-T path for rocks of basaltic protoliths from UHP metamorphic belt of Western Tianshan in NW China (Fig. 2.3). See Abbreviation List for all the abbreviations used, including most of the mineral abbreviations referred to Whitney & Evans (2010).

CHAPTER 3:

ANALYTICAL METHODS

3.1 BULK-ROCK GEOCHEMISTRY

Bulk-rock compositions for rocks of basaltic protoliths and sedimentary protoliths from Western Tianshan were analyzed by Lavis (Table C.1 in Appendix C; Lavis, 2005; Xiao *et al.*, 2012). Therefore, only rocks from North Qilian Mountain (N=80) were analyzed for bulk-rock compositions in this PhD project. Sample powders for the whole rock analysis were prepared in the Langfang Laboratory of the Chinese Geological Survey. Saw marks and the weathered surfaces were firstly removed from hand specimens, which were then cleaned in an ultrasonic bath in distilled water. A corundum jaw crusher was used to crush cleaned samples into chips. The fresh rock chips were selected and finally pulverized using agate ball mills. All the bulk-rock geochemical analysis for rocks from North Qilian Mountain was carried out in the summer of 2009 at the State Key Laboratory of Continental Dynamics in Northwest University, China.

3.1.1 Major Elements

Whole-rock major elements were analyzed using X-ray fluorescence spectrometry (Rigaku RIX 2100 XRF) on fused glass disks.

3.1.1.1 XRF

XRF is widely used for element identification qualitatively and measurement of the element concentrations quantitatively, especially for major elements. X-ray is a form of electromagnetic radiation with a wavelength from 0.01 to 10 nanometers, shorter than visible light (Als-Nielsen & McMorrow, 2011). After the excitation by the primary X-rays from the X-ray tube, the sample is irradiated and emits the secondary X-rays due to the electron (from K, L and M shells, the closest electron shell to the nucleus with the lowest average energy) jumps. These secondary X-rays passed the primary collimator, reach a rotated analyzing crystal, resulting in their diffraction. Through a set of secondary collimator, the diffracted beams are further parallelized and dispersed into a spectrum, which is finally obtained by the detector. The reflection angle is

related to the wavelength of the characteristic X-ray in response to a certain element. The count rate is used to estimate the intensity of the individual characteristic X-ray peak, in unit of 1000s counts per second. Excluding the intensity caused by background radiation, the net intensity is in proportion to the element concentration essentially, but the dead time and matrix effects will make this relation more complicated. See Gill (1997) for more related details on XRF.

3.1.1.2 Chemical pretreatments and data quality

Before the analysis of bulk-rock major element contents, we analyzed the loss on ignition (LOI) for each sample. To prepare the dry ceramic crucibles, we need to heat those clean ceramic crucibles in a muffle furnace at 1000°C for 40 min, and placed in a dessicator for 30 min after their sufficient cooling. Then, we measured the weight of these ceramic crucibles (the weight of which is defined as W1), and filled in ~ 1g sample (the weight of which is measured as W2). After that, crucibles were placed back in the muffle furnace at 1000°C for 2 hours and weighed as W3 after cooling. Finally, the value of LOI can be calculated through W1 + W2 – W3.

To avoid particle-size effects and possible absorption effects, sample powders require a fuse flux with light atomic number (Gill, 1997). In this study, lithium tetraborate ($Li_2B_4O_7$; 5.2 ± 0.001g) was used for fusion. We measured 0.7 ± 0.0001g sample, and well mixed it with the fuse flux $Li_2B_4O_7$, ammonium nitrate (NH_4NO_3; 0.3 ± 0.001g as oxidant), lithium fluoride (LiF; 0.4 ± 0.001g as mold-release agent) in acid-washed platinum crucibles. Consequently, the sample powders were diluted to be a mixture with a flux:sample ratio of 8:1 approximately. 1 – 2 drops of lithium bromide (LiBr) as mold-release agent were added before fusion. After heating at 1200°C for 480s using a radio high frequency furnace and sufficient cooling, the sample's name was labeled on top of the glass disk to make sure the more flatten bottom was used for subsequent analysis.

The glasses were then analyzed using XRF operated by Jianqi Wang from Northwest University in China. The analytical precision for major elements is better than 5 % as determined from the

duplicate analyses for every ten samples. Bulk-rock major element data for samples from North Qilian Mountain are given in Table D.3-5 in Appendix D.

3.1.2 Trace Elements

Bulk-rock trace element compositions were determined using Agilent 7500a Inductively Coupled Plasma Mass Spectrometry (ICPMS) on sample solutions (see detailed procedures in Rudnick *et al.*, 2004).

3.1.2.1 ICPMS

Thanks to the low detection limits (as the result of the low background signals), the high sensitivity and the fewest interferences for most elements of geological interests, together with its rapid analytical speed (near-simultaneous determination, e.g., < 0.06s for a single scan of charged particles with mass-to-charge ratio [m/z] from 4 to 240), ICPMS becomes the most widely used method for trace element analysis (Gill, 1997).

Plasma is defined as 'a luminous volume of gas that has some of its atoms or molecules ionized' (Gill, 1997). Either heating, strong electromagnetic field applied with a laser or microwave generator, or accompanied by the dissociation of molecular bonds could induce the ionization of the previous uncharged molecular or atoms (Sturrock, 1994; Browning, 2005). As for ICPMS, the plasma is generated within a torch by inductive coupling to the load coils situated around, which are made of hollow copper filled with cooling water flow and connected with a radio frequency generator. The ICP torch is made up of three concentric tubes, which are respectively filled with carrying argon coolant (or plasma) gas, auxiliary gas flow (to lift the plasma) and sample solution with carrier argon gas flow inwards. The maximum temperature of plasma intrigued by electron motions can be up to 10,000°C.

To avoid the matrix effects, solid sample powders have to be dissolved thoroughly before analysis. The sample solution, pumped by a peristaltic pump into a nebulizer, is converted into

an aerosol, and swept into the spray chamber by argon gas, while those large droplets will be expelled. When the sample aerosol is injected into the plasma torch, the extremely high temperature region, it will be rapidly volatilized, dissociated, and ionized. The sampling cone and the skimmer (two conical nickel apertures) allow only ions get through, which will then pass into the mass spectrometry as a function of the big pressure difference, while most atoms, undissociated molecules and unvolatilized particles will be deflected away. After deflection by extraction lens around the photon stop, ions can continue to move and pass into the mass filter (commonly a quadrupole mass filter) via the focusing of electrostatic lens assembly. Finally, they will reach the electron multiplier detector.

3.1.2.2 Chemical pretreatments and data quality

In order to completely digest all the minerals in the bulk rock, an HF + HNO_3 mixture was used to attack silicate minerals and dissolve sample powders in a fully sealed Teflon vial situated in a stainless steel pressure vessel (a high-pressure steel-jacketed vessel, or a 'bomb'). Specifically, 50 ± 0.5 mg sample powder was placed in a 15 mL Teflon vial, adding 1.5 mL concentrated HNO_3 + 1.5 mL concentrated HF + 0.01 mL concentrated $HClO_4$. After being dried firstly on the hot plate at 140°C to remove most of the silicon in form of the volatile SiF_4, 1.5 mL concentrated HNO_3 and 1.5 mL concentrated HF were added in vials again, and placed in the steel-jacketed vessel in the oven at 190°C for 48 hours to further dissolve samples. After being dried on the hot plate for the second time, added 3.0 mL concentrated HNO_3, and dried the sample for the third time to expel the residual HF and related F^- if present. Subsequently, added 3.0 mL 1:1 HNO_3 and placed the sealed steel-jacketed Teflon bombs in the oven again at 150°C for 12 hours to guarantee the thorough dissolution of samples. Finally, 1 g Rh, as an internal standard monitor for signal drifting correction during analysis, was added into the solution, which was diluted to 80.00 g by Milli-Q water (18.2 MΩ) afterwards.

United States Geological Survey (USGS) reference materials (AGV-2, BHVO-2, BCR-2 and GSP-1) were used as certificated external standards. Analytical accuracy, as indicated by

relative difference (relative error, RE) between measured and recommended values of reference materials, are within ±10% for most of the trace elements (Table B.1 in Appendix B). Exceptions are: 52.7% Be, -17.2% Cr and -13.2% Ni for BCR-2; -26.2% Sc and -20.1% Pb for BHVO-2; even more trace elements in GSP-1 with poor correspondence, which may be attributed to the lower contents of these elements in GSP-1 (Liu *et al.*, 2007; Table B.1 in Appendix B). The reproducibility (relative standard deviation, RSD), determined from duplicate sample analyses, is better than 10% (Table B.1 in Appendix B). Bulk-rock trace element data for samples from North Qilian Mountain are given in Table D.3-5 in Appendix D.

3.2 MINERAL GEOCHEMISTRY

Major element contents for minerals in the metamorphic rocks from North Qilian Mountain were analyzed using a JXA-8100 electron probe micro-analyzer (EPMA) at Chang'an University, China, while major element contents of those minerals in metamorphic rocks from Western Tianshan had been analyzed using scanning electron microscope – energy dispersive spectrometer (SEM-EDS) by Lavis for his PhD thesis (Table C.2 in Appendix C; Lavis, 2005, also see Xiao *et al.*, 2012). Mineral trace element contents and major element contents of anhydrous minerals were analyzed using laser ablation (LA)-ICPMS for those in metamorphic rocks from both two study areas. Most of the analyses were completed in Northwest University, Xi'an, while the others were performed at State Key Laboratory of Geological Processes and Mineral Resources, China University of Geosciences in Wuhan.

3.2.1 An Internal Standard-independent Calibration Method

For mineral *in situ* trace element analysis, the traditional method is to choose an element of known concentration in the sample (a mineral), which was analyzed using an independent method prior to the LA-ICPMS analysis (e.g., prior analyzed using EPMA). However,

considering the highly heterogeneous composition of metamorphic minerals, the mineral *in situ* analysis for both major and trace element contents simultaneously are required.

To solve this problem, Liu *et al.* (2008) developed an internal standard-independent calibration method for LA-ICPMS analysis of anhydrous minerals, and proposed that through the normalization of the sum of all metal oxides to 100 wt.% after external calibration against reference materials, an ablation yield correction factor (AYCF) can be used to correct the variations in absolute amount of materials ablated during each run:

$$\text{AYCF} = \frac{100}{\sum_{j=1}^{N}(cps_{sam}^{j} \times l^{j})}$$

$l^{j} = C_{rm}^{j} / cps_{rm}^{j}$, cps_{sam}^{j} and cps_{rm}^{j} are net count rates of analytical element *j* of the sample (sam) and reference material (rm) for calibration.

C_{rm}^{j} – The concentration of element *j* in the reference material; N – the number of elements that can be determined by LA-ICPMS.

If multiple external standards were used, *l* would be then calculated based on a best-fit calibration line through the linear regression.

3.2.2 Analytical Conditions and Data Quality

Polished thick "thin-sections" (100 μm) were used for mineral geochemical analysis.

Mineral major element analysis using a JXA-8100 EPMA was done using an accelerating voltage of 15 kV and 10 nA probe current with a 1 micron beam diameter. Standards used for calibration were: albite for Na, quartz for Si, orthoclase for K, apatite for P and Ca, magnetite for Fe, pyrophanite for Mn and Ti, chromite for Cr and Fe, forsterite for Mg, jadeite for Al. (Minwu Liu, 2009, personal communication; Chinese standard of Quantitative analysis method

for silicate minerals by EPMA, GB/T 15617-1995). Mineral major element compositional data obtained using EPMA for samples from North Qilian Mountain is given in Table D.6 in Appendix D.

The LA-ICPMS analysis used an Agilent 7500a equipped with GeoLas 2005 193 Eximer Laser sampler, and Varian 820-MS equipped with the same laser sampler. Laser ablation pit size ranges from 32 to 44 μm with a 5 – 8 Hz repetition rate. During each analysis, the acquisition times for the background and the sample ablation were 20 – 30s (gas blank) and 40 – 50s respectively. United States Geological Survey (USGS) glasses BCR-2G, BIR-1G, BHVO-2G and one synthetic glass, GSE-1G, were used as multiple reference materials for calibration. Off-line data reduction was completed using *ICPMSDataCal* (Liu *et al.*, 2008). All other analytical details including instrument conditions are given in Liu *et al.* (2008).

For anhydrous minerals (garnet, omphacite, rutile, titanite, feldspar), the concentrations of all elements of interest (both major and trace elements) were analyzed simultaneously using the innovative method developed by Liu *et al.* (2008), without using added internal standard (see section 3.2.1 above). We compared the analytical data using the AYCF LA-ICPMS method with those analyzed using EPMA for metamorphic minerals from North Qilian Mountain (Fig. 3.1) and with the SEM-EDS data (published in Xiao *et al.*, 2012) for metamorphic minerals from Western Tianshan (Figure B.1). These comparisons show that major element contents of anhydrous minerals analyzed using the AYCF LA-ICPMS method developed by Liu *et al.* (2008) are highly commendable with < ±10% deviation with respect to the EPMA/SEM-EDS data (except those elements with very low contents, e.g., Na_2O, K_2O in garnet, FeO in omphacite; Fig. 3.1). The apparent scatter for MgO and MnO in garnet (Figure B.1a) most likely reflects the compositional zoning.

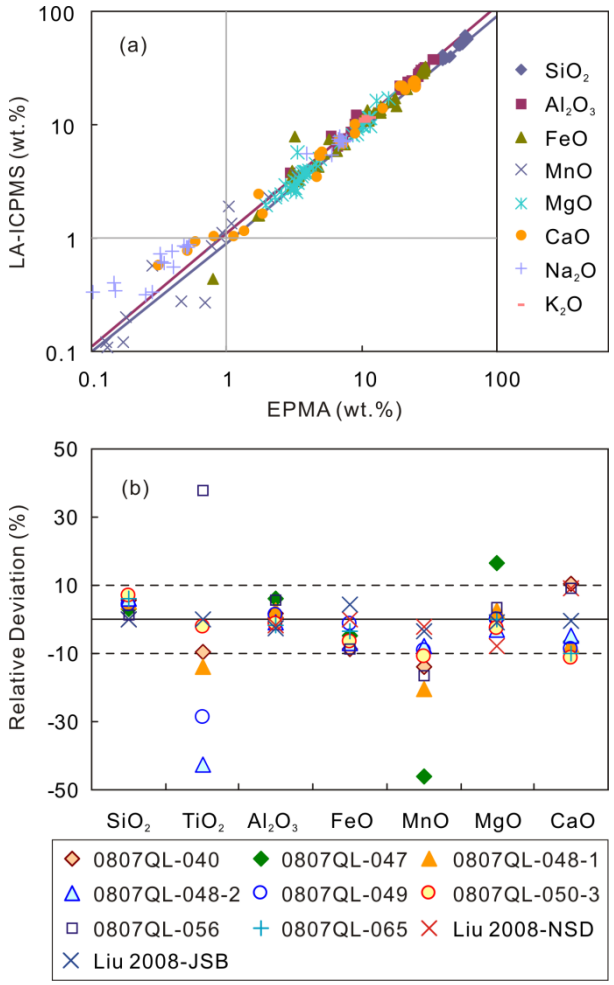

Figure 3.1 (a) Comparison of mineral major element contents using EPMA and LA-ICPMS calibrated by the method reported in Liu *et al.* (2008). The plots for major element contents less than 0.1 wt.% have not been shown considering their poor quality. Both selected anhydrous minerals (garnet, clinopyroxene) and hydrous minerals (phengite, epidote group minerals, amphibole, pumpellyite, lawsonite) from samples of North Qilian Mountain have been plotted. However, for hydrous minerals, the sum of all major element contents using EPMA has been normalized to 100% through excluding their H_2O content before plotting. Two diagonal lines represent the data with ±10% relative deviation, and thus the plots between these lines represent the data with relative deviations better than 10%. (b) A detailed comparison between analytical data using EPMA and LA-ICPMS for major element concentrations of garnet. Relative Deviation (%) = 100×([value obtained by LA-ICPMS] — [value obtained by EPMA]) / [value obtained by EPMA]. The relative deviation for two garnet grains from Liu *et al.* (2008) is also plotted for reference. The relative deviation for all the analyzed SiO_2, Al_2O_3, FeO and CaO is within ±10%; the same case for MgO except one point. The relatively big variation of MnO may be caused by the zoned garnet with varying compositions, e.g., the sample with big negative deviation of MnO has also big positive deviation of MgO (0807QL-047). The low content of TiO_2 in garnet resulted in the big deviation of TiO_2 (Na_2O and K_2O as well, not shown). This comparison for major element contents of anhydrous minerals indicates that the method developed by Liu *et al.* (2008) allows for acquiring good data quality.

For hydrous minerals (muscovite, paragonite, lawsonite, epidote group minerals, pumpellyite, apatite, amphiboles, chloritoid, and chlorite), we used the traditional method, for which we chose ^{29}Si (analytical data of SEM-EDS for samples of Western Tianshan, from Lavis [2005] and Xiao *et al.* [2012], also see Table C.2 in Appendix C; EPMA data for samples from North Qilian Mountain, Table D.6 in Appendix D) as the internal standard.

The analytical uncertainty is better than 5% (relative error, RE; except P, see Table B.2 in Appendix B) for data analyzed using both methods in terms of the repeated analysis of standard GSE-1G (which contains high trace element concentrations ranging from several ppm to commonly 100s ppm; Guillong *et al.*, 2005; Jochum *et al.*, 2005). The precision for all the analyzed major and trace elements in terms of GSE-1G is better than 10% (relative standard deviation, RSD; except P, see Table B.2). During analysis, we purposely avoided inclusions.

Mineral trace element compositional data obtained using LA-ICPMS are given in: Table C.3 (garnet), Table C.4 (epidote group minerals), Table C.5 (both phengitic muscovite and paragonite), Table C.6 (rutile and titanite), Table C.7 (clinopyroxene, feldspar), Table C.8 (amphiboles, chlorite) in Appendix C for samples from Western Tianshan; Table D.7 (anhydrous minerals) and Table D.8 (hydrous minerals) in Appendix D for samples from North Qilian Mountain. The major element compositional data by LA-ICPMS for anhydrous minerals have also been reported in relevant tables (Table C.3, Table C.6-7, and Table D.7).

CHAPTER 4:

TRACE-ELEMENT TRANSPORT DURING SUBDUCTION-ZONE ULTRA-HIGH PRESSURE METAMORPHISM: EVIDENCE FROM WESTERN TIANSHAN, CHINA

4.1 INTRODUCTION

In Chapter 1, we have clarified the significance of the subduction-zone metamorphism (SZM) to the arc magmatism and the deep mantle compositional heterogeneity. Therefore, the understanding of the subduction-zone metamorphism, especially the ultrahigh pressure (UHP) metamorphism is really essential. Considering the occurrence of UHP metamorphic belt in Western Tianshan, China (Chapter 2), in this chapter and Chapter 5, detailed studies on petrography, bulk-rock compositions (this chapter) and mineral compositions (Chapter 5) will be given for rocks of basaltic protoliths and sedimentary protoliths from this UHP metamorphic belt in Western Tianshan, China.

Focused on the study of petrography and bulk-rock compositions of these rocks, in this chapter, we attempt to reveal the general elemental behaviors during subduction-zone metamorphism and the contribution of subduction-zone metamorphism to the origin of subduction-zone magmatism and mantle compositional heterogeneity to a first order.

4.2 PETROGRAPHY

The UHP metamorphic belt in Western Tianshan is dominated by blueschist and eclogite pods and lenses, surrounded, in fault contacts, by greenschist-facies rocks (Fig. 2.1). In total, 50 samples were taken from locations broadly similar to those reported by Gao & Klemd (2003) and Zhang *et al.* (2003), including one rodingite TS02–34, which is dominantly made up of garnet (69.4 vol.%). An additional nine samples were provided by Lifei Zhang from localities described in Zhang *et al.* (2003). Detailed petrography is given in Table C.9 in Appendix C.

Rocks of sedimentary protolith (Fig. 4.1p) can be readily distinguished from rocks of basaltic protolith (Figs. 4.1a–o; some of which are sampled from the well-preserved pillows in the field)

by their very high modal abundances of quartz and carbonate, as well as more obvious foliations defined by high modes of white micas. Many samples of sedimentary protolith have ~ 50 vol.% quartz, and are termed as quartz mica schists (Fig. 4.1p; Table C.9 in Appendix C). Compared with rocks of basaltic protolith, rocks of sedimentary protolith tend to show stronger retrogressive overprints, particularly the extent of chloritization of minerals such as garnet and white mica.

Samples TS02–03B (Fig. 4.1a), TS02–15A, TS02–17b, and TS02–32A (Fig. 4.1b) belong to typical eclogite (where garnet + omphacite > 70 vol.% of the bulk rock). They are composed of garnet porphyroblasts and fine-grained omphacite matrix, along with varying amounts of accessory minerals, including amphibole (Na-amphibole and some [sodic-]calcic amphibole), (clino)zoisite, white mica (both phengitic muscovite and paragonite), rutile, titanite, quartz, and carbonate. Glaucophane and omphacite inclusions in garnet indicate that eclogites underwent a prograde blueschist-facies metamorphism prior to reaching the eclogite facies, i.e., stage 1 in Figure 2.3. Glaucophane also occurs as discrete relicts of prograde metamorphism in the matrix, and only some of them show the overgrowth of (sodic-)calcic amphibole on glaucophane (e.g., TS02–15A), indicating a highly progressive metamorphism and limited retrograde metamorphic overprints. The relatively low modal (clino)zoisite may be attributed to less retrograde (clino)zoisite formation and more pronounced breakdown of prograde (clino)zoisite evidenced by resorption features (e.g., Fig. 4.1f; also see John *et al.*, 2008). Although no coesite has been found in our samples, considering the occurrence of coesite and the absence of diamond in other eclogites from Western Tianshan (Lü *et al.*, 2008, 2009), the peak metamorphic condition estimated by Lü *et al.* (2009; 2.4 – 2.7 GPa and 470 – 510°C) is also used as the stage 2 condition in this study (Fig. 2.3), with the modeled peak mineral assemblage of Grt + Omp + Lws + Gln + Coe. The occurrence of big chloritoid poikiloblasts, which contain glaucophane, idioblastic (clino)zoisite, and white mica inclusions, in sample TS02-01 (not shown in Table C.9) points to the pressure of ~ 2.2 – 2.4 GPa (Pawley *et al.*, 1993; Schmidt & Poli, 1998; Lü *et al.*, 2009), and is also consistent with the UHP at peak metamorphic conditions.

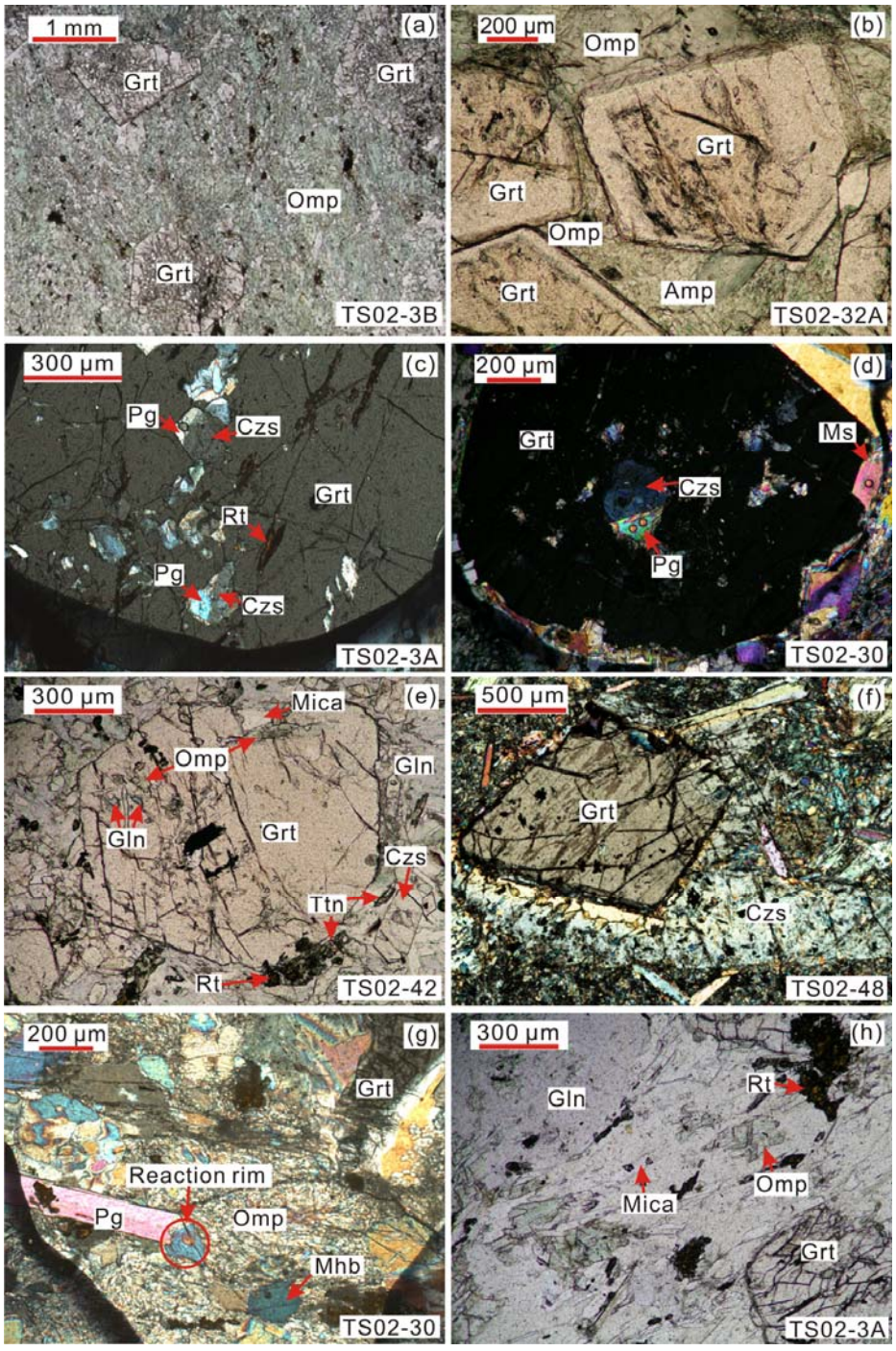
1 mm
(a)
Grt
Grt
Omp
Grt
TS02-3B
200 µm
Omp
(b)
Grt
Grt
Omp
Grt
Amp
TS02-32A
300 µm
(c)
Pg
Czs
Grt
Rt
Pg
Czs
TS02-3A
200 µm
(d)
Grt
Ms
Czs
Pg
TS02-30
300 µm
Mica
(e)
Omp
Gln
Gln
Grt
Czs
Ttn
Rt
TS02-42
500 µm
(f)
Grt
Czs
TS02-48
200 µm
(g)
Grt
Reaction rim
Pg
Omp
Mhb
TS02-30
300 µm
(h)
Rt
Gln
Omp
Mica
Grt
TS02-3A

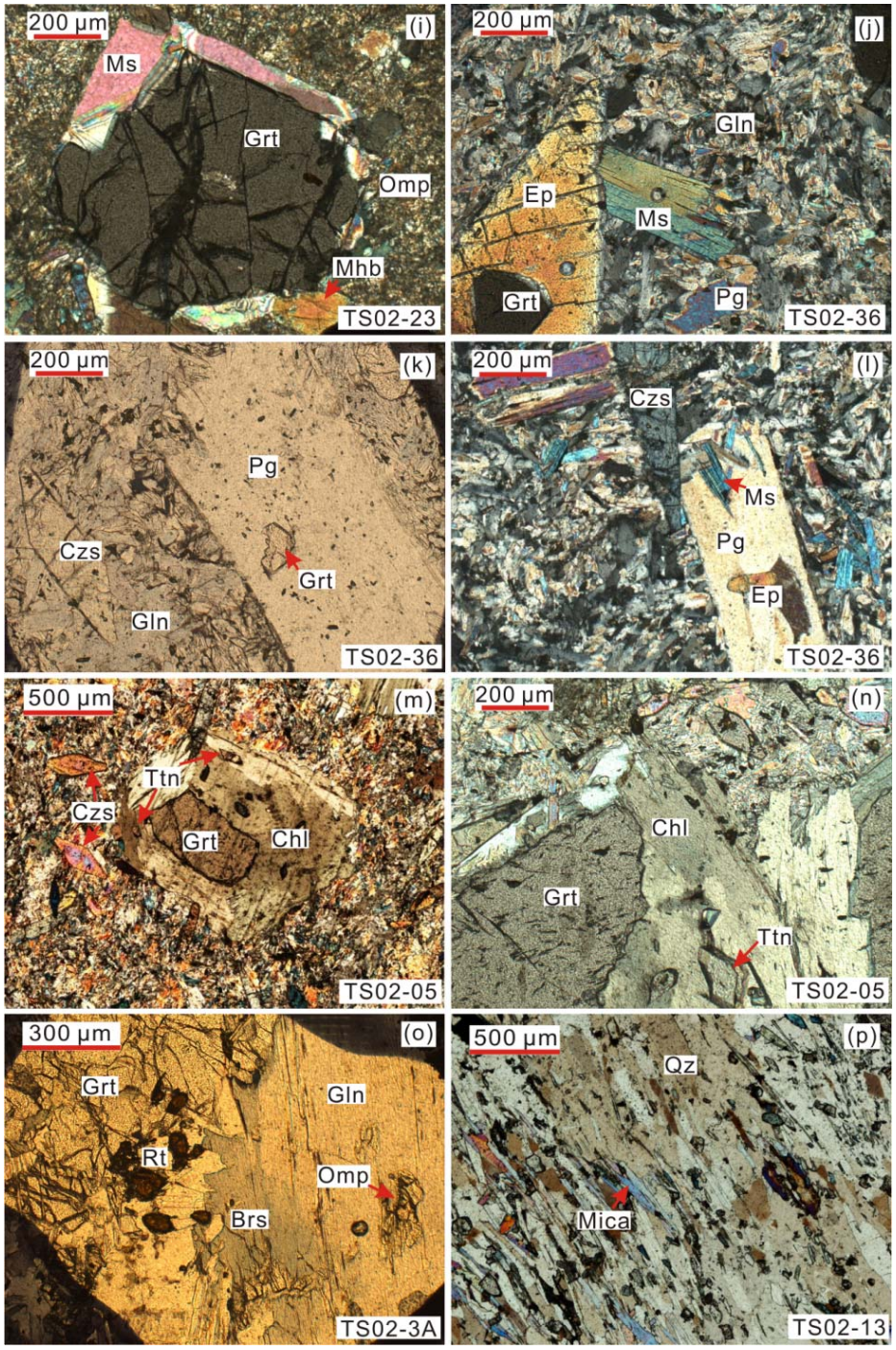

Figure 4.1 Representative photomicrographs of samples from Western Tianshan, (a–o) for samples of basaltic protolith and (p) for one sample of sedimentary protolith. (a–b, e, h, k, o) were taken under plane polarized light (PPL); others were taken under crossed polarized light (XPL). See Abbreviation List for mineral abbreviations.

(a-b) Classic eclogite, dominantly composed of garnet and omphacite. (c-d) Retrograde blueschist. Coexisting paragonite and clinozoisite preserved as tabular/box-shaped inclusions in garnet

poikiloblast may represent lawsonite pseudomorphs. In (d), one mica grain has replaced the rim of garnet, probably reflecting the rehydrating process during retrograde metamorphism. (e) Eclogitic blueschist. Idioblastic garnet with omphacite and glaucophane inclusions indicates a prograde blueschist-facies metamorphism. In the lower-right corner of this photo, rutile has been replaced by surrounding titanite during retrograde metamorphism. (f) Garnet omphacitite. One idioblastic garnet grain has grown at the expense of prograde clinozoisite nearby, resulting in the resorption grain boundary at the rim of the latter. (g) Retrograde epidote eclogitic blueschist. One paragonite grain with a reaction rim shows that it may be replaced by omphacite during high prograde metamorphism. However, garnet replaced by white mica at the upper-right corner is a retrograde overprint. (h) In eclogitic blueschist dominated by glaucophane, the presence of white mica and omphacite inclusions indicates that the glaucophane in this sample, TS02–03A, was produced by retrograde metamorphism rather than prograde metamorphism. This retrograde sample is used in later section 4.5.2 for discussing rehydration effects on re-enrichment, compared with eclogite TS02–03B (Fig. 4.1a). Also see Fig. 4.1o. (i) Epidote blueschist. The rim of garnet has been replaced by muscovite and Mg-hornblende, reflecting the effect of post-kinetic re-hydration. (j) Epidote blueschist. One garnet preserved as an inclusion in well-crystallized rhombic epidote. (k) One paragonite porphyroblast with a relic garnet inclusion probably reflects the rehydration during retrograde metamorphism. (l) Epidote and phengitic muscovite preserved as inclusions in a paragonite porphyroblast indicate that the paragonite is most likely produced due to retrograde rehydration while the epidote and muscovite inclusions are formed at earlier metamorphic stages. (m-n) Retrograde epidote blueschist with chlorite overprinting on garnet porphyroblast. Titanite with very well-crystallized prismatic crystal shape, together with chlorite, has largely replaced garnet. (o) Glaucophane has barroisite overgrowth at the rim, and one omphacite inclusion in the core, caused by retrograde overprints. (p) Chloritized quartz mica schist, characterized by abundant quartz and foliation fabrics.

Blueschist is dominated by glaucophane and (clino)zoisite with or without omphacite (e.g., Figs. 4.1h,j-l). (Clino)zoisite could be locally abundant. Glaucophane, omphacite, white micas, (clino)zoisite, carbonate, and quartz are typical inclusions in garnet poikiloblasts (e.g., Fig. 4.1e). An observation of particular note is the occurrence of (clino)zoisite and paragonite preserved as inclusions in garnet, forming box−shaped lawsonite pseudomorphs (e.g., Figs. 4.1c-d; this is also observed in eclogites) and suggesting a previous lawsonite-bearing blueschist-facies metamorphism, i.e., stage 1 in Fig. 2.3. Carbonate is common and can be abundant (Table C.9 in Appendix C). Some carbonate minerals are well crystallized, showing an equilibrium texture with coexisting silicate phases, reflecting their protolith inheritance and metamorphic recrystallization. However, retrograde carbonate also occurs as irregular patches or fine veinlets replacing other minerals (including garnet).

In addition to evidence for prograde metamorphism afforded by mineral inclusions in garnet (e.g., omphacite and glaucophane inclusions [Fig. 4.1e], lawsonite pseudomorphs [Fig. 4.1c-d]), prograde (clino)zoisite also shows amoeboid grain boundaries (also see Fig. 5 in John *et al.*, 2008) and a 'sponge' structure caused by replacement of newly-crystallized omphacite and garnet (e.g., Fig. 4.1f), corresponding to the reaction of 13 Gln + 6 Czs = 9 Prp + 26 Jd + 12 Di + 19 Coe/Qz +16 H_2O. The presence of prograde (clino)zoisite in the lawsonite stability field may result from the relatively low H_2O content in the system (Poli & Schmidt, 1997). Prograde white micas are also present (e.g., as inclusions in glaucophane in Fig. 4.1h), which, together with prograde (clino)zoisite, may also reflect the conditions of stage 1 (Fig. 2.3). The characteristic mineral assemblage at this stage is mainly composed of Lws + Czs + Gln + Omp + Grt + Ph + Pg + Rt.

On the other hand, the replacement of lawsonite inclusion by paragonite and clinozoisite in garnet indicates the breakdown of lawsonite, which may happen during retrograde eclogite facies (from stage 2 to stage 3 in Fig. 2.3), although the timing of this reaction remains debatable. For example, Gao *et al.* (1999), Gao & Klemd (2003) and Spandler *et al.* (2003)

assumed that it happened during prograde metamorphism from lawsonite blueschist to eclogite facies. Idioblastic retrograde (clino)zoisite and retrograde white micas are also present. White micas, especially paragonite, may also be re-produced at this stage, and replaced the rim of garnet (Figs. 4.1d,i), or include the prior garnet (Fig. 4.1k), epidote and muscovite (Fig. 4.1l). (Sodic-)calcic amphiboles are common, most of which have clearly replaced other minerals like garnet. Clear zonings, e.g., (sodic-)calcic amphibole having Na-amphibole cores, and even containing omphacite inclusions (e.g., Figs. 4.1h,o), indicate retrograde metamorphism from eclogite to (epidote-) amphibolite facies (at stage 3 to stage 4 in Fig. 2.3). Together with the development of titanite at the rim of rutile (e.g., Fig. 4.1e) and the significant replacement of garnet by retrograde epidote group minerals (Fig. 4.1j), chlorite, and importantly titanite (e.g., Figs. 4.1m,n), the characteristic mineral assemblage becomes Czs + Ttn + Brs/Act + Grt + Ph + Chl + Ab.

All the foregoing petrographic observations, especially of the mineral assemblage and the textural relationship (Fig. 4.1), together with the estimated metamorphic P-T path for coesite-bearing eclogite from Western Tianshan by Lü *et al.*, (2009), formed the basis for the schematic P-T path (Fig. 2.3) to illustrate the concept, although individual samples are likely to have undergone different extents of retrograde metamorphism.

4.3 MINERALOGY AND BULK-ROCK COMPOSITION

4.3.1 Mineral Compositions

Garnet shows a sharp compositional variation, with increasing pyrope composition at the rims in most samples (Table C.2 and Table C.3 in Appendix C). Clinopyroxene is omphacitic (Fig. 4.2a; Table C.2 and Table C.7 in Appendix C). Amphiboles vary in composition, from glaucophane to calcic and sodic-calcic amphiboles including actinolite, barroisite/katophorite, and magnesiohornblende (Fig. 4.2b). Representative analyses of specific types of amphiboles

are given in Table C.2 of Appendix C. Both phengitic muscovite and paragonite mica exist (Table C.2 in Appendix C), and are classified in terms of K/Na ratio. Compositions of epidote group minerals are also variable, especially in total FeO (Table C.2 in Appendix C).

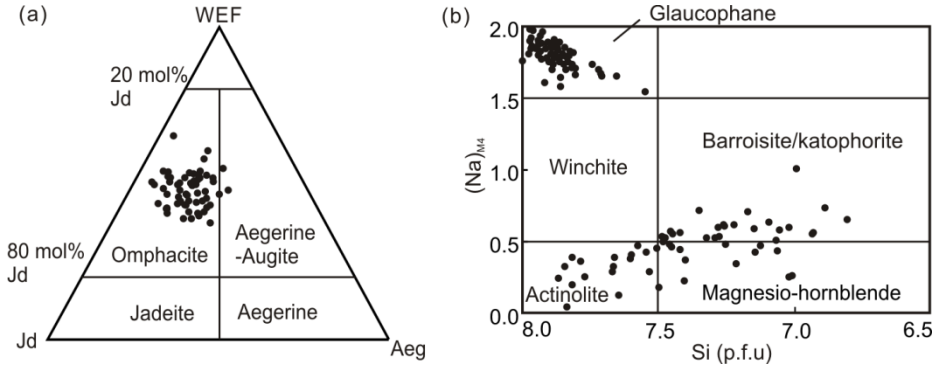

Figure 4.2 Compositional classification of clinopyroxene and amphibole. (A) WEF (wollastonite + enstatite + ferrosilite)–Jd–Aeg diagram following Morimoto (1988) for clinopyroxene compositions, all of which have omphacitic compositions. (B) $(Na)_{M4}$–Si (p.f.u.) diagram for amphiboles (Leake *et al.*, 1997), showing compositional distinctions between glaucophane and other amphiboles.

4.3.2 Bulk-Rock Major Element Analysis and Reconstructed Composition

Table C.1 shows bulk-rock major and trace element contents. Samples of sedimentary protolith have variably high SiO_2 (52.09 – 76.66 wt.%) and relatively low MgO (1.81 – 4.82 wt.%), CaO (1.29 – 7.67 wt.%), and TiO_2. Samples of basaltic protolith have low SiO_2 (40.96–53.19 wt.%) and Al_2O_3 (< 20 wt.%) and relatively high MgO (up to 8.56 wt.%). Major elements are highly variable, including loss on ignition (LOI), which is closely associated with the estimated carbonate modal abundances evidenced by their significant correlations (not shown). The pronounced high carbonate modal abundances in several samples also explain the high CaO and low SiO_2 contents (e.g., TS02-06, 106-14). Among different groups of samples of basaltic protolith (see the section 4.4.1 for classification), group 1 generally has the highest TiO_2 (1.62 – 3.85 wt.%) and K_2O (up to 3.63 wt.%). Group 2 shows the lowest TiO_2 (< 2 wt.%), except for two samples (TS02-15A and TS02-15B), which have major compositions distinctive from other samples of the same group, i.e., much higher TiO_2 (2.78 and 2.80 wt.%) but lower Mg# (31.10 and 32.19). One sample of ultramafic protolith (TS02-34) contains only 34.01 wt.% SiO_2 and

low Mg# (i.e., 20.44).

To understand the redistribution of elements (including flux in and out of the system) between mineral phases in our subsequent studies using *in situ* major- and trace-element analyses, it is necessary to perform a quantitative analysis of mineral modes. Detailed modal analyses of these rocks were done by point-counting using a James Swift automatic point counter, model F 415C. The modal data are given in Table C.9 in Appendix C. The calculation method and the calculated results are given in the caption of Figure C.1 in Appendix C. Comparisons of reconstructed bulk-rock major element compositions with actual analyses indicate that our estimations of mineral modes are reliable (Figure C.1 in Appendix C), although some uncertainties still exist (see discussions in the caption of Figure C.1 in Appendix C).

4.4 TRACE ELEMENT MOBILITY AND GEOCHEMISTRY OF SAMPLE GROUPS

4.4.1 Sample Grouping

Experimental studies (e.g., Manning, 2004; Kessel *et al.*, 2005; Hermann *et al.*, 2006) have shown that high field strength elements (HFSEs, i.e., Ti, Zr, Hf, Nb, Ta) together with Y and the middle to heavy rare earth elements (M-HREEs), are usually not mobile during fluid-rock interactions. These studies also show that Th and LREEs are usually immobile. Alkali and alkali earth elements such as Rb, Cs, and Ba are usually mobile, as are Na and K, used for the classification of modern lavas. For this reason, immobile elements should be used for rock classification and tectonic discrimination of protoliths of metamorphic rocks (e.g., Pearce & Cann, 1973; Winchester & Floyd, 1977).

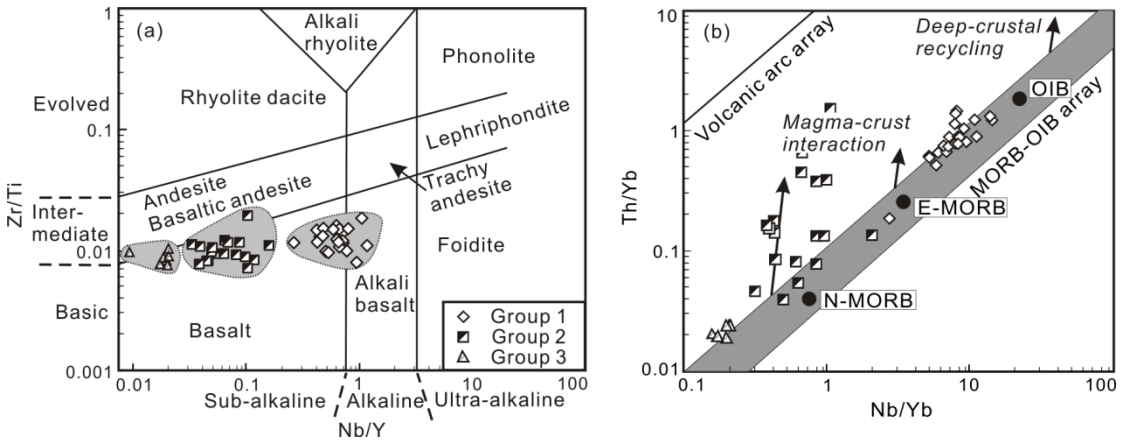

Figure 4.3 (a) Zr/Ti – Nb/Y diagram for rocks of basaltic protolith (after Winchester & Floyd, 1977; Pearce & Wyman, 1996). (b) Th/Yb – Nb/Yb for rocks of basaltic protolith (after Pearce, 2008). Ocean island basalt (OIB), enriched (E-), and normal (N-) mid-ocean-ridge basalt (MORB) are plotted for comparison (black solid circles; the values of oceanic basalts are from Sun & McDonough, 1989).

The Zr/Ti versus Nb/Y diagram (Winchester & Floyd, 1977) is often used as an immobile trace element equivalent of the TAS (total alkali vs. silica) diagram to classify volcanic rocks with varying degrees of alteration/metamorphism in the geological records. In Figure 4.3a, which uses the updated boundaries of Pearce & Wyman (1996), samples of basaltic protolith plot in three clusters, mainly in the sub-alkalic basalt field. They display a small range in Zr/Ti ratio (equivalent to a small SiO_2 variation) but a large range in Nb/Y ratio (equivalent to large total alkali variations). We term these group 1, group 2, and group 3 samples, respectively (see Tables C.1 and Tables C.9 in Appendix C for geochemical data and mineral assemblages).

Provided that Th, Nb, Ti, and Yb are immobile throughout the metamorphic process, the Th/Yb versus Nb/Yb and Ti/Yb versus Nb/Yb diagrams (Pearce, 2008) are effective in fingerprinting tectonic settings of magma eruption. The first of these diagrams features a diagonal MORB-OIB array containing N-MORB, E-MORB, and OIB compositions (Fig. 4.3b). Basalts with a subducted or assimilated continental crustal component plot above this array; these include volcanic arc basalts, some back-arc basin basalts, and basalts contaminated with continental crust materials. For our samples, the three groups defined in Figure 4.3a are also well separated on this projection. Samples from group 1 and group 3 plot within or at the field edge of the

MORB-OIB array. Their protoliths are most likely OIB- or E-MORB–like and depleted MORB-like rocks, respectively. The high Ti/Yb ratios of the former on the Ti/Yb-Nb/Yb diagram (not shown) demonstrate that these are OIB-like rather than E-MORB–like.

In contrast, group 2 samples define a distinct trend away from the MORB-OIB array into the volcanic arc/contamination field. Because this trend includes samples within the MORB-OIB array, it is likely to reflect the effect of crustal contamination of MORB-like magmas or a mixing relationship between MORB and arc materials (Pearce, 2008). Group 2 samples will be excluded from the study of element mobility in terms of bulk-rock geochemistry (following sections in Chapter 4) because alteration and contamination (or mixing) effects cannot be easily resolved in the bulk-rock studies.

4.4.2 Determination of Element Mobility/Immobility

Although HFSEs and HREEs have been widely considered to be immobile, there is some evidence that they are not always conserved during subduction-zone metamorphism (e.g., Gao *et al.*, 2007; John *et al.*, 2008), which is possible in the case of some subduction-zone fluids (e.g., supercritical H_2O-rich fluids, CO_2-rich fluids, and perhaps, even SiO_2-rich hydrous melts; Manning, 2004; Kessel *et al.*, 2005). Therefore, to understand the geochemical consequences of subduction-zone metamorphism properly, it is necessary to examine the actual mobility and immobility of each element of geochemical significance in our samples.

Because elemental behavior during the formation of igneous protoliths is governed by the partition coefficient during partial melting/crystallization, elements with similar incompatibility in igneous protoliths are expected to be significantly correlated. Based on this principle, one simple way to examine the element mobility or immobility is to see if these statistically significant correlations are preserved (or not) in our metamorphic samples, i.e., whether these elements have been fractionated from each other during metamorphism (e.g., Niu, 2004). If a significant correlation between two similarly incompatible elements is preserved in the

metamorphic rocks, then these two elements have remained immobile; otherwise, one of them or both may have been mobilized during metamorphism. Note that two mobile elements with similar incompatibility may also exhibit significant correlations. Therefore, we selected two HFSEs with different incompatibilities (i.e., Nb and Zr) and investigated their correlations with other trace elements with varying incompatibility, i.e., Nb with large ion lithophile elements (LILEs), LREEs, Th, U, and Ta, and Zr with MREEs, some LREEs, and Hf (Fig. 4.4).

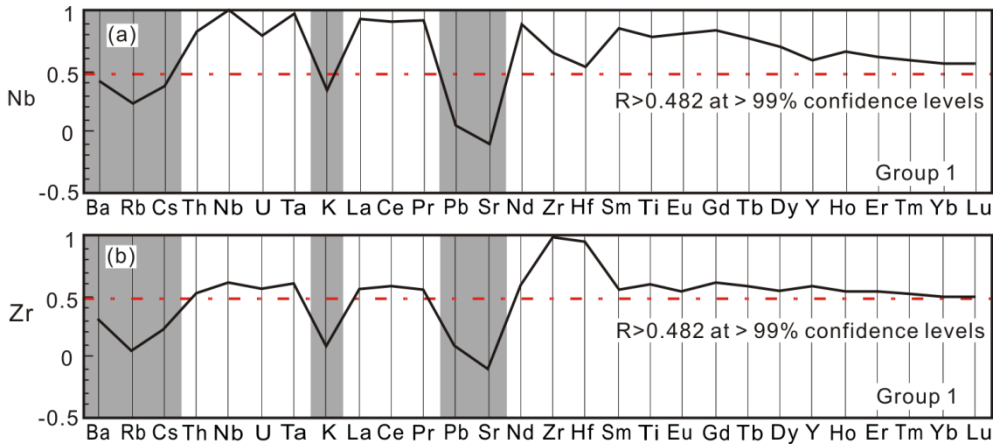

Figure 4.4 Correlation coefficient diagrams of Nb (a) and Zr (b) with other trace elements for samples of group 1 from Western Tianshan (Niu, 2004; Lavis, 2005). Elements along *x*-axis are ordered in terms of decreasing incompatibility from left to right. The red dotted-dashed lines represent the minimum significant correlation coefficient, i.e., 0.482 (refer to critical value of Pearson's correlation coefficient using a one-tail test) at 99% confidence levels for 23 samples (i.e., the degree of freedom is 21). Two immobile elements (Nb and Zr) were chosen considering their different incompatibility; therefore significant correlation coefficients with Nb or Zr can reflect immobility of elements with varying incompatibility. Similar conclusion can also be drawn for samples from group 3.

Investigations of correlation coefficients were carried out following the methods of Niu (2004) and Lavis (2005) for cogenetic rocks of basaltic protolith from group 1 (Fig. 4.4) and group 3 (not shown), and for rocks of sedimentary protolith in Table C.10 (although the method is less effective in meta-sedimentary rocks than for meta-basaltic rocks). Figure 4.4 shows the correlation coefficients of the immobile incompatible elements Nb and Zr with other trace elements, which are sorted in order of decreasing incompatibility from left to right following the order reported by Niu & Batiza (1997). For $N = 23$ (group 1) and $N = 6$ (group 3), only those

correlations above 0.482 and 0.882, respectively, are treated as statistically significant correlations at > 99% confidence levels. In Figure 4.4, we find that Ba, Cs, Rb, K, Pb, and Sr are not significantly correlated with Nb and Zr and have, therefore, been mobilized in our samples of basaltic protolith, during either prograde or retrograde metamorphism, or prior to subduction-zone metamorphism (i.e., during seafloor alterations). All other elements showing statistically significant correlations with Nb and Zr (i.e., REEs, HFSEs, Th, and U) have thus remained largely immobile.

Previous studies (e.g., John *et al.*, 2004) showed that LREEs, U, and Th can be fractionated from HFSEs and HREEs during subduction-zone metamorphism. However, Figure 4.5e shows that the U/Nb ratio of our samples is constrained within a small range similar to that of N-MORB, except for samples from group 2 that have been attributed to the contamination or mixing with materials with high, possibly variable, U/Nb ratios, such as continental crust (see section 4.4.1). In addition, Nb/La ratios of our samples are also relatively constant, i.e., 0.94 ± 0.15 (1δ; group 1) and 0.45 ± 0.06 (1δ; group 3). Together with the significant linear correlations between U and Th (Fig. 4.5f), all these values suggest that U, Th, and LREEs in our samples have not been mobilized since the formation of their protolith, as predicted for HFSEs and HREEs. Furthermore, the compositional range of altered ocean crust is relatively large with respect to U content, which may be enriched by up to five times in altered ocean crust, as shown in the super-composite composition of the tholeiitic section of ocean crust in Ocean Drilling Program Site 801 (Kelley *et al.*, 2003), and U shows its strong mobility during seafloor alteration (also see Niu, 2004). Thus, altered ocean crust may show a poor correlation of U with immobile elements (e.g., Fig. 4c in Kelley *et al.*, 2005) and have lower Th/U ratios (or Nb/U) in some rocks due to U enrichment. Therefore, the significant linear correlation of U with Th (or Nb, not shown) and the inferred immobility of U, as well as the distinctive Th/U ratios of all our samples from altered ocean crust (Fig. 4.5f), suggest that the component of altered ocean crust, if involved at all, is insignificant in the protoliths of our samples.

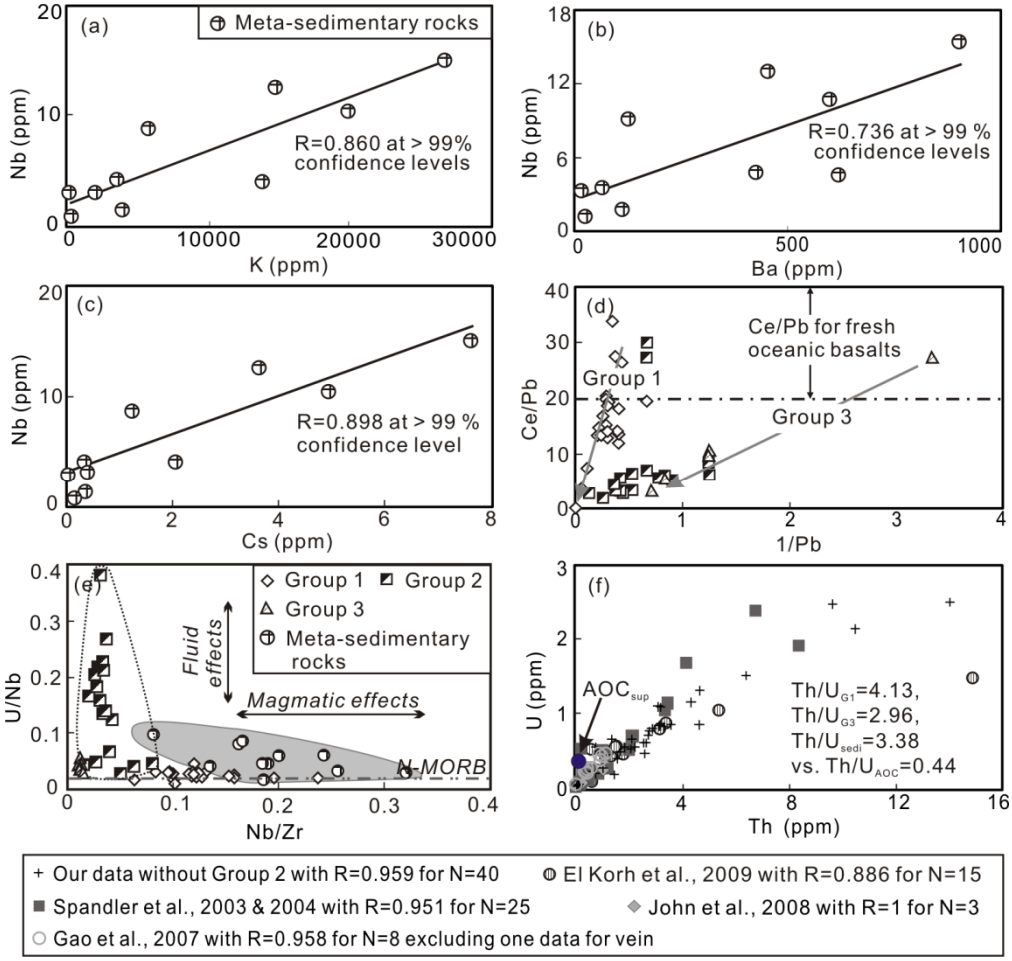

Figure 4.5 Elemental co-variation diagrams. (a–c) Statistically significant (at > 99% confidence levels; the critical value of Pearson's correlation coefficient using one-tail test for 10 samples is 0.7155) correlations of large ion lithophile elements (LILEs) with Nb in rocks of sedimentary protolith, suggesting relative immobility of K, Cs, Ba, and Rb (not shown here) during subduction-zone metamorphism. (d) Ce/Pb versus 1/Pb for rocks of basaltic protoliths (after John *et al.*, 2004). The Ce/Pb range for fresh oceanic crust is from Bebout (2007). Gray arrows indicate the trend of the Pb addition for group 1 and group 3. (e) U/Nb versus Nb/Zr for rocks of both sedimentary and basaltic protoliths (after John *et al.*, 2004). The U/Nb ratio of normal mid-ocean-ridge basalt (N-MORB) (= 0.02; represented by the horizontal dashed line) is from Sun & McDonough (1989). (f) Correlations between U and Th for rocks of basaltic (group 1 and group 3) and sedimentary protoliths in this study, as well as relevant data in the literature (Spandler *et al.,* 2003, 2004; Gao *et al.*, 2007; John *et al.*, 2008; El Korh *et al.*, 2009), without considering the effect of their different protoliths. The model composition of altered ocean crust (AOC_{sup}; super-composite of Ocean Drilling Program Site 801, representing tholeiitic section of ocean crust in Kelley *et al.*, 2003) is also plotted (the black solid circle). The average Th/U ratios of group 1 ($[Th/U]_{G1}$), group 3 ($[Th/U]_{G3}$), and meta-sediments ($[Th/U]_{sedi}$) in this study, and the Th/U ratio of model component of altered ocean crust ($[Th/U]_{AOC}$) are also given for comparisons. All the U-Th correlation coefficients in the text box beneath the plots are at > 99% the confidence levels.

Considering the much lesser mobility of Pb compared with U during seafloor alteration (e.g., Kelley *et al.*, 2005), together with the insignificant effects of seafloor alteration for our samples, it is most likely that the Pb mobility is the result of prograde and/or retrograde metamorphism after seafloor alteration, although the mobility of other LILEs (Rb, Cs, and K) may need further studies because of their higher mobility during seafloor alteration. Furthermore, the high Pb contents and low Ce/Pb compared with the range for fresh oceanic crust (see Bebout, 2007) may reflect the addition of Pb (Fig. 4.5d). As John *et al.* (2004) suggested, this Pb addition probably happened during exhumation of the slab rocks.

The significant inter-element correlations of HFSEs and REEs (Table C.10), and the good correlations of K, Rb (not shown), Cs, and Ba with HFSEs at > 99% confidence levels in rocks of sedimentary protolith (Figs. 4.5a-c) suggest their rather similar behavior during subduction-zone metamorphism. As HFSEs are immobile, K, Rb, Cs, Ba, and REEs in samples of sedimentary protolith are also immobile. The poor correlations of Pb and Sr with HFSEs may indicate their mobility during subduction-zone metamorphism. Therefore, based on the previous discussion, Pb and Sr are mobile, while REEs, HFSEs, Th, and U are immobile in both lithologies. The mobility and immobility of K, Rb, Cs, and Ba are protolith dependent, i.e., immobile in rocks of sedimentary protolith but mobile in rocks of basaltic protolith. Recently, Gao and co-workers (Gao *et al.*, 2007; John *et al.*, 2008) concluded that Nb, Ta, Ti, REEs, and LILEs are all mobile during subduction-zone metamorphism, based on a localized fluid-vein assemblage from Western Tianshan. Although their observations may be valid, we emphasize that caution should be taken not to generalize local phenomena as reflecting the prevailing nature of subduction-zone metamorphism. Our data demonstrate clearly that REEs and HFSEs are largely, if not entirely, immobile during subduction-zone metamorphism (Figs. 4.4-4.5).

4.4.3 Geochemistry of Different Sample Groups

Figure 4.6 shows N-MORB normalized multi-element diagrams for rocks of basaltic protolith (Figs. 4.6a-c) and for rocks of sedimentary protolith (Fig. 4.6d). All the mobile elements

discussed previously (i.e., LILEs, Pb, and Sr in the gray areas in Figs. 4.6a-c) display greater variability than immobile elements due to the "fluid effect" during subduction-zone metamorphism in the case of samples of basaltic protolith. Pb shows obvious enrichment in most samples, which is in correspondence with the previous assumption that Pb addition may occur during retrogressive metamorphism. No obvious Eu anomalies have been found. Mobile elements will not be used in the following discussion on the geochemistry of protoliths and their tectonic settings.

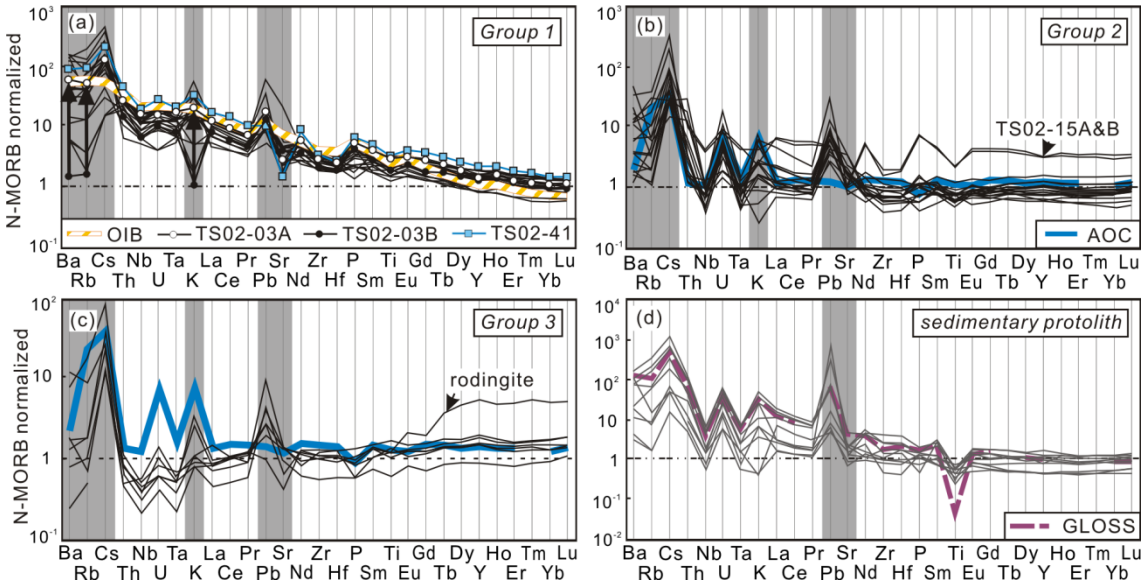

Figure 4.6 Normal mid-ocean-ridge basalt (N-MORB, Sun & McDonough, 1989) normalized multi-element diagrams of different groups for samples of basaltic protolith (a–c) and sedimentary protolith (d), following the decreasing order of elemental incompatibility determined by X/Y-X plots (Niu & Batiza, 1997). Average ocean island basalt (OIB) (a; Sun & McDonough, 1989), the model composition of altered ocean crust (b–c; super composite of Ocean Drilling Program Site 801, representing tholeiitic section of ocean crust in Kelley *et al.*, 2003), and global oceanic subducted sediments (GLOSS) (d; Plank & Langmuir, 1998) are plotted for comparison. Three representative samples are also highlighted in Figure 4.6a, and the vertical arrows represent the effect of re-enrichment caused by rehydration during retrograde metamorphism. Elements in light-gray areas are generally mobile as discussed in previous text (section 4.4.2).

Immobile incompatible elements are generally enriched in group 1, with a pattern similar to the average composition of OIB, which is also consistent with its high K_2O content. Group 2 displays a relatively flat pattern with stronger enrichments of U and Th relative to Nb and Ta (i.e., higher $[Th/Nb]_{N\text{-}MORB}$ and $[U/Ta]_{N\text{-}MORB}$), which are comparable to, or even much higher

than (in most samples), the model composition of altered ocean crust (Kelley *et al.*, 2003). Considering the contamination/mixing by continental or arc crustal materials (see Fig. 4.3b) as well as the insignificant contributions of altered ocean crust (if it is involved at all) in the protoliths (in group 1 and group 3), group 2 protolith may thus likely be derived from an N-MORB–like rock(s) with subsequent continental or arc crust contamination rather than seafloor alterations. Two samples (i.e., TS02-15A and TS02-15B) from group 2 show overall elevated trace element abundances (Fig. 4.6b) and lower Mg# (Table C.1), which are consistent with the protolith being more evolved basalts. Samples from group 3 are depleted in the progressively more incompatible elements and enriched in the less incompatible elements (such as HREEs), indicating a pattern similar to that of highly depleted MORB-like basalts (Fig. 4.6c).

As discussed already, LILEs are considered as immobile elements in rocks of sedimentary protolith; therefore, the large concentration range of LILEs shown in Figure 4.6d is inherited from the compositional heterogeneity of sedimentary protolith, rather than the mobility of LILEs. In contrast, variations in Pb and Sr concentrations are most likely attributed to their fractionations owing to their mobility. Most samples of sedimentary protolith have similar compositions to global oceanic subducted sediments (GLOSS; Plank & Langmuir, 1998) with enriched LILEs and depleted HFSEs, while those depleted in LILEs are likely rocks of graywacke protolith with arc basalt contributions.

Considering both the field study in Western Tianshan (e.g., Volkova & Budanov, 1999; Ai *et al.*, 2006) and the geochemical variability of modern seamounts from enriched OIB-like to depleted MORB-like basalts (such as those near East Pacific Rise seamounts; Niu & Batiza, 1997), we suggest that the UHP metamorphic rocks from Western Tianshan may have resulted from the subduction and exhumation of a tectonic mélange that was composed of normal seafloor with dismembered seamounts, sediments, and volcanic arc–derived materials.

4.5 DISCUSSION

4.5.1 Constraints on Trace Element Budgets

4.5.1.1 General thoughts

In the standard model of subduction-zone metamorphism, the transition from blueschist to eclogite facies was thought to mark the major dehydration reaction within the subducted ocean crust (e.g., Peacock, 1993; Liu *et al.*, 1996). However, in recent studies (e.g., Spandler *et al.*, 2003, 2004), it has been proposed that this transition does not necessarily result in the liberation of mobile elements with released fluids. This is consistent with the poor correlations of fluid soluble element contents with the glaucophane modal abundance (Fig. 4.7h), which could reflect the extent of eclogitization, i.e., the main dehydration process. Furthermore, considering the significant contribution of carbonate to LOI (the significant correlation between them, not shown) and its important influence on major elements in bulk-rock compositions, the lack of obvious relationship between carbonate mode and Sr (the expected preferential element in carbonate, e.g., van der Straaten *et al.*, 2008; Fig. 4.7d) may reflect the much lesser significance of carbonate to affect the migration of these trace elements, or it may be caused by the occurrence of different carbonate generations.

Observations and experimental studies of hydrous minerals (e.g., phengite, lawsonite, [clino]zoisite and allanite) under subduction-zone conditions (e.g., Pawley & Holloway, 1993; Schmidt & Poli, 1998) and studies on the distribution of fluid-soluble elements in different minerals (e.g., Spandler *et al.*, 2003; El Korh *et al.*, 2009) all indicate that these minerals are capable of accommodating fluids in the form of hydroxyl or H_2O as well as their preferential fluid-soluble elements. Specifically, phengite is the dominant host of K, Rb, Cs, and Ba in the whole rock (e.g., Zack *et al.*, 2001); epidote group minerals (i.e., epidote, [clino]zoisite, and allanite) and lawsonite can host most Sr, Pb, U, Th, and LREEs (e.g., Hermann, 2002; Spandler *et al.*, 2003; Feineman *et al.*, 2007). Therefore, the fluids and the otherwise mobile elements can

be carried in the subducting crust (and sediments) for as long and deep as the host hydrous minerals remain stable, e.g., 3.2 GPa for zoisite (~ 100 km; even up to 5.0 GPa at 700°C and 6.6 GPa at 950°C according to Poli & Schmidt, 1998), up to 12 GPa for lawsonite (~ 360 km; Schmidt, 1995), and 10 GPa for phengite (~ 300 km; e.g., Sorensen *et al.*, 1997), and K-hollandite to the deep mantle (i.e., > 16 – 23 GPa for LILEs, Pb, Th, U, and LREEs; Rapp *et al.*, 2008). These depths are far greater than the depth of amphibole stability (commonly 2 – 2.6 GPa at 700°C reported by Pawley & Holloway [1993], although it could be present at higher pressures), and thus those hydrous metamorphic minerals that are stable at the UHP metamorphic conditions control fluid-mobile element behavior during subduction-zone metamorphism.

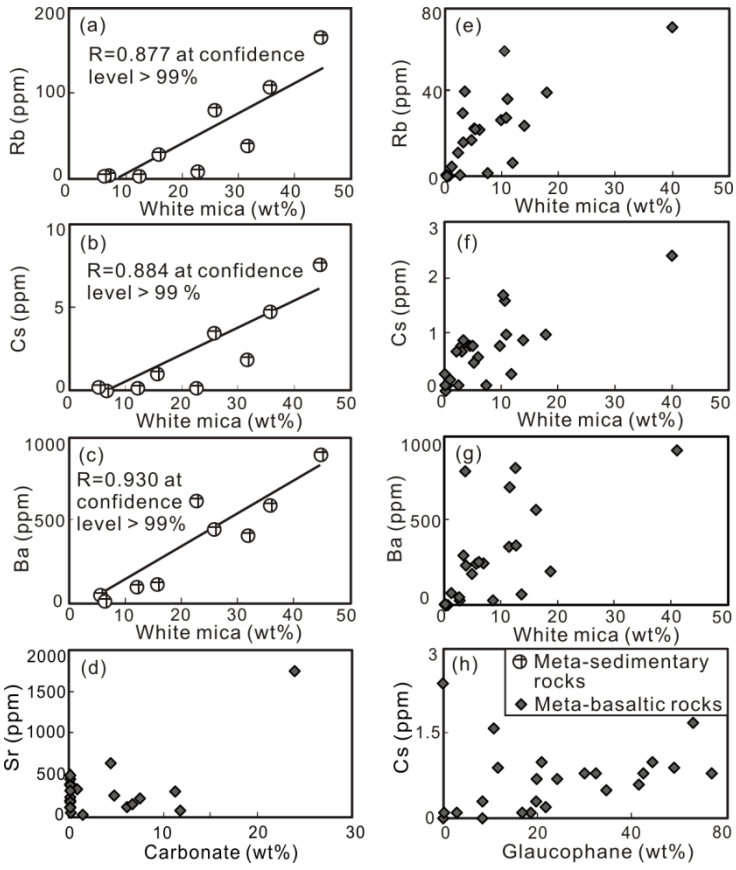

Figure 4.7 Scatter plots of mineral modal abundances with Rb, Cs, Sr, and Ba, (a-c) for meta-sedimentary rocks and (d–h) for meta-basaltic rocks from group 1 and group 3. (a–c) Statistically significant (at > 99% confidence levels) correlations of white mica modes (wt.%) with Rb, Cs, and Ba. (e–g) Scattered yet positive trends (statistically insignificant) between white mica modes (wt.%) and Rb, Cs, and Ba. (d) Sr shows no obvious trend, with highly variable carbonate

content (wt.%). Considering the significant contribution of carbonate to loss on ignition (LOI) and the strong capability of carbonate to host and carry Sr (perhaps to a lesser extent Pb and Ba), the absence of correlations between carbonate modal amount and these elements suggests the relatively insignificant effect of carbonate alteration on these elements or presence of different generations of carbonate, which lead to their ambiguous relationship. (h) Plot of glaucophane modal abundance (wt.%) against Cs content (ppm). Considering that with stronger eclogitization, glaucophane modes are decreased, the absence of significant correlation of Cs, the mobile element representative, with glaucophane, may reflect that the element mobility is not controlled by the main dehydration during the transition from blueschist to eclogite facies.

4.5.1.2 Constraints on the budget of LILEs

It is practically not possible to distinguish muscovite and paragonite petrographically unless analyzed grain by grain. Thus, for convenience in our modal analyses, these two minerals were considered together as "white mica". Importantly, both muscovite and paragonite, which occur as solid solutions, have important controls on LILEs, although LILEs concentrations in muscovite are about an order of magnitude greater than that in paragonite (see Chapter 5 for detailed mineral analysis). Therefore, imprecise identification of muscovite-rich or paragonite-rich grains could potentially affect estimated bulk-rock major-element and trace-element concentrations based on mineral modal abundances. We have found, however, that the expected positive trend between white mica modes and the bulk-rock LILEs abundances, to a first order, exists in our samples of both sedimentary (Figs. 4.7a-c) and basaltic protoliths (Figs. 4.7e-g), although correlations of the latter are less significant (see following).

The significant positive correlations of white mica modes with K, Rb, Cs, and Ba abundances in samples of sedimentary protolith (Figs. 4.7a-c, not shown for K) indicate that these elements are hosted by white mica as expected. The apparent immobility of these elements in samples of sedimentary protolith discussed previously suggests that white mica, as the primary host of LILEs, may have existed in the protolith and remained stable or recrystallized subsequently during metamorphism. Alternatively, the protolith may have hosted abundant clay minerals with adsorbed K, Rb, Cs, and Ba, and formed white mica in subsequent diagenesis and metamorphism. In any case, the abundances of LILEs in sedimentary protolith remained

unaffected by metamorphism because their host minerals have been stable throughout the petrogenetic history of the host rocks.

For rocks of basaltic protolith, there are no significant correlations between white mica modes and Rb, Cs, and Ba (Figs. 4.7e-g), suggesting that these elements may not be simply controlled by white mica. Unlike sedimentary rocks, white mica is absent in basaltic protolith, and its presence in rocks of basaltic protolith is of metamorphic origin. Therefore, protolith type and metamorphism both are important in determining the mobility/immobility of LILEs.

Given the low concentrations of K, Rb, Cs, and Ba in bulk-rock compositions of average ocean crust (see Table 1 in Niu & O'Hara, 2003), little muscovite may be produced from this kind of protolith during metamorphism. Nevertheless, E-MORB– or OIB-like protoliths, or altered ocean crust (see Table 6 in Kelley *et al.*, 2003), relatively enriched in K_2O compared with N-MORB, could supply enough K to produce significant amounts of white mica, which is evidenced by the more common presence of white mica in samples from group 1 (OIB-like source) than in samples from group 3 (depleted N-MORB–like source). On the other hand, the relative timing of white mica formation during metamorphism could also dictate the behavior of those mica-hosted elements. The origin of the poor correlation between LILEs and white mica could have resulted from addition of these elements during retrograde metamorphism (see further discussions in section 4.5.2), or removal during early stages of dehydration prior to the crystallization of white mica. However, once white mica has been formed, especially phengitic muscovite, most LILEs will be strongly conserved, and only some LILEs may be lost through the decomposition of phengite at > 5 GPa due to the increased potassium solubility in clinopyroxene (Schmidt & Poli, 1998).

4.5.1.3 Constraints on the budgets of Pb and Sr

Epidote group minerals and their favored trace elements, i.e., REEs, U, Th, Sr, and Pb (e.g., El Korh *et al.*, 2009), are not significantly correlated in metasedimentary rocks, and neither are

they correlated in metabasaltic rocks (not shown). Unlike white mica, which is the exclusive host mineral for K, Rb, Cs, and Ba, epidote group minerals are not the sole host for REEs, U, Th, Sr, and Pb (note that the bulk-rock contents of Pb and Sr are not significantly correlated at > 99% confidence levels). Based on the results in the recent literature (e.g., van der Straaten *et al.*, 2008; Beinlich *et al.*, 2010) and our work on these rocks (Chapter 5), Sr (and maybe Pb) can also be accommodated in carbonate and paragonite; REEs can also be incorporated into titanite, as can Sr, Th, U, and Pb to a lesser extent. The influence of these additional phases may therefore explain the observed poor correlations of epidote group minerals with their favored trace elements. Alternatively, considering the immobility of REEs, U, and Th in the bulk rock, the poor correlation is also likely caused by heterogeneous distributions of trace elements in epidote group minerals. In contrast, the poor correlations with Sr and Pb may also reflect the loss/gain of these two elements during the phase transition from lawsonite to epidote or the transition between different epidote generations.

4.5.2 Influence of Retrograde Metamorphism

Our samples have generally experienced varying extents of retrograde metamorphism during exhumation. For example, TS02–03A and TS02–03B are different portions of the same hand specimen. The latter sample is a classic eclogite (Fig. 4.1a), while the former has retrogressed to a blueschist assemblage with clear retrograde overprints (e.g., Figs. 4.1h,o). Owing to the absence of white mica, TS02–03B is strongly depleted in Rb, Cs, and Ba. However, as the result of localized rehydration, the relatively dry eclogite has been transformed to wet blueschist facies only in TS02–03A. The released K in the fluids (which may be from an external source) led to the formation of higher modal abundance of white mica with high Rb, Cs, and Ba concentrations in TS02–03A (Fig. 4.6a), up to ~ 100 times more enriched than in TS02–03B (as illustrated by the vertical arrows in Fig. 4.6a). Therefore, in order to understand the actual composition of rocks that have undergone subduction-zone metamorphism (i.e., $[P/D]_{out}$) and the implications for mantle compositional heterogeneity, we need to evaluate and remove the

geochemical effects of retrograde metamorphism first.

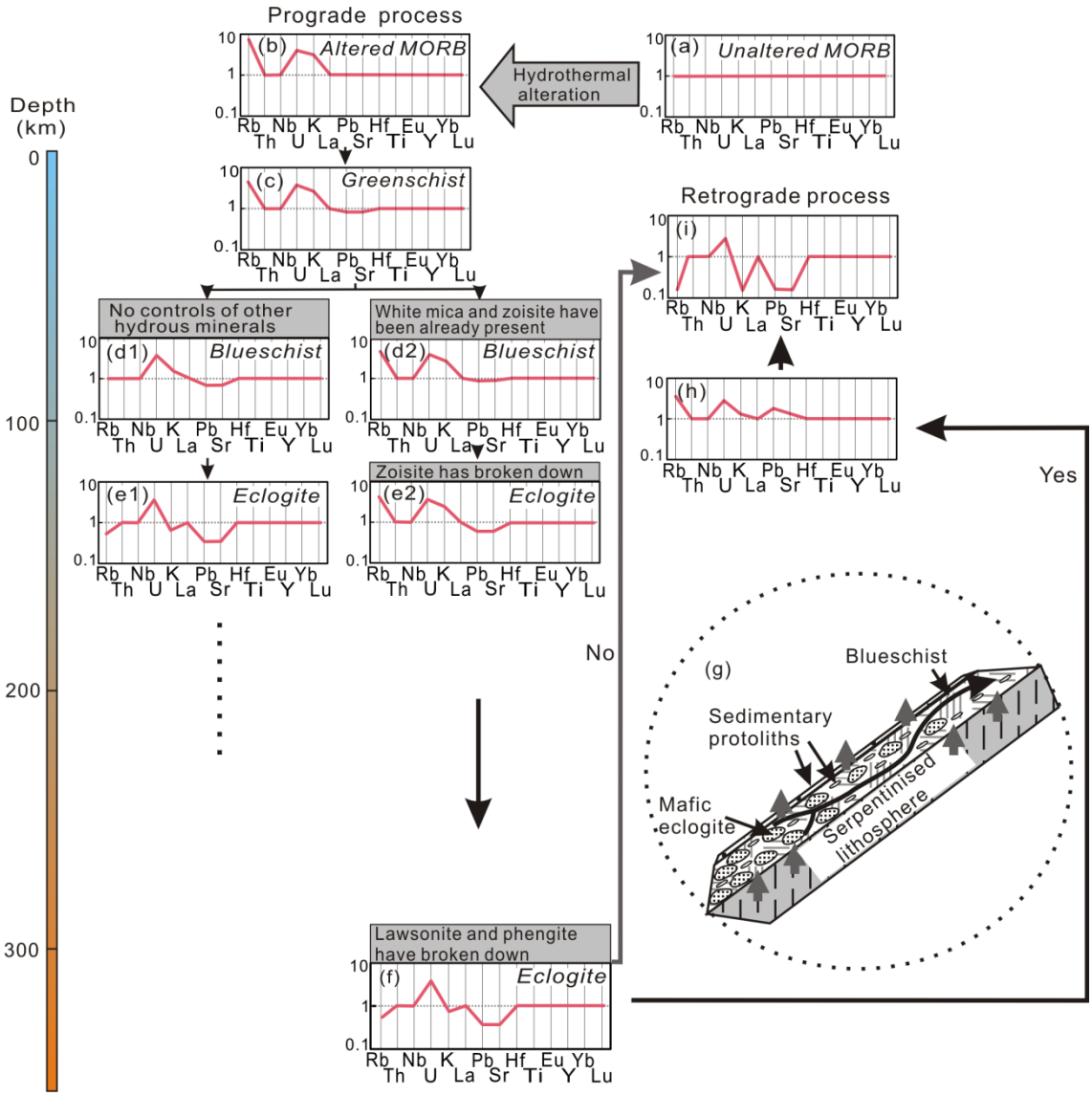

Figure 4.8 Schematic diagrams showing normal mid-ocean-ridge basalt (N-MORB) normalized trace element distribution patterns of rocks with theoretical N-MORB composition during hydrothermal alterations (a), prograde metamorphism (b–f), and retrograde metamorphism (g–i) in subduction zones. (d1–e1) Geochemical consequences without considering the presence of hydrous minerals (e.g., phengite, epidote group minerals) that can accommodate mobile elements. In this case, mobile elements (e.g., Cs, Sr, etc.) are released during the blueschist-to-eclogite transition. (d2–e2) The effects of hydrous phases that can retain certain otherwise mobile elements during the blueschist-to-eclogite transition. Considering the actual elemental behavior during subduction-zone metamorphism in this study, (f) gives the theoretical geochemical consequence at 12 GPa (~ 360 km), which is the depth at which phengite and lawsonite have broken down. (g–i) The geochemical processes during retrograde metamorphism. Two end-member trace-element distributed patterns (i

and h) represent whether the retrograde process may ("yes" path) or may not ("no" path) lead to mobile element re-enrichment as detailed in (g). The widely accepted dehydration of serpentines within mantle sections of the subducted slab may in general represent a "no" path. However, a "yes" path may be followed if the serpentinite-derived fluids could scavenge mobile elements from crustal rocks on their way up. Alternatively, it is also possible that some of the fluids come from dehydration reactions at greater depths within the subducting/subducted rocks (with or without mobile elements) to rehydrate the subducting/subducted rocks at shallow depths, and lead to a "yes" path or a "no" path, respectively.

Whether the rehydrated rocks will be enriched (i.e., in LILEs, Sr, and Pb) or not during retrograde metamorphism depends on the composition of rocks from which the fluids originated and through which the rising fluids have passed, e.g., enriched OIB- or depleted N-MORB–like basaltic rocks, altered ocean crust, sediments, or within-slab serpentines like "abyssal peridotites" (Niu, 2004).

The serpentinized lithospheric mantle of the subducted slab is one of the most significant fluid reservoirs (e.g., Schmidt & Poli, 1998) for retrograde metamorphism and plays an important role in the exhumation of subducted oceanic lithosphere due to its relatively low density (e.g., Pilchin, 2005). Because of the complex composition of serpentinite-derived fluids, lithologies modified by adding fluids from serpentine alone may be even more depleted (Fig. 4.8i). However, considering the enrichment of those retrograde metamorphic rocks (e.g., common enrichment of Pb) and the actual elemental mobility in this study, the depleted fluids derived from serpentines may have scavenged a significant portion of elements from the rocks through which they passed and with which they reacted (e.g., van der Straaten *et al.*, 2008), especially the more enriched rocks such as OIB-like protolith. This suggests that the infiltrated fluids derived from serpentines may be mixed with a subducting sediment– and/or basalt-derived component (the latter is more important for the re-enrichment of Ba, Cs, and Rb in this study; Figs. 4.8g-h). Alternatively, fluids derived from rocks that subducted to greater depths than our samples may migrate upward along the subduction channel (Fig. 4.8g) and could also carry those fluid-soluble elements to metasomatize shallower rocks rather than entering the overlying mantle wedge.

4.5.3 Implications for Subduction-Zone Magmatism

4.5.3.1 Elemental contributions to arc magmas: LILEs, Sr and Pb

From the previous discussion, it can be seen that although the transition from blueschist to eclogite facies can theoretically release significant amounts of fluids (Pawley & Holloway, 1993) and fluid-soluble elements for the formation of arc magmas, this may not necessarily be the case because some eclogites remain enriched in LILEs, e.g., TS02-41. This highly eclogitized sample without obvious retrograde overprints contains 12.9 wt.% white mica and only 0.67 wt.% (clino)zoisite, and it has an enriched K-Rb-Cs-Ba and depleted Sr signature without significant Pb enrichment (Fig. 4.6a). It is white mica that survives from the blueschist to eclogite dehydration, retaining/transporting these elements into the deep mantle. Therefore, the appearance and stability of the HP-UHP hydrous minerals (e.g., white mica, [clino]zoisite), which control the immobility/mobility of fluid-soluble elements during subduction-zone metamorphism (the detailed process is illustrated in Figs. 4.8d-e), consequently affect the geochemical signatures of arc lavas. Furthermore, it is the major element composition (including H_2O) and the oxidation state of the protolith that control modal abundances of hydrous minerals at given *P-T* conditions (e.g., Rebay *et al.*, 2010).

During the prograde *P-T* path of our samples, a significant portion of Sr and Pb may have first been hosted in lawsonite (as indicated by inclusions composed of paragonite + clinozoisite in garnet; e.g., Fig. 4.1c-d). Accompanied by prograde-retrograde *P-T* path transition (see Fig. 2.3) and continued heating for a period thereafter with decreased *P*/*T* ratios, (clino)zoisite replaced lawsonite and scavenged the liberated Sr and Pb. The presence of prograde (clino)zoisite indicates that some of the Sr and Pb may also have been largely hosted in (clino)zoisite because of less H_2O available in the original system (the H_2O content determines the modal lawsonite under blueschist facies, i.e., the higher H_2O content, the more lawsonite may form; e.g., Rebay *et al.*, 2010; Poli & Schmidt, 1997). Up to about ~100 km, or even greater depths in relatively cold subduction zones (~ 12 GPa; Schmidt, 1995), although a portion of Pb and Sr could be

transported further by K-hollandite and allanite, more (clino)zoisite or lawsonite will transform to garnet and omphacite, which cannot further accommodate Sr and Pb. Consequently, these two elements, or at least a large portion of them if not in their entirety, will be liberated along with released fluids into the subduction channel and, perhaps, contribute to the partial melts of the mantle wedge for arc (perhaps also back-arc) magmatism (Fig. 4.9).

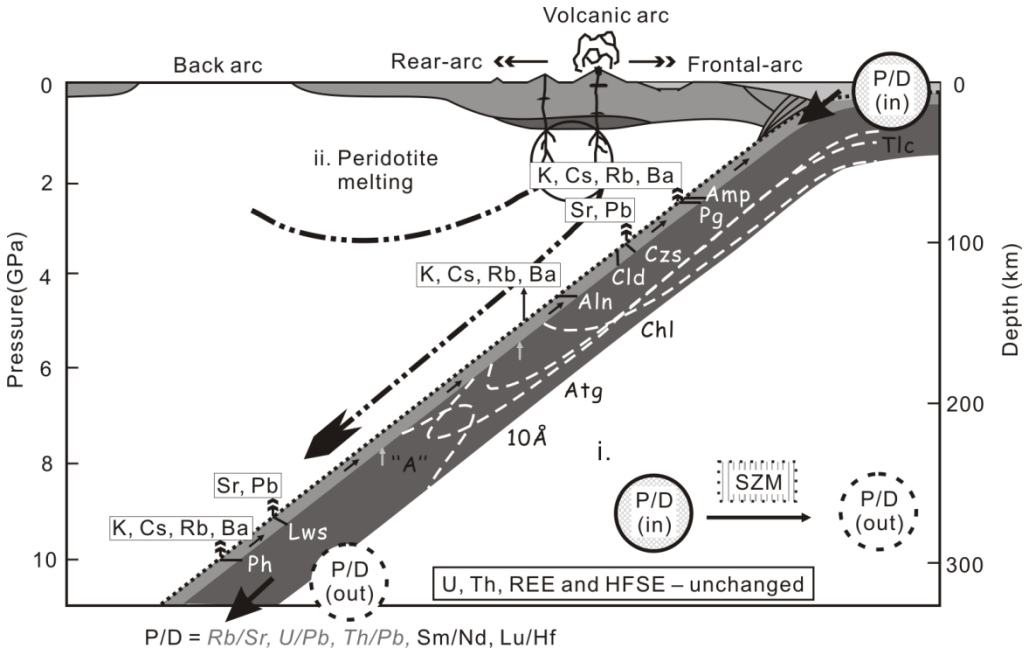

Figure 4.9 Schematic diagram showing multistage subduction-zone metamorphism (SZM; modified from Poli & Schmidt, 2002). The stability of significant minerals in the subducting/subducted slab along the subduction zone is labeled, including allanite, the stability of which has been indicated following Hermann's experimental study (2002). The distinctive geochemical responses of key trace elements to the mineral stability are also shown.

If paragonite were present prior to dehydration during subduction-zone metamorphism, LILEs would be transported within the subducted crust to a depth of at least ~ 70 km. If subducting sedimentary rocks and rocks of E-MORB–like or OIB-like protoliths with adequate K to produce muscovite are available at the early stage of metamorphism, then Rb, Ba, and Cs will be stabilized (refer to Figs. 4.8d2–e2 for the trace element redistributed model) until the muscovite breakdown at a depth up to ~ 300 km (e.g., Sorensen *et al.*, 1997; Poli & Schmidt, 2002). If no further minerals have already been produced (e.g., K-hollandite; Rapp *et al.*, 2008) for hosting these elements or if the supercritical fluids or melts are present, these elements will

contribute to the observed enrichment in back-arc magmatism (Fig. 4.9). Otherwise, if no paragonite or phengitic muscovite was present before dehydration reactions during subduction-zone metamorphism, these elements will be released with fluids beneath the forearc (see Figs. 4.8d1–e1 for the expected trace element redistribution), which is most likely the case for subducting depleted N-MORB–like rocks without significant seafloor alterations (i.e., low K and H_2O).

Elements such as LREEs, U, and Th, which are typically enriched in volcanic arc basalts (e.g., Dilek & Furnes, 2011), have previously been considered as being mobile elements in subduction-zone metamorphism (e.g., McCulloch & Gamble, 1991). Our studies, however, have shown the immobility of these elements in rocks of both sedimentary and basaltic protoliths, i.e., the correlated variations among these elements were maintained prior to and during subduction-zone metamorphism. This indicates that LREEs, U, and Th have not been released during subduction-zone metamorphism and would contribute little to subduction-zone magmatism as a function of dehydration, at least up to the peak conditions of these rocks (i.e., 75 km). Therefore, if the enrichments of these elements in arc lavas are indeed derived from the subducting ocean crust with the overlying sediments, other mechanisms, such as supercritical fluids or hydrous melts (which may happen at deeper depths), rather than simple metamorphic dehydration of aqueous fluids, are required. This is an important conclusion that encourages reconsideration of the standard model ("flux melting") for arc magmatism.

4.5.3.2 Redox conditions in subduction zones

Another important feature in the standard subduction model is its presumed highly oxidized state, as indicated by high Fe^{3+}/Fe^{2+} observed in arc volcanic rocks and in spinels from sub-arc mantle xenoliths. These oxidized conditions in the mantle wedge (unlike the more reduced condition in other tectonic settings, e.g., the asthenospheric mantle beneath mid-ocean ridges) are thought to be caused by the addition of slab-derived fluids (e.g., Wood *et al.*, 1990; Brandon & Draper, 1996). However, based on V/Sc ratios in sub-arc peridotites and arc lavas rather than

Fe^{3+}/Fe^{2+}, Lee *et al.* (2003, 2005) proposed that the oxygen fugacity in arc magma sources is actually similar to that of asthenospheric mantle beneath ocean ridges, i.e., as low as −1.25 - 0.5 log units relative to the FMQ (fayalite-magnetite-quartz) buffer. They also pointed out that it is inappropriate to use Fe^{3+}/Fe^{2+}, which only reflects the redox state in the last equilibrium process without any record of previous equilibrium history. The observation of CH_4 fluid inclusions in olivine from a mantle wedge harzburgite sampled from the Qilian suture zone, northwest China (Song *et al.*, 2009b), also indicates that the actual redox state in subduction zones may be more reduced than widely assumed.

Since U becomes fluid soluble or mobile only as U^{6+} under oxidized conditions (e.g., Langmuir, 1978; Niu, 2004), the existence of a significant U-Th correlation (Fig. 4.5f; not only in our samples, but also in samples from other studies in the literature) and the absence of fractionations of U from Nb (Fig. 4.5e) indicate the immobility of U, which may be in response to the form of U^{4+} (vs. U^{6+}) during subduction-zone metamorphism. These observations, together with the identification of graphite inclusions in porphyroblastic garnet from eclogite in Western Tianshan (Lü *et al.*, 2008, 2009), all indicate that subduction-zone metamorphism may indeed take place in a more reduced environment than previously thought. However, this is an open question, i.e., the immobility of U could also be controlled by other effects (e.g., stronger hosted mineral controls; see discussions in section 5.4.2 of Chapter 5). More effort is needed to understand the oxidation state of subduction zones at UHP metamorphism conditions, which has the potential to improve understanding of subduction-zone magmatism.

4.5.4 Implications for Mantle Compositional Heterogeneities

We have argued that fluids and a portion of fluid-soluble elements (i.e., LILEs, Sr, and Pb) could be released into the mantle wedge from rocks of basaltic protolith, while rocks of sedimentary protolith may host K, Rb, Cs, and Ba in phengite, stable up to depths of ~300 km. At greater depths, K-hollandite could become the stable phase hosting these elements (Rapp *et al.*, 2008).

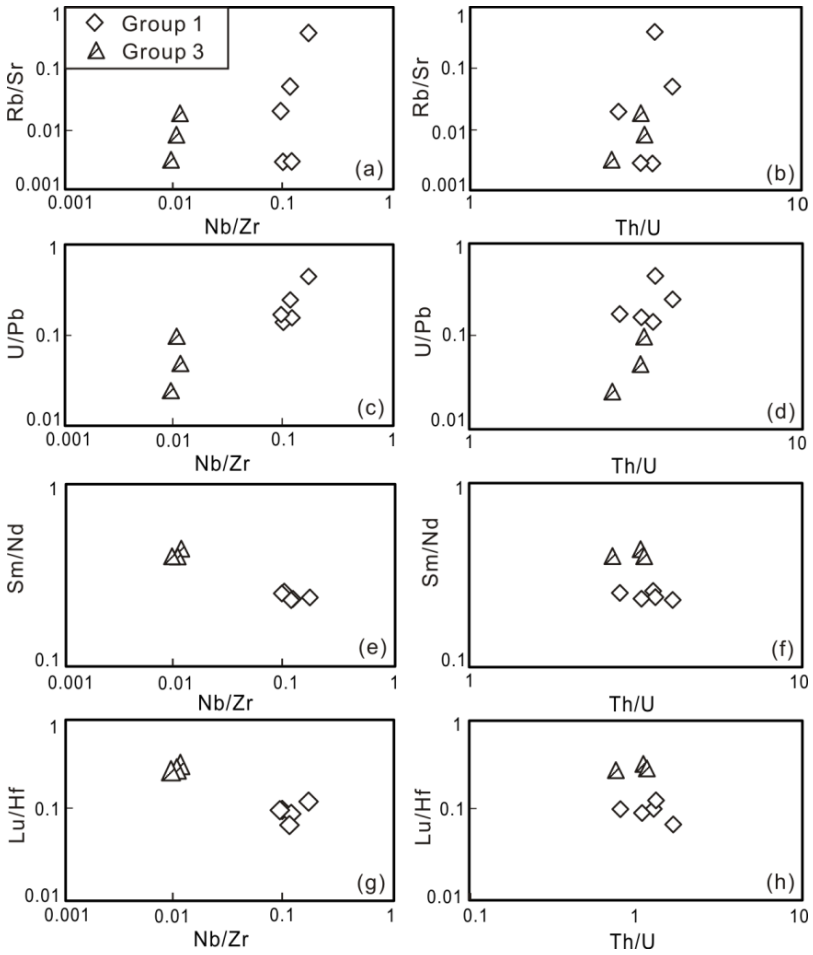

Figure 4.10 Scatter plots of parent/daughter (P/D) ratios (i.e., Rb/Sr, U/Pb, Sm/Nd, and Lu/Hf) against immobile element ratios (Nb/Zr and Th/U) for samples with minimal retrograde overprints (samples labeled in bold in Table C.9 in Appendix C).

Because our samples may not have been subducted beyond the depth more typical for subduction-zone magmatism (i.e., > ~100 km according to Tatsumi & Kogiso, 2003), they may not represent the actual $[P/D]_{out}$ brought to the deep mantle (see Figs. 1.1 and 4.9). However, systematic studies of the controls on the behavior of different elements and the direct geochemical consequence of subduction-zone metamorphism as a function of dehydration for depths > 75 km in our study still allow us to reasonably infer the $[P/D]_{out}$ into the deeper mantle. Therefore, we selected several eclogitic samples with minimal retrograde metamorphic overprints from group 1 and group 3 (the samples shown in bold in Table C.9 in Appendix C) and plotted their P/D ratios against ratios of immobile elements (i.e., Nb/Zr and Th/U) (Fig. 4.10). With relatively constant Nb/Zr and Th/U ratios in each group, Rb/Sr and U/Pb ratios vary

significantly (Figs. 4.10a-d), which is expected because Rb, Sr, and Pb are mobile. In contrast, Sm/Nd and Lu/Hf ratios are almost constant (Figs. 4.10e-h), consistent with their inherited magmatic signature and immobile behavior during subduction-zone metamorphism. These observations indicate that the element mobility/immobility may not only alter the element content, but it could also affect element ratios.

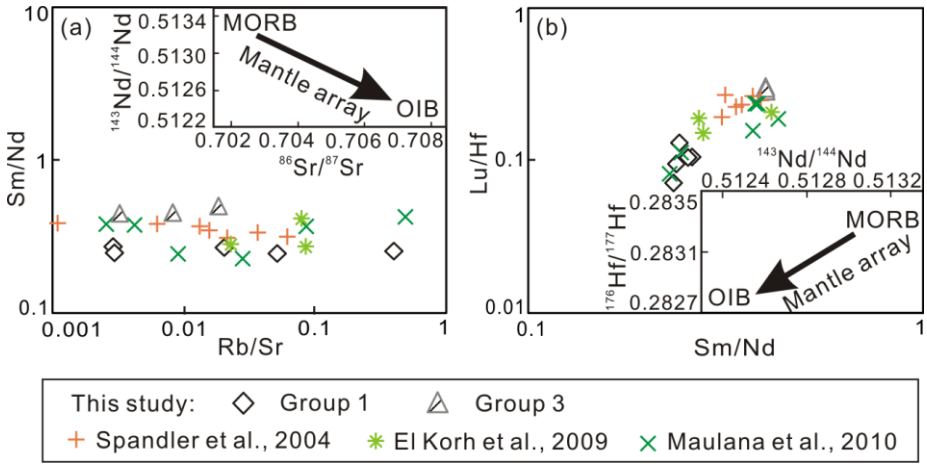

Figure 4.11 Comparisons of parent/daughter (P/D) ratios with radiogenic isotope ratios (the two insets are adapted from Hofmann [1997] and White & Patchett [1984]). Selected samples are the same as those in Figure 4.10. Several selected eclogitic metabasites in the literature are also plotted, and the relevant values are given in Table C.11. The positive Sm/Nd-Lu/Hf correlation is consistent with these rocks being potential source materials for ocean-island basalts (OIB) when subducted with a positive Hf – Nd isotopic relationship, but the lack of Rb/Sr-Sm/Nd (and Lu/Hf) correlation is inconsistent with the rocks being the major source materials for oceanic basalts that show significant inverse Sr-Nd and Sr-Hf isotopic systematics.

As radiogenic isotope ratios are a function of time, they may reflect the time-integrated evolution of radioactive parent to radiogenic daughter (P/D) in the ultimate subducted materials in the mantle. Together with several selected eclogitic metabasites from other locations in the world (Table C.11 in Appendix C), Sm/Nd consistently shows good correlation with Lu/Hf (Fig. 4.11b) but lacks correlation with Rb/Sr (Fig. 4.11a). When these rocks return into mantle source regions for oceanic basalts, they cannot contribute to the first-order negative Sr-Nd isotope correlation observed in oceanic basalts (Fig. 4.11a, inset; also see Fig. 4a in Niu & O'Hara, 2003), even though the significant positive Sm/Nd-Lu/Hf correlation is apparently consistent

with the $^{143}Nd/^{144}Nd$ versus $^{176}Hf/^{177}Hf$ correlation in oceanic basalts (Fig. 4.11b, inset; also see Fig. 4b in Niu & O'Hara, 2003). Therefore, the subducted ocean crust cannot be the major source materials of oceanic basalts in terms of Sr-Nd-Pb radiogenic isotopes (also see Niu & O'Hara, 2003; Niu, 2004).

The immobility of U during subduction-zone metamorphism and Pb fractionation in the subducting/subducted crust indicate that U/Pb in the subducted crust will have increased $[P/D]_{out}$ and will lead to a higher ratio of U/Pb in the deep mantle (there may be an elevated ratio of Th/Pb as well because of the similar behavior of Th and U during subduction-zone metamorphism; e.g., Fig. 4.5f). Therefore, such fractionations of U-Th (especially U) from Pb may contribute to the source of HIMU.

4.6 CONCLUSIONS

We have attempted to characterize elemental behaviors in response to subduction-zone metamorphism using detailed petrography and bulk-rock geochemistry of subduction-zone UHP metamorphic rocks from Chinese Western Tianshan. Several tentative conclusions are:

(1) Based on the studies of immobile elements, our samples of basaltic protolith can be divided into three groups: Group 1 points to a protolith resembling the present-day average OIB (or enriched seamount lavas); the protoliths of group 2 are similar to N-MORB contaminated by a continental crustal component; and the protoliths of group 3 are akin to highly depleted MORB. The association of these diverse metabasaltic compositions together with rocks of sedimentary protolith indicates that the input into subduction zones can be diverse, and may represent a tectonic mélange composed of normal ocean crust with dismembered seamounts, sediments, and arc-derived materials. We have also argued that the composition of the protolith plays an important role in determining the mineral assemblages and elemental fractionations during subduction-zone metamorphism.

(2) We have demonstrated and confirmed that HFSEs and REEs are in general immobile during subduction-zone metamorphism. The significant correlation of U with Th (and Nb) indicates that U is immobile and may point to a reduced environment, contrary to the common perception that subduction zones are relatively oxidized. The immobility of LREEs, U, and Th further implies that, at least in the absence of supercritical fluids or hydrous melts, these elements may not contribute to subduction-zone magmatism under metamorphic conditions of our study, i.e., up to ~ 75 km depth (i.e., > ~2.5 GPa). In addition, the immobility of U in this study suggests that the component of altered ocean crust, if involved at all, is insignificant in the protoliths of our samples.

(3) LILEs including Sr and Pb in rocks of basaltic protolith have been mobilized, although it is not clear whether this happened at the same time for all samples. LILEs in meta-sedimentary rocks appear to have remained immobile, most likely because these elements are largely hosted in white mica, which is stable over much of the subduction-zone metamorphism conditions. For meta-basaltic rocks, the timing of the appearance and stability of white mica during seafloor subduction is important in determining the mobility/immobility of their preferentially hosted elements. However, further studies on trace-element budgets in natural samples from other HP and UHP metamorphic suites are needed to verify this result (see Chapter 6).

(4) Compared with the abundances and ratios of immobile elements, we confirm that both abundances and ratios of mobile elements have been altered during subduction-zone metamorphism, and hence the $[P/D]_{in}$ (i.e., Rb/Sr and U/Pb input into the trench) differs from the $[P/D]_{out}$ of subduction-zone metamorphic systems. Therefore, it is inappropriate and misleading to use $[P/D]_{out}$ in the subducting crust, inferred from oceanic basalts, to constrain the $[P/D]_{in}$ of surface rocks that have entered trenches.

CHAPTER 5:

TRACE ELEMENT BUDGETS AND (RE-)DISTRIBUTION DURING SUBDUCTION-ZONE ULTRAHIGH PRESSURE METAMORPHISM: EVIDENCE FROM WESTERN TIANSHAN, CHINA

5.1 INTRODUCTION

Based on the discussion of bulk-rock compositions for the rocks of basaltic protoliths and sedimentary protoliths from ultrahigh pressure (UHP) metamorphic belt in Western Tianshan, China in Chapter 4, we have revealed the elemental geochemical behaviors during subduction-zone metamorphism, i.e., element mobility/immobility. However, the trace element (re-)distributions in minerals of the studied rocks and the controls on these elemental behaviors are still unclear. Therefore, we analyzed the constituent mineral phases of these studied rocks using LA-ICPMS. In this chapter, together with the detailed petrography study (see section 4.2 in Chapter 4), we will discuss the elemental responses to mineral stability at each metamorphic stage along the P-T path (Fig. 2.3), and attempt to improve our understandings on the origin of subduction-zone magmatism and mantle chemical and isotopic heterogeneity.

5.2 MINERAL GEOCHEMISTRY

We analyzed garnet (Table C.3), epidote group minerals (Table C.4), white micas (both phengitic muscovite and paragonite; Table C.5), Ti-rich minerals (rutile and titanite; Table C.6), omphacite (Table C.7), amphiboles (Table C.8), and a few feldspar crystals (Table C.7) and chlorite (Table C.8). See data in Table C.3-8 of Appendix C.

5.2.1 Major Composition

Garnet is almandine-rich and shows pyrope component increase towards rims (e.g., TS02-03A in Table C.3) in response to the prograde growth. Clinopyroxene is omphacitic (Table C.7). The composition of amphibole is variable, from calcic, sodic-calcic to sodic amphibole (amphibole classification follows Leake *et al.*, 1997), and (sodic-)calcic amphibole is often present as a retrograde product. Some amphibole crystals show zoning, as evidenced by those with glaucophane cores overprinted by the rim of (sodic-)calcic amphibole. The composition of

epidote group minerals is also variable. Allanite is present as the core of some clinozoisite crystals (Lavis, 2005). TFeO and Al_2O_3 are negatively correlated (not shown) due to the complementary $Fe^{3+} \Leftrightarrow Al$ substitution. Some grains of epidote group mineral display clear zoning with Al_2O_3 increasing (TFeO decreasing) towards the rim, probably indicating increasing temperature (Deer *et al.*, 1992).

5.2.2 Mineral Trace Element Systematics

Experimental studies (e.g., Feineman *et al.*, 2007) and studies of natural rocks (e.g., Spandler *et al.*, 2003) have shown that different minerals in a given metamorphic rock prefer to host a particular set of elements. For example, phengite has been found to be the major host of K, Ba, Rb and Cs (Sorensen *et al.*, 1997; Becker *et al.*, 2000; Melzer & Wunder, 2000; Zack *et al.*, 2001); garnet is commonly enriched in HREEs (El Korh *et al.*, 2009); epidote group minerals (i.e., epidote, [clino]zoisite, allanite) and lawsonite are important hosts of REEs, Th, U, Pb and Sr (Nagasaki & Enami, 1998; Becker *et al.*, 2000; Hermann, 2002; Spandler *et al.*, 2003; Feineman *et al.*, 2007); Sr could also reside in carbonate (van der Straaten *et al.*, 2008; Beinlich *et al.*, 2010); rutile and titanite host essentially all the Ti, Nb and Ta in the bulk rock (Stalder *et al.*, 1998); zircon is responsible for hosting almost all the Zr and Hf in the rock (e.g., Rubatto & Hermann, 2006). In the following, we discuss our mineral trace element data.

5.2.2.1 Garnet

Garnet is rich in middle (M-) to heavy (H-)REEs, up to ~ 10^3 times the chondrite, but low in light (L-)REEs (Fig. 5.1a). The content of HREEs is variable even within single garnet crystal, showing a general depletion in HREEs from core to rim (e.g., one garnet crystal from sample TS02-53 in Fig. 5.1a, one garnet porphyroblast from TS02-03A in Table C.3). In chondrite-normalized spider gram (Fig. 5.1a), some garnets show MREEs > HREEs. Considering the higher contents of MREEs relative to HREEs in some titanite crystals (e.g., the one from TS02-43 in Fig. 5.1g), the MREEs > HREEs in garnet may have resulted from

redistribution of MREEs with the transition from titanite with high MREEs to rutile during the prograde metamorphism (also see Spandler *et al.*, 2003; Konrad-Schmolke *et al.*, 2008). No compositional anomalies appear to be associated with distinctive textures (e.g., inclusions preserved in clinozoisite in Fig. 4.1j or paragonite in Fig. 4.1k, relict replaced by chlorite in Fig. 4.1m-n), suggesting the strongest preference of garnets for M-HREEs relative to other minerals (e.g., King *et al.*, 2004). The contents of Nb, Ta and Hf are low; mostly below the detection limit or only a few ppb (Zr can be up to several ppm).

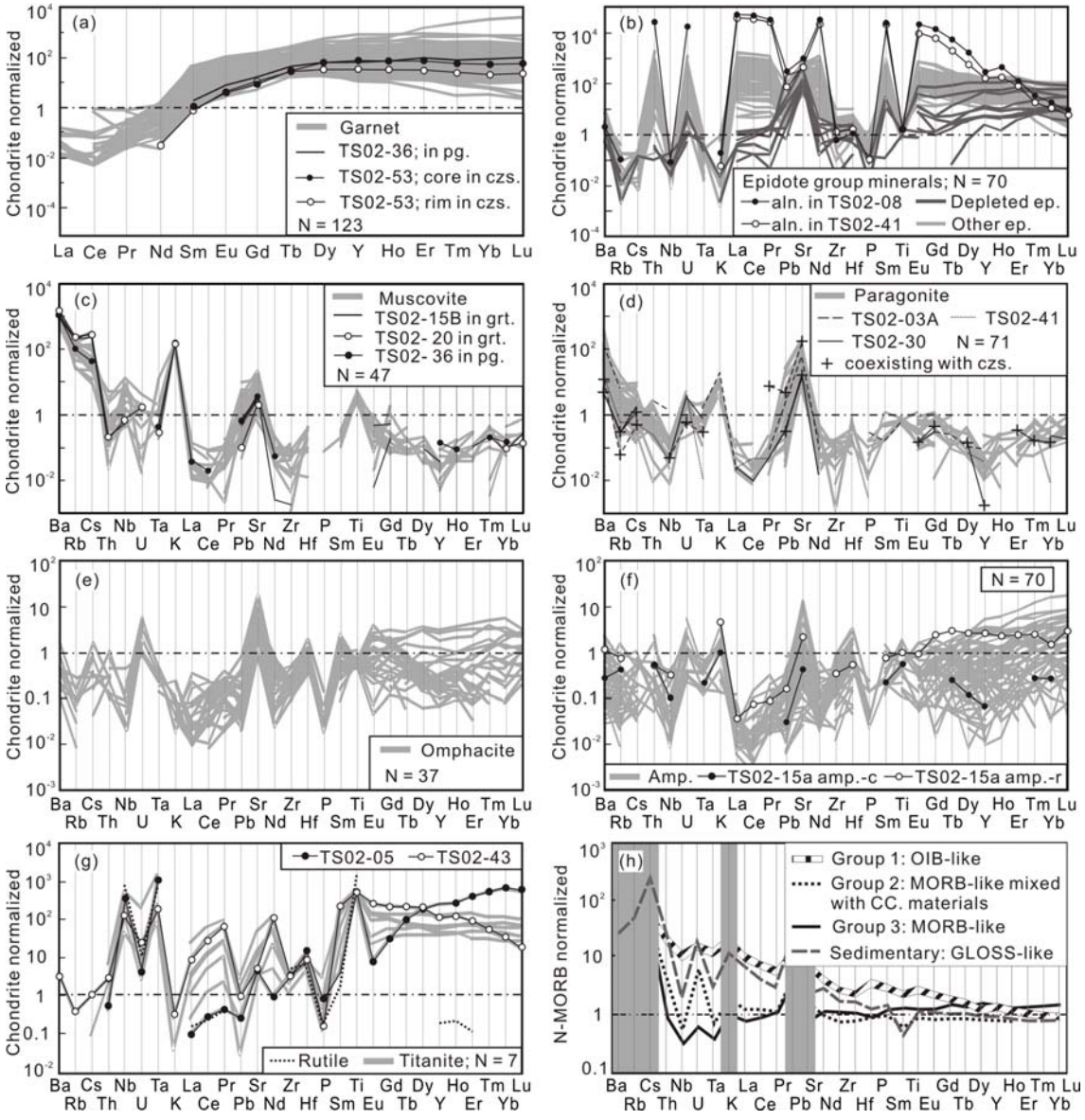

Figure 5.1 Chondrite normalized trace element patterns of different minerals studied (a-g; see Table C.3 – 8 for data) and N-MORB normalized trace element patterns for schematic bulk-rock

compositions of different protoliths (h). The trace element contents of chondrite and N-MORB are referred to Sun & McDonough (1989). (a) REE and Y distribution of garnet (the grey lines; the position for Pm between Nd and Sm is omitted for clarity). The garnet relic inclusions preserved in other minerals have been highlighted. (b) Different groups of epidote group minerals; the extremely enriched group (two highlighted sample plots; allanite, aln.); the depleted group (the dark grey lines); and the others (the light grey lines). (c) Phengitic muscovite (grey lines). Muscovite inclusions in garnet or paragonite have been highlighted. (d) Paragonite (grey lines). Paragonite inclusions in garnet have been highlighted. Compared with muscovite, paragonite shows lower LILEs and K but higher Sr and Pb. (e) Omphacite (the grey lines). (f) Amphiboles (grey lines). The compositions of both core and rim of one glaucophane grain from TS02-15A have been highlighted for comparison (see data in Table C.8 in Appendix C). The (sodic-)calcic rim formed by retrograde alteration displays higher HREEs than the sodic amphibole core, which may result from the breakdown of garnet. (g) Rutile (the dotted black curve) and titanite (the grey lines). Two titanite grains discussed in details in section 5.2.2.4 have been highlighted, i.e., one titanite crystal with the highest HREEs in chlorite replacing garnet (from TS02-05), one titanite grain with high MREEs that may have replaced epidote group minerals (from TS02-43). (h) N-MORB normalized trace element distributed patterns of schematic bulk-rock compositions for different groups of basaltic protoliths and sedimentary protoliths. Those estimated mobile elements (Xiao *et al.*, 2012; Chapter 4) have been hidden. Considering the different geochemical behavior, Ba, Rb, Cs and K as immobile elements have been shown for rocks of sedimentary protoliths but not for basaltic protoliths. CC. – continental crust.

5.2.2.2 White micas

Both phengite and paragonite are rich in Li (generally 10s – 100s ppm) and Be (several ppm) (Table C.5). They also display high LILE concentrations including, to varying extent, Pb and Sr (Figs. 5.1c,d). Most muscovite and paragonite crystals have very low concentrations of Nb and Ta, but Nb can be up to a few ppm in several muscovite crystals.

Phengitic muscovite. Among the analyzed minerals, muscovite has the highest abundances of Ba, Rb, Cs and K, about 2 – 3 orders of magnitude × chondrite (Fig. 5.1c). The highly variable LILEs with relatively constant K content (not shown) suggests that K is stoichiometrically constrained in muscovite, but Ba, Rb and Cs are not, even though they occupy the K lattice site. No inter-LILE correlations exist, except for a good correlation between Rb and Cs (Figs. 5.2b,d).

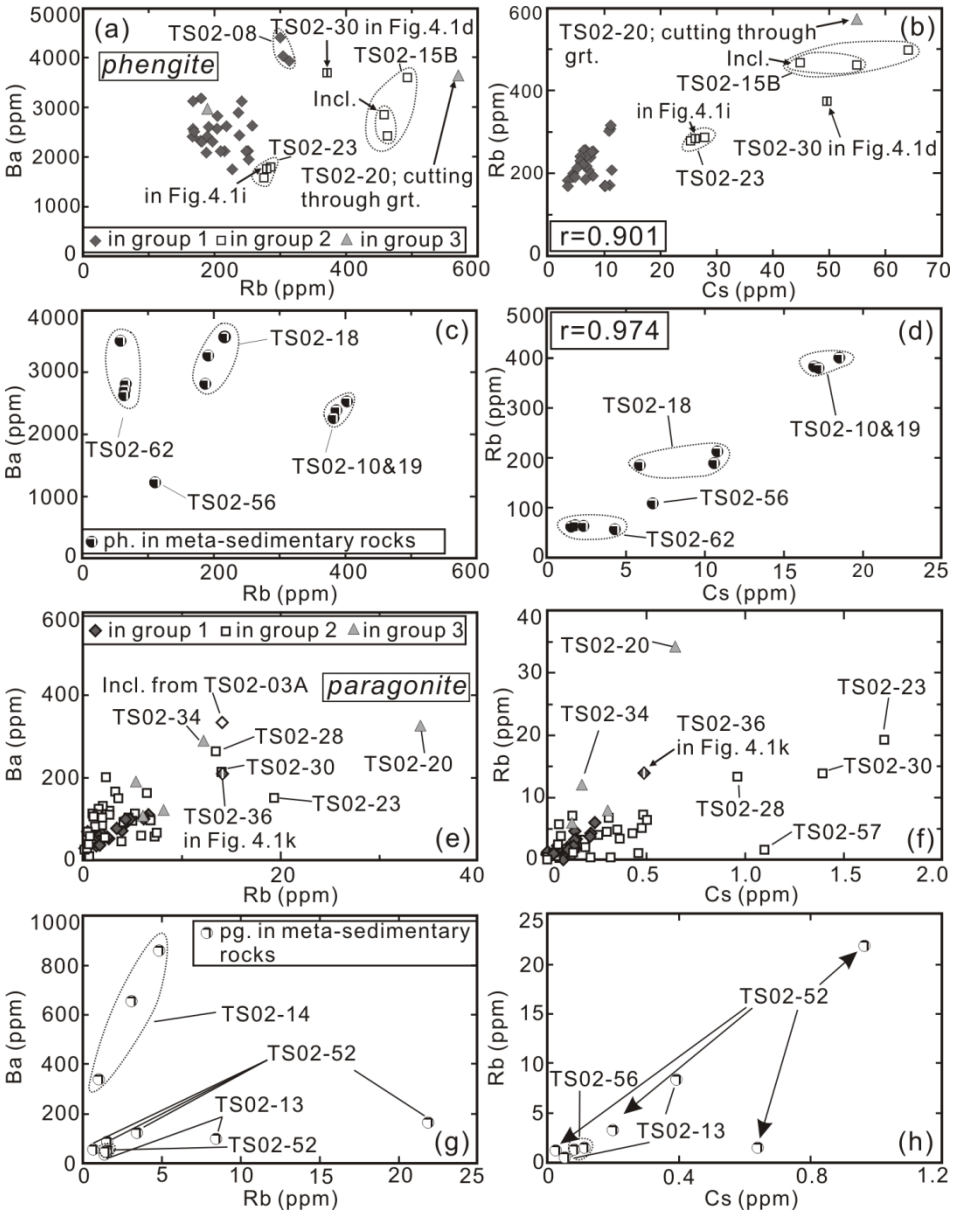

Figure 5.2 Co-variation diagrams of K-Rb-Cs-Ba for muscovite (a-d) and paragonite (e-h). (a-b, e-f) are for different groups of rocks of basaltic protolith (see sample grouping in sections 4.4.1 and Fig. 5.1h; Xiao *et al.*, 2012), and (c-d, g-h) for rocks of sedimentary protolith. The scattered points have been specifically labeled. These points may reflect the effect of different protolith compositions, but more importantly stronger controls by metamorphism in rocks of basaltic protoliths. The labeled points with a vertical bar inside (two phengite crystals from TS02-30 and TS02-23, and one paragonite crystal from TS02-36) represent those grains that have also been shown in photomicrographs of Fig. 4.1 in Chapter 4.

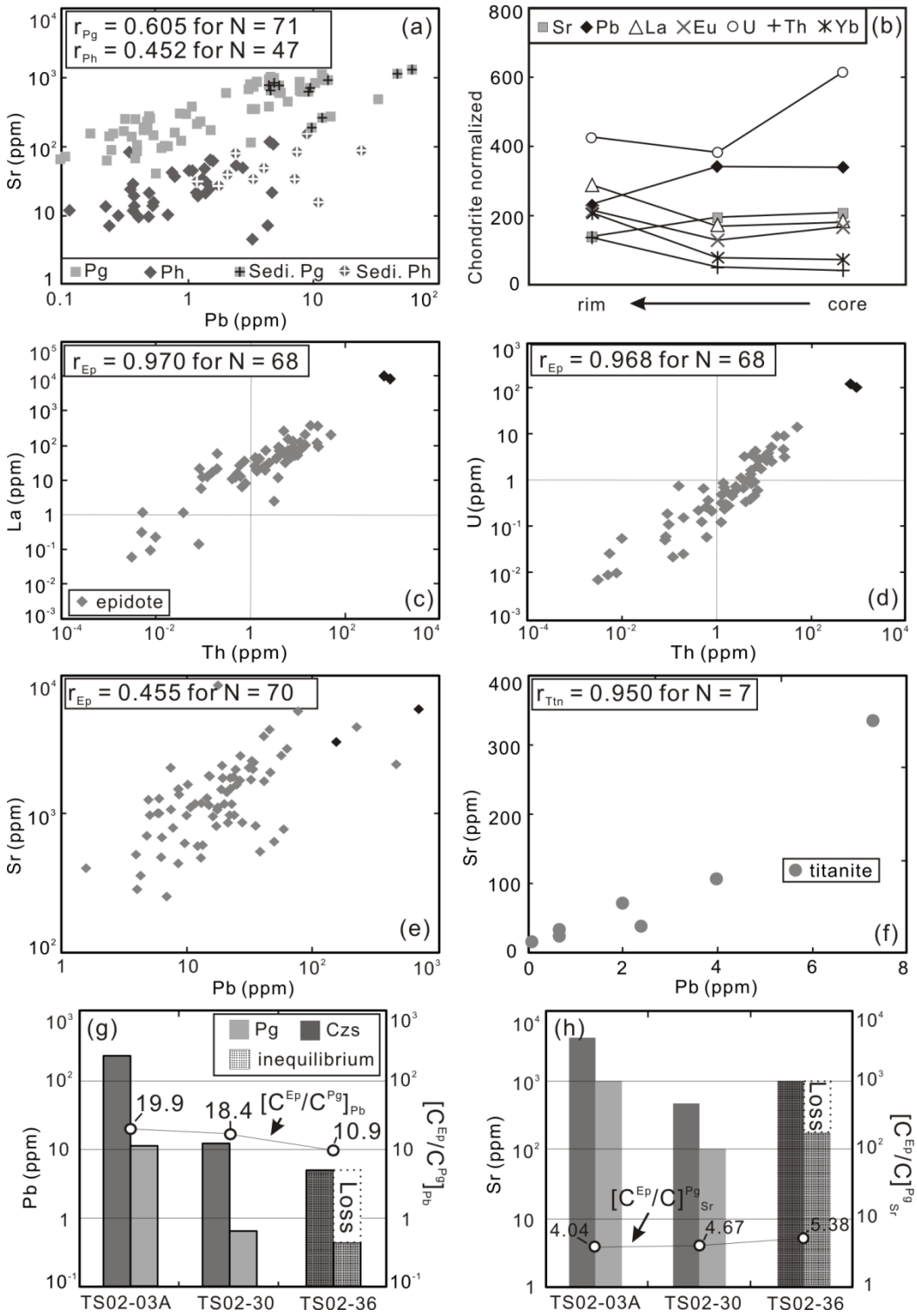

Figure 5.3 Elemental co-variation diagrams for metamorphic minerals. (a) Correlated variation of Pb and Sr for both paragonite and phengitic muscovite. The legends with crosses represent micas from rocks of sedimentary protolith. Both paragonite and phengitic muscovite from rocks of sedimentary protolith have higher Pb and Sr than from rocks of basaltic protolith. The highest Pb in paragonite could be comparable to those in epidote group minerals in Fig. 5.3e. (b) The compositional profile of

one epidote grain from TS02-36 for selective elements, which are considered to be largely hosted by epidote group minerals (see data in Table C.4). Different multiplication factors have been given for elements to clarify: (Sr, Th, La, Eu) × 1; (U, Yb) × 10; Pb × 100. It shows increase in REEs and Th but decrease in Pb and Sr from core to rim. (c-e) Co-variations of La, Th, U, Pb and Sr for epidote group minerals (two allanite analytical points are colored black). As the major host for these elements, all these correlations in epidote group minerals may also lead to the same correlations in the bulk rock. (f) shows the significant correlation between Pb and Sr in titanite. (g-h) Histograms of Pb and Sr distributed in the paragonite and clinozoisite. The first two pairs of columns in each panel show the Pg – Czs pair preserved as inclusions in garnet, i.e., lawsonite pseudomorphs (Fig. 4.1c,d). The contents of Pb and Sr in these two neighboring minerals (i.e., $[C^{ep}/C^{pg}]_{Pb}$ and $[C^{ep}/C^{pg}]_{Sr}$) can be used to infer the partition coefficient between these two minerals in equilibrium, represented by the black circles connected by the curve; ~ 20 and ~ 4 for $Kd_{Pb}^{ep/pg}$ and $Kd_{Sr}^{ep/pg}$ (the right vertical axis). The paragonite porphyroblast and the clinozoisite relict preserved as its inclusion (Fig. 4.1l) are also plotted in the last pair of columns, labeled as 'inequilibrium'. The blank areas defined by the dotted boundary lines represent the loss of Pb and Sr during the paragonite-clinozoisite transition.

The contents of Ba, Rb and Cs in muscovite among different rocks of basaltic protoliths, especially between some of those from different groups, are relatively variable (Table C.5 and Figs. 5.2a,b), which reflects the effect of compositional inheritance from their protoliths. However, muscovite of the same generation within a rock of basaltic protolith has relatively constant LILE contents, and almost all the muscovite grains in rocks of basaltic protoliths are generally plotted as the Ba-Rb-Cs data cluster (Figs. 5.2a,b), which may indicate the stronger effect of alteration at the main stage of SZM after the protolith inheritance. Several "exotic" data points are also shown in Figs. 5.2a,b, however, they still display a relatively uniform content of Ba-Cs-Rb in muscovite within a sample. Furthermore, together with the detailed petrography study, the most scattered data points within a sample represent the retrograde muscovite crystals. For example, one muscovite grain replacing the rim of garnet from TS02-15B contains higher Ba, Rb and Cs than those two inclusions from the same sample (Figs. 5.2a,b), although muscovite inclusions from TS02-15B also show high contents of these elements (Figs. 5.1c, 5.2a-b; see data in Table C.5).

In rocks of sedimentary protolith, although no different muscovite generations can be identified petrographically, the abundances of Ba, Rb and Cs in muscovite are more variable within the

sample (Figs. 5.2c,d) than those from rocks of basaltic protolith (Figs. 5.2a,b), which may indicate the stronger protolith control and less later SZM effects (Figs. 5.2c,d). Contents of Li, Sr, and importantly Pb, are also generally higher in phengite from rocks of sedimentary protolith than in those of basaltic protoliths (Fig. 5.3a and Table C.5).

Paragonite. Paragonite has 10 – 100 × chondrite of LILEs (Fig. 5.1d), and contains up to an order of magnitude higher Sr relative to muscovite (Fig. 5.3a and Table C.5). Except for TS02-14, all the other paragonite crystals from rocks of both sedimentary and basaltic protoliths show good correlations of K with Ba and Rb (not shown).

The paragonite coexisting with clinozoisite as inclusions in garnet (e.g., TS02-03A, TS02-30, TS02-41) shows lower Ba, Rb and Cs concentrations (except one from TS02-03A), and, to a lesser extent, Pb and Sr than other paragonite from the same sample (Fig. 5.1d and Table C.5). Those retrograde paragonite, e.g., the one replaced the rim of garnet or even include the garnet relict (Fig. 4.1k), generally contains the highest Ba, Cs and Rb within a sample (Figs. 5.2e,f). Together with this relatively constant Ba, Rb and Cs in paragonite of the same generation within a rock, a similar Ba-Rb-Cs data cluster like that of muscovite (Figs. 5.2a,b) for paragonite in rocks from different groups (Figs. 5.2e,f) suggests the similarly stronger control of alteration at different stages of SZM on these elements than the effect of compositional inheritance from their protoliths. Those "exotic" data points in Figs. 5.2e,f also represent the retrograde paragonite.

The Pb and Sr content in paragonite from rocks of sedimentary protolith is higher than in those from rocks of basaltic protolith (Fig. 5.3a), and a stronger protolith control on Ba, Cs and Rb could also be inferred for the former (Figs. 5.2g,h) like the case for muscovite.

5.2.2.3 Epidote group minerals

Compared with other minerals, epidote group minerals, especially allanite, have the highest Th, U and LREEs (Fig. 5.1b; up to ~ 1000 ppm for Th, 100s ppm for U and 10^5 ppm for LREEs in

allanite, e.g., Table C.4). HREEs, Sr and Pb are also highly enriched, up to 100 – 1000 × chondrite (Fig. 5.1b). The abundances of all these elements, especially LREEs, are highly variable (Fig. 5.1b), within or between samples, or even between different parts of a single epidote grain (shown as the compositional zoning of epidote, e.g., Fig. 5.3b). Three groups can be distinguished roughly in terms of the extent of LREE enrichments: the extremely enriched group, i.e., allanite (one inclusion in garnet from TS02-08 and the core of a single grain in the omphacitic matrix of TS02-41); the extremely depleted group (TS02-13; TS02-16; TS02-62; one in TS02-43; one in TS02-52; one in TS02-54); and the others. The large compositional variability may result from several factors, such as variable bulk-rock compositions of the protolith rocks (no depleted epidote crystals are from samples of group 1 OIB-like protolith; see Table C.4), the competition of coexisting minerals and the possibly large range in mineral-fluid partition coefficients of REEs for epidote group minerals (which may depend on metamorphic temperatures; Brunsmann *et al.*, 2001; Feineman *et al.*, 2007; Martin *et al.*, 2011).

(Clino)zoisite inclusions, which coexist with paragonite in garnet, generally show lower Sr and possibly Pb, compared with the matrix (clino)zoisite from the same sample (e.g., TS02-30 in Table C.4). In addition, the significant Th-U correlation in epidote group minerals (Fig. 5.3d) may account for their significant correlation in the bulk rock (i.e., r = 0.968 for epidote group minerals of N = 68 vs. r = 0.9516 for bulk-rock composition of N = 48 at > 99% confidence levels).

5.2.2.4 Rutile and titanite

Both rutile and titanite are primary hosts for Ti, Nb and Ta.

Because of the small grain size, only one rutile grain with reliable analytical data is available in this study. It contains high Nb and Ta, ~ 10^3 × chondrite, and Zr and Hf (Table C.6) but lower REEs than titanite (Fig. 5.1g). The concentrations of HFSEs in titanite are commonly less than those in rutile (Table C.6). The content of Sr in titanite can be up to 100 × chondrite (Fig. 5.1g).

As the third important host for Pb and Sr, titanite also defines a significant Pb-Sr correlation (r = 0.950 for N = 7, Fig. 5.3f). REEs generally show high HREEs or slightly convex-up ($MREE_N$ > $L/HREE_N$) patterns (Fig. 5.1g). LREEs in titanite vary from 100 × chondrite to even a little depleted (Fig. 5.1g). The variability of REEs in titanite is closely associated with the minerals, at the expense of which the titanite has grown or recrystallized. Specifically, the retrograde titanite grains with a good prismatic shape included in chlorite (e.g., Figs. 4.1m-n), which has replaced the rim of HREE-rich garnet are characterized by its very high HREEs, comparable with or even higher than those in the related garnet, and relatively low LREEs (e.g., 5.1g; also see data in Table C.6); one titanite replacing MREE-rich clinozoisite in TS02-43 shows a slightly convex-up pattern (Fig. 5.1g).

5.2.2.5 Omphacite, glaucophane, associated varieties and other amphiboles

Omphacite contains high Li concentrations (10s ppm in Table C.7) as reported previously (e.g., John *et al.*, 2008). It also contains high Sr (Fig. 5.1e), up to 135 ppm (Table C.7). For glaucophane, also only a few elements are above ppm levels; Li is up to tens of ppm (Table C.8). It is notable that the late-formed (sodic-)calcic amphibole shows generally higher LILEs, Sr and Pb than the early-formed Na-amphibole (Table C.8 and Fig. 5.1f), as clearly shown by the growth zoning. HFSE contents are low in both amphibole and omphacite, especially Ta that is always below the detection limit (Tables C.7-8).

5.2.2.6 Other minerals

Several grains of albite (Table C.7) and chlorite (Table C.8) were also analyzed. Except for Sr and Ba in albite (100s ppm and 10s ppm respectively) and Li in chlorite (10s ppm), these two minerals contain low concentrations of all the other analyzed incompatible trace elements, having poor hosting capacity.

Because no lawsonite (some lawsonite pseudomorphed by clinozoisite and paragonite) was found, and apatite and zircon are either too small or too rare to be identified petrographically,

these minerals were not analyzed in this study (but see analytical data and discussion on lawsonite and apatite for samples from North Qilian Mountain in Chapter 6).

5.3 DISCUSSION

5.3.1 Elemental Mobility/Immobility During SZM

5.3.1.1. Mobility/Immobility and variations of K, Ba, Rb and Cs

The original composition of K and Na in the protolith rocks governed the presence and amount of phengite and paragonite in metamorphic rocks we study. Ba, Rb and Cs preferentially partition into white micas, in which the abundances of these elements are also controlled by their concentrations in the protolith if they were not lost before white micas had been formed and stabilized. Once these elements incorporated into the mineral lattice and stabilized in the mineral host, these elements, along with the mineral modes, determine their bulk-rock abundances shown in Fig. 5.5. Therefore, K, Ba, Rb and Cs in white micas largely account for their bulk-rock abundances. In comparison with the relatively scattered Ba-Cs-Rb contents of white mica among different samples of sedimentary protolith (Figs. 5.2c,d,g,h), the constant Ba-Cs-Rb contents in white micas of the same generation within a sample, including the Ba-Cs-Rb data cluster for white micas from rocks of basaltic protolith (Figs. 5.2a,b,e,f), suggests that they may have been altered at different stages of SZM to a first order and reflects the mobility of these elements. The different behaviors of K, Ba, Cs and Rb in different lithologies (immobile in rocks of sedimentary protolith, but mobile in rocks of basaltic protolith) have also been recognized on the basis of bulk-rock geochemistry (Xiao *et al.*, 2012; Chapter 4).

The trace elemental contents of white micas vary among different generations of white micas in rocks of basaltic protolith: generation 1 of white micas (G1) is defined as inclusions in garnet

(especially the core of garnet) produced during the early prograde metamorphism; generation 2 of white micas (G2) are those crystals preserved in the omphacite matrix that may be equilibrated with the later prograde metamorphic condition; generation 3 of white micas (G3) is defined as those retrograde white micas. To exclude the effect of protolith control, considering the most obvious petrographic evidence to show the generations of white micas, we choose several paragonite crystals of these three generations from one sample (TS02-30; see data in Table C.5), including those coexisting with clinozoisite as inclusions in garnet (G1; Fig. 4.1d), a single relict with a reaction rim in the omphacite matrix (G2; Fig. 4.1g) and a retrograde one replacing garnet (G3) at the rim.

The contents of Ba, Rb, Cs, Pb and Sr in G2 are higher than those in G1, which are probably inherited from their precursor minerals like lawsonite with low contents of Ba, Rb and Cs. Meanwhile, because REEs, Pb and Sr in prior lawsonite would be preferentially incorporated into the newly-formed clinozoisite relative to paragonite (i.e., $[C^{Czs}/C^{Pg}]_{Pb}$ = ~ 20 and $[C^{Czs}/C^{Pg}]_{Sr}$ = ~ 4 in Figs. 5.3g-h), it leads to even lower Pb and Sr in the neighboring paragonite inclusions.

The retrograde paragonite (G3) has the highest Ba, Rb and Cs among all the analyzed paragonite grains from TS02-30 (forming one of the exotic points in Figs. 5.2e,f). This could be attributed to the infiltration of an external fluid with enriched Ba, Rb and Cs. This significant re-enrichment effect can also be observed in other samples, e.g., one retrograde muscovite from TS02-15B shows its much higher Ba and Cs contents than two muscovite inclusions from the same sample (Figs. 5.2a,b). Except for the effect of protolith controls, the scattered points in Figs. 5.2a,b,e,f represent retrograde white micas, which may imply that the re-enriched process happened during retrograde metamorphism (also see Lü *et al.*, 2012 for other evidence of this re-enrichment for the UHP eclogites from Western Tianshan). The fluids released from the subducted oceanic crust during the eclogitisation or from the underlying serpentinized lithosphere will move upwards (because of their low density), and rehydrate metamorphic rocks

at shallower levels (see section 4.5.2 in Chapter 4; Xiao *et al.*, 2012). During this retrogressive process, LILEs may also migrate with the fluids, and be incorporated into newly-formed minerals, especially new generations of white micas. Further analysis for the profile of white micas can be done to make this more clearly.

5.3.1.2 Geochemical behavior of other key trace elements

As shown above most of the LREEs, Th and U, and some Pb and Sr are hosted in epidote group minerals (Figs. 5.1b, 5.5), which accordingly control the budget of these elements in the bulk rock. The stability of epidote group minerals thus affects the behavior of these elements during SZM. The significant inter-correlations of LREEs, Th, and U (Figs. 5.3c,d) but the poor correlations of these elements with Sr or Pb (not shown) in the epidote group minerals suggests that the behavior of LREEs, Th and U is decoupled from that of Pb and Sr during SZM.

On the basis of experimental studies of trace element partition coefficients between zoisite and aqueous fluid, Feineman *et al.* (2007) calculated the composition of the fluids produced during specific dehydration reactions when (clino)zoisite breaks down. Pb and Sr are highly enriched while the contents of LREEs are more variable in the calculated fluid compositions depending on the chosen composition of zoisite inputs (see Feineman *et al.*, 2007). This higher Sr content relative to low LREEs in the calculated fluid composition is also reported by Martin *et al.* (2011) recently. During one of the main reactions of the blueschist-to-eclogite transition: 13 Gln + 6 Czs = 9 Prp + 26 Jd + 12 Di + 19 Coe/Qz +16 H_2O (Reaction 3 in Feineman *et al.*, 2007), the calculated bulk partition coefficients of Pb and Sr for the reaction products (Grt + Cpx + Qz) are much lower (i.e., 0.01 and 0.3 respectively) than those of LREEs (e.g., 6 for La, 15 for Ce) (Feineman *et al.*, 2007), which may indicate that Pb and Sr are mobile relative to LREEs. Pb and Sr mobilized during this dehydration reaction are then carried by those released fluids, which are manifested by dehydration veins, leaving the subducting/subducted oceanic crust for the geochemistry of arc magmas.

Moreover, because lawsonite, epidote group minerals, garnet, titanite and rutile are stable over a large P-T range during SZM (Fig. 2.3), the REEs, Th, U and HFSEs hosted by these minerals could be exchanged among these minerals and largely redistributed in the newly-formed minerals without significant loss from the system, resulting in their immobility throughout SZM. In contrast, although epidote group minerals may contain high Pb and Sr contents (paragonite to a lesser extent), the low partition coefficient of Sr between lawsonite and fluids reported recently (Martin *et al.*, 2011) can explain that some Sr may leave the system in fluids that are in equilibrium with lawsonite. The mobility of Pb and Sr may be further supported by the difference in their abundances between a paragonite porphyroblast and an included epidote relict (Fig. 4.1l). The Pb and Sr in clinozoisite are ~ 10 × and ~ 5 × those in the paragonite respectively (see last pair of columns in Figs. 5.3g,h). When clinozoisite was replaced by this paragonite porphyroblast, the paragonite cannot host all the Pb and Sr previously hosted by the clinozoisite, resulting in the local mobility of these two elements during this replacement.

5.3.2 Elemental Distribution/Redistribution During SZM

The trace element budgets are controlled by key minerals in which they are hosted, which in turn depends on the protolith compositions, metamorphic conditions (P, T, fluids) and SZM history. The trace element (re-)distributions in response to SZM, as illustrated by Fig. 5.4, are discussed in this context as follows.

5.3.2.1 Constraints on prograde and peak metamorphism (P < 3 GPa)

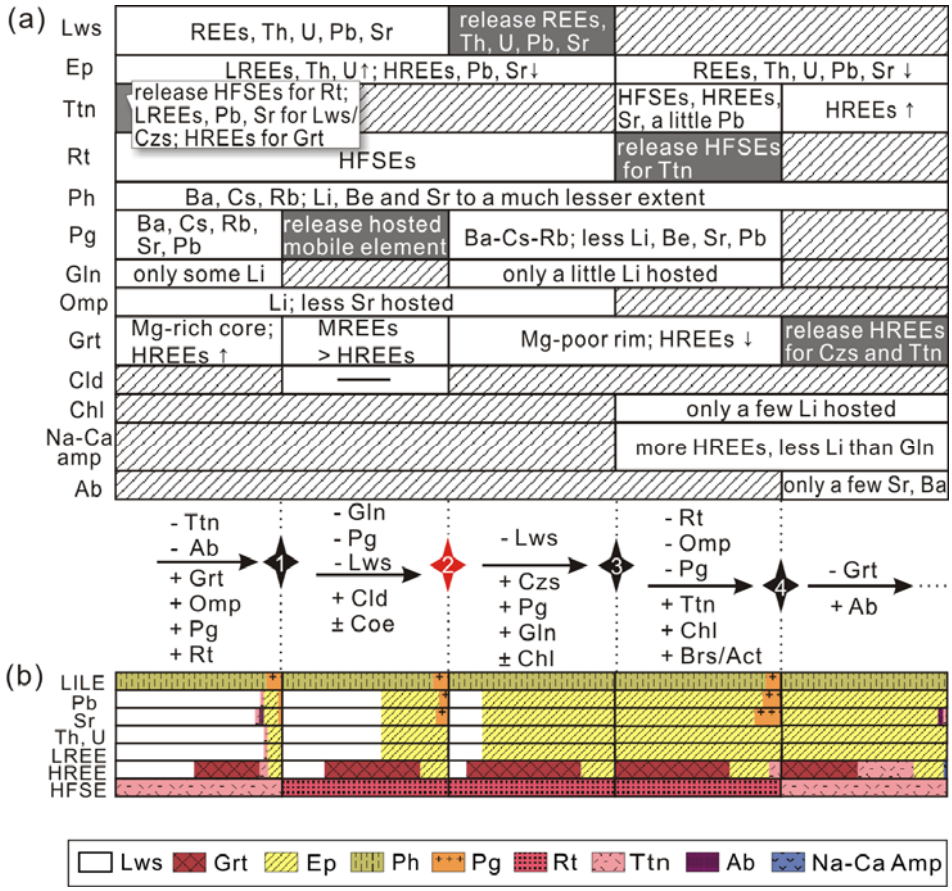

Figure 5.4 Schematic diagram showing the sequence of mineral appearance and disappearance (a) and the related trace element distribution/redistribution (b) for rocks of basaltic protoliths in responses to the SZM. The time line is also given between these two diagrams with each diamond corresponding to the stages shown in Fig. 2.3.

Under the blueschist facies metamorphic condition, the significant phases for hosting incompatible trace elements are lawsonite (REEs, Sr, Pb, U, and ±Th), titanite (HFSEs, REEs, and, to a lesser extent Pb and Sr,), phengite (LILEs, and a little Sr and Pb), and epidote (REEs, Th, U, Pb and Sr), whose modal abundance depends on the amount of H_2O available in the system (Poli & Schmidt, 1997; Rebay *et al.*, 2010).

With the eclogitization (stage 1), significant amount of H_2O would be released during the transition from blueschist to eclogite facies. With the breakdown of clinozoisite, some Pb and Sr would be liberated in fluids because of their low bulk rock – fluid partition coefficients (e.g.,

Feineman *et al.*, 2007). However, all the REEs previously hosted by epidote group minerals will be redistributed into newly formed allanite and garnet (the dominant host for HREEs subsequently). Phengite, together with paragonite, when formed will incorporate almost all the Ba, Cs and Rb. Additionally, titanite may become unstable and replaced by rutile during this process, through which REEs are transferred into newly-formed garnet and allanite, and HFSEs are entirely redistributed into rutile. Although Gao *et al.* (1999), Gao & Klemd (2003) and Spandler *et al.* (2003) suggested that lawsonite may also have been broken down at this stage, those trace elements hosted by prior lawsonite would largely, if not entirely, be conserved by newly-formed epidote group minerals (e.g., allanite) and garnet.

Up to the peak metamorphic condition (stage 2), a large proportion of REEs has been accumulated and sequestered in already produced lawsonite, epidote group minerals and garnet, and thus less REEs can be supplied for the late produced relevant minerals, typically reflected by a generally rim-ward decrease of HREEs in garnet (Fig. 4.1a; also see King *et al.*, 2004; Bebout, 2007; John *et al.*, 2008; El Kohn *et al.*, 2009). For LILEs, as phengite could be stable even up to 10 GPa (~ 300 km; e.g., Sorensen *et al.*, 1997), those already hosted elements would be entirely carried by phengite into the deep mantle.

5.3.2.2 Constraints on retrograde metamorphism

During retrograde metamorphism, amphibole (mostly [sodic-]calcic amphibole with some glaucophane), paragonite, epidote group minerals and chlorite replaced garnet, omphacite and lawsonite (stages 3 and 4). Retrograde epidote group minerals crystallize again, but may contain lower REE contents when all the lawsonite has been reacted out because less REEs are available as they have largely stored in the epidote group minerals already present (although some more HREEs could be provided during the breakdown of garnet). Meanwhile, rutile was replaced by titanite, through which Ti, Nb and Ta would be transferred back to titanite again (Lucassen *et al.*, 2010, 2011). Owing to the further breakdown of garnet (stage 4 and after), HREEs would be largely taken up by the newly-formed retrograde titanite. The titanite grains from TS02-05,

together with chlorite, have replaced garnet (Fig. 4.1n) and have HREE contents even higher than those in the garnet they are replacing. This may also be the reason for relatively higher HREEs in the newly-formed retrograde (sodic) calcic amphiboles compared with the prograde glaucophane (Fig. 5.1f and Table C.8).

5.4 IMPLICATIONS

5.4.1 Trace Element Budgets in UHP Metamorphic Rocks

To better understand trace element budgets in UHP metamorphic rocks from the subducting/subducted slab, we selected several representative samples, and reconstructed the trace element budgets in these rocks (Fig. 5.5) based on analyzed mineral trace element concentrations (Table C.3-8) and mineral modal abundances (Table C.9). Detailed modal analyses of these rocks were done by point-counting using a James Swift automatic point counter (see details in the caption of Figure C.1 in Appendix C; Xiao *et al.*, 2012). Although large uncertainties exist as a result of mineral compositional variability, mineral heterogeneous distribution, and unanalyzed accessory minerals like zircon and apatite, most of the trace element budgets in Fig. 5.5 are reasonably well constrained.

Garnet is the main host of HREEs. Phengitic muscovite and paragonite essentially accommodate all the Ba, Rb and Cs, the former hosting the majority of these elements (e.g., Fig. 5.5a). Paragonite can also host a significant portion of Sr and Pb (Fig. 5.5a). Epidote group minerals contain more than 95% of LREEs, Th, U, Pb and Sr, around 60% of MREEs and less than 30% of HREEs in the bulk rock. Concentrations of Pb and Sr in clinozoisite are respectively ~ 20 times and ~ 4 times of those in the coexisting paragonite in equilibrium (Figs. 5.3g,h), supported by lawsonite pseudomorphs in garnet (e.g., Fig. 4.1c-d). All the Ti, Nb and Ta prefer to reside in rutile and titanite. Titanite can also accommodate some REEs, Sr and Pb, especially HREEs, e.g., up to 30% in retrograde titanite that replaced the rim of garnet (Figs.

4.1m-n, 5.5b). Although omphacite and amphibole may volumetrically constitute a large proportion of mineral assemblages, they contribute little to the bulk-rock trace element budgets owing to their very low contents of all the trace elements but Li and Be (not shown).

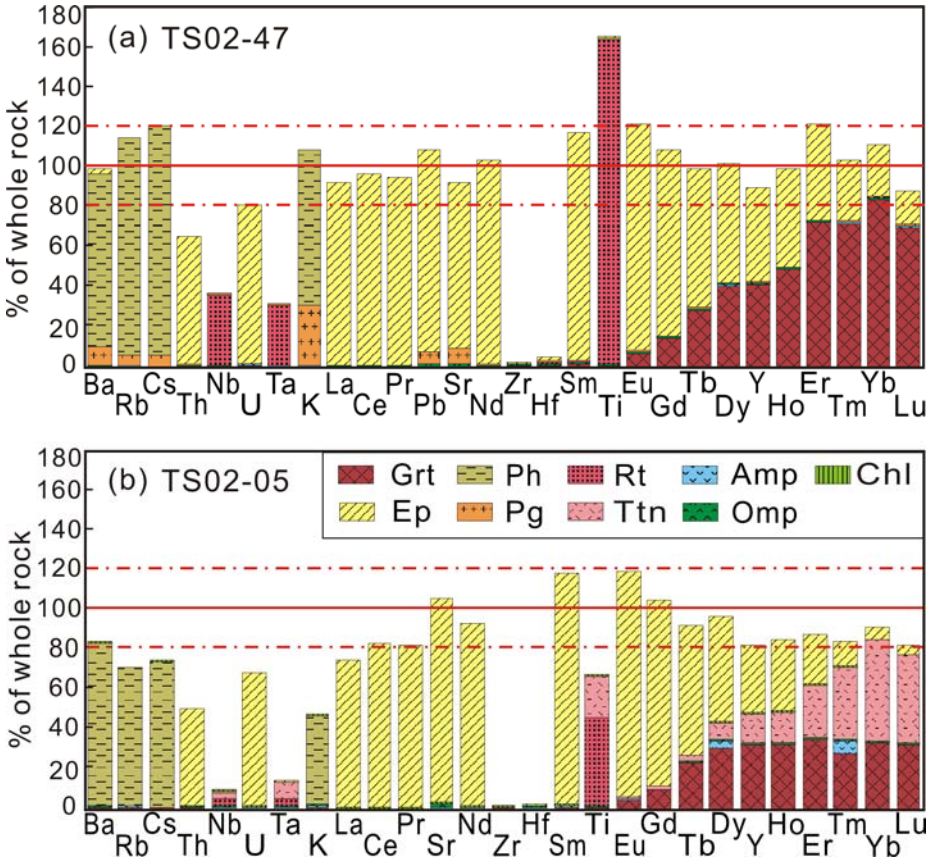

Figure 5.5 Reconstructed trace element budgets normalized by the analyzed bulk-rock compositions for representative rocks of basaltic protoliths, i.e., TS02-47 (omphacitite) and TS02-05 (retrograde blueschist). Two dot-dashed lines in each panel represent the deviation of our reconstructed bulk-rock composition from the analyzed composition with ±20%. It shows that the reconstructed element contents in each panel mostly deviate within 20%. For the big gaps of Zr and Hf, that is because zircon is hard to find petrographically for analyses. In addition, because the budget of Ti, Nb and Ta is only reconstructed using one rutile crystal from TS02-15A (see data in Table C.6), the large range of the contents of these elements in rutile (e.g., John *et al.*, 2008) is responsible for the big deviation of Ti, Nb and Ta in each panel.

5.4.2 On the Geochemistry of Arc Magmas

Arc magmas have been widely accepted to be produced by slab-dehydration induced mantle wedge melting, which gives the typical arc signatures, enriched in LILEs, Pb, Sr, U, Th and

LREEs while depleted in HFSEs (e.g., McCulloch & Gamble, 1991; Keppler, 1996). Eclogites from Western Tianshan are considered to have experienced > 2.5 GPa SZM evidenced by the occurrence of coesite (Lü *et al.*, 2008, 2009). Although no coesite found in our eclogitic samples, they were collected from the same locations with the same mineral assemblages, and thus can be used to evaluate the geochemical consequences of subduction-zone metamorphism up to 75 km or deeper (see detailed discussions in section 2.1.3.2 in Chapter 2; Xiao *et al.*, 2012). The enrichment of LILEs, Pb and Sr is apparently consistent with the relative mobility of these elements during SZM as discussed above in section 5.3.1 (also see section 4.4.2 in Chapter 4 for evidence from bulk-rock composition; Xiao *et al.*, 2012). The geochemical behavior of LREEs during SZM is controversial; they are claimed as immobile by many (e.g., Kogiso *et al.*, 1997; Usui *et al.*, 2007) and mobile by others (e.g., Brunsmann *et al.*, 2000, 2001; John *et al.*, 2004, 2008). Because of the high partition coefficients of REEs, Th and U between bulk rock and produced fluids during the breakdown of clinozoisite, and the large stability fields of the minerals that host these elements (i.e., lawsonite, titanite, epidote group minerals), we have shown that these elements most likely have not contributed to the enrichment of REEs, Th or U in subduction-zone magmatism up to a 75 km depth. These observations are important because it simply means that the standard "flux-melting" (simple slab-dehydration induced mantle wedge melting) may not be effective for arc magmatism (Xiao *et al.*, 2012). Rather, slab contributions may actually take the form of hydrous melts (e.g., Hermann & Rubatto, 2009) or supercritical fluids beyond the second critical endpoint (see definition in section 1.3.4 in Chapter 1; Schmidt *et al.*, 2004a; Mibe *et al.*, 2011) at higher temperatures and greater depths, under which conditions, REEs, Th and U could be mobilized (e.g., Kessel *et al.*, 2005).

A recent experimental study (Schmidt *et al.*, 2004a) shows that phengite could be dissolved in a supercritical fluid beyond the second critical endpoint (> 3.5 GPa as shown in Fig. 2.3 and Fig. 2.6, Mibe *et al.*, 2011; 5 – 6 GPa for K-/mica-rich lithologies of the subducted oceanic crust in Schmidt *et al.*, 2004a; Kessel *et al.*, 2005). Therefore, the supercritical fluids may carry phengite-hosted elements (e.g., K, Ba, Cs and Rb) to metasomatize the overlying mantle wedge,

and further lead to melts enriched in these elements. Based on the experimental studies, supercritical fluids also display a much higher fluid-solid partition coefficient for LREEs, Th, U and Sr than those in aqueous fluids (see Kessel *et al.*, 2005). Alternatively, hydrous melts of subducting ocean crust and sediment may be responsible for the enrichment of these elements in the arc magmas, e.g., allanite (one of the most important carriers for LREEs and Th, U to a lesser extent) can be dissolved in a coexisting hydrous granitic melt at high temperatures but not in a fluid, evidenced by experimental studies of Hermann (2002).

On the other hand, the good correlations in arc magmas between elements with similar incompatibility during mantle melting (including mantel wedge melting), especially those between mobile elements proposed previously (e.g., U) and immobile elements (e.g., Nb – U, Nb – La; Fig. 5.6) contradict the standard slab-dehydration induced mantle wedge melting, in which the mobile elements should not correlate with immobile elements. Therefore, the correlations in Fig. 5.6 also indicate that the arc signatures may be caused by supercritical fluids or hydrous melts of subducting ocean crust/sediments, rather than dehydrated aqueous fluids (Hermann *et al.*, 2006; Hermann & Rubatto, 2009).

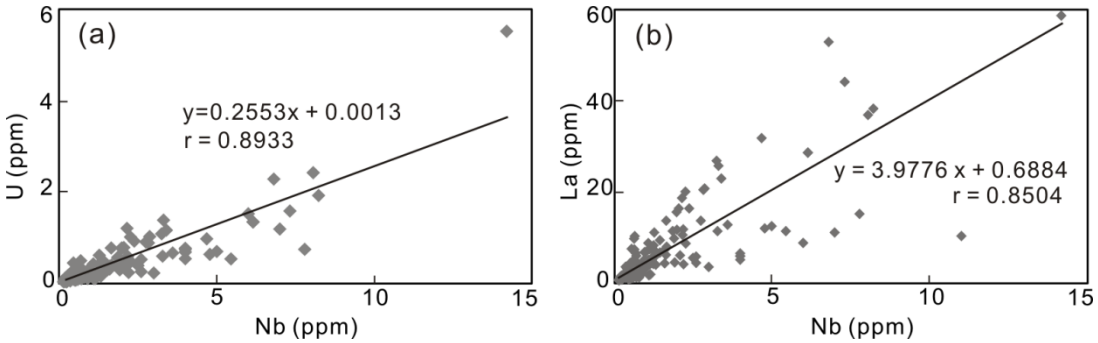

Figure 5.4 Correlations of Nb with U and La in observed arc magmas (data from Elliott, 2003). The significant correlations of immobile elements with mobile elements proposed previously (e.g., U) in arc magmas indicate the importance of supercritical fluids or hydrous melts of rutile-bearing eclogite (vs. aqueous fluids) for the "arc signatures".

In addition, through the detailed discussion on the apparent immobility of U (see section 4.4.2 in Chapter 4) which indicates the form of U^{4+} (Bailey & Ragnarsdottir, 1994), it has been inferred that the redox condition in subduction zones may be more reduced (see section 4.5.3.2

in Chapter 4; Lee *et al.*, 2003, 2005; Song *et al.*, 2009b; Xiao *et al.*, 2012) than previously thought (oxidized condition in subduction zones, e.g., Wood *et al.*, 1990; Brandon & Draper, 1996). In this study, we have shown that the immobility of U like Th and their significant linear correlations (Fig. 5.3d) are largely controlled by epidote group minerals (lawsonite maybe to a lesser extent). Therefore, it may indicate that it is the preference of epidote group minerals for U over aqueous fluids, irrelevant to the valence of U, that controls the geochemical behavior of U during SZM (the similarly stronger control by mineral on the geochemical behavior of U, rather than distinctive redox conditions, has also been proposed based on the experimental work of rutile-melt partitioning by Klemme *et al.*, 2005). However, further studies are required to figure out the redox condition in subduction zones and the implication of geochemical behavior of U to this issue.

5.4.3 On Mantle Compositional Heterogeneity

After SZM, mobile elements have been lost with the breakdown/dissolution of their host minerals (Schmidt, 1995), while those relatively immobile elements conserved in those stable minerals of the dehydrated oceanic crust can be carried into the deep mantle. These altered mobile elements and conservative immobile elements have direct bearing on the deep mantle compositional heterogeneity as reflected by the geochemical variability of oceanic basalts (e.g., Weaver, 1991; Hofmann, 1997; Niu & O'Hara, 2003; Niu, 2004). Furthermore, if those mobile elements are controlled by different minerals (e.g., phengite for Rb, clinozoisite for Sr) or the mobility of these elements is controlled by different processes during subduction (e.g., only supercritical fluids or hydrous melts for U if possible, aqueous fluids for Pb), the ratios relevant to these mobile elements in the residual subducted rocks will determine the relevant elemental ratios in the deep mantle (e.g., Rb/Sr, U/Pb), that cannot be the same as in rocks entering the trenches prior to SZM.

Both previous studies and this work have revealed that REEs, Th and U are largely hosted in lawsonite, epidote group minerals and garnet, and LILEs are hosted by white micas during SZM.

After SZM, the Lu/Hf ratio in the residual subducted oceanic crust remains constant because immobile elements, Lu and Hf, have been largely conserved in garnet, the latter also significantly hosted in zircon; Sm/Nd could also be constant because they are similarly hosted by epidote group minerals (e.g., allanite) and thus have similar geochemical behaviors. However, the Rb/Sr ratio is significantly modified with the mobility of Rb and Sr during SZM, and affected by both white micas (for Rb) and epidote group minerals (for Sr). The U/Pb ratio may also change because U and Pb are mobilized by different mechanisms (aqueous fluids for Pb vs. supercritical fluids/melts for U). Therefore, alteration during SZM will result in the absence of correlations between Rb/Sr (and possibly U/Pb) and Sm/Nd or Lu/Hf, which, with time, will lead to similarly poor correlations between $^{87}Sr/^{86}Sr$ (or $^{206}Pb/^{204}Pb$) and $^{143}Nd/^{144}Nd$ or $^{176}Hf/^{177}Hf$ in the residual slab materials subducted in the deep mantle. Therefore, although altered ocean crust (AOC) is expected to contribute to mantle compositional heterogeneity, it cannot be the major source materials for oceanic basalts because subduction-zone-processed residual ocean crust will result in Rb-Sr decoupling and hence Sr-Nd and Sr-Hf isotopic decoupling, which cannot explain the first order Sr-Nd-Hf isotope correlations defined by oceanic basalts, in particular OIB (also see detailed discussions in terms of bulk-rock composition in section 4.5.4 of Chapter 4; Niu & O'Hara, 2003; Xiao *et al.*, 2012).

5.5 CONCLUSIONS

Garnet, epidote group minerals, white micas, and Ti-bearing minerals are the most important minerals hosting incompatible elements in the subducting/subducted oceanic crust and sediment. Their presence and stability largely control the geochemical behaviors of elements during SZM. Different fluid properties (e.g., aqueous fluids, supercritical fluids, hydrous melts) and resultant partitioning are also important for controlling element behaviors during SZM (e.g., different mobility of Pb and Sr from LREEs, Th and U during the breakdown of epidote group minerals). Therefore, Ba, Rb, Cs, K, Pb and Sr are mobilized in meta-basaltic rocks, while only Pb and Sr

are also mobile in meta-sedimentary rocks with the aqueous fluids (at least up to 75 km in our studies); LREEs, Th and U can only be migrated in supercritical fluids or hydrous melts. The protolith composition, metamorphic conditions and metamorphic history, all together in turn, control the mineral assemblages and the stability of these minerals.

The common enrichments of U, Th and LREEs observed in arc magmas but the immobility of these elements during the dehydration of aqueous fluids may indicate that hydrous melts generated at the temperature beyond the water-saturated solidus or supercritical fluids beyond the second critical endpoint are significant in generating ‘‘arc signatures’’. In addition, because elements such as LILEs and LREEs are hosted in different mineral phases and because elements are released by different mechanisms, the AOC, after the SZM, can no longer be responsible for the Sr – Nd (Hf) isotopic correlations observed in oceanic basalts and therefore cannot be the major source materials for OIB.

CHAPTER 6:

ELEMENTAL RESPONSES TO SUBDUCTION-ZONE METAMORPHISM: CONSTRAINTS FROM THE NORTH QILIAN MOUNTAIN, NW CHINA

6.1 INTRODUCTION

Through detailed studies of both bulk-rock (Chapter 4) and mineral compositions (Chapter 5) of rocks of basaltic and sedimentary protoliths from ultrahigh pressure (UHP) metamorphic belt of Western Tianshan, China, we have identified specific elemental responses to subduction-zone metamorphism (SZM), especially to high/ultrahigh pressure metamorphic reactions. We have also revealed the most likely geochemical consequences of SZM and their potential contributions to arc magmatism and mantle compositional heterogeneities. However, further studies on high pressure (HP) metamorphic rocks from other subduction zones are essential to prove our previous conclusions. In addition, further analysis on the unanalyzed minerals from subduction-zone metamorphic rocks in previous studies are required, e.g., rutile, lawsonite; also, those low-grade metamorphic minerals, e.g., pumpellyite. All of these mineral analyses are crucial to improve our previous understandings on elemental responses to subduction-zone metamorphism along a series of metamorphic reactions.

The two metamorphic sub-belts of North Qilian Mountain (ONQ) in China (high-grade blueschist/eclogite metamorphic belt, HGB and low-grade blueschist metamorphic belt, LGB) have not only different peak metamorphic conditions (see details in section 2.2), but also distinctive protolith compositions and experienced different metamorphic histories (e.g., Wu *et al.*, 1993; Song, 1997; Song *et al.*, 2009a; Zhang *et al.*, 2009; Fig. 2.6), i.e., the HGB is considered to be produced by the subduction of mature ocean seafloor, while the formation of the LGB may be attributed to the subduction of back-arc basin seafloor. These differences between the LGB and the HGB allow a better understanding of the elemental behaviors during SZM as a function of metamorphic conditions and protolith compositions. Therefore, the elemental budgets and elemental redistributions in SZM rocks from North Qilian Mountain, along with their bulk-rock compositional studies, will be discussed in this chapter.

6.2 SAMPLES AND PETROGRAPHY

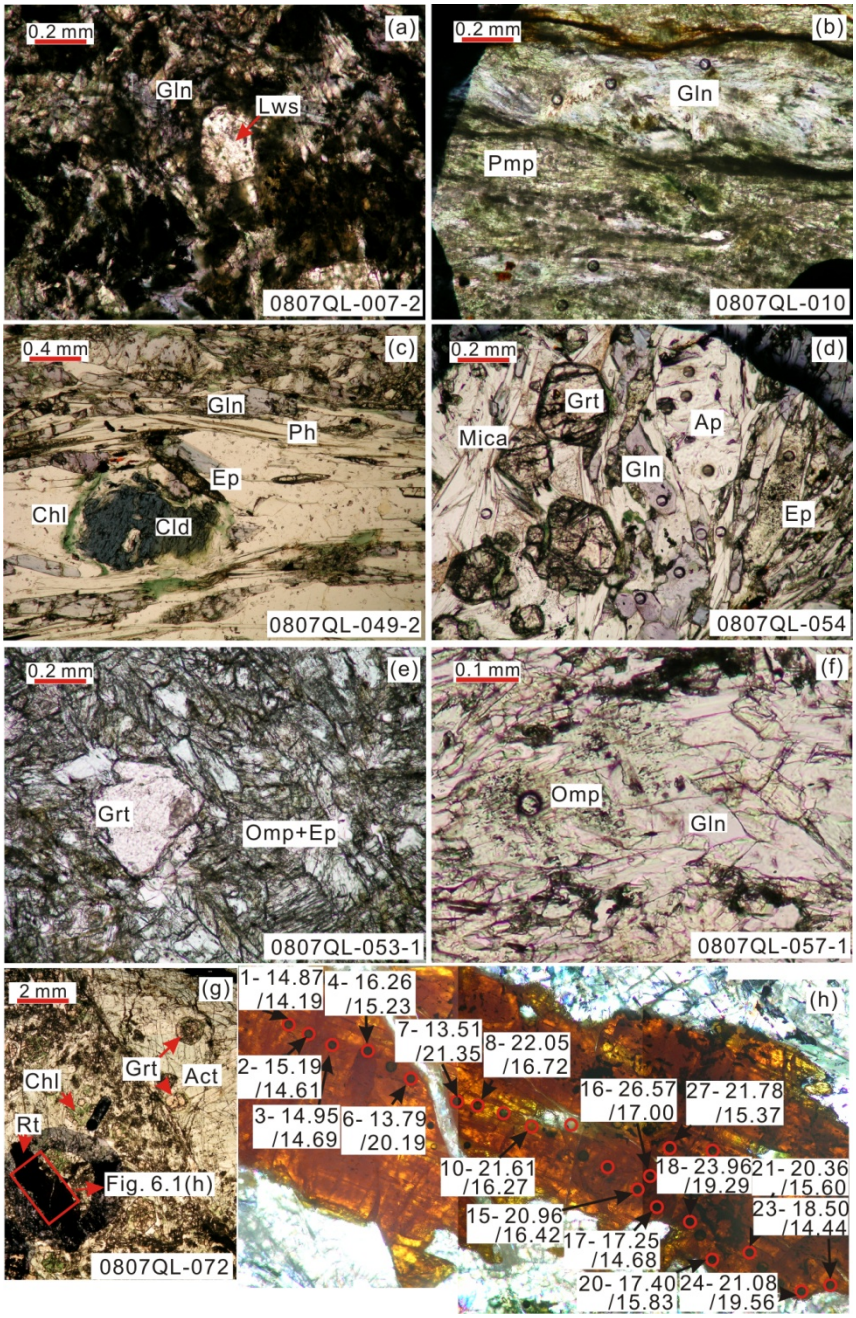

Figure 6.1 Photomicrographs of representative samples from both LGB (a-b) and HGB (c-h). All the photos are taken under PPL. (a). Lawsonite glaucophanite. Lawsonite, with characteristic box-shape, exists as porphyroblast in fine grained matrix. (b). Glaucophane pumpellyite schist. Interbedded glaucophane and pumpellyite defined the clear schistosity. (c). Grt-Cld-Gln-Ph schist, the representative of meta-pelite, characterized by the common occurrence of chloritoid porphyroblast. (d). Blueschist-facies meta-sedimentary rock. The high proportions of quartz and white micas in mineral assemblages are distinctive features of meta-sedimentary rocks. (e-f). Eclogitic blueschist, composed of garnet porphyroblast and the matrix made up of omphacite, glaucophane and epidote.

0807QL-057-1 is also used for bulk-rock composition reconstruction in Fig. 6.5a. (g). Amphibolite. One huge rutile is found up to 2 mm length. (h) is the close up of the rutile shown in (g). Nb/Ta and Zr/Hf ratios using LA-ICPMS are labeled besides each analyzed point (x – y / z; x = the number of the analyzed point; y = the Nb/Ta ratio; z = the Zr/Hf ratio).

Sample locations are shown in Fig. 2.4b, and GPS position for each sample is given in Table D.9. Rocks of basaltic protoliths are sampled from both LGB and HGB, while rocks of sedimentary protoliths are only sampled from HGB. The representative mineral assemblages in distinctive types of metamorphic rocks from LGB and HGB are summarized in Table D.2 and shown in Fig. 6.1, the caption of which gives a detailed petrographic description.

6.3 MINERAL GEOCHEMISTRY

6.3.1 Mineral Major Elements

We analyzed garnet, white micas (both muscovite and paragonite), lawsonite, epidote group minerals, rutile, titanite, amphiboles, clinopyroxene, chlorite, chloritoid, and pumpellyite plus some carbonate, serpentine and albite grains using EPMA (Table D.6).

Garnet crystals are dominantly almandine and generally show normal zoning of pyrope (increasing rimward), reflecting prograde growth (e.g., Lü *et al.*, 2009). The tiny garnet crystals in samples from Baishiya contain very high spessartine (e.g., garnet from 0807QL-043 as shown in Table D.6). The inherited magmatic clinopyroxene relict in meta-basaltic rocks from LGB is augite, while the clinopyroxene from HGB is omphacitic. Most analyzed amphibole crystals are glaucophane, but some calcic amphiboles (e.g., actinolite, tremolite) and sodic calcic amphiboles (e.g., barroisite) have also been identified in some samples (see Leake *et al.* [1997] for amphibole nomenclature). The composition of epidote group minerals is highly variable. FeOt and Al_2O_3 are negatively correlated (not shown) as a result of Al-Fe^{3+} substitution. White micas are predominantly phengite with minor paragonite, which is distinguished from

phengite in terms of its relatively higher Na/K ratios.

6.3.2 Mineral Trace Elements

We found that the most important trace element hosts are pumpellyite (Fig. 6.2a), lawsonite (Fig. 6.2b), epidote (Fig. 6.2c), garnet (Fig. 6.2d), phengite (Fig. 6.2e), paragonite (Fig. 6.2f), rutile (Fig. 6.2g), titanite (Fig. 6.2h), and apatite (Fig. 6.2i). Albite can also contain high Sr (Table D.7). Omphacite (Fig. 6.2j), glaucophane (Fig. 6.2k), chloritoid (Fig. 6.2l) and chlorite (Fig. 6.2l) have low contents of almost all the analyzed trace elements. Representative analytical data are given in Table D.7 for anhydrous minerals and Table D.8 for hydrous minerals.

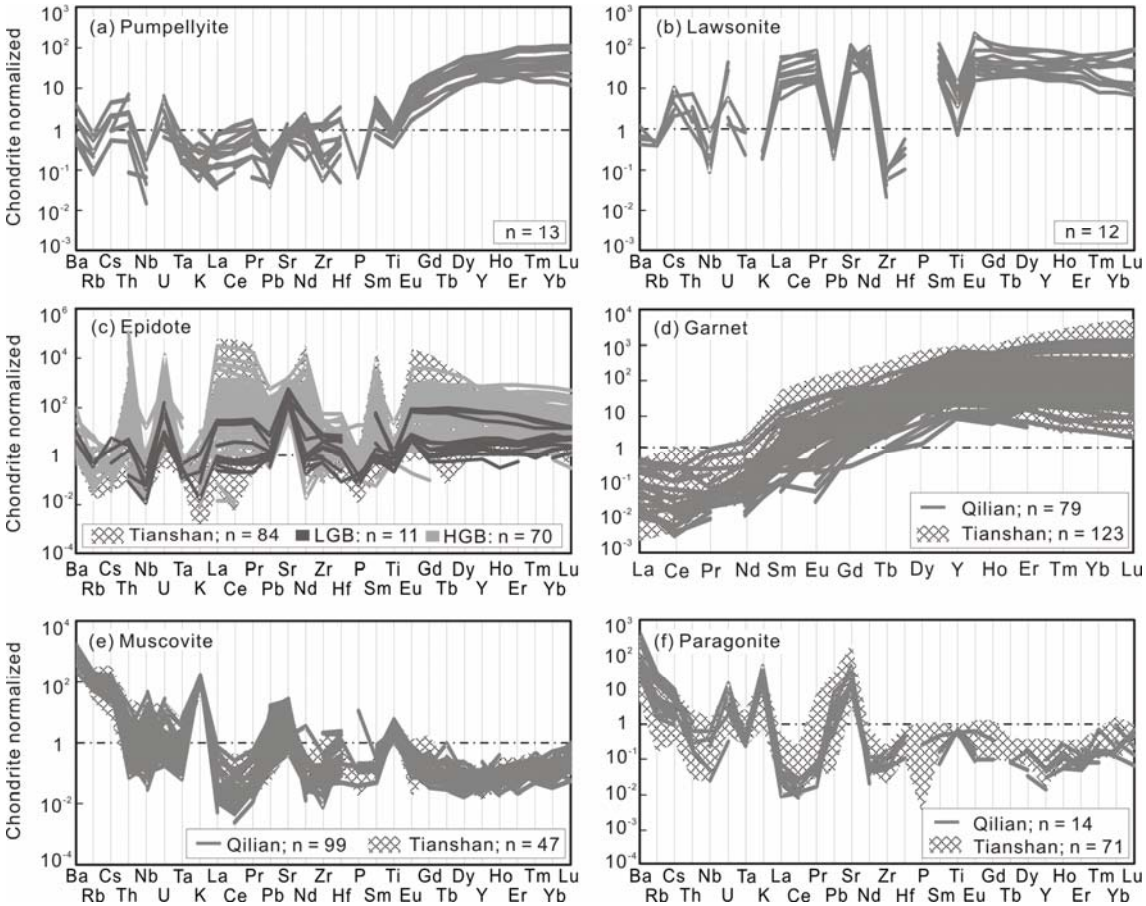

Figure 6.2 Chondrite-normalized multi-element distributed diagrams for minerals in blueschist and eclogite facies rocks from LGB and HGB. The values of chondrite are referred to Sun & McDonough (1989). The analytical results of relevant minerals in blueschist/eclogite facies rocks from Western Tianshan, NW China, are also plotted for comparison, which are represented by the hatched areas in (c-f, h, j-k).

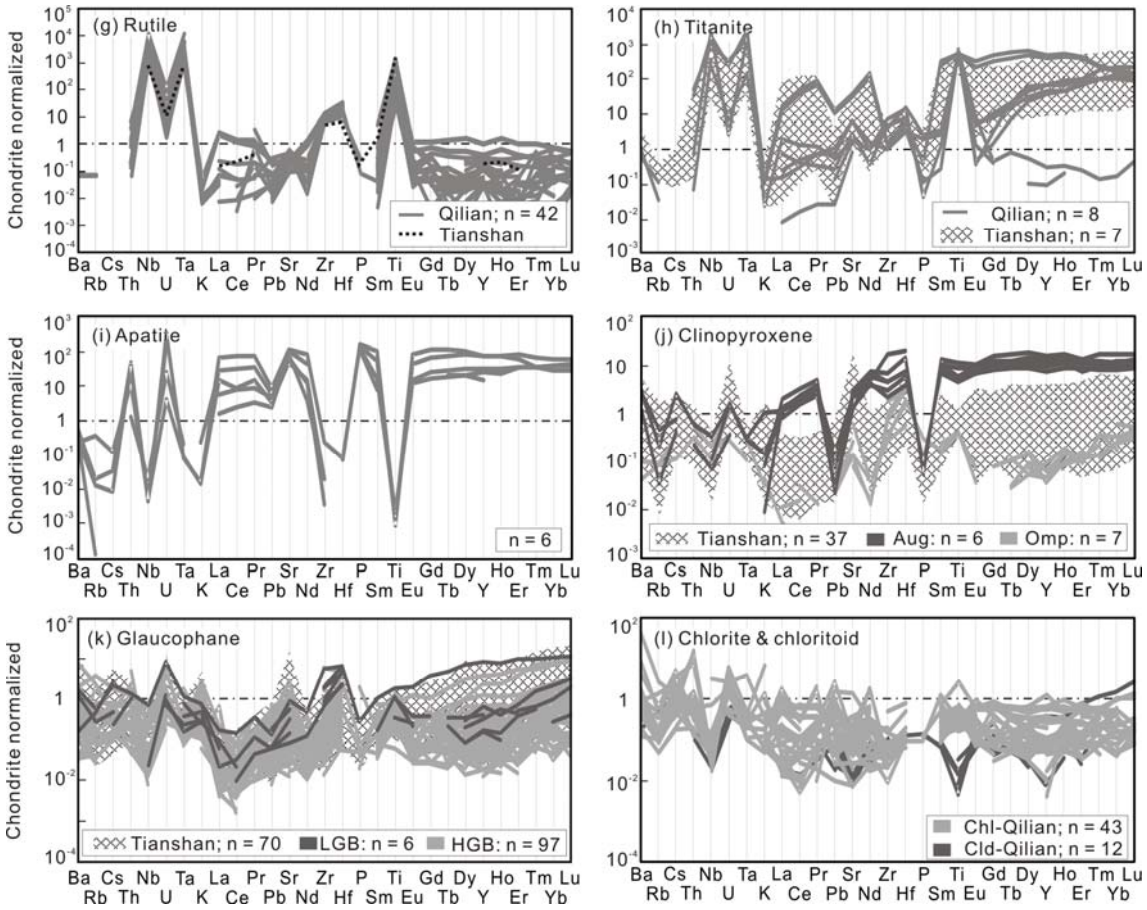

Pumpellyite is an important index mineral in low-grade metamorphic rocks, but rare analysis has been done for its trace element contents (to our knowledge, only Spandler *et al.* [2003]). It has highly elevated abundances of heavy REEs (HREEs; Fig. 6.2a), similar to those in garnet (Fig. 6.2d). Sr and Ba are present at ppm levels, along with detectable Th, U, Cs, Rb and Pb. Lawsonite is characterized by consistently high REEs and Sr (Fig. 6.2b). REE fractionation is slight ($[LREEs/HREEs]_{chondrite} \leq 1$). Apatite shares similar trace element patterns to lawsonite, except for its characteristic high P and slightly higher Pb, Th and U but lower Ti and Cs (Fig. 6.2i vs. Fig. 6.2b). Epidote group minerals show variable REEs, Th and U (Fig. 6.2c), and consistently high Sr and Pb. Garnet is characterized by variably high HREEs (Fig. 6.2d). Some garnet grains show high middle-REEs (MREEs; $[MREEs > HREEs]_{chondrite}$), which is likely inherited from the precursor phases (e.g., MREE-rich amphiboles, titanite) during high pressure prograde metamorphism (Spandler *et al.*, 2003; Lucassen *et al.*, 2010). Alternatively, presence of zircons locally can strongly draw HREEs, resulting in HREE depletion of the nearby garnet

because zircons have higher Kd (HREEs) than garnet (e.g., Rubatto & Hermann, 2007).

Both phengite and paragonite commonly contain high Ba, Cs, Rb, Pb, Sr, Li (10s of ppm) and Be (several ppm). In addition, phengite contains one order of magnitude higher Ba, Cs, Rb than paragonite, whereas paragonite generally has higher Pb and Sr (Fig. 6.2e vs. 6.2f). Phengite from meta-sedimentary rocks has obviously higher Pb and Sr than those from meta-basaltic rocks (Table D.8), and also relatively more scattered Ba, Cs and Rb, which are especially variable among white micas from different rocks.

Rutile and titanite contain high amounts of Nb and Ta (Figs. 6.2g & h). Titanite can also have variably high REEs with varying REE fractionation patterns ($[MREEs > HREEs]_{chondrite}$ or $[MREEs < HREEs]_{chondrite}$ in Fig. 6.2h). Albite is depleted in all the trace elements but Sr, and to a less extent, Ba (Table D.7). Although omphacite in eclogitic rocks from HGB contains low contents of almost all the analyzed trace elements (except Sr), several analyzed magmatic clinopyroxene relicts (i.e., augite) in metamorphic rocks from LGB show a HREE-rich pattern (more than 10 × chondrite; Fig. 6.2j).

6.4 BULK-ROCK GEOCHEMISTRY AND TECTONIC DISCRIMINATION

In the following, we discuss our samples and data, together with the data (Lavis, 2005; Song *et al.*, 2009a) in the literature on ONQ samples from the same sampling location.

6.4.1 Geochemistry of Metamorphic Rocks From LGB

The LGB samples are mainly epidosite, lawsonite glaucophanite and glaucophane pumpellyite schist, and are basaltic in composition with 45.91 to 53.67 wt.% SiO_2 (Table D.3). Different hydrous minerals, especially high H_2O-bearing minerals (e.g., pumpellyite, lawsonite, chlorite, containing up to 12.5 wt.% H_2O), are widely present in mineral assemblages of rocks from LGB,

and thus resulted in commonly high loss on ignition (LOI) in LGB metamorphic rocks (> 2.33 wt.%; see Table D.3), which is even especially higher in rocks with high carbonate amount, e.g., 0807QL-015-2 (25 vol.% carbonate and 7.01 wt.% LOI). Epidosite, is dominated by epidote (> 40 vol.%, see Table D.9), carbonate to a variable extent, and it thus contains higher CaO (15.15 – 16.66 wt.%) than the other two lithologies in LGB (i.e., 5.10 – 8.74 wt.%), but lower MgO (2.03 – 3.83 wt.% vs. 6.75 – 8.80 wt.%) and Mg#. Considering the higher contents of Sr and Pb in epidote than pumpellyite and glaucophane, epidosite also shows higher contents of Sr and Pb.

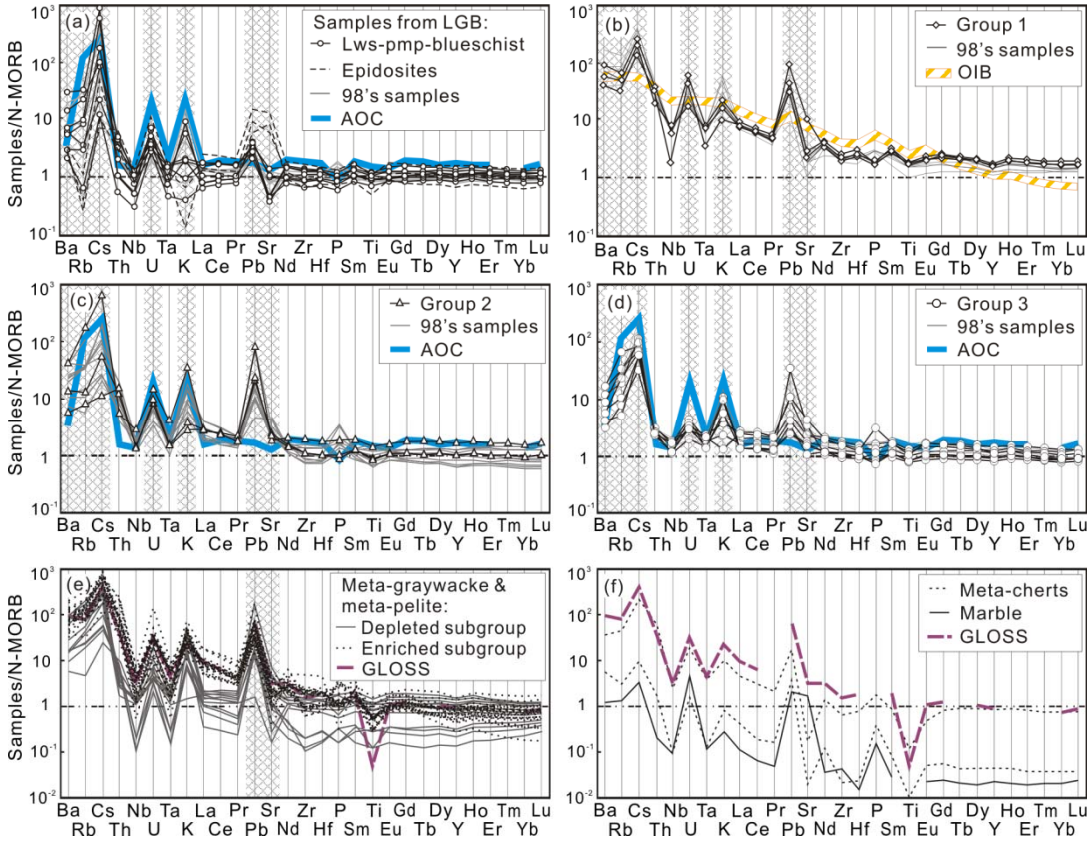

Figure 6.3 N-MORB normalized multi-element distributed diagrams for bulk-rock compositions of metamorphic rocks from LGB (a) and HGB (b-f) of ONQ. Mobile elements discussed in the relevant text of section 6.5.2 are plotted in hatched areas in (a-e). The grey curves in (a-d) represent 1998's samples from Song *et al.* (2009) and Lavis (2005). Group classification for mafic blueschist and eclogites from HGB (b-d) refers to the section 6.4.2.1. Oceanic island basalts (OIB; referred to the values in Sun & McDonough, 1989) and the altered oceanic crust (AOC; Kelley *et al.*, 2003) are plotted in (b) and (a, c-d) respectively for comparison with meta-basaltic rocks. Global oceanic subducted sediment (GLOSS; Plank & Langmuir, 1998) is plotted in (e-f) for comparison with meta-sedimentary rocks.

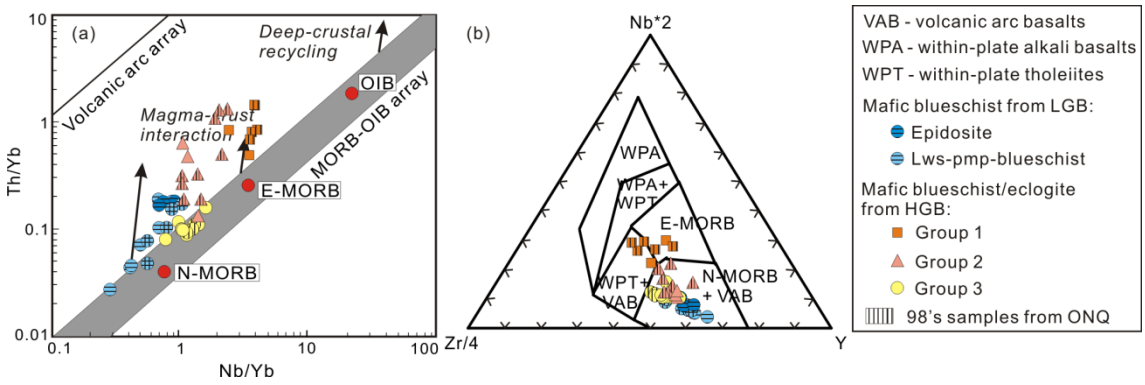

Figure 6.4 Discrimination diagrams for basaltic blueschists and eclogites from both LGB and HGB. (a) Th/Yb vs. Nb/Yb (after Pearce, 2008). OIB, E-MORB and N-MORB are plotted for comparison (i.e., the red solid circles; the values of oceanic basalts are referred to Sun & McDonough, 1989). (b) Nb*2-Zr/4-Y (Meschede, 1986).

In the N-MORB-normalized multi-element diagram (Fig. 6.3a), except for Ba, Rb, Cs, U, K, Pb and Sr, which are assumed to be mobile during metamorphism (or prior seafloor weathering effects), the generally flat elemental patterns of LGB metamorphic rocks reflect their geochemical affinity to N-MORB. However, assuming high field strength elements (HFSEs) and HREEs are immobile during SZM, the plots in Fig. 6.4a define a trend slightly away from MORB – oceanic island basalts (OIB) array. Together with the obvious Nb-Ta depletion in Fig. 6.3a, this indicates that they possess arc-related geochemical signatures (Pearce, 2008). Therefore, protoliths of LGB metamorphic rocks are probably originated from a back-arc basin (vs. an oceanic ridge setting) as previously suggested (Song *et al.*, 2009a), which is also consistent with the presence of wehrlite intrusions (vs. troctolite; the indicator of the high fluid content during crystallization, Niu, 2005) and high volume of volcanic breccias and terrigenous-sedimentary rocks in the field (Jiugequan) (e.g., Song *et al.*, 2009a).

6.4.2 Geochemistry of Metamorphic Rocks From HGB

6.4.2.1 Blueschists/eclogites

The SiO_2 content of blueschists and eclogites from HGB varies from 45.14 to 50.06 wt.% (Table D.4). Although the occurrence of epidote group minerals and glaucophane (which contain ~ 2.0 – 2.2 wt.% H_2O, Poli & Schmidt, 1995) as well as white micas (~ 4.3 – 4.6 wt.% H_2O, Poli &

Schmidt, 1995) as hydrous minerals in rocks from HGB, the absence of high H_2O-bearing minerals (e.g., lawsonite, pumpellyite), and the more widely presence of anhydrous minerals (e.g., garnet and omphacite) resulted in generally lower LOI in HGB meta-basaltic rocks than those in LGB metamorphic rocks. However, the relatively high abundance of carbonate in several meta-basaltic rocks can also result in high LOI (e.g., up to 3.90 wt.% LOI in 0807QL-053-2, Table D.4). All the HGB rocks of basaltic protolith may be readily divided into three groups in terms of their geochemistry (Table D.4 and Figs. 6.3-6.4): samples from Group 1 contain high TiO_2 and K_2O, and low MgO; samples from Group 2 have high MgO and Al_2O_3; samples from Group 3 show high CaO and low TFe_2O_3. Consistently, all the phengite-rich eclogites reported by Song *et al.* (2009) belong to Group 1; while epidote-rich eclogites in their study have been included in Group 2 and Group 3.

Samples from Group 1 show higher concentrations of large ion lithophile elements (LILEs), Th, and overall REEs (∑REEs), and higher LREE/HREE ratios (Fig. 6.3b). Group 1 and Group 2 samples plot in the E-MORB and N-MORB fields in Fig. 6.4b respectively. However, they deviate from the MORB-OIB array in Fig. 6.4a, and show pronounced depletions in Nb and Ta, especially in Figs. 6.3b. Thus, these rocks reflect an arc signature and their protoliths may be assimilated with some continental margin materials. As for Group 3, all samples show a flat pattern of REEs and HFSEs with variably enriched Ba, Rb, Cs, U, K, Pb and Sr in Fig. 6.3d, and plot in the MORB-OIB array (Fig. 6.4a), suggesting an N-MORB-like protolith. All of these indicate that protoliths of HGB meta-basaltic rocks probably possess geochemical features of N- to E-MORB from ridges or near-ridge seamounts (Song *et al.*, 2009a), intermingled with some arc materials (Group 1 and Group 2).

6.4.2.2 Meta-sedimentary rocks

Because of the highly variable mineral assemblages in meta-sedimentary rocks (Table D.2 and Table D.9 in Appendix D), they show large major element compositional variations relative to HGB meta-basaltic rocks. Generally, meta-sedimentary rocks have higher SiO_2 and LOI, but

lower MgO and TiO_2 (Table D.5 in Appendix D). The large amount of phengite accounts for the high K_2O in meta-sedimentary rocks (e.g., up to 5.61 wt.% K_2O in 0807QL-067 for 45 vol.% phengite). The multi-element patterns of meta-sedimentary rocks (Figs. 6.3e,f), including meta-graywacke, meta-pelite, meta-chert and marble, are generally similar to that of global oceanic subducted sediments (GLOSS; Plank & Langmuir, 1998). Meta-graywackes and meta-pelites seem to show two subgroups in terms of Th and U contents and ratios of REEs (Fig. 6.3e), and the subgroup with higher Th and U possesses higher LREE/HREE ratios. The great variability of these elements reflects the complex provenance for the protoliths of meta-sedimentary rocks.

6.5 DISCUSSION

6.5.1 Trace Element Budgets

We used estimated mineral modes (Table D.9) and analyzed mineral trace element contents (e.g., Table D.7-8) to reconstruct trace element budgets for three distinct protolith lithologies from HGB (Fig. 6.5). The consistency of reconstructed compositions with analyzed bulk-rock compositions for most trace elements illustrates the reliability of our reconstruction, although uncertainties exist due to the highly variable mineral compositions, the heterogeneous mineral distributions and the presence of non-analyzed accessory minerals (e.g., zircon).

Since paragonite is rare in metamorphic rocks from the ONQ and it contains lower LILEs than phengite, we conclude that phengite accommodates almost all the K, Ba, Rb and Cs in the bulk rock. Some Pb and Sr can also reside in phengite (Fig. 6.5b). All the Ti, Nb and Ta are hosted in rutile, and to a lesser extent in titanite. Apatite contains more than 95 % P, but because of its low modal abundance, the contribution of apatite to the budgets of Th, U, Pb, Sr and REEs in the bulk-rock composition is insignificant although apatite can contain moderate abundance of these elements (Fig. 6.2i). Almost all the M-HREEs are dominated by garnet and epidote group

minerals. When garnet is absent (e.g., blueschist-facies meta-graywacke in Fig. 6.5c), epidote group minerals become more significant for M-HREEs. All the Th, U and LREEs, plus some Pb and Sr, are hosted in epidote group minerals. Chlorite, glaucophane and omphacite contribute little to bulk-rock trace element budgets (except for Li and Be), although they are volumetrically the major phases in these rocks.

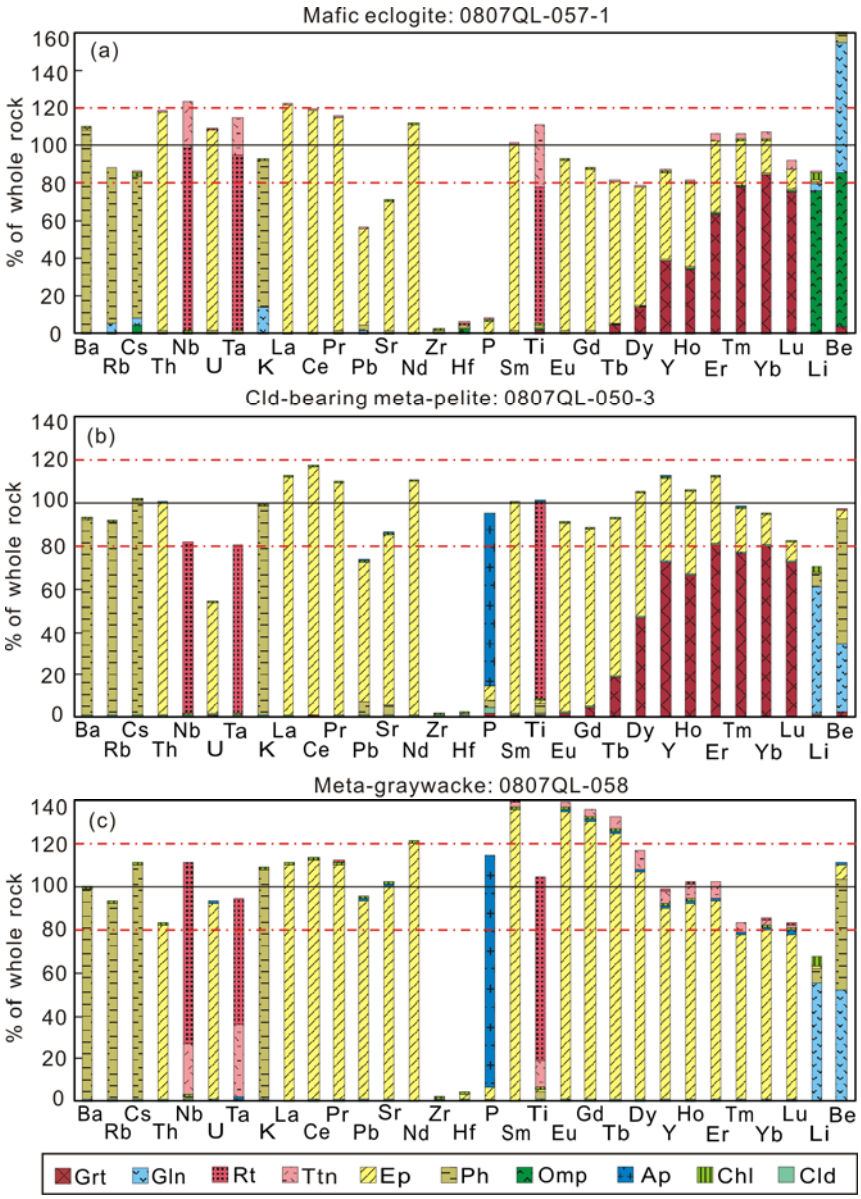

Figure 6.5 Reconstructed trace element budgets compared with analyzed bulk-rock compositions for three representative rocks from HGB of ONQ, with different protolith lithologies, i.e., mafic eclogite, meta-pelite and meta-graywacke. In each panel, the black horizontal line represents the composition comparable to the analyzed bulk-rock composition, and two red dotted-dashed lines represent ±20% deviation from the analyzed bulk-rock composition. Most trace element budgets

are comparable with the analyzed bulk-rock trace element contents. However, because it is hard to petrographically find zircon for analysis, there are big gaps for Zr and Hf in reconstructions.

For metamorphic rocks from LGB, because of the inherited magmatic texture and the fine grain size, the reconstruction is not possible. However, considering the mineral trace element contents (Fig. 6.2) and the relatively mineral abundances (Table D.9 in Appendix D), the most important hosts for REEs, Th, U, Pb and Sr are lawsonite, epidote, and pumpellyite (importantly for HREEs; probably titanite as well) and to a lesser extent apatite, while LILEs are hosted in white micas. Albite and carbonate may also host some Sr and Pb (also see van der Straaten *et al.*, 2008).

6.5.2 Element Mobility/Immobility and Their Controls

Assuming HFSEs are immobile, their correlation coefficients with elements having similar incompatibility in basaltic protoliths would reflect the mobility or immobility of these elements (see Niu, 2004; Xiao *et al.*, 2012; Fig. 6.6). If their correlations are insignificant, it means that this element has been mobilized during later metamorphism. Otherwise, it indicates the element is as immobile as the reference HFSE. Therefore, Figs. 6.6a,b suggest that for rocks of basaltic protoliths from both LGB and Group 3 of HGB, Li, Ba, Rb, Cs, Pb and Sr are mobile, while Be, REEs and HFSEs are immobile. This is broadly similar to our observations on metamorphic rocks from Western Tianshan (section 4.4.2 in Chapter 4; Xiao *et al.*, 2012). As for Th, the clearly positive trends between Nb and Th for Group 3 of HGB, especially for rocks of basaltic protoliths from LGB (Fig. 6.7a), suggest the immobility of Th. U is moderately mobile, especially in Group 3 of HGB (Figs. 6.6a,b), in contrast to our previous study on Tianshan samples (section 4.4.2 in Chapter 4; Xiao *et al.*, 2012).

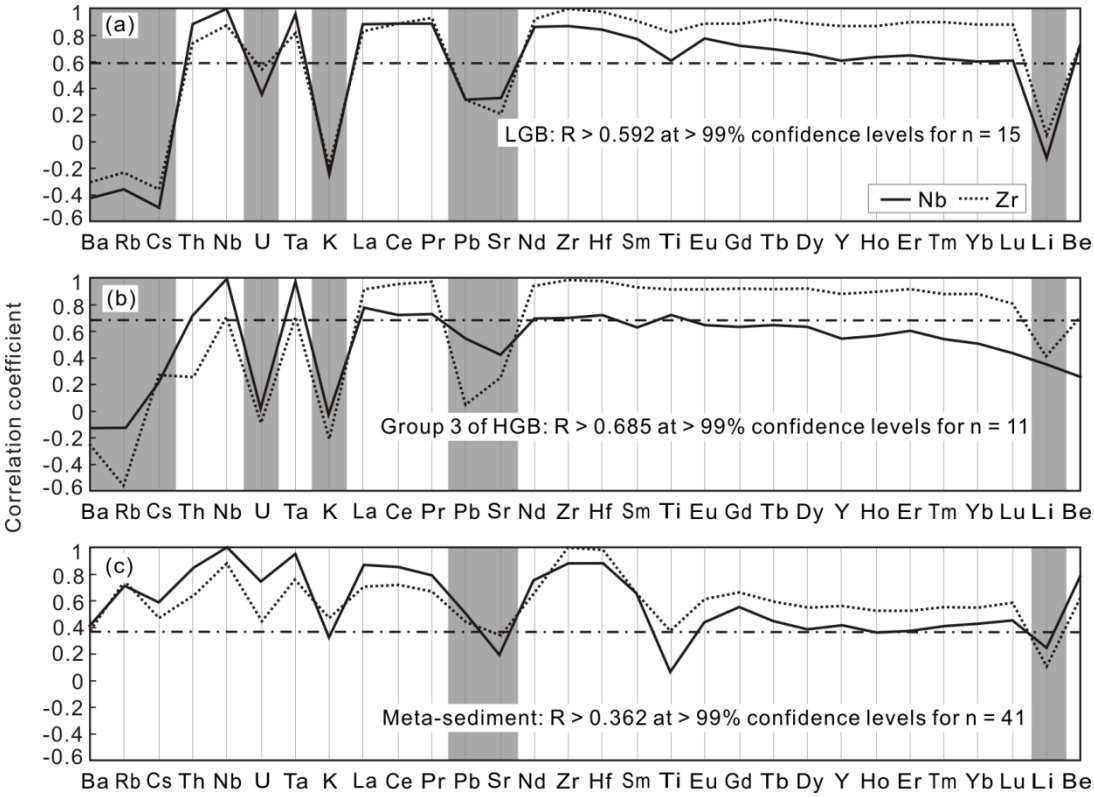

Figure 6.6 Correlation coefficient diagrams of Nb and Zr with other trace elements for (a) rocks from LGB, (b) rocks from HGB (Group 3 is chosen as its clear origin), and (c) meta-sedimentary rocks from North Qilian Mountain (the methodology is referred to Niu, 2004 and Xiao *et al.*, 2012). Elements along X-axis are ordered in terms of decreasing incompatibility from left to right. Two immobile elements (Nb and Zr) are chosen considering their different incompatibilities during magmatic processes. The dotted-dashed lines represent the minimum significant correlation coefficients for a certain sample size above 99% confidence levels (referred to critical values of Pearson's correlation coefficient using one-tail test). Therefore, generally, the element with correlation plotted below the dotted-dashed lines is mobile element, which has been constrained by the grey areas, while those plotted above are immobile elements during subduction-zone metamorphism.

For meta-sedimentary rocks (Fig. 6.6c), Th, U, REEs and HFSEs are clearly immobile, while Pb, Sr and Li are mobile. The positive trend of Rb with Nb in Fig. 6.7b (also Ba, Cs and K with Nb, not shown) indicates their moderate immobility, in contrast with those in meta-basaltic rocks.

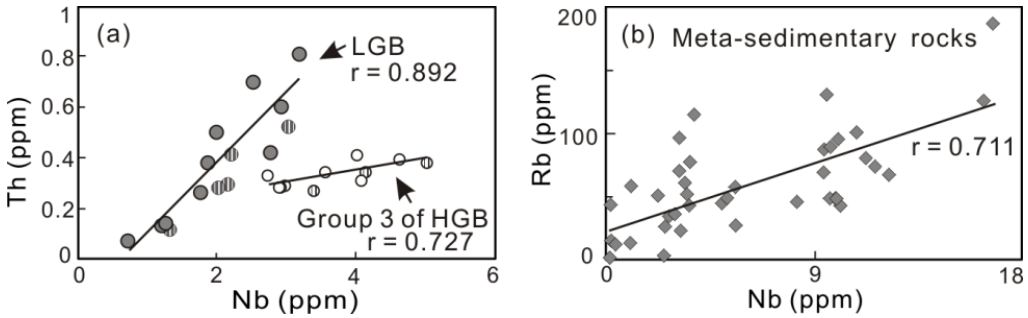

Figure 6.7 Element co-variation diagrams for clarification of those unclear correlations in Fig. 6.6. (a) Nb vs. Th for rocks from LGB and Group 3 of HGB. The hatched circles represent 1998's samples from Song *et al.* (2009) and Lavis (2005). (b) Nb vs. Rb for rocks of sedimentary protoliths from HGB. The clear trend for the correlation between Nb and Rb in meta-sedimentary rocks indicates the moderate immobility (vs. mobility) of Ba, Cs and Rb (similar trends could also be obtained for Cs and Ba with Nb, although the trend with Ba is not so obvious) in meta-sedimentary rocks.

The unclear correlations of U with those assumed immobile elements for rocks of basaltic protoliths (Figs. 6.6a,b) indicates U may have been mobilized since the last magmatic process, which involved both seafloor alteration and subsequent subduction-zone metamorphism. Our study on Western Tianshan samples, which experienced similar metamorphic transitions to HGB metamorphic rocks from the ONQ (Fig. 2.6) shows that U is immobile as Th and HFSEs during the SZM (Xiao *et al.*, 2012). Therefore, it is less likely that the mobility of U shown in the samples from ONQ is caused by SZM.

One of the most significant geochemical features caused by hydrothermal alteration is the general enrichment of U in altered/weathered seafloor basalts (e.g., Staugidel *et al.*, 1995; Kelley *et al.*, 2003). Although the immobility of U in blueschists/eclogites from Western Tianshan may reflect the heterogeneity of hydrothermal alteration and/or the possibility of erosion the altered seafloor materials during subduction (which may result in the input of only unaltered seafloor materials into subduction zones), the mobility of U in this study may reflect enrichment caused by this seafloor modification, which is also consistent with the comparable U content of Group 3 with altered oceanic crust (AOC; Fig. 6.3d). Some Ba, Rb, Cs and K may have also been enriched by seafloor hydrothermal alteration before their further modifications during SZM.

During prograde SZM, with the transition from pumpellyite-prehnite facies to epidote eclogite facies, HREEs are mainly transferred from pumpellyite (Fig. 6.2a) and augite (Fig. 6.2j) to garnet (Fig. 6.2d). As more epidote is produced at the expense of lawsonite, LREEs are redistributed between them. HFSEs are completely transferred from titanite to rutile. For Pb and Sr, although they could be hosted and redistributed among albite, apatite, white micas, carbonate and epidote to different extents, a portion of them may be released with the breakdown of epidote during the main reaction of the blueschist-to-eclogite transition: 13 Gln + 6 Czs = 9 Prp + 26 Jd + 12 Di + 19 Qz +16 H_2O, as evidenced by experimental work (Feineman *et al.*, 2007). Ba, Cs and Rb, dominantly hosted in phengite, are mobile in rocks of basaltic protoliths from both LGB and HGB, and may have been released partly before the formation of phengite. However, because of white micas already present in sedimentary protoliths, these elements could be conserved.

6.5.3 The Preservation of Nb/Ta Ratio During SZM

We have analyzed some well-crystallized and preserved rutile grains (Figs. 6.1g,h). As rutile and titanite accommodate almost all the Nb and Ta in the bulk rock (Fig. 6.5), the composition of these two minerals can help understand possible Nb-Ta fractionation in rutile-bearing eclogites. For Zr and Hf, even though these Ti-bearing minerals can also contain high Zr and Hf (10 – 100 times of chondrite in Figs. 6.2g,h; also see data in Table D.7), the unanalyzed trace zircons are still the primary host for Zr and Hf in the bulk-rock composition, and thus expectedly underestimated Zr and Hf in the reconstruction relative to the analyzed bulk-rock Zr and Hf (Fig. 6.5). Therefore, we focus here on the control of Ti-bearing minerals on Nb-Ta systematics.

The arithmetic average Nb/Ta ratio in rutile and titanite are similar, 18.50 ± 3.78 (1σ; n=42) in rutile vs. 19.50 ± 6.95 (1σ; n=8) in titanite, which also seems to be the case for the geometrical average of Nb/Ta ratio in rutile and titanite in terms of the slope of the Nb-Ta correlations within the error (13.822 ± 0.690 vs. 12.976 ± 3.733; Fig. 6.8a). Zr and Hf contents of rutile and titanite

are also plotted (Fig. 6.8b). The Nb/Ta ratio is highly variable, and shows both superchondritic and subchondritic values in both rutile and titanite, while the Zr/Hf ratio in both Ti-bearing minerals is only subchondritic (Fig. 6.8c). The variability of Nb/Ta and Zr/Hf ratios can be found even within a single crystal (Fig. 6.1h), and this may be closely associated with the HFSE contents of minerals nearby (most likely titanite), at the expense of which rutile is formed.

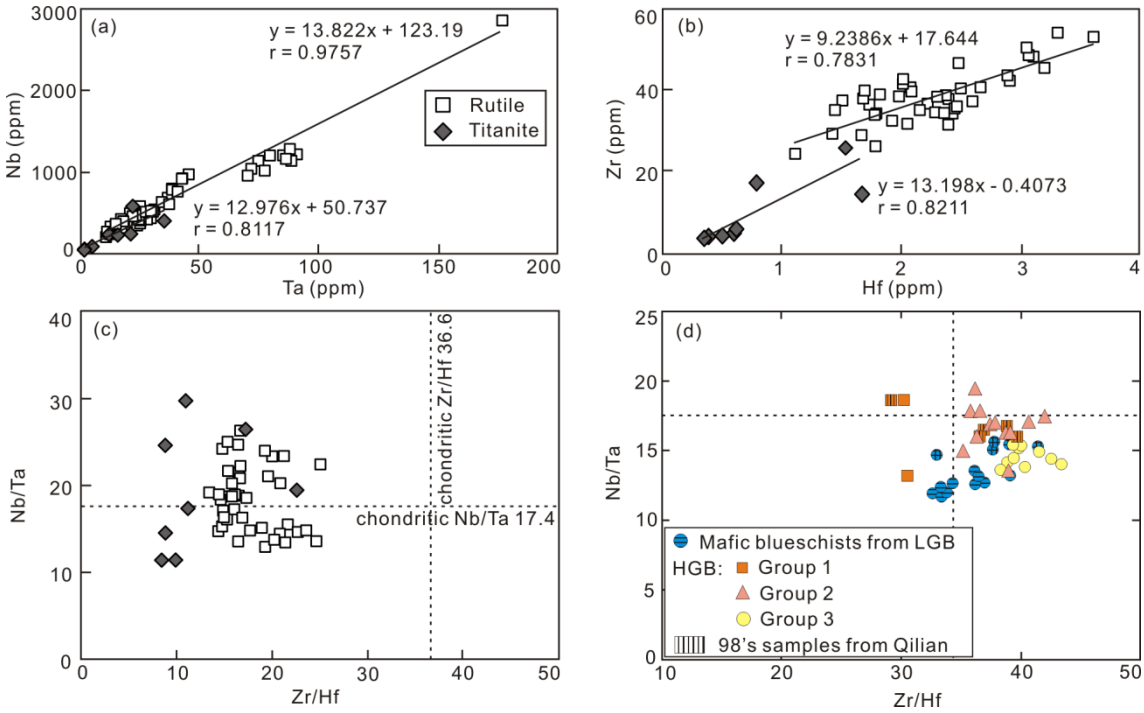

Figure 6.8 (a-b) The co-variation diagrams of Nb vs. Ta and Zr vs. Hf for both rutile and titanite. Slops of the linear correlation represent the geometrical average of Nb/Ta and Zr/Hf ratios for rutile and titanite respectively. (c) Plots of Nb/Ta vs. Zr/Hf ratios for rutile and titanite. The Nb/Ta ratios in rutile and titanite are both superchondritic and subchondritic. All the Zr/Hf ratios in rutile and titanite are subchondritic. (d) Bulk-rock Nb/Ta vs. Zr/Hf ratios. The relevant hatched symbols represent those 1998's samples referred to Song *et al.* (2009) and Lavis (2005). The dotted lines in (c-d) denote the chondritic values of Nb/Ta (= 17.4; Jochum *et al.*, 2000) and Zr/Hf (= 36.6; Sun & McDonough, 1989) respectively.

Bulk-rock Nb/Ta and Zr/Hf ratios plotted in Fig. 6.8d, display no obvious superchondritic Nb/Ta ratio. Therefore, subducted rutile-bearing ocean crust may not be the missing Nb (vs. Ta) reservoir responsible for the subchondritic Nb/Ta in bulk silicate Earth (Rudnick *et al.*, 2000; Niu, 2012).

6.6 IMPLICATIONS FOR SUBDUCTION-ZONE MAGMATISM

The arc basalts differ from MORB in their enrichment in LILEs and depletion in HFSEs, or the characteristic "arc signature". This arc signature, plus the high water contents, has been the primary evidence for slab-dehydration induced mantle wedge melting for arc magmatism. If this interpretation is correct, then it is logical to say that without subduction-zone dehydration metamorphism, there would be no arc magmatism.

Our studies on samples both from North Qilian Mountain (this study) and Western Tianshan, NW China (Xiao *et al.*, 2012) pointed out the mobility of Ba, Rb, Cs, Pb and Sr (in rocks of basaltic protolith) while immobility of REEs and HFSEs (in rocks of both sedimentary and basaltic protoliths) in response to the subduction-zone metamorphism, which is broadly consistent with the estimated mobility/immobility inferred for the petrogenesis of arc lavas (e.g., Tamura *et al.*, 2007). The observed enrichments of LILEs in arc lavas (Fig. 6.9) are thus most likely attributed to their mobility in released fluids from subducting/subducted ocean crust. As for immobile REEs, the comparable REE patterns of island arc basalts (IAB) with E-MORB (Fig. 6.9) may reflect their similar source compositions and melting process (without additional processes). The strongly depleted Nb and Ta may result from their retention in rutile in subducted slab rocks, consistent with the common presence of rutile in eclogites from our studies.

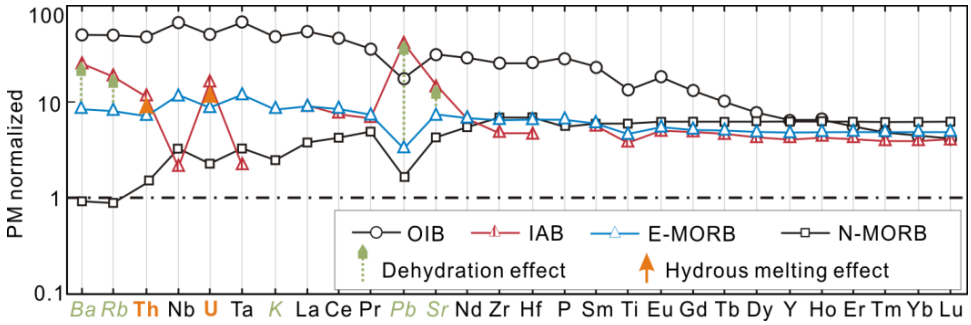

Figure 6.9 Primitive mantle (PM) normalized multi-element distributed patterns for OIB, IAB and N-/E-MORB. The reference values for OIB, PM, E-MORB and N-MORB are from Sun & McDonough (1989), and the values for IAB are referred to Elliott (2003). The element names in green are those elements most likely controlled by dehydration process, while those in orange are elements that

require supercritical fluids or hydrous melts for their enrichments in arc lavas.

Owing to the redistribution into newly formed minerals, Th and U are immobile in both meta-basaltic and meta-sedimentary rocks during SZM (although U shows its mobility during seafloor alteration in this study), which is well demonstrated by those rocks from Western Tianshan (Chapter 4; Xiao *et al.*, 2012). Thus, these two elements are not expected to be carried into the mantle wedge by fluids. Although the geochemical behavior of LILEs in SZM and their enrichments in arc lavas seem to show the consistence with the model of slab-dehydration induced mantle wedge melting, the relative enrichments in Th and U commonly observed in IAB (Fig. 6.9) and their immobility during SZM may suggest some other medium (rather than aqueous fluids) may transport them from the subducting slab to the source of IAB.

We suggest that the transport of the apparently fluid-immobile Th and U, plus LREEs to a lesser extent, to mantle wedge may have accomplished through supercritical fluids beyond the second endpoint or hydrous melts from greater depths for arc magmatism, rather than simply subduction-zone dehydration metamorphism. Supercritical fluids or hydrous melts, generated at depths beyond those represented by our samples (up to 75 km deep for metamorphic rocks from Western Tianshan, Xiao *et al.*, 2012) is necessarily required for arc magmatism (e.g., Kessel *et al.*, 2005; Hermann & Rubatto, 2009).

6.7 CONCLUSIONS

(1) Consistent with the observations on HP and UHP metamorphic rocks from Western Tianshan, the North Qilian Mountain samples also show that Ba, Rb and Cs are mobile in meta-basaltic rocks and immobile in meta-sedimentary rocks, whereas REEs and HFSEs are immobile and Pb and Sr are mobile in both lithologies. Thus, Ba, Rb, Cs, Pb and Sr could contribute to the mantle wedge source regions of arc lavas through subducting-slab derived aqueous fluids, while enrichments of Th and U and LREEs in arc lavas require transport through supercritical fluids

or hydrous melts generated deeper than 75 km.

(2) Metamorphic mineral controls on element behavior are important during SZM. Phengite (and, to a lesser extent, paragonite) accommodates essentially almost all the Ba, Rb and Cs; titanite and rutile accommodate all the HFSEs, with titanite also hosting REEs, Th, U, Sr, and Pb; epidote and garnet are responsible for all the M-HREEs transferred from pumpellyite and augite that are stable in low grade metamorphic rocks; almost all the Th, U and LREEs, and a large proportion of Sr and Pb are also hosted in epidote group minerals. Apatite, like lawsonite, may contain moderate-to-high concentrations of Th, U, Pb, Sr and REEs during SZM, but because of their low modal abundance, epidote is still the dominant host for these elements.

(3) The Nb/Ta ratio in rutile varies significantly, probably as a result of competing effects of spatially coexisting phases on petrographic scales. The subchondritic Nb/Ta ratio in eclogites of the residual ocean crust protoliths indicates that the ocean crust, if subducted to the deep mantle, cannot be the Nb-rich reservoir needed to balance the missing Nb (i.e., the subchondritic Nb/Ta ratio) in the bulk silicate Earth.

CHAPTER 7:

IS THE SUBDUCTION-ZONE MAGMATISM REALLY CAUSED BY FLUX-MELTING?

7.1 INTRODUCTION

Subduction-zone magmatism is widely accepted to have resulted from slab dehydration-induced mantle wedge peridotite melting (e.g., McCulloch & Gamble, 1991; Tatsumi & Eggins, 1995). As the slab-dehydration is in essence a process of metamorphism, it is thus logical to state that subduction-zone magmatism is a straightforward consequence of subduction-zone metamorphism (SZM). The process of subduction-zone magma generation has also been termed (slab-derived fluid) flux melting of mantle wedge peridotite. This concept is underpinned by the high H_2O content (6 – 8 wt%; Wallace, 2005), high abundances of water-soluble elements (e.g., Ba, Cs, Rb, Pb, Sr) and relatively low abundances of water-insoluble elements (e.g., Nb, Ta, Ti) in island arc basalts (IAB). This geochemical systematics of IAB is the familiar ‘‘arc signature’’ (Stopler & Newman, 1994; Elliot, 2003; John *et al.*, 2004; Fig. 7.1).

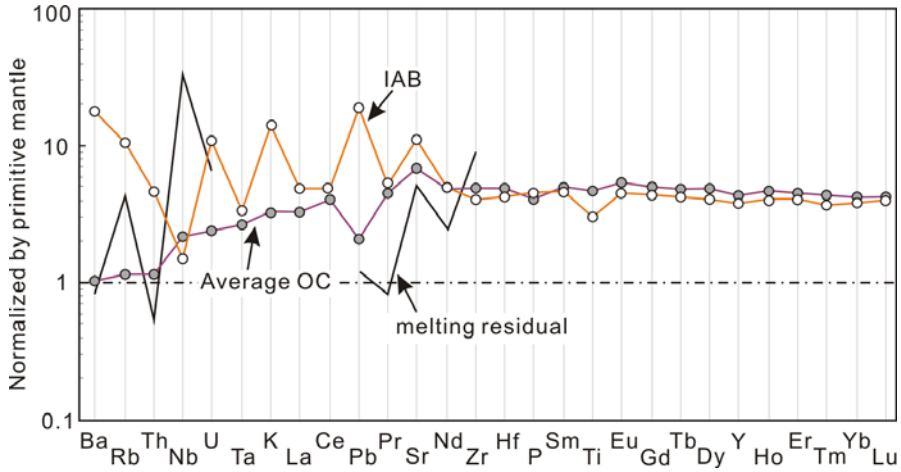

Figure 7.1 Comparison of primitive mantle normalized trace element pattern of IAB with that of average ocean crust, OC (‘‘bulk ocean crust’’, composed of 40% N-MORB + 60% average gabbro). See data of IAB and average ocean crust in Niu & O'Hara (2003). One mafic granulite (DIET3) from Dietensdorf (Saxonian Granulite Massif, Germany) high temperature-high pressure terraces (900 – 1000°C at 1.5 – 2.0 GPa) is also plotted, the data of which is referred to Becker *et al.* (2000). It shows a depleted pattern with low LILEs, Th and U and high HFSEs, likely to be the melting residue of eclogite (see relevant discussions in section 7.4). The data for primitive mantle are referred to Sun & McDonough (1989).

The above is the description of the standard model for subduction-zone magmatism, where enrichments of the water-soluble elements (e.g., Ba, Cs, Rb, Pb, Sr) plus light rare earth

elements (LREEs) in IAB are explicitly derived from the subducting ocean crust owing to the mobility of these elements in the slab-derived dehydrated fluids. On the other hand, the HFSE and HREE depletions in arc magmas may originate from the conservation of those water-insoluble or immobile elements in the residual subducting ocean crust and overlying sediment during SZM, which will be carried into the deep mantle afterwards (McCulloch & Gamble, 1991; Stopler & Newman,1994).

Recent studies of arc magmas, especially the across-arc geochemical variations (e.g., Morris & Ryan, 2003; Tamura *et al.*, 2007), experimental studies and studies on subduction-zone metamorphic rocks (e.g., Becker *et al.*, 2000; Spandler *et al.*, 2003; Bebout, 2007; Hermann & Rubatto, 2009; Xiao *et al.*, 2012), however, have indicated that the relationship between the IAB arc signature and the geochemical contribution of the subducting ocean crust (and overlying sediments) is much more complex than previous thought. For example, it has been suggested that ‘‘mobile elements’’ in previous studies are not simply mobilized by the metamorphic dehydration in subducting slab rocks (e.g., Spandler *et al.*, 2003). As strongly controlled by their hosted minerals, including the accessory minerals, e.g., LILEs by phengite, LREEs by allanite, these ‘‘mobile elements’’ can be largely conserved as immobile elements in the subducting ocean crust (and sediment) during dehydration, and thus cannot be responsible for the enrichment of these elements in arc magmas in that case (e.g., Spandler *et al.*, 2003; Hermann, 2002; Hermann & Spandler, 2009; El Korh *et al.*, 2009; Xiao *et al.*, 2012). Therefore, other models have been invoked to explain the geochemical contributions of subducting/subducted slab rocks to the arc signature, e.g., hydrous melting of subducting ocean crust with sediments, infiltration/alteration by high fluid flux (e.g., Stern *et al.*, 2006; Tommasini *et al.*, 2007; Zack & John, 2007; John *et al.*, 2008; Hermann & Rubatto, 2009; Mibe *et al.*, 2011). However, comprehensive studies on eclogites from HP-UHP terranes are required to fully evaluate this new interpretation. In this context, both forward modeling (on the basis of studies on actual SZM rocks) and reverse modeling (on the basis of geochemical studies of actual arc magmas and related melt inclusions; e.g., Cervantes & Wallace, 2003; Walker *et al.*, 2003; Tamura *et al.*,

2007) should be considered together.

7.2 FORWARD MODEL: MOBILIZED ELEMENTS DURING SZM

On the basis of the analysis of inter-elemental correlations shown by bulk-rock compositions of HP-UHP metamorphic rocks from North Qilian Mountain (Chapter 6) and Western Tianshan, Northwest China (Chapter 4; Xiao *et al.*, 2012), we have identified that REEs and Th show similar immobility with HFSEs during SZM. On the other hand, Ba, Rb and Cs in rocks of basaltic protoliths are mobile, but immobile in rocks of sedimentary protoliths (see Xiao *et al.*, 2012). Pb and Sr are mobile in rocks of both basaltic and sedimentary protoliths during SZM. Such elemental behavior during SZM is the same shown in both HP-UHP rock suites. However, U shows immobility in SZM rocks from Western Tianshan, but apparent mobility in rocks from North Qilian Mountain. The apparent mobility of U recorded in the latter rock suites may have been inherited from the seafloor alteration/weathering rather than SZM (also see Becker *et al.*, 2000). Nevertheless, through examination of the bulk-rock compositional data for the worldwide HP-UHP rocks, we can conclude that the statistically significant correlation between U and Th (Fig. 7.2a) is consistent with U and Th both being immobile during SZM, which is supported by the recent experimental work (Hermann *et al.*, 2006).

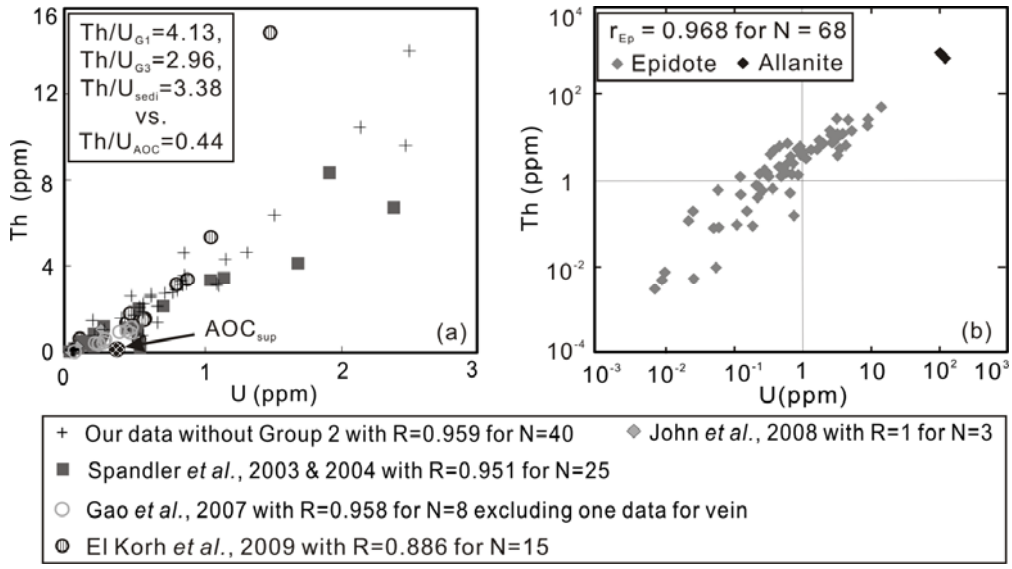

Figure 7.2 Co-variation of Th – U. (a) Plot of bulk-rock compositions, including data of HP-UHP metamorphic rocks from Western Tianshan (Xiao *et al.*, 2012), and in the recent literature. Note the scattered, yet statistically significant correlation between Th and U. The Th/U ratio may be variable among different lithologies formed in different tectonic settings (see the inset: G1 – rocks of basaltic protolith from group 1, OIB-like; G3 –rocks of basaltic protolith from group 3, N-MORB-like; sedi. – rocks of sedimentary protoliths). The super-composite of Ocean Drilling Program Site 801 in Kelley *et al.* (2003), representing the tholeiitic section of ocean crust, is also plotted (AOC_{sup}). (b) Th – U for epidote group minerals in HP-UHP metamorphic rocks from Western Tianshan, whose bulk-rock compositions are also plotted in (a).

Our *in situ* LA-ICP-MS analytical data of mineral compositions for these HP-UHP metamorphic rocks from these two HP-UHP sample suites revealed that: (1) lawsonite, apatite and epidote group minerals are, to varying extents, the primary hosts for REEs (mainly LREEs), Sr, Pb, Th and U; (2) pumpellyite and garnet are important for HREEs; (3) white micas (phengite and paragonite) are major hosts for Ba, Cs, Rb and to a lesser extent, Pb and Sr; (4) Ti-bearing minerals (rutile and titanite) and unanalyzed zircon are essentially the sole hosts for HFSEs; titanite could also host some REEs.

Both the petrography and elemental analysis of the HP and UHP rocks have revealed that the presence and stability of the above mentioned minerals (which may even exist as accessory minerals) exert the primary controls on the geochemical behaviors of these elements during SZM (also see Hermann & Rubatto, 2009; El Korh *et al.*, 2009). Specifically, the immobility of

HFSEs, REEs, Th and U is controlled by the stability of their host minerals under one condition, and by the newly formed minerals that are also stable (e.g., rutile, allanite) during SZM, as underpinned, for example, by the statistically significant U-Th correlations in Figure 7.2. These newly-formed minerals thus selectively carry their preferential elements into greater depths until their potential breakdown/dissolution if they become unstable and if there were no further stable host phases form. The different geochemical behavior of Ba, Rb and Cs in meta-sedimentary rocks (immobile) vs. meta-basaltic rocks (mobile) may be caused by the different formation timings of white mica. White micas may be inherited from the sedimentary protoliths, and thus can conserve LILEs since the beginning of SZM. On the contrary, for rocks of basaltic protoliths, white mica is of metamorphic origin; if LILEs were lost before its formation during SZM, these elements should show "inherited mobility". Based on our studies of HP-UHP metamorphic rocks from Western Tianshan and North Qilian Mountain, therefore, it is apparent that the simple dehydration of SZM rocks can only result in the mobilization of LILEs, Pb and Sr in the subducting/subducted ocean crust (with sediments), which can further lead to their enrichment in arc lavas. On the other hand, additional process(es), other than dehydration, is required to account for the enrichment of Th, U and LREEs in arc lavas (Fig. 7.1).

7.3 REVERSE MODEL: ARC SIGNATURES

Considering the higher LILEs, U and LREEs in IAB relative to those in MORB and OIB, these elements are thought to be carried by H_2O derived from subducting ocean crust (possibly with the overlying sediments; e.g., Cervantes & Wallace, 2003). On the other hand, HFSE and HREE depletions may originate in the depleted mantle wedge (e.g., McCulloch & Gamble, 1991; Ayers & Watson, 1993; Walker *et al.*, 2001) and/or originate in the subducting slab (e.g., Plank & Langmuir, 1993; Turner *et al.*, 1996; Turner & Hawkesworth, 1997; Turner & Foden, 2001; Hawkesworth *et al.*, 1997; Becker *et al.*, 2000; Walker *et al.*, 2001). U was thought to be readily mobilized in fluids in the form of U^{6+} under oxidized conditions (Bailey & Ragnarsdottir, 1994),

while Th is much more incompatible than U in melting processes involving rutile-bearing eclogites, i.e., D_U = 0.015 and D_{Th} = 0.0017 (see Beattie, 1993; LaTourrette *et al.*, 1993; Klemme *et al.*, 2005), e.g., ~ 30% Th in subducting oceanic sediments have been recycled through melting and constitute ~ 90% of the Th in arc lavas (Hawkesworth *et al.*, 1997). Since the different elemental behaviors between Th and U, the U/Th ratio will be increased in arc magmas that have been affected by the aqueous fluids derived from the subducting slab rocks, e.g., Marianas, South Sandwich Islands, Tonga-Kermadecs, and Vanuatu summarized by Hawkesworth *et al.* (1997).

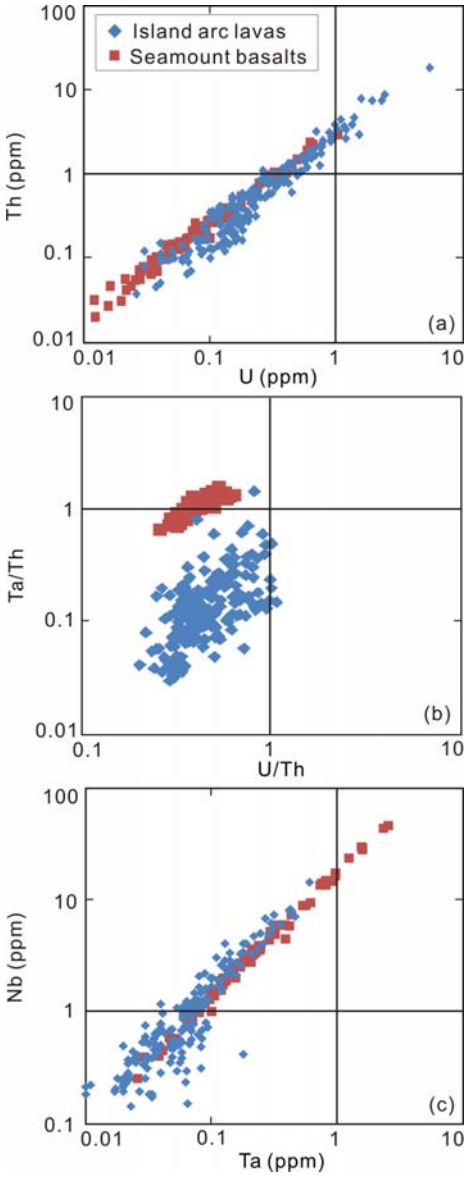

Figure 7.3 Comparison between arc basalts (Elliott, 2003) and near-ridge seamount MORB lavas (Niu & Batiza, 1997). (a) Th vs. U. (b) U/Th vs. Ta/Th. (c) Nb vs. Ta. (a,c) show linear correlation between Th and U, Nb and Ta in arc magmas, which are significantly similar to seamount MORB lavas. It follows that U is as immobile as Th during arc magmatism, although the geometric average of the Th/U ratio may be different (i.e., the slope of their linear correlation in [a], 3.39 in arc magmas vs. 3.13 in seamount basalts; for Nb/Ta in [c], 19.95 in arc magmas vs. 18.20 in seamount basalts; the arithmetic average of Th/U ratios has also been given in the relevant text). The similar trend between Ta/Th ratio and U/Th ratio in IAB to those in seamount MORB lavas in (b), consistent with the similarly less incompatibility of U and Ta than Th ($D_{Nb} \approx D_{Th} < D_{Ta} \approx D_U$; Niu & Batiza, 1997), further indicates that U shows similar geochemical behaviors for the generation of IAB, like HFSEs and Th, controlled by magmatic processes. Moreover, the similar range of U/Th ratio in arc magmas to those in seamount basalts also suggests that U shows the similar geochemical behaviors to Th for the generation of IAB, rather than its distinctive mobility caused by the dehydration during subduction-zone metamorphism. The obviously lower Ta/Th ratio range in arc magmas than those in seamount MORB lavas indicates the lower content of Ta in the source of arc magmas.

Th in arcs magmas, including those taken as the product induced by the dehydration of the subducting slab (see Hawkesworth *et al.*, 1997), however, shows statistically significant correlation with U like that in seamount MORB lavas (Fig. 7.3a; see data for IAB in Elliott [2003] and data for seamount MORB lavas in Niu & Batiza [1997]), although the Th/U ratios are different (3.39 in arc magmas vs. 3.13 in seamount basalts, read from the slope of the regression line in Fig. 7.3a). Furthermore, the similar trend of U/Th vs. Ta/Th in arc magmas with those in seamount basalts (Fig. 7.3b), together with the similar trend of Nb and Ta (Fig. 7.3c), indicates that U, Th and HFSEs do have the same immobility during the petrogenesis of IAB, and may be controlled by magmatic processes in subduction zones, but not by the dehydration during subduction-zone metamorphism. The obviously lower Ta/Th ratios in arc magmas within the similar U/Th ratio range relative to those in the seamounts (Fig. 7.3b), suggests the lower Ta contents resulted from the magmatic process for the formation of arc magmas than those for MORB. The mantle wedge is made up of depleted mantle peridotite, and its composition is assumed to resemble the mantle source for MORB. Therefore, the mantle wedge cannot supply a melt with arc signature, including the depletion of HFSEs.

7.4 IMPLICATIONS AND FUTHER PROBLEMS

Hydrous melts (or SiO_2-rich fluids, H_2O < 35 wt.%; e.g., Hermann *et al.*, 2006; Hermann & Rubatto, 2009) or supercritical fluids/transitional fluids beyond the second critical point (where the closure of the fluid-melt solvus intersected with the fluid-saturated solidus, Schmidt *et al.*, 2004a; see section 1.3.4 for detailed description of supercritical fluid under SZM conditions) derived from the subducting/subducted ocean crust and/or overlying sediments have been used in recent years to explain the petrogenesis of IAB (e.g., Schmidt *et al.*, 2004a; Kessel *et al.*, 2005; Stern *et al.*, 2006; Mibe *et al.*, 2011). These studies show that the melting processes involving rutile-bearing eclogites can lead to the 'arc signatures' including the depletion of HFSEs in IAB with rutile present as a residual phase.

The average subduction depth of ocean crust beneath the arc is ~ 100 km (Tatsumi & Kogiso, 2003); typically ranging from 70 km to 170 km (Syracuse & Abers, 2006). Although our samples from Western Tianshan, have subducted to a depth of no less than 75 km from a cold subduction zone, they experienced only dehydration without showing melting phenomenon (similar case to our samples from North Qilian Mountain). Hence, these samples can only represent the geochemical consequences of dehydration during SZM. Because of the immobility of U like Th and HFSEs observed in our HP-UHP metamorphic rocks, considering the higher partitioning of trace elements, especially Th, U and LREEs, into supercritical fluids (e.g., Kessel *et al.*, 2005) or hydrous melts than aqueous fluids (e.g., Hermann & Rubatto, 2009), it follows that if the enrichment of these elements in arc lavas are indeed derived from the subducting ocean crust with the overlying sediments, then supercritical fluids or hydrous melts, which may form at greater depths, rather than simple metamorphic dehydration of aqueous fluids, are required. This reasoning is consistent with the significant correlation of U with Th (Fig. 7.3a) and HFSEs (Fig. 7.3b) observed in arc magmas discussed above. This is an important conclusion that encourages reconsideration of the standard model ("fluid-flux melting") for arc magmatism. This indicates that although flux melting may be possible for the formation of arc magmas as a result of lowering solidus temperature caused by subduction-zone dehydration, other processes and mechanisms are required to be responsible for the enrichment of those not so mobilized elements in arc lavas.

On the other hand, however, if melting of rutile-bearing eclogites is indeed the case responsible for the depletion of HFSEs in arc magmas, the conservation of HFSEs by rutile will result in the complementary enrichment of these elements in the residual ocean crust after the melting. Such a residue has been reported by Becker *et al.* (2000), i.e., one mafic granulite (DIET3) from Dietensdorf (Saxonian Granulite Massif, Germany) high temperature-high pressure terraces (900 – 1000°C at 1.5 – 2.0 GPa), which contains low Ba, Rb, Pb, Sr, Th and U, but high HFSE contents (no data for Ta; Fig. 7.1). However, this is not widely observed. In addition, high $^{230}Th/^{238}U$ ratios or the positive disequilibria of $^{230}Th/^{238}U$ ratios (excess Th) have only been

found in MORB and OIB possibly caused by the $[D_U > D_{Th}]_{garnet}$ (Beattie, 1993; LaTourrette *et al.*, 1993), while lower $^{230}Th/^{238}U$ ratios in arc magmas are interpreted to be caused mainly by the mobility of U. Thus, if it is the hydrous melting derived from the rutile-bearing eclogitic rocks (subducting ocean crust and/or overlying sediments) that may have led to the subduction-zone magmatism and contributed to the arc signatures, then the high $^{230}Th/^{238}U$ ratios (i.e., excess Th vs. excess U) in arc magmas is also expected as in oceanic basalts. However, this is rarely observed (e.g., plots in Turner & Hawkesworth, 1997; Hawkesworth *et al.*, 1997). Moreover, considering the occurrence of garnet (in which HREEs are strongly compatible), hydrous melts or supercritical fluids in equilibrium with the rutile-bearing eclogites should also possess the depleted HREEs and decreased Sm/Nd ratios, but these have only been observed in adakite with different origin. Therefore, more work is required, but we proposed here with emphasis that the traditionally accepted fluid flux induced-melting model needs reconsideration in order to explain the arc signature in melts produced through subduction-zone magmatism.

CHAPTER 8:

THESIS CONCLUSIONS AND FUTURE WORK

8.1 THESIS CONCLUSIONS

In this thesis, we studied rocks of both basaltic and sedimentary protoliths from two Palaeozoic subduction zone complexes in Tianshan and Qilian Orogenic Belts, NW China. The one in Western Tianshan is an ultra-high pressure (UHP) metamorphic belt, while the other from North Qilian Mountain, is composed of two sub-belts, low grade blueschist metamorphic belt (LGB) and high grade blueschist/eclogite metamorphic belt (HGB). Based on the bulk-rock compositional data, potential protolith rock types and the tectonic settings of these protolith rocks were pointed out in the thesis.

(1) Western Tianshan:
   - I Rocks of basaltic protoliths have been classified into three groups: (1) group 1, OIB-like; (2) group 2, MORB-like contaminated/mixed with arc materials; and (3) group 3, MORB-like.
   - II Rocks of sedimentary protoliths widely resemble to the geochemical features of global oceanic subducted sediments (GLOSS).

(2) North Qilian Mountain:
   - I Low grade blueschist metamorphic belt (LGB): only rocks of basaltic protoliths are found, which possess both geochemical features of MORB and IAB. Together with evidence from the field, their protoliths may be originated from a back-arc setting.
   - II High grade blueschist/eclogite belt (HGB):
     - (a) Rocks of basaltic protoliths are also divided into three groups, i.e., group 1 and group 2 (OIB-like and MORB-like but contaminated/mixed with arc materials), and group 3 (MORB-like).
     - (b) Rocks of sedimentary protoliths, including meta-graywacke, meta-pelite (always chloritoid-bearing), meta-chert and marble, generally resemble to the geochemical features of GLOSS.

The correlation of high field strength elements (HFSEs) with other trace elements having similar incompatibility was calculated to identify the actual mobility/immobility of these elements during the subduction-zone metamorphism (SZM; especially the main dehydration process caused by eclogization). The elements showed highly consistent mobility/immobility for samples from two field areas.

(1) Mobile elements in both lithologies (meta-sedimentary and meta-basaltic rocks): Pb and Sr.

(2) Immobile elements in both lithologies: Th, U (although the seafloor alteration can lead to the mobility of U to different extents), rare earth elements (REEs) and HFSEs.
(3) Ba, Rb, Cs and K (large ion lithophile elements, LILEs) are mobilized in rocks of basaltic protoliths, but immobile in rocks of sedimentary rocks.

Using innovative method developed by Liu et al. (2008), we also reported the trace element concentrations in different metamorphic minerals using LA-ICPMS. Together with the estimated mineral modes, including the point counting results for rocks from Western Tianshan, we reconstructed the trace element budgets in bulk rocks and revealed the significant mineral phases for hosting different elements during subduction-zone metamorphism.

(1) Ba, Rb, Cs and K: almost all hosted by phengite and paragonite.
(2) HFSEs: entirely hosted by rutile and titanite.
(3) Heavy (H-)REEs: pumpellyite may be the most important host for HREEs at low grade metamorphic conditions; garnet and epidote group minerals became more important and replaced pumpellyite at higher grade metamorphic conditions; titanite is also important, especially if garnet is absent or instable, e.g., at greenschist facies.
(4) Light (L-)REEs, Th and U: the most significant host for these elements is epidote group minerals, especially allanite; lawsonite may be more important for hosting these elements during early stage of oceanic crust subduction, considering its lower stable temperature; apatite and titanite to a lesser extent.
(5) Pb and Sr: epidote group minerals are the most important host for these two elements; titanite, apatite, and paragonite are also capable to carry some, carbonate and albite to a lesser extent.

Furthermore, together with the detailed petrographic study, we also revealed the significant control of different minerals on the elemental mobility/immobility in response to the specific metamorphic history.

(1) The different geochemical behaviors of LILEs have been attributed to the different appearance timing of phengite in meta-basaltic rocks (of metamorphic origin) and meta-sedimentary rocks (inherited from the protolith rocks and recrystallized). Therefore, if LILEs were lost before the formation of phengite during SZM, these elements should show "inherited mobility".
(2) The similar immobility of U like that of Th and HFSEs, is most likely caused by its

conservation by epidote group minerals, including allanite.

The mobility of LILEs, Sr and Pb allow these elements to be carried by the aqueous fluids and led to the characteristic arc signatures through the fluid-induced partial melting. However, the immobility of Th, U and LREEs in this study means that they cannot be carried by the dehydrated aqueous fluids from the subducting/subducted slab, and thus cannot be responsible for the enrichment of these elements in arc magmas. If the enrichment of these elements in arc magmas really originated from the subducting ocean crust and overlying sediments, there must be some other mechanisms (forming supercritical fluids beyond the second critical endpoint or hydrous melting) leading to these enrichment.

On the other hand, alteration during SZM will result in the absence of correlations between Rb/Sr (and possibly U/Pb) and Sm/Nd or Lu/Hf, which, with time, will lead to similarly poor correlations between $^{87}Sr/^{86}Sr$ (or $^{206}Pb/^{204}Pb$) and $^{143}Nd/^{144}Nd$ or $^{176}Hf/^{177}Hf$ in the residual slab materials subducted in the deep mantle. Therefore, although altered ocean crust (AOC) is expected to contribute to mantle compositional heterogeneity, it cannot be the major source materials for oceanic basalts because subduction-zone-processed residual ocean crust will result in Rb-Sr decoupling and hence Sr-Nd and Sr-Hf isotopic decoupling, which cannot explain the first order Sr-Nd-Hf isotope correlations defined by oceanic basalts, in particular OIB.

8.2 FUTURE WORK

(1) As Gao *et al.* (2007) found the occurrence of needle-like rutile crystals preserved in high-pressure segregation and transport vein in eclogites from Western Tianshan, China, they argued the mobility of Ti, Nb and Ta during the dehydration process with the transition from blueschist to eclogite in a high fluid flux system. Therefore, the further field works on the vein-wall rock system will be done:
   - I to reveal if the difference between the geochemical consequences of high fluid flux vs. low fluid flux system, especially for the geochemical behaviors of U, Th, REEs and HFSEs during subduction-zone metamorphism;
   - II to constrain the fluid compositions in subduction zones;
   - III to quantify the extent of elemental mobility.

(2) The controls on the immobility of U. U is widely accepted to be immobile in the form of

U^{4+}, while mobile in the form of U^{6+} (Bailey & Vala Ragnarsdottir, 1994). Therefore, the mobility/immobility of U is considered as an indicator of the redox condition. Unlike the reduced condition in the source of MORB and OIB, subduction zones are thought to be under an oxidized condition and thus U is expected to be mobilized. However, in this study, U shows obviously immobility as evidenced by its significant correlation with HFSEs and Th during subduction-zone metamorphism. Furthermore, U is largely hosted by epidote group minerals and lawsonite, and thus the geochemical behavior of U may be controlled by minerals, rather than dehydrated aqueous fluids in oxidized conditions.

APPENDIX A:

BASIC CONCEPT AND GENERAL INFORMATION USED IN THE THESIS

Table A.1 The ratio of radioactive parent (P)/radiogenic daughter (D) and related radiogenic isotope ratios in different OIB end-members

Isotope ratio P/D ratio	$^{87}Sr/^{86}Sr$ Rb/Sr	$^{143}Nd/^{144}Nd$ Sm/Nd	$^{206}Pb/^{204}Pb$, $^{208}Pb/^{204}Pb$ U/Pb, Th/Pb	Examples*
DM	Very low	Very high	Very low	
HIMU	Low	High	Very high	St.Helena, Old Rurutu, Mangaia, Tubuai
EM I	High	Low	Low	Tristan da Cunha, Gough, Pitcairn
EM II	Very high	Very low	High	Samoa-Malumalu & Savai'i, Society-Tahaa & Moorea & Huahine, Marquesas-Tahuata & Ua Pou, Azores-Sao Miguel

*OIB examples are referred to Willbold & Stracke (2006).

Table A.2 Comparison between intra-oceanic- and continental-type subduction-zone metamorphism

	Oceanic type	Continental type
Feature	· Low temperature blueschist and eclogite (normally T < 550°C) · Ophiolite suite · Island-arc igneous sequence · Mélange	· Mediate to high T eclogite (T > 600°C); ultrahigh pressure metamorphism more likely · Granitic gneiss (~ 80 vol.%) · Paragneiss (meta-pelite and white schist) · Garnet peridotite; Jadeite quartzite
Example	· Circum Pacific · West Alps to Turkey · North Qilian Mountains · Western Tianshan · PuertoRico	· Dabie-Sulu, Central-East China · Western Gneiss Region in Norway, Western Alps · North Qaidam, China · Ivrea zone, Italy

Table A.3 H_2O contents in major hydrous minerals in subduction zones (after Schmidt & Poli, 2003)

Mineral	Chemical formula	H_2O (wt.%)	Pelite/ graywacke	Basalt	Meta-gabbro	Peridotite
Phengite	$K(Mg,Fe)_{0.5}Al_2Si_{3.5}O_{10}(OH)_2$	4.3	+++*	+*	-	-
Biotite/ Phlogopite	$K(Mg,Fe)_{2.8}Al_{1.4}Si_{2.8}O_{10}(OH)_2$	4.1	++*	+	-	-
Paragonite	$NaAl_3Si_3O_{10}(OH)_2$	4.6	+	++	+	-
K-richterite	$KCa(Mg,Fe)_4AlSi_8O_{22}(OH)_2$	2.0	-	-	-	+
Glaucophane - barroisite	$NaCa(Mg,Fe)_3Al_3Si7O_{22}(OH)_2$ – $Na_2(Mg,Fe)_3Al_2Si_8O_{22}(OH)_2$	2.2	+	+++	+++	-
Hornblende - pargasite	$Ca_2(Mg,Fe)_4Al_2Si_7O_{22}(OH)_2$ – $NaCa_2(Mg,Fe)_4Al_3Si_6O_{22}(OH)_2$	2.2	-	+++	+++	+
Lawsonite	$CaAl_2Si_2O_7(OH)_2•H_2O$	11.2	+	++	++	-
Zoisite/ epidote	$CaAl_2(Al,Fe^{3+})Si_3O_{12}(OH)$	2.0	+	++	++	-
Chloritoid	$(Mg,Fe)_2Al_4Si_2O_{10}(OH)_4$	7.5	++	+	++	-
Chlorite	$(Fe,Mg)_5Al_2Si_3O_{10}(OH)_8$	12.5	++	+++	+++	+
Talc	$(Mg,Fe)_3Si_4O_{10}(OH)_2$	4.8	++	+	++	+
Antigorite	$(Mg,Fe)_{48}Si_{34}O_{85}(OH)_{62}$	12.3	-	-	+	+++
Phase A	$(Mg,Fe)_7Si_2O_8(OH)_6$	11.8	-	-	?	+++
Phase E	$(Mg,Fe)_{2.2}Si_{1.1}O_{2.8}(OH)_{3.2}$	11-18	-	-	?	++
10 Å phase	$(Mg,Fe)_4Si_3O_{10}(OH)_2•H_2O$	8-14	Likely	-	Likely	+
Aragonite/ calcite	$CaCO_3$		+	+	+	-
Dolomite	$CaMg(CO_3)_2$		+	+	+	+
Magnesite	$MgCO_3$		+	+	+	+

*+++: > 20 vol%; ++: 5-20 %; +: < 5 %.

APPENDIX B:

ANALYTICAL DATA QUALITY

Table B.1 Analytical results of the USGS reference standards for analysis of whole rock trace element contents at Northwest University, China

Isotope	Isotope number	Recommended value* (in ppm)				Analyzed value (in ppm)				RE (%)				RSD (%)
		AGV-2	BCR-2	BHVO-2	GSP-1	AGV-2	BCR-2	BHVO-2	GSP-1	AGV-2	BCR-2	BHVO-2	GSP-1	Duplicate samples
Li	7	11.0	9.00	4.80	31.0	11.0 ~ 11.2	9.44 ~ 9.91	4.74 ~ 4.90	30.2 ~ 31.5	0.70	7.49	0.52	-0.47	0.21 ~ 3.98
Be	9	2.30	1.60	1.10	1.40	2.24 ~ 2.32	2.34 ~ 2.54	1.14 ~ 1.17	1.28 ~ 1.36	-1.24	52.7	4.98	-5.58	0.10 ~ 3.61
Sc	45	13.0	33.0	32.0	6.20	12.9 ~ 13.5	34.2 ~ 35.6	13.4 ~ 33.0	6.55 ~ 6.94	0.85	5.86	-26.2	8.80	0.07 ~ 2.80
V	51	120	416	317	53.0	117 ~ 121	420 ~ 428	318 ~ 325	52.1 ~ 53.5	-1.49	1.85	1.50	-0.37	0.06 ~ 2.21
Cr	52	17.0	18.0	280	13.0	15.8 ~ 21.4	14.5 ~ 15.3	277 ~ 280	10.2 ~ 10.5	9.68	-17.2	-0.76	-20.5	0.08 ~ 5.13
Cr	53	17.0	18.0	280	13.0	15.0 ~ 19.9	13.7 ~ 14.0	278 ~ 283	9.43 ~ 9.58	2.35	-23.2	-0.18	-26.9	0.02 ~ 5.36
Co	59	16.0	37.0	45.0	6.60	15.7 ~ 16.6	37.9 ~ 38.5	45.2 ~ 45.9	7.13 ~ 7.29	-0.22	3.30	1.02	9.19	0.02 ~ 3.21
Ni	60	19.0	13.0	119	8.80	18.1 ~ 20.3	11.1 ~ 11.5	117 ~ 118	6.92 ~ 7.02	1.43	-13.2	-1.16	-20.8	0.16 ~ 7.69
Cu	65	53.0	19.0	127	33.0	50.3 ~ 51.4	18.5 ~ 20.1	130 ~ 133	33.6 ~ 34.7	-4.41	1.64	2.93	3.53	0.19 ~ 2.85
Zn	66	86.0	127	103	104	85.6 ~ 87.1	127 ~ 131	98.7 ~ 103	100 ~ 102	0.18	1.77	-1.78	-2.93	0.03 ~ 1.37
Ga	71	20.0	23.0	21.7	23.0	20.5 ~ 21.0	22.0 ~ 22.4	21.2 ~ 21.6	25.5 ~ 26.9	3.27	-3.29	-1.43	13.9	0.18 ~ 1.03
Ge	74	0.00	0.00	1.60	1.36	1.18 ~ 1.23	1.57	1.60 ~ 1.64	1.75 ~ 1.81	-	-	0.69	31.0	0.23 ~ 1.68
Rb	85	68.6	48.0	9.80	254	68.7 ~ 70.7	48.5 ~ 49.5	8.80 ~ 9.89	256 ~ 263	1.52	2.07	-4.32	2.14	0.10 ~ 5.25
Sr	88	658	346	389	234	653 ~ 669	337 ~ 345	390 ~ 399	231 ~ 234	0.17	-1.38	1.29	-0.69	0.15 ~ 1.53
Y	89	20.0	37.0	26.0	26.0	20.0 ~ 21.9	36.4 ~ 39.5	22.5 ~ 28.9	27.3 ~ 29.9	5.36	2.66	-1.83	9.94	0.09 ~ 1.30
Zr	90	230	188	172	530	232 ~ 237	187 ~ 188	169 ~ 172	637	1.64	-0.16	-0.69	20.2	0.47 ~ 3.30
Nb	93	14.5	13.2	18.1	27.9	14.0 ~ 14.4	12.3 ~ 12.7	18.5 ~ 18.8	27.9 ~ 28.3	-2.22	-5.55	2.82	0.74	0.10 ~ 3.09
Cs	133	1.16	1.10	0.10	1.02	1.15 ~ 1.18	1.17	0.10 ~ 0.11	1.02	0.36	6.08	5.34	0.18	0.22 ~ 2.57
Ba	135	1140	683	130	1310	1137 ~ 1159	691 ~ 702	131 ~ 135	1317 ~ 1348	0.48	2.01	2.53	1.70	0.10 ~ 1.32

(Continued)

Table B.1 (continued)

Isotope	Isotope number	Recommended value (in ppm)				Analyzed value (in ppm)				RE (%)				RSD (%)
		AGV-2	BCR-2	BHVO-2	GSP-1	AGV-2	BCR-2	BHVO-2	GSP-1	AGV-2	BCR-2	BHVO-2	GSP-1	Duplicate samples
La	139	38.0	25.0	15.0	184	38.2 ~ 38.8	25.8 ~ 26.2	14.5 ~ 16.1	182 ~ 185	1.58	4.08	2.06	-0.27	0.01 ~ 3.04
Ce	140	68.0	53.0	38.0	399	69.3 ~ 70.7	53.8 ~ 54.5	36.6 ~ 39.3	433 ~ 445	2.86	2.18	-0.56	9.98	0.11 ~ 2.75
Pr	141	8.30	6.80	5.29	52.0	8.37 ~ 8.50	6.92 ~ 7.12	5.22 ~ 5.61	54.6 ~ 57.1	1.33	3.20	1.82	7.43	0.17 ~ 1.43
Nd	146	30.0	28.0	25.0	196	30.9 ~ 31.3	29.3 ~ 29.5	23.9 ~ 25.5	203 ~ 212	3.87	5.02	-1.45	5.90	0.14 ~ 1.10
Sm	147	5.70	6.70	6.20	26.3	5.75 ~ 5.84	6.90 ~ 6.95	6.12 ~ 6.50	26.8 ~ 27.6	1.71	3.34	1.45	3.27	0.13 ~ 1.26
Eu	151	1.54	2.00	2.07	2.33	1.60 ~ 1.62	2.03 ~ 2.04	2.01 ~ 2.14	2.31 ~ 2.37	4.39	1.77	0.01	0.41	0.04 ~ 1.61
Gd	157	4.69	6.80	6.30	12.1	4.91 ~ 4.99	7.06 ~ 7.18	6.09 ~ 6.59	14.4 ~ 14.8	5.40	4.75	0.06	20.9	0.10 ~ 1.02
Tb	159	0.64	1.07	0.90	1.34	0.64 ~ 0.65	1.07	0.89 ~ 0.95	1.39	0.62	-0.19	2.63	3.88	0.17 ~ 1.30
Dy	161	3.60	6.41	5.31	5.50	3.63 ~ 3.67	6.66	5.28 ~ 5.58	6.33 ~ 6.41	1.26	3.90	2.06	15.8	0.01 ~ 1.85
Ho	165	0.71	1.33	1.04	1.01	0.72 ~ 0.73	1.41 ~ 1.44	1.02 ~ 1.08	1.04 ~ 1.05	2.05	7.11	1.01	3.68	0.08 ~ 2.01
Er	166	1.79	3.66	2.54	2.70	1.84 ~ 1.88	3.73 ~ 3.78	2.47 ~ 2.62	2.53	4.14	2.60	0.08	-6.33	0.06 ~ 2.55
Tm	169	0.26	0.54	0.33	0.38	0.26	0.53 ~ 0.54	0.33 ~ 0.34	0.30	0.52	-0.71	1.36	-20.7	0.06 ~ 2.66
Yb	172	1.60	3.50	2.00	1.70	1.65 ~ 1.71	3.44 ~ 3.48	1.94 ~ 2.06	1.73 ~ 1.76	4.78	-1.04	0.10	2.87	0.14 ~ 1.90
Lu	175	0.25	0.51	0.28	0.21	0.25 ~ 0.26	0.52	0.27 ~ 0.29	0.25	2.60	2.66	0.75	17.5	0.14 ~ 1.23
Hf	178	5.08	4.80	4.10	15.5	4.91 ~ 4.97	4.72 ~ 4.76	4.26 ~ 4.31	15.4 ~ 16.0	-2.79	-1.33	4.43	1.29	0.16 ~ 3.19
Ta	181	0.89	0.78	1.14	0.97	0.84 ~ 0.86	0.79 ~ 0.80	1.18 ~ 1.20	0.90 ~ 0.92	-4.25	1.93	4.62	-6.13	0.29 ~ 4.70
Pb	208	13.0	11.0	2.60	55.0	13.1 ~ 13.2	10.7 ~ 10.8	1.67 ~ 2.51	61.6 ~ 63.0	0.99	-2.09	-20.1	13.3	0.14 ~ 2.46
Th	232	6.10	6.20	1.20	106	6.58 ~ 6.67	6.44 ~ 6.61	0.80 ~ 1.39	114 ~ 119	9.38	5.17	-8.21	9.84	0.25 ~ 3.49
U	238	1.88	1.69	0.42	2.54	1.86 ~ 1.88	1.70	0.42 ~ 0.44	2.41 ~ 2.50	-0.45	0.47	2.29	-3.31	0.11 ~ 2.72

*Recommended values of element concentrations in the reference standards are from the GeoReM database (http://georem.mpch-mainz.gwdg.de/).

Table B.2 RE (%) and RSD (%) for mineral compositional analysis using LA-ICPMS determined by all the GSE-1G data

Isotope	No.	Unit	Recommonded value*	Average		RE		RSD	
				ESIS†	AYCF†	ESIS	AYCF	ESIS	AYCF
Li	7	ppm	430	430	431	-0.11	0.33	4.81	4.12
Be	9	ppm	490	490	492	0.003	0.45	3.19	2.43
Na_2O	23	wt.%	3.9092	4.00	4.02	2.44	2.90	4.30	3.84
MgO	25/24§	wt.%	3.48243	3.49	3.50	0.12	0.57	2.89	2.10
Al_2O_3	27	wt.%	12.99907	13.1	13.2	0.89	1.35	3.21	2.52
SiO_2	29	wt.%	53.69643	53.7	53.9	-0.06	0.40	1.39	0.97
P_2O_5	31	wt.%	0.016039	0.019	0.019	19.4	20.1	81.8	81.8
K_2O	39	wt.%	2.65012	2.64	2.65	-0.44	-0.001	3.46	2.48
CaO	42/43	wt.%	7.41576	7.38	7.41	-0.46	-0.02	3.39	2.39
Sc	45	ppm	530	529	531	-0.20	0.24	3.78	2.87
TiO_2	49	wt.%	0.075074	0.074	0.075	-0.82	-0.38	4.30	3.46
V	51	ppm	440	432	434	-1.84	-1.41	4.05	3.22
Cr	53/52	ppm	400	397	400	-0.71	-0.12	4.15	3.47
MnO	55	wt.%	0.076181	0.077	0.077	0.83	1.27	3.65	2.67
FeO	57	wt.%	12.69776	12.7	12.7	-0.14	0.30	3.52	2.53
Co	59	ppm	380	380	381	-0.12	0.31	3.52	2.58
Ni	60	ppm	440	438	440	-0.42	0.02	3.51	2.59
Cu	63	ppm	380	382	384	0.50	0.95	3.33	2.34
Zn	66	ppm	460	455	457	-1.03	-0.59	4.36	3.67
Ga	69	ppm	490	488	490	-0.35	0.09	3.43	2.40
Ge	72	ppm	320	321	322	0.17	0.61	3.68	2.78
Rb	85	ppm	356	356	358	0.09	0.53	4.58	3.80
Sr	88	ppm	447	450	452	0.60	1.04	4.96	4.19
Y	89	ppm	410	411	413	0.25	0.68	5.31	4.56
Zr	91	ppm	410	412	414	0.48	0.91	5.44	4.67
Nb	93	ppm	420	421	423	0.18	0.61	5.33	4.59

(Continued)

Table B.2 (continued)

Iso.	No.	Unit	Recommonded value	Average		RE		RSD	
				ESIS	AYCF	ESIS	AYCF	ESIS	AYCF
Cs	133	ppm	310	310	311	0.03	0.47	5.81	5.11
Ba	137	ppm	427	429	431	0.48	0.92	6.11	5.41
La	139	ppm	392	392	394	-0.003	0.42	6.09	5.39
Ce	140	ppm	414	415	416	0.16	0.58	6.03	5.33
Pr	141	ppm	460	460	462	0.02	0.44	5.96	5.24
Nd	143	ppm	453	453	455	0.07	0.50	6.05	5.33
Sm	147	ppm	488	488	491	0.01	0.53	6.08	5.37
Eu	151	ppm	410	410	412	-0.01	0.41	6.15	5.43
Gd	155	ppm	490	490	492	0.05	0.47	6.47	5.75
Tb	159	ppm	480	480	482	0.02	0.44	6.42	5.72
Dy	163	ppm	524	524	526	0.03	0.45	6.46	5.76
Ho	165	ppm	501	501	503	0.02	0.45	6.55	5.86
Er	166	ppm	595	595	598	0.07	0.50	7.07	6.45
Tm	169	ppm	500	500	502	0.05	0.48	6.63	5.95
Yb	173	ppm	520	520	522	0.04	0.46	6.63	5.94
Lu	175	ppm	518	518	520	0.04	0.47	6.81	6.13
Hf	178	ppm	395	395	397	0.06	0.48	6.95	6.27
Ta	181	ppm	390	390	392	0.05	0.47	6.71	6.02
Pb	208	ppm	378	378	380	0.07	0.50	6.68	6.02
Bi	209	ppm	320	320	321	0.08	0.47	6.54	5.87
Th	232	ppm	380	380	382	0.12	0.55	7.31	6.71
U	238	ppm	420	420	422	0.02	0.45	7.01	6.39
As	75	ppm	260	260	261	0.00	0.29	0.00	0.19
Sb	121	ppm	450	450	451	0.02	0.32	0.01	0.18
W	182	ppm	430	430	431	0.002	0.29	0.005	0.19

[*]Recommonded value: preferred values of elemental compositions in the GSE-1G from the GeoReM database (http://georem.mpch-mainz.gwdg.de/).

[†]ESIS: the data taking ^{29}Si as the internal standard; AYCF: the data using internal standard-independent calibration method developed by Liu *et al.* (2008).

[§]The isotopic number before the slash is used in Wuhan's lab, while the second after the slash is used in the lab of Xi'an.

RE: relative error in %; RSD: relative standard deviation in %.

Figure B.1 Comparison of mineral major element contents using SEM-EDS and LA-ICPMS calibrated by the method reported in Liu *et al.* (2008) for samples from Western Tianshan. Both selected anhydrous minerals (garnet, omphacite) and hydrous minerals (phengite, paragonite, epidote group minerals, and amphibole) have been plotted. However, for hydrous minerals, the sum of all major element contents using EDS has been normalized to 100% through excluding their H_2O content before plotting. Two diagonal lines represent the data with ±10% relative deviation, and thus the plots between these lines represent the data with relative deviations better than 10%. Most of the data points representing the value > 1 wt.% have relative deviation within 10%, which shows the reliability of our mineral major elemental data using LA-ICPMS, although the elements in a low elemental content may be not well constrained either by LA-ICPMS or EDS. This comparison indicates that the method developed by Liu *et al.* (2008) is recommendable for analyzing major element contents of anhydrous minerals.

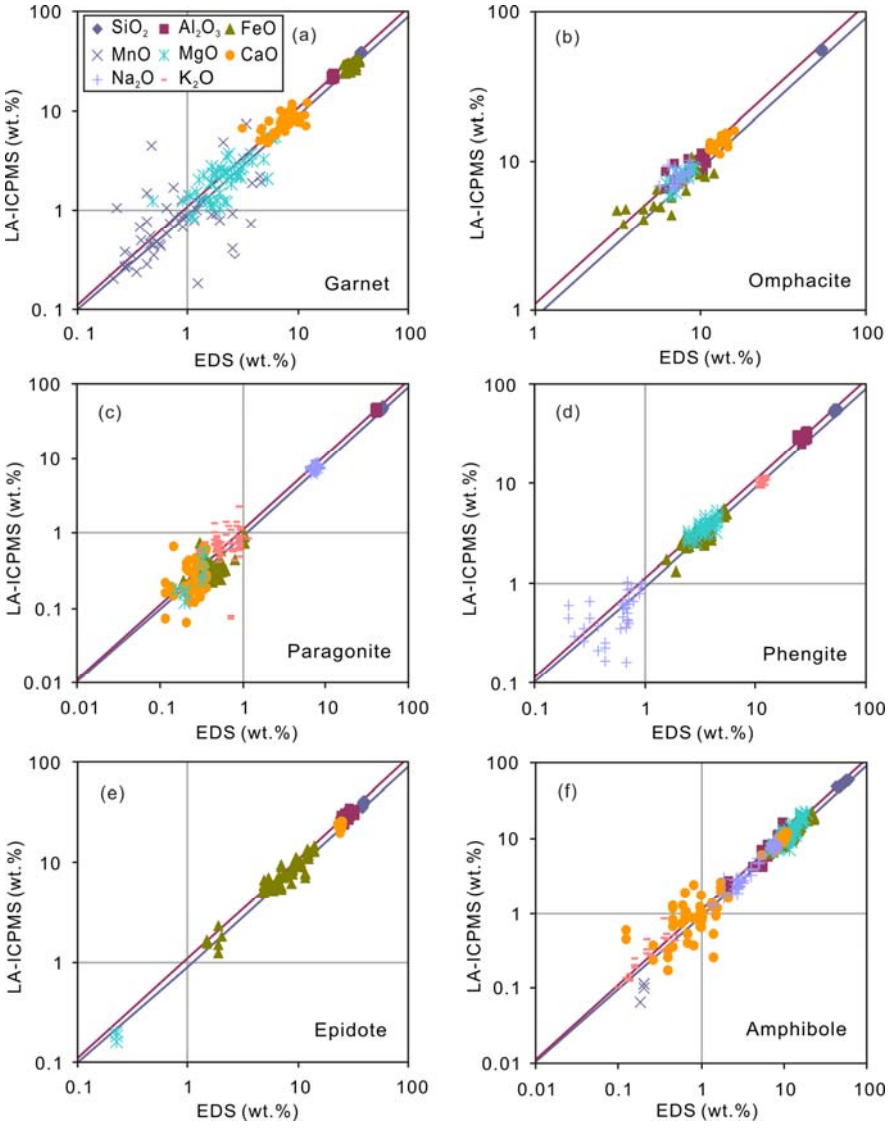

APPENDIX C:

WESTERN TIANSHAN DATA

Table C.1 Bulk-rock compositions for samples from Western Tianshan, China*

Element	Group 1											
	TS02-01	TS02-02	TS02-03A	TS02-03B	TS02-04	TS02-05	TS02-06	TS02-08	TS02-09	TS02-11	TS02-35	TS02-36
weight percent (wt.%) using ICP OES												
SiO_2	48.57	52.63	44.17	51.29	46.54	47.19	40.96	47.49	52.35	48.46	49.07	48.01
TiO_2	2.45	2.83	3.72	2.15	3.52	2.38	2.48	3.85	1.76	1.82	2.80	2.60
Al_2O_3	14.84	13.13	13.91	9.38	14.38	14.90	14.96	19.04	14.21	14.06	17.44	18.50
$Fe_2O_3^{\dagger}$	14.60	14.47	14.93	11.63	14.47	11.04	13.18	15.06	9.81	11.48	13.01	14.42
MnO	0.08	0.24	0.15	0.11	0.18	0.14	0.14	0.05	0.10	0.14	0.09	0.13
MgO	6.81	5.36	6.06	5.47	4.05	8.03	4.29	1.61	6.90	6.59	4.63	4.70
CaO	6.85	7.24	7.25	11.90	9.44	6.06	8.93	4.02	9.67	8.62	7.71	5.71
Na_2O	3.50	3.29	2.72	3.55	3.14	3.66	2.99	1.95	3.72	3.04	3.81	2.99
K_2O	1.34	0.74	1.40	0.08	1.41	1.18	3.63	2.12	0.11	1.05	1.05	2.33
P_2O_5	0.39	0.55	0.64	0.44	0.59	0.50	0.35	0.44	0.27	0.22	0.36	0.16
LOI	1.56	0.78	3.68	3.59	1.78	3.50	8.13	3.84	1.20	3.69	1.20	1.89
Total	101.0	101.3	98.63	99.59	99.50	98.58	100.0	99.47	100.1	99.17	101.2	101.5
Mg#	48.3	42.6	44.8	48.5	35.9	59.3	39.4	17.6	58.5	53.5	41.6	39.5
parts per million (ppm) using ICPMS												
Sc	35.8	28.2	26.9	16.7	25.9	19.9	25.6	30.2	24.7	27.4	29.9	48.9
V	152	96.8	120	177	168	170	226	86.0	236	184	287	318
Cr	80.0	9.54	93.4	64.8	26.1	223	206	91.9	269	210	35.9	159
Co	39.8	33.5	48.5	30.3	37.0	46.4	49.3	21.5	37.5	40.0	45.5	50.6
Cu	36.4	28.1	39.6	23.0	32.0	24.7	28.1	16.6	60.3	75.3	47.5	20.2
Zn	116	122	106	85.1	136	97.7	120	185	72.4	71.3	137	86.8
Ga	23.0	21.7	20.1	15.2	24.8	20.1	20.4	27.6	22.1	17.1	26.8	21.4
Rb	40.2	17.6	27.1	0.872	28.2	23.1	104	71.2	1.80	23.6	22.5	59.9
Sr	366	209	268	316	129	406	138	164	195	215	398	248
Y	40.2	49.9	36.6	34.7	52.0	31.5	37.1	44.7	22.1	22.0	39.0	42.2
Zr	191	271	180	152	296	157	172	231	158	132	207	182
Nb	18.2	31.6	35.1	14.9	37.6	37.3	26.9	35.0	14.9	15.9	25.0	11.2
Cs	1.01	0.753	0.776	0.040	1.61	0.784	3.98	2.40	0.139	0.914	0.619	1.66
Ba	205	190	351	9.20	359	250	771	924	35.4	141	253	705
La	23.9	32.5	31.6	19.7	33.5	34.2	27.6	28.5	22.8	16.7	27.9	11.4
Ce	52.9	71.7	69.4	43.3	74.2	71.8	60.6	66.4	47.8	36.8	65.5	29.1
Pr	7.08	9.47	9.80	6.12	10.0	9.49	8.40	9.13	6.37	5.16	8.65	4.36
Nd	30.6	40.3	42.0	26.6	43.5	37.8	34.7	39.4	26.0	22.0	36.3	20.0
Sm	7.51	9.41	10.3	6.94	10.3	8.05	7.79	9.79	5.95	5.49	8.94	5.66
Eu	2.52	2.98	3.09	2.28	3.11	2.54	2.49	3.11	1.97	1.86	2.74	2.08
Gd	7.96	9.79	10.1	6.69	10.5	7.56	7.56	9.46	5.75	5.48	8.59	6.16
Tb	1.27	1.55	1.53	1.12	1.66	1.16	1.23	1.52	0.847	0.872	1.27	1.11
Dy	7.32	8.80	8.24	6.66	9.22	6.33	7.17	8.73	4.44	4.89	7.19	7.18
Ho	1.39	1.71	1.52	1.33	1.77	1.19	1.39	1.73	0.803	0.935	1.39	1.49
Er	3.50	4.52	3.79	3.37	4.64	3.04	3.54	4.53	2.00	2.37	3.71	4.05
Tm	0.478	0.666	0.527	0.490	0.685	0.450	0.520	0.683	0.296	0.340	0.538	0.615
Yb	2.54	3.91	3.16	2.87	4.03	2.71	3.16	4.23	1.82	2.03	3.42	4.01
Lu	0.362	0.564	0.498	0.396	0.581	0.403	0.458	0.612	0.276	0.292	0.488	0.610
Hf	4.49	5.96	4.55	3.86	6.40	3.31	3.45	5.19	3.74	3.56	4.45	4.18
Ta	1.17	1.99	2.22	1.02	2.15	2.28	1.66	2.17	0.918	0.991	1.58	0.723
Pb	3.48	3.47	4.70	3.40	2.74	n.d.	2.32	9.10	3.42	2.56	3.93	1.53
Th	2.24	3.14	2.78	1.69	3.19	3.58	2.72	3.20	2.59	1.58	2.57	0.743
U	0.539	0.834	0.761	0.480	0.849	0.843	0.702	0.826	0.460	0.394	0.601	0.193
Nb/Ta	15.5	15.9	15.8	14.6	17.5	16.4	16.2	16.1	16.1	16.0	15.8	15.5
Zr/Hf	42.4	45.5	39.5	39.3	46.3	47.6	49.7	44.4	42.3	37.0	46.6	43.4

(Continued)

Table C.1 (continued)

Element	Group 1										
	TS02 -38	TS02 -41	TS02 -42	TS02 -47	TS02 -48	TS02 -99	105 -1	105 -12	106 -3A	106 -14	110 -3
weight percent (wt.%) using ICP OES											
SiO_2	49.53	46.90	47.82	46.99	47.54	47.08	47.54	47.49	47.84	41.17	49.75
TiO_2	2.25	3.80	3.31	2.40	1.62	2.21	3.02	2.86	2.44	2.40	1.76
Al_2O_3	14.04	14.06	13.38	14.82	18.44	12.89	17.88	15.51	14.53	15.27	16.22
Fe_2O_3	12.95	13.30	12.99	8.56	10.16	9.83	14.57	12.20	12.23	11.16	11.33
MnO	0.17	0.16	0.19	0.07	0.18	0.11	0.19	0.16	0.16	0.21	0.18
MgO	4.91	3.31	6.79	4.18	3.71	5.73	3.94	6.71	5.56	3.19	3.93
CaO	8.91	8.31	8.77	15.11	10.04	14.35	7.11	8.48	9.98	15.70	11.15
Na_2O	3.33	3.22	2.88	3.28	3.82	3.51	2.54	3.23	1.83	0.41	3.05
K_2O	1.15	2.26	1.04	0.12	0.36	0.32	1.92	0.93	1.24	0.07	1.63
P_2O_5	0.26	0.70	0.49	0.33	0.24	0.25	0.56	0.42	0.19	0.56	0.47
LOI	2.29	3.87	1.16	2.80	2.90	2.90	1.37	1.21	4.16	10.14	1.30
Total	99.79	99.89	98.83	98.66	99.01	99.17	100.6	99.20	100.2	100.3	100.8
Mg#	43.13	33.24	51.12	49.41	42.21	53.83	35.11	52.39	47.63	36.38	40.96
parts per million (ppm) using ICPMS											
Sc	33.5	27.4	25.6	35.4	27.2	28.5	31.3	23.9	23.0	19.6	32.5
V	301	293	305	327	201	240	285	243	217	199	239
Cr	52.9	n.d.	105	215	24.0	171	22.9	141	67.5	140	178
Co	36.6	29.3	37.3	51.2	28.6	19.4	41.4	37.6	26.0	29.7	25.0
Cu	72.4	43.6	41.2	82.4	50.6	32.3	15.6	25.2	42.1	27.9	67.9
Zn	96.7	133	114	63.1	74.3	90.1	128	104	83.6	69.5	46.5
Ga	22.9	28.6	28.7	27.3	20.2	19.0	25.5	24.7	23.8	29.5	18.5
Rb	30.4	52.6	22.8	1.90	6.80	7.10	37.1	16.5	24.4	0.952	40.7
Sr	233	134	465	656	343	342	390	326	509	1763	191
Y	38.3	61.2	49.9	30.1	28.3	22.8	50.9	36.5	45.1	34.9	29.0
Zr	198	245	196	169	148	243	175	259	218	190	139
Nb	16.3	41.3	25.5	19.9	13.8	24.3	27.4	29.4	26.8	22.6	13.9
Cs	0.776	1.37	0.478	0.100	0.281	0.207	1.03	0.715	0.922	0.054	0.926
Ba	300	545	261	32.9	68.8	87.0	819	799	570	32.3	240
La	20.2	43.7	28.8	24.4	13.2	20.3	27.8	29.2	32.0	27.1	16.2
Ce	45.2	98.0	64.7	54.0	29.4	42.9	62.8	63.6	69.4	61.5	33.6
Pr	6.05	13.0	8.85	7.14	3.96	5.66	8.40	8.40	8.94	7.99	4.61
Nd	25.4	54.2	38.1	29.7	16.9	22.6	34.8	34.2	35.6	32.9	18.9
Sm	6.41	13.1	9.62	7.07	4.30	4.83	8.31	8.01	7.89	7.93	4.45
Eu	2.11	3.93	2.92	2.42	1.50	1.55	2.78	2.64	2.61	2.52	1.45
Gd	6.92	13.3	9.40	6.89	4.60	4.91	8.59	8.18	7.99	7.38	4.39
Tb	1.14	2.09	1.52	1.02	0.804	0.728	1.46	1.24	1.30	1.18	0.744
Dy	6.76	11.6	8.76	5.71	4.92	4.00	8.83	6.72	7.62	6.70	4.61
Ho	1.31	2.10	1.68	1.08	0.97	0.76	1.73	1.29	1.55	1.22	0.926
Er	3.41	5.26	4.46	2.76	2.58	1.95	4.41	3.17	4.02	3.02	2.51
Tm	0.492	0.742	0.636	0.389	0.363	0.264	0.621	0.449	0.570	0.441	0.364
Yb	3.09	4.52	3.87	2.39	2.35	1.70	3.95	2.74	3.37	2.86	2.29
Lu	0.472	0.667	0.558	0.359	0.347	0.260	0.574	0.420	0.487	0.429	0.341
Hf	4.50	5.23	4.27	3.85	3.40	5.29	3.72	5.98	4.96	4.34	3.72
Ta	1.02	2.56	1.62	1.27	0.857	1.65	1.66	1.83	1.60	1.60	0.830
Pb	2.48	2.86	4.94	4.06	2.53	3.59	3.37	3.27	3.50	17.2	2.52
Th	1.84	4.65	2.87	2.11	1.20	2.07	2.65	3.31	4.64	3.20	1.46
U	0.537	1.30	0.794	0.655	0.427	0.519	0.598	0.815	0.842	1.07	0.167
Nb/Ta	15.9	16.1	15.7	15.7	16.0	14.7	16.5	16.1	16.7	14.1	16.8
Zr/Hf	44.1	46.8	46.0	43.9	43.4	46,0	47.1	43.3	43.9	43.9	37.3

(Continued)

Table C.1 (continued)

Element	Group 2											
	TS02-12	TS02-15A	TS02-15B	TS02-23	TS02-26	TS02-27	TS02-28	TS02-29	TS02-30	TS02-43	TS02-46	TS02-50B
weight percent (wt.%) by ICP OES												
SiO_2	49.06	46.88	46.99	46.65	47.79	48.61	46.24	52.65	48.26	49.88	52.92	46.17
TiO_2	1.00	2.78	2.80	0.59	1.06	0.96	0.83	0.74	0.94	1.55	0.79	0.97
Al_2O_3	17.80	13.23	13.49	15.02	13.94	13.21	14.84	14.98	17.06	13.88	17.20	15.26
Fe_2O_3	11.92	18.39	18.50	7.77	12.25	11.80	10.17	7.03	8.59	15.48	9.55	9.45
MnO	0.16	0.32	0.34	0.13	0.22	0.17	0.18	0.11	0.12	0.24	0.16	0.14
MgO	6.15	4.15	4.39	7.52	6.99	8.56	7.61	5.73	6.60	5.35	5.66	4.80
CaO	5.46	8.62	8.52	12.15	11.79	10.40	13.58	9.96	12.24	9.91	7.90	14.19
Na_2O	5.25	3.09	3.04	2.78	3.46	2.68	3.75	4.84	3.58	3.04	4.77	3.41
K_2O	0.18	0.17	0.31	0.43	0.19	0.20	0.11	0.44	0.59	0.11	0.35	0.19
P_2O_5	0.13	0.88	0.93	0.09	0.08	0.13	0.07	0.14	0.07	0.13	0.07	0.17
LOI	1.72	0.32	0.76	5.94	1.84	1.92	3.16	2.11	1.49	0.41	1.47	5.60
Total	98.82	98.83	100.1	99.06	99.61	98.64	100.6	98.72	99.52	99.98	100.8	100.4
Mg#	50.79	31.10	32.19	65.94	53.30	59.20	59.95	61.98	60.58	40.88	54.25	50.40
parts per million (ppm) by ICPMS												
Sc	43.8	39.0	38.9	36.8	47.7	44.2	47.4	34.8	48.2	47.2	41.3	35.9
V	344	201	218	251	295	279	280	221	312	421	264	291
Cr	n.d.	n.d.	n.d.	156	89	101	430	215	490	n.d.	153	302
Co	34.5	36.4	33.6	38.4	34.5	41.5	36.6	29.4	31.2	43.9	38.2	33.7
Cu	145	76.9	43.9	75.0	33.7	46.2	69.1	35.4	52.9	72.6	120	56.9
Zn	63.1	140	133	60.7	81.8	86.1	78.5	48.3	54.6	103	74.3	68.0
Ga	15.8	21.7	23.6	14.4	15.3	14.3	13.9	16.3	17.4	19.0	15.4	16.8
Rb	1.15	6.09	14.0	10.0	3.44	3.98	1.17	16.6	22.1	2.04	5.94	3.83
Sr	218	91.4	97.2	143	73.5	151	171	96.4	154	95.2	157	341
Y	17.7	91.0	93.4	22.4	37.8	31.5	26.9	24.6	29.7	47.0	17.6	31.2
Zr	50.4	119	149	29.2	76.2	67.2	41.3	86.1	43.7	104	54.8	54.5
Nb	2.09	9.49	9.21	1.04	2.45	2.20	1.20	2.58	1.15	1.56	1.54	1.77
Cs	0.173	0.673	1.42	0.556	0.140	0.204	0.238	0.178	2.39	0.192	0.300	0.559
Ba	23.6	35.3	86.1	77.6	70.5	43.3	11.4	78.0	209	24.1	111	314
La	6.11	17.0	15.9	3.15	5.54	5.45	3.01	11.5	3.33	3.33	4.09	3.07
Ce	14.1	45.0	41.1	7.17	12.5	12.5	7.65	23.9	8.23	10.7	9.70	8.61
Pr	2.24	7.80	7.11	1.09	1.77	1.75	1.24	3.07	1.34	1.97	1.48	1.46
Nd	10.6	40.5	37.1	5.43	7.99	7.78	6.36	12.6	6.96	10.6	7.05	7.57
Sm	3.18	13.0	11.9	2.04	2.62	2.51	2.37	3.30	2.58	4.01	2.22	2.72
Eu	1.12	4.60	4.30	0.812	0.913	0.833	0.915	0.906	0.953	1.42	0.792	1.10
Gd	3.53	16.8	15.2	2.84	3.71	3.48	3.13	3.71	3.31	5.24	2.49	3.55
Tb	0.564	3.03	2.71	0.545	0.812	0.702	0.608	0.630	0.647	1.06	0.438	0.722
Dy	3.31	19.1	17.1	3.74	5.66	4.90	4.13	3.98	4.49	7.17	2.81	4.70
Ho	0.700	4.03	3.59	0.801	1.26	1.07	0.920	0.817	1.01	1.60	0.600	1.01
Er	2.01	11.2	9.85	2.22	3.57	3.06	2.64	2.34	2.90	4.58	1.72	2.88
Tm	0.323	1.72	1.50	0.350	0.552	0.481	0.413	0.360	0.434	0.725	0.269	0.442
Yb	2.08	11.0	9.54	2.39	3.63	3.21	2.74	2.41	2.85	4.84	1.80	2.88
Lu	0.324	1.72	1.50	0.479	0.575	0.492	0.430	0.470	0.417	0.759	0.279	0.432
Hf	1.51	3.78	4.29	0.894	2.03	1.83	1.19	2.21	1.25	2.77	1.50	1.38
Ta	0.118	0.610	0.584	0.060	0.172	0.155	0.079	0.192	0.073	0.103	0.092	0.111
Pb	2.43	1.52	1.51	2.28	2.82	1.92	1.19	8.14	2.45	1.49	2.68	4.05
Th	0.807	1.45	1.26	0.425	1.61	2.09	0.382	3.68	0.425	0.220	0.678	0.229
U	0.261	0.445	0.380	0.277	0.564	0.472	0.190	0.986	0.210	0.070	0.342	0.240
Nb/Ta	17.4	15.6	15.9	17.3	14.4	14.7	15.0	13.6	16.4	15.6	17.1	16.1
Zr/Hf	33.4	31.5	34.7	32.8	37.5	36.7	34.7	39.0	35.0	37.4	36.5	39.5

(Continued)

Table C.1 (continued)

Element	Group 2						Group 3						Ultramafic
	TS02-53	TS02-54	TS02-55	TS02-57	TS02-58A	984-1	117-1	TS02-16	TS02-17b	TS02-20	TS02-32A	TS02-33	TS02-34
weight percent (wt.%) using ICP OES													
SiO_2	53.1	46.4	44.4	43.9	46.4	41.06	48.1	47.4	52.9	46.5	46.4	51.32	34.01
TiO_2	0.79	1.04	1.23	0.97	0.96	0.72	0.80	2.27	1.58	1.56	1.71	1.34	1.56
Al_2O_3	13.8	13.8	15.2	13.7	12.2	13.70	10.7	11.24	11.71	14.0	13.6	12.68	18.19
Fe_2O_3	11.03	9.43	11.20	10.2	10.2	7.89	11.76	22.6	15.3	18.1	16.6	14.10	27.33
MnO	0.18	0.14	0.19	0.19	0.15	0.14	0.14	0.31	0.20	0.30	0.26	0.22	0.69
MgO	5.14	5.86	6.70	5.98	5.81	3.95	5.99	4.84	4.93	6.02	6.62	5.62	3.51
CaO	7.29	14.5	12.0	14.3	14.0	19.82	14.8	9.82	9.65	10.8	11.33	10.10	10.33
Na_2O	3.83	4.68	2.13	3.53	4.78	2.92	3.38	1.70	3.06	2.19	2.60	2.95	0.19
K_2O	0.10	0.11	0.19	0.07	0.02	0.04	0.06	0.07	0.06	0.20	0.08	0.27	0.08
P_2O_5	0.13	0.12	0.14	0.18	0.05	0.09	0.07	0.16	0.12	0.13	0.10	0.11	0.07
LOI	4.83	4.83	5.11	6.20	4.38	10.22	4.13	0.23	0.69	0.34	0.19	0.39	5.46
Total	100.	101.	98.6	99.3	99.1	100.6	100.	100.	100.	100.	99.6	99.09	101.4
Mg#	48.2	55.4	54.4	53.9	53.2	50.04	50.4	29.9	39.1	39.8	44.2	44.36	20.44
parts per million (ppm) using ICPMS													
Sc	37.3	46.5	47.1	41.5	45.6	35.4	43.3	52.0	46.7	53.5	54.0	50.4	74.7
V	291	315	336	301	312	263	332	827	504	515	456	346	339
Cr	3.67	441	315	462	517	459	-	28.2	26.3	13.4	35.5	64.6	142
Co	36.8	48.0	42.6	45.0	48.5	29.7	37.3	56.1	49.3	52.5	44.7	43.9	47.3
Cu	88.0	74.8	84.7	78.5	91.6	36.2	30.2	114	51.7	92.3	85.7	24.8	6.46
Zn	121	94.6	76.0	67.1	84.4	68.5	102	160	86.3	113	120	89.9	165
Ga	16.0	14.8	15.5	14.8	14.7	17.0	17.7	20.2	20.5	19.6	17.1	18.4	13.5
Rb	1.93	1.08	2.10	0.55	0.74	2.58	0.61	1.07	0.34	11.6	0.42	4.95	1.1
Sr	145	131	169	196	89.7	318	87.0	60.6	36.8	128	125	123	135
Y	24.4	27.1	36.3	30.1	19.1	22.1	26.4	57.6	43.9	55.0	43.0	45.9	161
Zr	51.3	57.8	72.5	55.0	63.7	45.6	42.4	103	86.5	79.3	79.3	84.2	94.3
Nb	0.96	2.21	1.82	1.92	3.11	1.12	0.49	1.17	0.91	1.09	0.73	0.940	1.43
Cs	0.28	0.37	0.26	0.17	0.23	0.363	0.115	0.32	0.02	0.69	0.05	0.172	0.150
Ba	141	16.1	26.3	12.3	10.5	7.50	5.06	8.78	1.56	51.4	10.8	76.2	11.4
La	2.58	2.46	2.50	2.11	1.77	2.70	1.16	2.19	2.13	2.08	1.79	2.38	3.90
Ce	6.74	6.82	7.86	5.92	5.10	7.52	4.04	8.17	8.18	7.62	6.23	8.33	8.43
Pr	1.12	1.16	1.46	1.05	0.85	1.29	0.80	1.63	1.64	1.51	1.22	1.62	1.30
Nd	5.62	6.06	7.86	5.56	4.34	6.65	4.62	9.46	9.47	8.74	7.10	9.29	6.27
Sm	1.99	2.17	2.93	2.13	1.48	2.28	1.96	4.15	3.78	3.6	2.84	3.66	2.73
Eu	0.68	0.78	1.10	0.84	0.54	0.858	0.89	1.58	1.34	1.41	1.11	1.33	2.20
Gd	2.58	2.84	4.02	3.15	2.11	2.82	2.81	5.98	4.90	5.20	4.49	4.81	7.74
Tb	0.53	0.56	0.81	0.66	0.46	0.527	0.59	1.23	0.95	1.09	0.94	0.990	2.56
Dy	3.67	4.02	5.60	4.56	3.09	3.60	4.23	8.53	6.55	7.85	6.47	6.89	21.8
Ho	0.79	0.87	1.22	0.98	0.63	0.768	0.91	1.83	1.41	1.71	1.45	1.57	5.20
Er	2.36	2.51	3.47	2.87	1.64	2.15	2.58	5.05	3.89	4.85	4.17	4.45	15.5
Tm	0.38	0.39	0.55	0.44	0.23	0.354	0.41	0.81	0.61	0.77	0.68	0.702	2.53
Yb	2.48	2.60	3.59	2.99	1.49	2.51	3.01	5.57	4.25	5.42	4.18	4.67	16.7
Lu	0.40	0.40	0.53	0.45	0.23	0.401	0.49	0.88	0.67	0.85	0.64	0.713	2.44
Hf	1.46	1.48	1.82	1.41	1.71	1.24	1.25	2.74	2.33	2.03	2.29	2.30	2.64
Ta	0.05	0.13	0.12	0.12	0.14	0.074	0.03	0.08	0.07	0.07	0.05	0.065	0.078
Pb	1.93	0.75	2.41	1.10	0.75	1.29	1.36	0.77	0.31	0.80	1.17	0.581	2.98
Th	0.39	0.20	0.13	0.15	0.19	0.209	0.05	0.13	0.10	0.09	0.08	0.110	0.056
U	0.16	0.15	0.09	0.27	0.09	0.234	0.01	0.03	0.03	0.02	0.02	0.045	0.070
Nb/Ta	16.0	17.0	14.0	16.0	20.7	16.0	16.3	13.0	13.0	15.6	14.8	13.4	17.9
Zr/Hf	35.1	39.1	39.8	39.0	37.3	36.8	33.9	37.6	37.1	39.1	34.6	36.6	35.7

(Continued)

Table C.1 (continued)

Element	Meta-sedimentary rocks									
	TS02 -10	TS02 -13	TS02 -14	TS02 -18	TS02 -19	TS02 -52	TS02 -56	TS02 -62	106 -3B	986 -1
weight percent (wt.%) using ICP OES										
SiO_2	69.66	68.14	56.11	65.68	60.37	52.09	59.55	56.24	76.66	71.28
TiO_2	0.52	0.70	0.69	0.42	0.81	0.91	0.57	0.68	0.31	0.36
Al_2O_3	12.45	13.64	16.85	12.98	17.96	13.67	13.27	16.34	3.86	8.81
Fe_2O_3	4.70	5.25	9.41	7.73	7.44	12.34	5.16	7.65	4.27	3.77
MnO	0.08	0.07	0.11	0.08	0.10	0.15	0.05	0.09	0.03	0.20
MgO	2.02	2.24	4.25	2.22	3.70	4.45	3.13	4.82	3.60	1.81
CaO	1.74	2.11	3.64	1.97	1.29	7.67	5.95	3.67	6.10	5.01
Na_2O	1.81	3.25	4.24	5.12	2.36	4.48	2.10	7.35	1.58	1.23
K_2O	2.40	1.78	0.44	0.25	3.22	0.03	1.66	0.46	0.03	0.70
P_2O_5	0.17	0.22	0.17	0.12	0.16	0.09	0.12	0.14	0.15	0.05
LOI	3.84	1.71	3.63	2.41	3.51	3.61	7.21	2.05	3.38	8.22
Total	99.39	99.11	99.52	98.98	100.9	99.49	98.77	99.51	99.97	101.4
Mg#	46.23	46.05	47.46	36.49	49.87	41.91	54.82	55.76	62.78	48.99
parts per million (ppm) using ICPMS										
Sc	10.5	15.9	29.5	28.1	19.1	41.7	19.6	29.3	6.59	6.60
V	70.6	109	159	72.7	121	380	107	257	80.7	51.2
Cr	26.2	50.3	25.4	4.17	91.3	n.d.	19.7	n.d.	n.d.	11.2
Co	11.4	13.4	13.8	10.5	18.7	43.5	10.2	23.8	15.5	9.26
Cu	18.7	23.9	19.3	47.0	25.7	47.8	39.5	49.2	18.7	68.4
Zn	98.1	63.3	77.1	47.7	99.4	109	286	65.9	35.6	198
Ga	15.8	15.8	14.3	16.0	24.1	18.5	17.8	17.2	6.43	9.87
Rb	109	81.5	7.38	4.44	169	0.869	36.4	3.82	0.895	28.6
Sr	105	192	202	63.2	173	170	122	76.5	129	369
Y	25.8	28.1	20.7	23.0	35.9	31.4	12.7	13.9	12.6	42.8
Zr	176	309	74.2	71.0	189	69.4	134	57.3	33.1	105
Nb	10.7	13.0	4.51	3.43	15.4	1.19	4.45	1.69	3.24	9.08
Cs	4.93	3.56	0.272	0.362	7.57	0.106	2.05	0.348	0.040	1.16
Ba	599	455	620	68.0	902	26.5	426	114	19.5	129
La	37.9	32.7	8.17	6.84	44.0	3.75	7.42	4.26	15.5	25.3
Ce	72.2	70.3	16.2	14.6	86.4	9.76	15.9	10.2	33.3	57.7
Pr	8.41	8.38	2.44	2.12	10.3	1.64	2.07	1.53	4.03	7.43
Nd	30.2	31.0	10.7	9.14	36.9	8.10	8.38	6.97	15.7	28.7
Sm	5.45	6.19	2.99	2.53	7.30	2.84	1.98	1.95	3.14	6.58
Eu	1.23	1.41	1.23	0.75	1.57	0.94	0.49	0.70	0.83	1.84
Gd	4.85	5.15	3.80	2.83	6.40	3.52	1.89	2.17	2.45	6.23
Tb	0.71	0.80	0.74	0.54	1.03	0.68	0.33	0.35	0.36	1.07
Dy	4.09	4.83	4.95	3.73	6.11	4.59	2.12	2.16	2.21	6.77
Ho	0.846	0.960	1.12	0.796	1.24	1.02	0.436	0.453	0.493	1.40
Er	2.45	2.59	3.35	2.23	3.48	3.03	1.26	1.29	1.46	3.75
Tm	0.396	0.409	0.545	0.363	0.551	0.488	0.213	0.200	0.237	0.568
Yb	2.47	2.82	3.63	2.59	3.63	3.25	1.57	1.33	1.61	3.47
Lu	0.377	0.450	0.591	0.409	0.552	0.504	0.259	0.200	0.252	0.468
Hf	4.47	7.64	3.33	1.99	5.04	1.85	3.55	1.52	0.841	2.89
Ta	0.728	0.833	0.299	0.197	1.01	0.074	0.314	0.101	0.211	0.553
Pb	20.8	15.8	4.29	1.67	15.2	2.19	198	1.38	1.29	94.7
Th	10.5	9.65	3.10	1.36	14.1	0.546	4.33	0.753	1.02	6.41
U	2.12	2.45	1.09	0.651	2.48	0.216	1.14	0.545	0.263	1.50
Nb/Ta	14.6	15.6	15.0	17.2	15.2	17.0	14.4	16.9	15.4	16.5
Zr/Hf	39.4	40.4	22.2	35.7	37.5	37.5	37.7	37.7	39.4	36.5

[*] These samples were analyzed by Lavis (2005), and already published in Xiao *et al.* (2012).

[†] Fe_2O_3 - total Fe as Fe_2O_3.

ICP OES: Inductively Coupled Plasma Optical Emission Spectrometer; see Abbreviation List.

Table C.2 SEM-EDS analytical results of representative mineral compositions and formulae*

Mineral	Garnet								Omphacite						White mica								
Sample	TS02-03A		TS02-15A		TS02-17b		TS02-32A		TS02-17b	TS02-32A		TS02-41		TS02-42	TS02-3A	TS02-10		TS02-17b	TS02-30		TS02-35		TS02-41
Position/ Component	Core	Rim	Core	Rim	Core	Rim	Core	Rim							Ph	Ph	Pg	Pg	Pg	Ph	Pg	Ph	Ph
wt.%																							
SiO_2	36.80	37.41	36.34	36.87	36.42	37.27	36.59	36.94	55.68	54.41	56.07	54.26	54.11	55.22	51.26	50.13	45.72	45.87	46.17	53.89	46.65	50.72	52.38
TiO_2	-	-	0.21	-	-	-	-	-	-	-	-	-	0.18	-	0.42	0.33	0.25	-	-	0.34	-	0.51	0.32
Al_2O_3	20.67	21.12	20.58	21.11	20.41	21.19	20.51	20.71	9.04	7.99	10.20	8.40	9.04	6.19	24.59	27.72	38.73	38.15	39.30	22.85	39.05	28.42	22.38
$FeO^{\dagger}$	34.19	30.31	35.01	32.63	32.33	30.35	34.13	33.55	6.63	7.63	3.44	12.14	12.28	8.37	2.18	3.48	0.29	0.43	0.28	1.56	0.76	2.73	3.62
MnO	0.56	0.27	0.37	0.43	3.38	0.27	0.74	-	-	-	-	-	-	-	-	-	-	-	-	-	-	-	-
MgO	1.19	3.01	1.22	2.52	0.97	3.27	1.56	2.39	8.07	7.95	9.00	5.26	4.63	9.29	4.24	2.38	-	0.20	-	4.96	0.15	3.06	4.10
CaO	7.08	8.67	7.30	7.34	6.84	8.10	6.76	6.99	13.98	14.26	14.79	11.76	10.46	16.17	-	-	-	0.15	0.34	-	0.13	-	-
Na_2O	-	-	-	-	-	-	-	-	7.27	6.81	6.67	7.81	8.81	5.65	0.35	0.42	7.37	7.07	6.48	0.36	6.53	0.66	-
K_2O	-	-	-	-	-	-	-	-	-	-	-	-	-	-	10.78	10.11	0.60	0.49	0.62	9.05	0.88	9.54	10.48
Total	100.5	100.8	101.0	100.9	100.3	100.5	100.3	100.6	100.7	99.05	100.2	99.63	99.51	100.9	93.82	94.94	92.96	92.35	93.19	93.01	94.16	95.64	93.29
Si	5.94	5.93	5.87	5.89	5.92	5.92	5.93	5.93	4.00	4.00	3.99	4.03	4.02	4.02	6.96	6.76	5.98	6.04	6.01	7.25	6.03	6.72	7.17
Ti	0.00	0.00	0.03	0.00	0.00	0.00	0.00	0.00	0.00	0.00	0.00	0.00	0.01	0.00	0.04	0.03	0.02	0.00	0.00	0.03	0.00	0.05	0.03
Al	2.95	2.96	2.94	2.98	2.93	2.97	2.94	2.94	0.57	0.52	0.64	0.55	0.59	0.40	2.95	3.30	4.48	4.44	4.52	2.72	4.46	3.33	2.71
Fe^{2+}	2.31	2.01	2.36	2.18	2.20	2.01	2.31	2.25	0.20	0.23	0.10	0.38	0.38	0.25	0.12	0.20	0.02	0.02	0.02	0.09	0.04	0.15	0.21
Mn	0.04	0.02	0.03	0.03	0.23	0.02	0.05	0.00	0.00	0.00	0.00	0.00	0.00	0.00	0.00	0.00	0.00	0.00	0.00	0.00	0.00	0.00	0.00
Mg	0.14	0.36	0.15	0.30	0.12	0.39	0.19	0.29	0.43	0.44	0.48	0.29	0.26	0.50	0.43	0.24	0.00	0.02	0.00	0.50	0.01	0.30	0.42
Ca	0.61	0.74	0.63	0.63	0.60	0.69	0.59	0.60	0.54	0.56	0.56	0.47	0.42	0.63	0.00	0.00	0.00	0.01	0.02	0.00	0.01	0.00	0.00
Na	0.00	0.00	0.00	0.00	0.00	0.00	0.00	0.00	0.25	0.24	0.23	0.28	0.32	0.20	0.02	0.03	0.47	0.45	0.41	0.02	0.41	0.04	0.00
K	0.00	0.00	0.00	0.00	0.00	0.00	0.00	0.00	0.00	0.00	0.00	0.00	0.00	0.00	0.47	0.43	0.03	0.02	0.03	0.39	0.04	0.40	0.46

(Continued)

Table C.2 (continued)

Mineral	Amphibole														Epidote group minerals									
Sample	TS02-3A		TS02-15A							TS02-17b			TS02-35		TS02-01	TS02 -17b	TS02-35		TS02 -41	TS02 -47	TS02 -48	TS02 -50B		
Position/ Component	Gln[§]	Brs	Gln	Brs	Brs	Brs	Act	Gln	Mhb	Gln	Gln	Mhb	Gln	Gln										
wt.%																								
SiO_2	57.19	51.64	57.00	47.03	47.22	46.47	51.34	56.09	48.22	57.19	57.79	51.41	57.74	58.16	36.94	37.29	38.35	38.25	38.67	37.07	38.28	38.46	38.16	38.22
TiO_2	-	0.20	-	0.23	-	-	-	-	-	-	-	-	-	-	-	-	-	-	-	-	0.26	0.31	-	-
Al_2O_3	11.03	8.21	10.18	10.30	8.97	10.54	4.17	10.72	6.26	10.71	10.98	6.26	10.80	11.25	23.39	22.83	26.25	25.64	27.33	25.65	27.75	29.08	27.26	27.56
FeO	10.17	12.39	12.89	17.69	17.35	17.56	15.23	11.97	20.77	8.04	8.30	11.39	11.71	10.09	13.74	13.30	8.55	10.14	8.85	9.15	6.92	5.28	7.88	7.26
MnO	-	-	-	-	-	-	-	-	0.27	-	-	-	-	-	-	-	-	-	-	-	-	-	-	-
MgO	10.46	13.34	9.19	9.72	10.09	9.48	13.45	9.40	9.66	11.81	11.43	14.98	9.96	11.00	-	-	-	-	-	-	-	-	-	-
CaO	0.45	8.03	0.47	8.75	8.90	8.49	10.45	0.76	9.65	1.33	0.76	10.21	0.57	0.59	22.64	22.63	24.18	23.60	23.95	23.08	24.26	24.29	23.89	24.09
Na_2O	7.62	3.96	8.00	3.89	3.50	3.79	1.90	7.34	2.96	7.09	7.56	2.55	7.73	7.77	-	-	-	-	-	-	-	-	-	-
K_2O	-	0.20	-	0.28	0.34	0.33	0.16	-	0.29	-	-	-	-	-	-	-	-	-	-	-	-	-	-	-
Total	96.93	97.97	97.72	97.89	96.37	96.65	96.69	96.28	98.07	96.18	96.82	96.80	98.52	98.86	96.71	96.05	97.33	97.63	98.80	94.95	97.47	97.42	97.19	97.13
Si	7.93	7.38	7.96	6.97	7.10	6.97	7.57	7.91	7.25	7.93	7.95	7.43	7.94	7.91	5.96	6.05	6.04	6.03	5.99	6.00	5.99	5.98	6.00	6.00
Ti	0.00	0.02	0.00	0.03	0.00	0.00	0.00	0.00	0.00	0.00	0.00	0.00	0.00	0.00	0.00	0.00	0.00	0.00	0.00	0.00	0.03	0.04	0.00	0.00
Al	1.80	1.38	1.68	1.80	1.59	1.86	0.72	1.78	1.11	1.75	1.78	1.07	1.75	1.80	3.33	3.27	3.66	3.57	3.74	3.67	3.84	4.00	3.79	3.83
Fe^{2+}	1.18	1.48	1.51	2.19	2.18	2.20	1.88	1.41	2.61	0.93	0.96	1.38	1.35	1.15	1.25	1.22	0.76	0.90	0.77	0.84	0.61	0.46	0.70	0.64
Mn	0.00	0.00	0.00	0.00	0.00	0.00	0.00	0.00	0.03	0.00	0.00	0.00	0.00	0.00	0.00	0.00	0.00	0.00	0.00	0.00	0.00	0.00	0.00	0.00
Mg	2.16	2.84	1.91	2.15	2.26	2.12	2.96	1.98	2.17	2.44	2.34	3.23	2.04	2.23	0.00	0.00	0.00	0.00	0.00	0.00	0.00	0.00	0.00	0.00
Ca	0.07	1.23	0.07	1.39	1.43	1.36	1.65	0.11	1.56	0.20	0.11	1.58	0.08	0.09	1.96	1.97	2.04	1.99	1.99	2.00	2.03	2.02	2.01	2.03
Na	2.05	1.10	2.17	1.12	1.02	1.10	0.54	2.01	0.86	1.91	2.02	0.71	2.06	2.05	0.00	0.00	0.00	0.00	0.00	0.00	0.00	0.00	0.00	0.00
K	0.00	0.04	0.00	0.05	0.07	0.06	0.03	0.00	0.06	0.00	0.00	0.00	0.00	0.00	0.00	0.00	0.00	0.00	0.00	0.00	0.00	0.00	0.00	0.00

[*] These samples were analyzed by Lavis (2005), and already published in Xiao *et al.* (2012). [†]FeO - total Fe as FeO. [§]See Leake *et al.* (1997) for amphibole classification.

Oxygen measured by stoichiometry. The formulae of garnet, omphacite and white micas were calculated based on 12, 6 and 11 oxygens respectively. The formulae of amphibole and epidote group minerals were calculated based on 23 and 12.5 oxygens respectively. See mineral abbreviations in Abbreviation List.

Table C.3 Compositions of representative garnet using LA-ICPMS

Group	Group 1						Group 3			Sedimentary
Sample	TS02-03A					TS02-36	TS02-32A			TS02-56
Lithology	Retrograde blueschist					Epidote blueschist	Eclogite			Quartz mica schist
Position	core → rim					incl. in pg	rim	mantle	core	rim
weight percent (wt.%)										
SiO_2	37.98	38.39	37.60	37.58	37.97	36.53	38.25	37.45	37.64	37.60
TiO_2	0.14	0.13	0.12	0.11	0.10	0.07	0.04	0.12	0.15	0.06
Al_2O_3	21.58	21.65	22.34	22.10	22.06	22.56	22.50	22.11	21.83	21.86
TFeO*	30.57	30.26	30.25	29.76	29.30	31.19	25.22	31.36	30.95	26.68
MnO	0.46	0.42	0.41	0.38	0.38	0.67	0.26	0.65	1.71	1.82
MgO	1.54	1.66	1.82	1.97	2.17	2.77	3.70	1.60	1.25	1.14
CaO	7.56	7.29	7.34	7.97	7.90	6.07	9.90	6.55	6.31	10.74
Na_2O	0.01	0.01	0.01	0.01	0.01	0.02	0.02	0.01	0.01	0.01
K_2O	n.d.	0.001	n.d.	0.01	n.d.	n.d.	n.d.	n.d.	< 0.001†	0.00
P_2O_5	0.01	0.01	0.01	0.01	0.02	0.02	< 0.08	< 0.11	< 0.10	0.04
parts per million (ppm)										
Li	0.75	0.69	< 0.81	1.13	1.30	3.03	< 1.43	< 1.53	< 1.66	0.23
Be	< 1.39	n.d.	1.21	< 0.99	n.d.	n.d.	< 1.68	1.75	n.d.	< 0.12
Sc	42.6	69.9	47.8	40.7	46.2	172	133	59.4	103	22.2
V	158	86.7	78.0	83.5	84.9	66.9	119	114	79.4	46.1
Cr	116	193	47.4	52.4	52.7	82.5	47.4	105	88.8	9.76
Co	20.6	22.9	23.8	25.6	26.9	51.4	42.1	23.3	18.6	2.76
Ni	< 2.19	n.d.	n.d.	7.30	n.d.	< 1.58	< 1.64	n.d.	n.d.	< 1.44
Cu	n.d.	< 1.62	n.d.	5.37	< 1.34	n.d.	n.d.	2.14	4.91	1.06
Zn	36.1	33.0	31.6	41.9	45.5	45.4	91.6	31.8	37.5	32.5
Ga	10.1	11.5	10.7	11.2	9.78	6.75	7.55	9.45	7.62	6.03
Ge	4.69	3.22	3.60	2.78	3.02	4.06	4.02	< 4.42	3.89	7.78
Rb	n.d.	< 0.20	n.d.	0.47	n.d.	0.24	< 0.16	n.d.	< 0.21	0.10
Sr	0.14	0.87	0.05	0.29	< 0.04	0.02	0.06	< 0.06	0.05	0.10
Y	147	149	147	129	118	103	53.2	62.3	145	122
Zr	0.98	1.14	1.09	1.26	0.91	< 0.92	< 0.59	0.81	0.64	1.57
Nb	n.d.	0.03	< 0.03	n.d.	0.01	n.d.	0.01	0.01	0.01	n.d.
Cs	< 0.04	< 0.04	n.d.	< 0.04	n.d.	< 0.04	< 0.05	n.d.	n.d.	n.d.
Ba	n.d.	n.d.	0.02	1.21	n.d.	n.d.	0.02	n.d.	0.10	0.50
La	< 0.01	n.d.	n.d.	0.02	< 0.01	n.d.	0.01	n.d.	0.01	< 0.03
Ce	0.56	n.d.	n.d.	0.04	0.38	n.d.	n.d.	n.d.	0.01	< 0.03
Pr	0.07	0.06	n.d.	0.02	0.01	n.d.	n.d.	< 0.02	n.d.	< 0.02
Nd	0.55	0.11	0.20	0.36	0.21	0.04	< 0.08	0.14	< 0.09	n.d.
Sm	3.86	3.20	3.00	2.49	2.62	0.25	0.47	1.89	0.61	< 0.14
Eu	4.40	4.28	3.67	2.80	3.02	0.40	0.62	1.87	0.63	0.16
Gd	23.8	25.2	22.6	19.3	19.5	3.56	5.67	10.5	5.14	1.70
Tb	5.07	5.09	4.93	4.32	4.20	1.58	1.61	2.04	2.35	0.93
Dy	32.4	32.3	32.9	27.7	26.2	16.4	10.2	12.6	23.7	11.4
Ho	5.82	6.10	6.11	5.19	4.65	4.16	2.02	2.33	5.61	3.07
Er	16.0	16.9	16.9	13.5	11.6	16.2	5.26	6.32	17.1	9.69
Tm	1.86	1.85	2.11	1.43	1.30	2.14	0.70	0.80	2.22	1.55
Yb	10.9	12.0	11.7	8.59	7.21	16.0	4.07	5.02	14.2	8.98
Lu	1.58	1.67	1.53	1.12	0.89	2.45	0.55	0.73	2.25	1.00
Hf	0.03	< 0.08	n.d.	0.01	0.03	n.d.	0.04	0.01	0.01	0.06
Ta	n.d.	n.d.	0.01	n.d.	n.d.	0.004	n.d.	n.d.	0.01	0.004
Pb	n.d.	n.d.	< 0.05	< 0.06	0.05	< 0.04	n.d.	n.d.	n.d.	0.43
Bi	0.01	0.01	< 0.02	n.d.	< 0.01	< 0.02	n.d.	0.01	n.d.	n.d.
Th	0.06	0.01	< 0.02	n.d.	n.d.	n.d.	n.d.	0.01	n.d.	< 0.02
U	n.d.	n.d.	n.d.	< 0.01	0.01	0.02	n.d.	n.d.	n.d.	< 0.03

*TFeO: total Fe as Fe^{2+}. †< value: lower than detection limits.

See abbreviations in Abbreviation List. These are as used in the following tables.

Table C.4 Trace element contents (ppm) of representative epidote group minerals using LA-ICPMS

Group	Group 1										
Sample	TS02-30			TS02-36				TS02-41			
Lithology	Eclogitic blueschist			Epidote blueschist				Mica-bearing eclogite			
Mineral	Czs incl. in grt mantle	Czs	Czs	Ep incl. in pg	Ep			Ep incl. in grt	Ep incl. in grt	Ep incl. in grt	Aln relict
					rim	mantle	core				
Li	n.d.	< 1.81	1.10	2.53	< 1.70	2.50	< 1.90	< 1.33	< 1.56	1.65	< 1.59
Be	< 1.57	0.98	< 0.16	< 1.84	< 1.61	n.d.	< 2.27	n.d.	0.25	< 1.63	0.23
Sc	21.0	23.4	65.9	42.7	67.6	30.1	44.4	21.8	26.6	16.3	23.9
V	626	453	1080	551	634	496	491	659	601	541	502
Cr	387	521	628	258	300	240	187	1.05	13.34	8.21	< 13.8
Co	1.44	0.45	2.81	6.52	2.09	2.58	1.64	1.30	1.50	1.69	9.81
Ni	< 1.88	n.d.	2.62	9.53	< 2.17	2.30	< 1.87	< 1.70	< 2.06	< 1.65	7.45
Cu	< 1.40	< 2.47	< 0.49	8.79	< 1.94	3.20	n.d.	< 1.70	< 1.66	< 1.82	5.94
Zn	9.75	< 4.06	12.7	12.4	5.88	5.17	5.77	12.0	17.4	18.4	87.4
Ga	29.5	39.4	87.5	45.3	49.4	55.0	59.1	42.5	46.7	39.7	92.8
Ge	< 3.97	4.22	2.25	3.28	4.77	2.74	1.41	6.38	4.73	4.14	37.6
Rb	< 0.29	n.d.	< 0.08	< 0.26	0.83	0.89	n.d.	< 0.23	< 0.19	n.d.	< 0.14
Sr	482	801	1126	986	1019	1427	1519	1186	989	1188	3393
Y	88.6	52.4	132	59.0	87.5	63.2	72.1	131	130	147	226
Zr	12.1	2.84	7.70	3.85	5.37	5.98	5.49	12.8	6.80	16.8	2.51
Nb	< 0.04	n.d.	< 0.05	< 0.06	0.006	0.009	n.d.	0.02	0.006	n.d.	< 0.04
Cs	< 0.06	n.d.	< 0.07	< 0.08	n.d.	< 0.09	< 0.06	< 0.06	n.d.	n.d.	< 0.06
Ba	1.79	7.10	3.53	6.15	7.28	7.59	7.34	3.61	2.49	4.21	5.06
La	16.0	18.9	44.6	56.4	69.2	40.7	43.5	42.0	34.6	70.4	9041
Ce	40.7	50.5	116	141	183	106	112	113	99.4	186	21020
Pr	6.20	7.93	18.3	19.7	26.1	15.5	16.4	18.1	15.7	28.6	2358
Nd	33.8	40.4	107	95.7	130	75.9	83.3	95.8	85.5	150	10577
Sm	12.3	13.0	39.8	24.2	35.8	21.6	25.8	29.5	27.8	42.6	2374
Eu	4.36	3.73	11.8	8.09	12.6	7.59	9.94	8.84	8.09	11.9	573
Gd	14.7	14.3	43.5	22.9	34.9	21.8	28.5	31.3	30.5	46.1	1149
Tb	2.22	1.96	4.88	2.84	4.58	2.85	3.80	4.46	4.29	6.09	65.2
Dy	15.1	10.3	28.3	14.7	22.9	15.6	18.3	26.1	25.1	31.4	135
Ho	3.03	1.97	5.37	2.29	3.71	2.62	3.05	4.98	4.77	5.41	9.73
Er	8.14	5.25	11.8	5.97	9.13	6.18	6.18	13.8	11.5	12.6	11.5
Tm	0.82	0.58	0.94	0.51	0.82	0.40	0.41	1.40	1.00	1.19	0.41
Yb	4.74	2.93	3.71	2.21	3.57	1.38	1.26	8.13	4.63	5.35	1.68
Lu	0.45	0.37	0.28	0.20	0.37	0.17	0.08	0.76	0.47	0.55	0.13
Hf	0.46	0.15	0.40	0.18	0.23	0.17	0.18	0.37	0.35	0.63	0.17
Ta	< 0.02	n.d.	0.007	< 0.02	n.d.	n.d.	0.003	0.003	0.003	n.d.	< 0.02
Pb	12.6	7.66	17.5	4.95	5.76	8.47	8.45	22.6	21.8	19.7	153
Bi	0.04	0.07	0.65	0.04	n.d.	< 0.04	< 0.06	0.09	0.15	0.18	0.88
Th	0.15	2.02	7.16	5.00	4.04	1.53	1.25	1.24	0.73	2.08	901
U	0.73	0.48	2.02	0.38	0.34	0.31	0.49	0.32	0.23	0.46	106

(*Continued*)

Table C.4 (continued)

Group	Group 2				Group 3		Sedimentary protoliths		
Sample	TS02-55				TS02-32A		TS02-52		
Petrology	Epidote-bearing blueschist				Eclogite		Gln-Grt Schist		
Mineral	Czs core	Czs rim	Czs rim	Czs rim	Ep incl. in grt	Czs	Czs	Ep	Czs
Li	< 0.87	1.40	< 1.24	< 0.91	< 1.41	4.65	< 1.14	2.27	< 1.02
Be	< 1.50	< 1.36	< 1.56	0.47	< 1.53	< 5.71	< 1.81	0.26	0.56
Sc	134	151	182	176	32.2	20.6	36.8	7.14	21.2
V	918	1224	1567	1005	566	645	946	2218	351
Cr	398	242	771	468	22.2	81.7	59.4	18.7	27.5
Co	0.58	1.58	1.00	0.61	0.91	3.29	0.99	1.88	< 0.38
Ni	< 2.58	2.72	< 2.03	< 2.36	< 1.86	2.62	1.65	< 1.59	n.d.
Cu	< 1.38	1.78	2.72	2.97	2.17	3.96	n.d.	70.5	< 2.21
Zn	3.71	3.63	4.52	5.54	5.64	22.4	12.6	5.86	< 2.11
Ga	81.2	80.4	69.8	109	39.3	60.4	89.1	56.1	63.2
Ge	3.73	2.94	< 3.11	< 2.62	4.82	< 4.43	3.95	33.5	< 3.58
Rb	< 0.21	< 0.16	< 0.23	< 0.14	< 0.18	0.44	n.d.	< 0.14	< 0.17
Sr	878	676	511	1476	1050	1931	2227	8722	708
Y	114	232	130	96.8	115	34.9	56.8	36.8	7.38
Zr	9.70	5.50	6.36	7.89	0.91	0.97	4.24	6.36	2.56
Nb	0.008	n.d.	0.008	< 0.04	< 0.04	< 0.06	n.d.	n.d.	n.d.
Cs	< 0.05	< 0.05	< 0.05	< 0.05	< 0.07	< 0.10	< 0.05	< 0.04	< 0.06
Ba	3.13	2.74	3.16	5.78	3.60	5.56	6.36	16.8	5.67
La	19.1	15.0	32.5	43.8	11.9	12.7	55.6	1.17	< 0.02
Ce	57.3	49.6	102	130	40.2	42.9	148	2.61	0.10
Pr	9.39	8.45	16.8	21.1	6.84	7.30	24.7	0.46	< 0.02
Nd	51.6	47.7	99.1	116	40.6	39.8	137	2.99	0.07
Sm	17.5	21.2	33.1	35.5	13.7	12.3	47.7	1.05	0.10
Eu	7.88	12.2	10.4	10.7	4.26	3.84	14.5	1.28	0.09
Gd	19.1	28.1	33.2	35.4	18.7	10.6	48.6	2.87	0.18
Tb	2.89	5.31	4.53	4.30	3.43	1.49	4.12	0.59	0.06
Dy	18.4	36.8	26.1	22.9	20.7	8.08	14.2	4.21	0.92
Ho	3.97	8.10	4.67	3.64	4.31	1.24	2.01	1.03	0.23
Er	11.7	23.6	13.4	7.96	11.0	2.58	4.67	3.17	0.99
Tm	1.42	2.72	1.42	0.67	1.43	0.16	0.52	0.45	0.20
Yb	7.99	14.4	8.25	2.30	7.86	0.69	2.72	3.66	1.59
Lu	0.97	2.06	1.01	0.27	1.17	0.09	0.40	0.55	0.27
Hf	0.50	0.28	0.43	0.58	< 0.07	0.13	0.36	0.22	0.06
Ta	0.006	< 0.02	< 0.02	n.d.	< 0.02	0.007	n.d.	n.d.	n.d.
Pb	21.3	6.18	3.85	18.2	16.9	15.1	18.8	17.1	4.71
Bi	0.39	0.19	0.16	0.13	0.05	0.10	0.26	0.02	0.03
Th	1.31	0.51	2.47	3.51	0.12	0.61	5.22	< 0.02	n.d.
U	0.49	0.66	0.77	0.66	< 0.03	0.06	1.63	0.03	0.01

Table C.5 Trace element contents (in ppm) of muscovite and paragonite using LA-ICPMS

Group	Group 1				Group 2			Sedimentary
Sample	TS02-35	TS02-36	TS02-41	TS02-47	TS02-15B			TS02-56
Lithology	Eclogitic blueschist	Epidote blueschist	Mica-bearing eclogite	Garnet omphacitite	Eclogitic blueschist			Quartz mica schist
Mineral	Ph	Ph incl. in pg	Ph	Ph	Ph in Grt	Ph in Grt	Ph	Ph
Li	10.9	10.1	6.51	10.9	278	147	506	26.1
Be	5.14	7.20	14.8	3.02	5.31	8.01	5.51	1.47
Sc	1.56	7.41	2.25	1.92	2.64	1.50	10.2	2.04
V	296	442	241	242	429	290	460	145
Cr	75.6	309	21.0	286	< 11.5	14.3	16.7	115
Co	14.7	13.5	32.0	10.2	15.7	20.0	12.9	1.81
Ni	14.9	24.0	73.6	99.9	3.94	11.5	7.06	3.01
Cu	0.49	< 2.19	< 1.63	n.d.	3.66	< 2.07	< 3.18	2.69
Zn	61.5	30.4	211	57.2	126	161	99.8	42.9
Ga	145	44.8	67.0	56.8	85.2	91.3	131	118
Ge	1.00	n.d.	n.d.	< 2.43	< 2.08	< 2.68	< 2.20	< 1.41
Rb	220	237	215	205	464	459	494	111
Sr	48.5	25.2	10.6	29.2	22.3	29.9	64.5	84.5
Y	0.03	0.22	< 0.05	< 0.05	0.05	< 0.06	< 0.06	< 0.04
Zr	< 0.49	< 0.34	0.27	< 0.61	< 0.39	< 0.40	0.16	< 0.41
Nb	0.29	0.10	0.89	0.38	0.18	0.18	0.45	1.31
Cs	6.46	7.83	7.05	11.5	44.8	54.7	63.8	6.75
Ba	2643	2908	2115	2854	2433	2872	3621	1226
La	n.d.	0.01	n.d.	0.003	0.01	< 0.02	0.01	< 0.06
Ce	n.d.	0.01	n.d.	n.d.	n.d.	< 0.02	0.008	< 0.06
Pr	0.005	n.d.	n.d.	0.005	< 0.02	n.d.	< 0.02	< 0.04
Nd	< 0.20	0.03	n.d.	n.d.	n.d.	< 0.09	0.02	0.11
Sm	n.d.	n.d.	< 0.13	n.d.	< 0.10	n.d.	n.d.	0.04
Eu	n.d.	< 0.03	< 0.05	0.01	0.02	< 0.03	0.03	n.d.
Gd	0.11	n.d.	n.d.	n.d.	0.10	< 0.10	< 0.11	n.d.
Tb	n.d.	0.002	< 0.02	0.002	< 0.02	< 0.02	< 0.02	n.d.
Dy	n.d.	n.d.	n.d.	n.d.	< 0.09	0.02	0.01	< 0.14
Ho	0.005	0.005	n.d.	n.d.	< 0.03	< 0.02	< 0.02	< 0.04
Er	0.04	n.d.	n.d.	0.02	n.d.	0.02	< 0.05	n.d.
Tm	< 0.02	0.01	n.d.	n.d.	< 0.02	0.006	< 0.02	n.d.
Yb	n.d.	0.02	n.d.	n.d.	0.03	0.01	< 0.08	n.d.
Lu	0.005	n.d.	< 0.02	n.d.	< 0.02	0.006	< 0.02	< 0.02
Hf	n.d.	< 0.06	0.01	< 0.05	< 0.06	< 0.09	< 0.07	< 0.08
Ta	n.d.	0.01	< 0.02	0.02	< 0.02	< 0.02	< 0.03	n.d.
Pb	1.37	1.51	0.70	0.37	1.16	1.40	1.51	7.44
Bi	n.d.	n.d.	< 0.04	< 0.02	< 0.02	< 0.02	< 0.03	n.d.
Th	< 0.02	< 0.04	0.01	n.d.	0.005	< 0.06	< 0.04	0.15
U	n.d.	0.12	n.d.	0.003	0.01	< 0.03	< 0.03	< 0.03

(Continued)

Table C.5 (Continued)

	Group 1			Group 2				Sedimentary	
Sample	TS02-03A	TS02-36		TS02-30				TS02-13	
Lithology	Retro. blueschist	Epidote blueschist		Eclogitic blueschist				Quartz mica schist	
Mineral	Pg incl. in grt	Pg with grt incl.	Pg with ep incl.	G3* of Pg	G2* of Pg	Pg incl. in grt as G1*		Pg	Pg
Li	95.7	10.9	16.6	5.09	5.80	10.8	11.3	43.5	32.8
Be	30.2	19.7	28.0	1.51	3.89	< 5.70	< 5.35	21.3	17.6
Sc	< 2.06	< 1.07	< 1.48	0.78	< 1.40	< 2.00	< 2.13	< 1.13	< 1.43
V	169	154	135	151	165	64.9	82.3	75.1	89.0
Cr	131	175	160	359	480	248	209	70.2	76.1
Co	< 0.45	0.59	< 0.51	< 0.18	< 0.54	0.63	0.83	0.18	0.53
Ni	< 3.93	< 2.34	< 2.99	< 1.37	< 3.53	2.86	3.70	< 4.03	3.44
Cu	5.49	8.05	< 3.47	< 0.50	4.25	17.1	12.0	4.82	< 3.12
Zn	< 5.00	< 3.43	< 4.00	0.73	< 3.78	< 4.00	5.15	4.56	< 4.77
Ga	18.0	23.8	20.8	32.4	34.5	10.4	9.26	35.2	35.3
Ge	< 3.62	< 3.91	< 4.13	< 1.47	< 6.15	< 4.50	< 4.72	< 3.49	< 3.64
Rb	< 0.35	14.2	1.65	14.1	5.31	0.64	0.63	1.24	8.41
Sr	1052	178	183	553	541	103	102	1170	1343
Y	< 0.08	< 0.06	< 0.12	< 0.08	< 0.11	< 0.07	< 0.07	< 0.05	< 0.10
Zr	< 0.78	< 0.83	0.59	< 1.16	0.49	< 0.52	< 0.81	< 0.37	< 0.40
Nb	< 0.06	0.01	< 0.09	< 0.06	0.01	n.d.	0.01	< 0.05	0.03
Cs	0.08	0.48	< 0.11	1.39	0.48	0.22	0.32	< 0.10	0.39
Ba	31.2	209	60.7	215	113	11.7	10.9	39.1	101
La	< 0.03	n.d.	< 0.04	< 0.04	n.d.	n.d.	0.006	< 0.03	n.d.
Ce	< 0.03	n.d.	< 0.03	< 0.04	0.010	< 0.07	0.006	0.006	< 0.03
Pr	0.69	0.01	n.d.	0.004	n.d.	n.d.	0.004	0.01	< 0.03
Nd	n.d.	0.02	0.03	< 0.29	< 0.13	< 0.20	< 0.13	n.d.	n.d.
Sm	0.04	< 0.12	< 0.16	< 0.22	< 0.21	0.03	< 0.22	0.07	0.07
Eu	n.d.	n.d.	< 0.04	0.05	0.007	0.008	0.008	< 0.05	0.04
Gd	< 0.21	< 0.11	< 0.15	0.24	n.d.	0.08	< 0.14	< 0.22	< 0.23
Tb	n.d.	n.d.	n.d.	< 0.05	0.004	< 0.05	< 0.03	< 0.02	< 0.02
Dy	< 0.13	< 0.07	< 0.09	< 0.12	< 0.12	0.03	n.d.	n.d.	< 0.11
Ho	< 0.02	< 0.02	n.d.	< 0.07	< 0.02	< 0.02	0.004	< 0.07	0.01
Er	< 0.11	0.02	< 0.11	< 0.13	n.d.	0.053	n.d.	n.d.	0.03
Tm	0.003	< 0.02	< 0.05	< 0.03	0.007	0.004	< 0.02	< 0.02	0.01
Yb	n.d.	< 0.08	< 0.15	< 0.24	< 0.10	< 0.11	0.04	< 0.12	0.05
Lu	< 0.03	n.d.	< 0.03	< 0.03	< 0.03	< 0.03	0.004	0.01	< 0.03
Hf	0.01	< 0.06	0.02	0.01	< 0.11	< 0.12	0.03	< 0.24	0.06
Ta	0.004	0.01	< 0.03	< 0.03	< 0.02	0.005	0.01	< 0.03	0.006
Pb	11.3	0.44	0.45	5.10	4.86	0.68	0.64	46.0	59.1
Bi	0.01	< 0.03	0.04	< 0.03	0.03	< 0.05	< 0.03	< 0.04	< 0.07
Th	< 0.05	0.01	n.d.	< 0.03	0.006	< 0.05	< 0.06	< 0.07	0.03
U	0.004	< 0.03	0.01	< 0.02	0.006	< 0.05	0.03	0.009	< 0.05

*G1, G2 and G3: the three generations of paragonite in TS02-30 discussed in section 5.3.1.1 in Chapter 5.

See abbreviations used in Abbreviation List.

Table C.6 Compositions of representative rutile and titanite using LA-ICPMS

Mineral	Titanite						Rutile
Group	Group 1		Group 2			Group 3	Group 2
Sample	TS02-03A	TS02-05	TS02-15A	TS02-50B	TS02-57	TS02-32A	TS02-15A
Lithology	Retro. blueschist	Retro. blueschist	Eclogite	Ompha-citite	Eclogitic blueschis	Eclogite	Eclogite
weight percent (wt.%)							
SiO_2	29.00	28.16	27.37	28.73	27.54	28.41	0.06
TiO_2	37.76	39.29	43.83	38.29	41.22	39.59	99.21
Al_2O_3	1.50	1.67	1.06	1.74	1.23	1.39	0.02
TFeO*	0.20	0.29	0.20	0.17	0.09	0.17	0.33
MnO	0.01	0.03	0.01	0.01	0.01	0.01	n.d.
MgO	0.004	0.004	0.01	0.01	0.004	0.04	0.01
CaO	31.12	29.96	27.28	30.79	29.58	29.37	0.10
Na_2O	0.02	0.02	0.04	0.03	0.02	0.02	0.004
K_2O	< 0.002	< 0.002	< 0.002	n.d.	n.d.	n.d.	n.d.
P_2O_5	0.18	0.18	0.04	0.04	0.11	0.87	0.05
Total	99.80	99.61	99.84	99.79	99.81	99.86	99.77
parts per million (ppm)							
Li	n.d.	< 0.65	< 0.82	< 0.89	< 0.69	< 1.22	n.d.
Be	n.d.	0.54	< 0.87	< 1.32	n.d.	< 1.14	1.02
Sc	1.20	2.09	1.28	1.26	0.60	< 0.76	< 1.46
V	398	226	426	273	322	365	1074
Cr	45.0	62.8	3.47	227	174	41.1	n.d.
Co	n.d.	< 0.22	< 0.24	0.64	n.d.	4.02	< 0.46
Ni	< 5.85	< 1.57	n.d.	1.30	0.69	9.21	< 3.20
Cu	< 3.50	< 1.31	8.04	3.37	1.40	32.3	< 3.05
Zn	3.90	3.02	4.92	3.41	3.13	2.86	7.15
Ga	1.49	1.17	2.54	1.07	0.41	2.00	< 0.07
Ge	3.10	5.19	3.24	3.36	2.22	2.82	n.d.
Rb	n.d.	< 0.17	n.d.	< 0.14	< 0.10	n.d.	n.d.
Sr	335	32.4	72.1	24.9	15.3	107	1.82
Y	104	394	204	65.1	91.4	71.8	0.32
Zr	10.8	13.2	10.3	4.78	11.0	8.28	20.2
Nb	138	84.7	97.2	35.1	68.7	11.8	180
Cs	n.d.	< 0.03	< 0.03	< 0.04	0.02	< 0.04	< 0.11
Ba	< 0.10	0.02	1.74	< 0.20	0.03	1.49	0.50
La	5.99	0.02	0.85	0.06	0.27	0.69	0.04
Ce	37.2	0.18	7.89	0.75	3.03	6.96	0.14
Pr	9.09	0.04	2.77	0.23	1.07	2.58	0.04
Nd	58.1	0.41	26.8	2.52	10.8	24.2	< 0.13
Sm	23.1	0.64	20.3	2.43	8.01	17.7	0.21
Eu	8.01	0.46	8.48	1.31	2.04	5.74	< 0.04
Gd	23.8	5.97	29.2	7.24	11.6	21.1	< 0.24
Tb	3.19	1855	5.21	1.53	2.26	2.98	0.01
Dy	18.9	47.4	36.0	10.6	16.9	15.8	< 0.09
Ho	3.99	15.2	8.00	2.53	3.72	2.68	0.01
Er	12.4	65.2	24.3	8.57	13.8	5.51	0.02
Tm	1.69	13.3	3.09	1.26	1.96	0.86	< 0.03
Yb	10.7	113	20.3	8.22	14.1	4.96	< 0.15
Lu	1.58	14.6	2.63	0.99	1.85	0.72	0.04
Hf	1.18	1.50	0.92	0.49	0.70	0.94	0.70
Ta	20.0	15.0	7.83	3.62	2.77	1.15	9.84
Pb	7.27	0.68	1.98	0.66	0.08	3.98	< 0.14
Bi	0.55	0.02	0.01	0.05	0.03	0.45	n.d.
Th	0.20	0.02	0.01	0.02	0.06	0.03	n.d.
U	1.62	0.04	0.12	0.02	0.16	0.08	0.09
Nb/Ta	6.9	5.6	12	9.7	25	10	18
Zr/Hf	9.1	8.8	11	9.8	16	8.8	29

*TFeO: total Fe as Fe^{2+}.

Table C.7 Compositions of representative omphacite and albite using LA-ICPMS

Mineral	Omphacite								Albite
Group	Group 1			Group 2			Group 3		Group 2
Sample	TS02-42			TS02-15A			TS02-20		TS02-50B
Lithology	Eclogitic blueschist			Eclogite			Eclogitic blueschist		Omphacitite
weight percent (wt.%)									
SiO_2	53.67	52.82	53.38	53.98	54.08	53.39	53.41	53.78	68.84
TiO_2	0.04	0.03	0.04	0.048	0.049	0.045	0.05	0.05	n.d.
Al_2O_3	7.00	6.46	7.76	8.97	9.00	7.91	6.88	7.53	18.09
TFeO	7.79	8.46	6.90	8.90	8.86	9.96	8.63	7.92	0.58
MnO	0.02	0.02	0.01	0.089	0.092	0.026	0.02	0.01	0.01
MgO	9.01	9.06	8.98	6.77	6.60	6.98	8.18	8.16	0.79
CaO	14.90	16.09	14.90	13.08	12.93	13.96	15.71	15.02	0.27
Na_2O	7.44	6.87	7.88	8.04	8.21	7.59	6.63	7.01	11.34
K_2O	0.02	< 0.001	< 0.002	< 0.002	0.03	< 0.001	< 0.002	n.d.	0.03
P_2O_5	< 0.02	< 0.02	n.d.	< 0.02	< 0.02	0.02	< 0.02	0.01	< 0.04
Total	99.88	99.80	99.86	99.87	99.86	99.87	99.50	99.50	99.94
parts per million (ppm)									
Li	39.3	38.3	43.0	29.5	29.5	25.2	24.6	26.3	7.56
Be	6.90	5.42	9.97	3.53	1.93	2.57	1.10	0.55	1.60
Sc	14.0	18.5	23.0	64.0	65.6	33.3	46.8	48.2	< 1.26
V	299	513	490	362	369	424	2422	2381	< 10.0
Cr	4.33	70.9	24.9	8.42	4.85	10.7	20.3	41.1	41.6
Co	21.6	24.0	17.3	24.6	24.9	22.2	37.3	35.4	2.36
Ni	32.0	43.3	37.8	8.50	9.34	6.46	33.7	31.7	6.02
Cu	4.71	3.29	2.93	3.58	12.1	3.00	2.77	33.0	8.51
Zn	111	115	110	184	190	152	123	113	5.68
Ga	27.0	30.9	22.4	33.7	33.3	41.1	23.2	23.4	4.88
Ge	< 1.88	n.d.	2.69	< 2.18	< 2.20	< 1.66	< 2.87	n.d.	n.d.
Rb	< 0.19	n.d.	0.02	< 0.18	0.64	< 0.14	< 0.16	< 0.17	< 0.28
Sr	85.5	135	16.0	43.2	38.1	75.6	30.8	29.1	173
Y	0.28	0.18	0.11	5.00	2.87	0.37	0.46	0.40	0.10
Zr	1.22	1.00	1.18	0.77	0.81	0.60	1.24	1.03	< 0.48
Nb	0.11	0.05	n.d.	0.06	0.03	n.d.	0.01	0.01	0.01
Cs	0.04	< 0.03	< 0.04	n.d.	0.07	n.d.	< 0.05	n.d.	0.14
Ba	0.88	0.06	< 0.13	1.05	0.93	0.17	0.58	0.37	25.8
La	n.d.	n.d.	n.d.	0.02	< 0.01	0.01	0.01	0.01	0.01
Ce	0.02	0.06	n.d.	0.09	0.07	0.10	0.04	0.04	0.02
Pr	0.01	0.02	n.d.	0.02	0.02	0.025	< 0.01	0.02	n.d.
Nd	0.06	0.17	0.02	0.28	0.21	0.31	0.17	0.13	n.d.
Sm	0.14	0.22	n.d.	0.24	0.28	0.39	0.20	0.17	n.d.
Eu	0.04	0.12	n.d.	0.16	0.12	0.22	0.06	0.08	n.d.
Gd	0.21	0.30	0.02	0.64	0.30	0.33	0.28	0.18	0.03
Tb	0.02	0.03	n.d.	0.10	0.08	0.04	0.03	0.03	0.01
Dy	0.11	0.07	0.02	0.96	0.75	0.08	0.13	0.09	0.07
Ho	< 0.01	0.01	0.01	0.21	0.12	0.01	0.03	0.01	0.01
Er	0.03	0.01	0.01	0.73	0.38	0.03	0.05	< 0.04	0.05
Tm	n.d.	n.d.	n.d.	0.13	0.10	< 0.01	n.d.	< 0.01	n.d.
Yb	< 0.06	n.d.	n.d.	0.98	0.47	< 0.04	n.d.	0.03	< 0.10
Lu	0.01	n.d.	n.d.	0.08	0.06	0.002	n.d.	0.01	0.005
Hf	0.13	0.06	0.11	0.08	0.10	0.10	0.12	0.12	n.d.
Ta	n.d.	n.d.	n.d.	< 0.01	n.d.	< 0.01	0.01	n.d.	0.01
Pb	1.01	1.92	0.10	0.47	0.47	0.78	0.16	0.17	0.28
Bi	0.01	n.d.	0.01	< 0.02	n.d.	< 0.03	n.d.	0.01	n.d.
Th	n.d.	n.d.	0.01	< 0.02	n.d.	< 0.02	n.d.	n.d.	n.d.
U	0.01	n.d.	n.d.	< 0.05	< 0.02	0.02	0.02	< 0.02	0.01

Table C.8 Trace element contents (in ppm) of representative amphiboles and chlorite using LA-ICPMS

Mineral	Amphibole					Chlorite
Group	Group 1			Group 2		Group 1
Sample	TS02-42		TS02-47	TS02-15A		TS02-05
Lithology	Eclogitic blueschist		Garnet omphacitite	Eclogite		Retro. blueschist
			core	core	rim	
Li	6.05	< 1.12	16.5	15.7	1.97	25.9
Be	2.98	5.83	1.97	5.34	3.57	n.d.
Sc	8.83	11.0	9.16	38.5	66.2	2.74
V	162	200	168	367	424	70.0
Cr	63.3	61.9	212	15.9	< 9.59	245
Co	53.2	42.6	51.4	69.2	65.9	138
Ni	226	187	737	28.9	12.4	540
Cu	< 1.67	< 1.81	0.39	5.58	17.7	10.4
Zn	292	297	252	424	445	459
Ga	9.93	7.60	9.06	37.9	46.0	21.2
Ge	2.38	1.21	0.62	2.47	< 2.45	< 2.60
Rb	< 0.20	0.19	< 0.06	1.01	1.81	< 0.19
Sr	12.7	8.32	0.40	3.03	15.8	0.06
Y	0.12	0.07	< 0.04	0.11	4.45	n.d.
Zr	0.64	0.53	0.48	< 0.18	1.42	n.d.
Nb	< 0.03	0.005	0.10	0.02	0.08	0.02
Cs	< 0.04	< 0.05	< 0.04	< 0.07	< 0.06	< 0.06
Ba	< 0.12	0.09	0.24	0.67	3.02	< 0.13
La	n.d.	< 0.02	0.01	n.d.	0.009	n.d.
Ce	n.d.	< 0.02	0.009	0.006	0.05	0.01
Pr	n.d.	n.d.	< 0.01	n.d.	0.009	0.002
Nd	0.02	n.d.	0.05	n.d.	< 0.10	0.04
Sm	0.01	n.d.	0.06	0.033	0.12	n.d.
Eu	< 0.02	0.01	< 0.03	n.d.	0.06	0.009
Gd	0.08	< 0.13	< 0.13	< 0.06	0.52	0.02
Tb	0.002	0.005	< 0.02	0.009	0.12	n.d.
Dy	< 0.05	< 0.06	0.35	0.03	0.72	n.d.
Ho	0.006	0.006	< 0.01	n.d.	0.14	< 0.01
Er	< 0.04	0.02	< 0.04	< 0.03	0.43	n.d.
Tm	0.005	0.005	0.05	0.007	0.07	0.007
Yb	< 0.06	< 0.07	< 0.10	0.05	0.26	n.d.
Lu	n.d.	0.02	< 0.01	n.d.	0.08	n.d.
Hf	< 0.05	0.06	< 0.04	n.d.	0.06	n.d.
Ta	n.d.	n.d.	< 0.01	0.003	< 0.02	n.d.
Pb	0.14	0.12	< 0.06	0.08	0.42	0.06
Bi	n.d.	0.01	< 0.02	0.008	< 0.02	n.d.
Th	< 0.03	n.d.	0.008	0.02	0.02	< 0.02
U	0.01	< 0.03	< 0.01	< 0.02	0.02	n.d.

Table C.9 GPS data and petrographic summary of metamorphic rocks from Chinese Western Tianshan in terms of mineral modal abundances (wt.%)

Group*	Samples	GPS	Lithologies and brief descriptions	Retrograde alteration	Grt	Gln	Omp	Ttn	Mica	Ca	Chl	Qz	Rt	Czs	Other minerals	Total†
Group 1	TS02-02		Omphacite blueschist; omphacite vein surrounded by Qz and Mica	Overgrowth of Ttn	11.7	42.6	23.4	5.38	4.42	0.00	0.00	2.67	2.16	7.75		1538
	TS02-03A		Retrograde blueschist; from same hand specimen with 3B but much less Omp	Grt carbonated; obvious overgrowth of Ttn	27.1	32.5	16.2	3.15	9.66	4.68	0.26	2.61	3.92	0.00		1400
	TS02-03B§	N42°34.417′ E81°10.148	Eclogite	Grt carbonated	14.9	0.06	62.0	0.00	0.06	11.2	0.00	10.8	1.08	0.00		1564
	TS02-04		Retrograde blueschist	Grt inclusions in Amp; overgrowth of Amp; several fractures	33.5	10.8	30.8	2.63	10.6	6.05	0.00	4.68	0.94	0.00	Hbl 2.41	1619
	TS02-05		Epidote blueschist	Grt and Mica chloritized;overgrowth of Ttn	11.3	57.1	7.92	1.23	4.91	0.00	2.20	0.86	1.07	13.5		1246
	TS02-06		Carbonated omphacitite; foliated	Grt and Gln carbonated; overgrowth of Amp	16.2	5.32	39.7	0.00	14.1	14.7	0.09	3.95	0.41	5.53		1648
	TS02-08		Chloritized garnet mica schist; foliated	Grt greatly chloritized	26.9	0.00	3.59	0.72	39.9	6.62	5.69	16.5	0.11	0.00		1380
	TS02-09	N42°27.117′ E81°17.022′	Garnet-bearing blueschist	Grt and Czs chloritized; Grt inclusion in Czs	17.1	50.3	0.00	0.00	0.00	0.00	9.24	2.32	0.00	21.0		1514
	TS02-11		Chloritized epidote-bearing blueschist	Ca vein with Chl; Grt chloritized	2.19	61.2	0.00	0.00	0.00	8.93	11.6	3.10	0.23	12.7		1256
	TS02-35	N42°32.035′ E81°11.057′	Epidote-bearing eclogitic blueschist	Overgrowth of Amp and Ttn	15.6	41.6	12.8	4.07	5.83	0.00	0.20	0.21	4.97	14.7		1111
	TS02-36		Epidote blueschist	Grt chloritized; Grt inclusions in Amp	8.85	53.1	2.00	0.00	10.3	0.00	0.33	0.00	1.76	22.5	Ab 1.21	689

(Continued)

Table C.9 (continued)

Group	Samples	GPS	Lithologies and brief descriptions	Retrograde alteration	Grt	Gln	Omp	Ttn	Mica	Ca	Chl	Qz	Rt	Czs	Other minerals	Total
Group 1	TS02-38	N42°09.822′ E81°21.647′	Omphacite blueschist	Grt chloritized	10.7	30.1	32.8	1.20	2.88	7.42	0.26	1.97	1.63	11.1		1695
	TS02-41	N42°28.794′ E81°22.044′	Mica-bearing eclogite		23.5	1.20	44.9	0.00	12.9	6.03	0.04	5.76	4.91	0.67		1765
	TS02-42		Eclogitic blueschist; omphacite vein surrounded by Qz and Mica	Overgrowth of Amp and Ttn; Omp inclusions in Gln	17.7	34.7	24.1	2.56	5.10	0.00	0.00	1.09	3.84	10.9		1593
	TS02-47	N42°30.442′ E81°21.290′	Garnet omphacitite	Overgrowth of Ttn	9.07	2.95	43.1	0.00	7.28	4.31	0.00	2.00	3.94	27.3		915
	TS02-48		Garnet omphacitite	Overgrowth of Ttn	9.38	8.40	41.7	3.52	11.7	0.74	0.00	1.56	0.84	22.2		1238
	105-1		Retrograde epidote blueschist	Grt inclusions in Czs and Mica; overgrowth of Amp	20.4	44.5	2.84	0.00	10.8	0.00	0.00	1.29	2.19	18.0		1369
	105-12		Epidote-bearing eclogitic blueschist	Overgrowth of Ttn	25.1	24.3	28.5	4.56	2.98	0.00	0.00	0.97	3.22	10.5		1272
	106-3A		Eclogitic blueschist	Grt inclusions in Amp	20.2	11.7	37.3	3.66	13.8	0.00	0.00	6.97	2.34	4.07		1154
	106-14		Carbonated epidosite	Strongly carbonated	13.9	0.26	6.26	0.00	2.40	23.9	0.00	12.9	0.09	40.3		1510
	110-3		Epidote-bearing blueschist	Grt inclusions in Czs	11.3	49.1	14.0	3.57	3.25	0.00	0.04	0.19	1.00	17.6		1707
Group 2	TS02-12	N42°28.352′ E81°11.249′	Mica-bearing blueschist; foliated	Grt and mica chloritized; Grt inclusions in mica; overgrowth of Ttn	12.6	26.7	18.4	1.78	14.6	2.24	3.00	0.00	0.31	6.41	Ab 14.0	1332
	TS02-15A	N42°29.103′ E81°11.060′	Eclogite; from the same hand specimen with 15B but more Omp	Qz vein with Ca around; overgrowth of Ttn and Amp	38.4	10.9	38.5	4.49	0.11	0.00	0.00	4.99	2.16	0.00		1464

(Continued)

Table C.9 (continued)

Group	Samples	GPS	Lithologies and brief descriptions	Retrograde alteration	Grt	Gln	Omp	Ttn	Mica	Ca	Chl	Qz	Rt	Czs	Other mineral	Total
Group 2	TS02 -15B	N42°29.103′ E81°11.060′	Retrograde blueschist	Overgrowth of Ttn and Amp	39.9	21.8	24.6	4.79	0.13	0.00	0.00	5.54	3.26	0.00		1278
	TS02-23		Epidote blueschist	Strongly chloritized; a Ca vein	9.56	18.9	14.7	0.00	7.96	10.4	14.4	6.35	1.13	16.6		2394
	TS02-26		Eclogitic blueschist; omphacite vein	Grt chloritized; Ca vein	14.3	17.4	39.8	0.00	5.38	6.09	0.16	0.98	3.84	12.1		1926
	TS02-27		Blueschist	Strongly chloritized; a Ca vein	7.10	51.4	4.12	0.00	4.54	6.18	6.74	7.71	2.05	10.2		1607
	TS02-28	N42°31.418′ E81°10.898′	Eclogitic blueschist	Grt carbonated; overgrowth of Amp; a Ca vein	25.0	13.6	39.5	0.00	5.73	7.98	0.08	0.00	2.48	5.67		1885
	TS02-29		Mica-bearing eclogite		12.4	0.82	56.7	0.00	11.8	4.56	0.09	1.61	2.19	9.84		1780
	TS02-30		Epidote eclogitic blueschist	Grt replaced by Amp; overgrowth of Ttn	21.3	23.9	27.0	0.00	9.33	0.58	0.00	0.72	1.57	15.7		1552
	TS02-43	N42°29.088′ E81°21.272′	Epidote eclogitic blueschist	Grt chloritized; Grt inclusions in Czs	30.3	20.5	18.0	1.64	2.54	0.00	7.68	2.43	0.00	17.0		1331
	TS02-46	N42°30.442′ E81°21.290′	Omphacitite; foliated	Overgrowth of Amp	14.4	7.54	53.2	1.48	10.8	0.82	0.00	5.35	0.16	6.20		793
	TS02-50B		Omphacitite; foliated	A big Ca vein	19.0	0.44	50.1	1.06	2.95	11.6	1.19	3.56	0.00	10.1		1482
	TS02-53	N42°26.474′ E81°51.303′	Eclogitic blueschist	A felsic vein with Ca	22.4	10.1	26.7	0.00	13.9	7.56	0.70	7.28	0.26	11.1		1613
	TS02-54		Epidote omphacitite	A Ca vein; overgrowth of Ttn	12.9	0.95	44.4	0.59	5.51	13.6	0.04	2.79	0.00	19.3		1803

(Continued)

Table C.9 (continued)

Group	Samples	GPS	Lithologies and brief descriptions	Retrograde alteration	Grt	Gln	Omp	Ttn	Mica	Ca	Chl	Qz	Rt	Czs	Other mineral	Total
Group 2	TS02-55		Epidote blueschist	Grt carbonated and chloritized	13.8	32.1	0.67	1.89	7.22	10.8	8.64	5.90	0.00	19.0		1617
	TS02-57	N42°26.474′ E81°51.303′	Eclogitic blueschist	Overgrowth of Amp	19.8	15.2	38.09	0.53	4.81	10.0	0.00	1.75	0.07	9.80		1780
	TS02-58A		Carbonated epidote eclogite; subtle foliation	Grt carbonated; A Ca vein	13.0	0.43	54.38	1.27	2.45	13.0	0.34	1.43	0.00	13.7		1510
	984-1		Eclogitic blueschist	Strongly carbonated	19.4	1.31	20.7	0.00	1.39	30.4	0.40	4.33	0.00	22.1		959
Group 3	117-1		Eclogitic amphibolite	Actinolite composition of Amp	15.1	18.6	30.1	1.28	0.47	11.7	0.10	2.42	0.18	20.0		733
	TS02-16		Eclogitic blueschist	Overgrowth of Ttn	33.8	19.8	25.1	5.49	0.00	0.06	0.00	8.80	4.83	2.09		1473
	TS02-17b	N42°29.103′ E81°11.060′	Eclogite	Overgrowth of Ttn	33.3	8.39	47.5	3.05	0.15	1.33	0.00	5.11	0.70	0.45		1052
	TS02-20		Eclogitic blueschist	Grt inclusions in Amp; overgrowth of Ttn	39.8	19.9	26.6	3.57	2.05	0.00	0.00	2.00	3.24	2.91		1681
	TS02-32A	N42°32.035′ E81°11.057′	Eclogite; garnet has obvious zoning	Rare overgrowth of Ttn	41.6	16.9	35.8	1.06	0.09	0.00	0.04	1.13	2.42	1.01		1869
	TS02-33		Eclogitic blueschist	Grt inclusions in Amp	35.9	22.5	32.7	0.97	0.06	0.00	4.19	0.27	3.48	3.38		1383
Ultra-mafic	TS02-34		Rodingite; Gln inclusions in Grt		75.7	0.00	1.65	0.00	3.23	9.26	0.31	2.05	3.38	4.46		1678

(Continued)

Table C.9 (continued)

Group	Samples	GPS	Lithologies and brief descriptions	Retrograde alteration	Grt	Gln	Omp	Ttn	Mica	Ca	Chl	Qz	Rt	Czs	Other minerals	Total
Meta-sedimentary rocks	TS02-10	N42°27.117′ E81°17.022′	Chloritized quartz mica schist; foliated	Qz, Mica and Ca chloritized	0.00	0.00	0.00	0.00	35.8	3.74	14.7	45.9	0.00	0.00		1268
	TS02-13	N42°28.352′ E81°11.249′	Chloritized quartz mica schist; foliated	Chloritized	3.33	0.00	0.24	4.07	25.7	0.00	6.60	57.7	0.15	2.22		1035
	TS02-14		Mica-bearing glaucophane schist; foliated	Chloritized; overgrowth of Ttn	17.5	35.0	5.24	5.32	22.7	2.31	1.39	10.6	0.00	0.00		1626
	TS02-18	N42°29.103′ E81°11.060′	Garnet-bearing quartz mica schist; foliated	Chloritized; overgrowth of Ttn	16.1	4.15	0.52	1.25	5.76	3.42	7.57	61.1	0.19	0.00		1613
	TS02-19		Chloritized quartz mica schist mica schist; foliated	Strongly chloritized	5.34	0.00	0.00	0.00	44.6	0.96	11.8	36.8	0.40	0.00		1550
	TS02-52	N42°26.474′ E81°51.303′	Gln-Grt schist; foliated	Chloritized; Ca veins	23.9	15.1	10.0	0.00	6.69	5.99	8.55	20.6	0.00	9.21		1819
	TS02-56		Quartz mica schist; foliated	Strongly chloritized	0.99	0.00	0.00	0.00	31.7	12.1	12.3	43.0	0.00	0.00		1232
	TS02-62		Chloritized quartz mica schist; foliated	Strongly chloritized; overgrowth of Amp	4.36	21.4	1.28	4.09	12.1	0.00	17.5	35.7	0.00	3.52		1310
	986-1		Quartz mica schist	Carbonated	0.00	0.00	0.00	0.00	15.6	9.18	0.00	74.6	0.00	0.00		1325

[*] See details of grouping for meta-basaltic rocks in sections 4.4.1 and 4.4.3 in Chapter 4.

[†]Total: the total number of counted points in each thin-section.

[§]The samples with name in bold are taken as representatives of highly eclogitic rocks with minimal retrograde overprints for discussions in section 4.5.4 in Chapter 4 and Figs. 4.10-4.11.

See mineral abbreviations used in Abbreviation List.

Table C.10 Correlation coefficients (R's) for selected elements of rocks of sedimentary protoliths from Western Tianshan, China

	K	Ba	Rb	Cs	Th	Nb	U	Ta	La	Ce	Pb	Sr	Zr	Ti	Yb
K	**1.00***														
Ba	**0.85**	**1.00**													
Rb	**0.97**	**0.82**	**1.00**					For N = 10, R ＞ 0.7155 at > 99% confidence levels							
Cs	**0.98**	**0.82**	**1.00**	**1.00**											
Th	**0.94**	**0.81**	**0.97**	**0.96**	**1.00**										
Nb	**0.86**	**0.74**	**0.91**	**0.90**	**0.98**	**1.00**									
U	**0.89**	**0.80**	**0.89**	**0.88**	**0.97**	**0.97**	**1.00**								
Ta	**0.88**	**0.77**	**0.93**	**0.92**	**0.99**	**1.00**	**0.97**	**1.00**							
La	**0.83**	0.66	**0.91**	**0.89**	**0.95**	**0.96**	**0.89**	**0.96**	**1.00**						
Ce	**0.79**	0.61	**0.88**	**0.86**	**0.94**	**0.96**	**0.89**	**0.96**	**1.00**	**1.00**					
Pb	0.21	0.08	0.01	0.04	0.08	0.02	0.11	0.03	-0.08	-0.06	**1.00**				
Sr	0.00	0.05	0.06	0.03	0.26	0.35	0.28	0.31	0.28	0.35	0.23	**1.00**			
Zr	**0.75**	0.60	**0.73**	**0.73**	**0.80**	**0.83**	**0.89**	**0.83**	**0.72**	**0.73**	0.11	0.16	**1.00**		
Ti	0.26	0.38	0.28	0.29	0.18	0.10	0.17	0.12	0.01	-0.01	-0.21	-0.08	0.28	**1.00**	
Yb	0.20	0.41	0.33	0.31	0.42	0.46	0.41	0.44	0.37	0.39	-0.23	0.63	0.25	0.36	**1.00**

*Values in bold are those significant correlations at > 99% confidence levels.

Table C.11 Summary of radioactive parent and radiogenic daughter contents and their ratios in selected eclogitic metabasites from others' published work*

	Sample	Rb	Sr	Sm	Nd	Lu	Hf	Rb/Sr	Sm/Nd	Lu/Hf
Refer to: Spandler *et al.*, 2004, Chemical Geology										
New Caledonia	705	2.57	119	4.07	13.16	0.5	2.62	0.022	0.309	0.191
1.9 GPa,	707	1.50	113	2.00	5.40	0.3	1.14	0.013	0.370	0.263
~ 600 °C	706	1.59	101	1.89	5.44	0.31	1.34	0.016	0.347	0.231
	3102	5.36	145	3.29	9.79	0.53	2.37	0.037	0.336	0.224
	3101	11.28	181	4.12	13.07	0.72	2.69	0.062	0.315	0.268
	803	0.09	83.2	4.26	11.00	0.79	3.20	0.001	0.387	0.247
	805	0.56	89.2	4.00	10.46	-	3.13	0.006	0.382	-
Refer to: El Korh *et al.*, 2009, Journal of Petrology										
Ile de Groix, France	GR 21	16.00	199	4.8	11.6	0.5	2.4	0.080	0.414	0.208
1.6 - 2.5 GPa,	GR 24a	13.40	156	4.4	16.3	0.64	3.4	0.086	0.270	0.188
550 - 650 °C	GR 29	3.60	158	7.5	27	0.9	6.0	0.023	0.278	0.150
Refer to: Maulana *et al.*, 2010, PROCEEDING, INDONESIAN PETROLEUM ASSOCIATION										
Sulawesi, Indonesia	BM11	18.70	665.94	4.02	17.7	0.37	4.31	0.028	0.227	0.086
1.8 - 2.4 GPa,	BM15B	1.38	152.67	8.97	36.97	1.19	9.9	0.009	0.243	0.120
580 - 620 °C	BP04	17.65	205.84	3.17	8.55	0.55	3.32	0.086	0.371	0.166
(Parkinson *et al.*, 1998)	CP03E	31.40	64.36	1.23	2.86	0.54	2.73	0.488	0.430	0.198
	BP01	3.37	1311.88	0.99	2.6	0.28	1.12	0.003	0.381	0.250
	BM15C	3.83	908.23	0.85	2.26	0.24	0.96	0.004	0.376	0.250

*These data are used in Figure 4.11 for understanding the contribution of residual eclogitic rocks after subduction-zone metamorphism to mantle compositional heterogeneity.

Figure C.1 Comparisons of reconstructed bulk-rock compositions with analytical (actual) compositions

Reconstructions of bulk-rock major element compositions used the formula $Z_j = \sum_{i=1,j=1}^{i=n,j=m} X_i Y_j$, where i refers to different mineral phases (i.e., garnet, glaucophane, omphacite, rutile, titanite, white mica, carbonate, chlorite, quartz, (clino)zoisite etc.), j refers to different oxides (i.e., SiO_2, TiO_2, Al_2O_3, FeO, MnO, CaO, MgO, K_2O, Na_2O), X refers to mineral weight proportions, Y refers to element abundances in mineral i, Z refers to bulk-rock concentrations of element j. In the calculation, the less abundant opaque minerals have been excluded and all the other minerals are normalized to 100%. Before the calculation of Z values, mineral modes, which are in volume percent, must be converted to weight proportions by multiplying their relevant mineral densities. The values of mineral density used are from http://webmineral.com/. They are (g cm^{-3}): garnet = 4.09, glaucophane = 3.07, omphacite = 3.34, titanite = 3.48, white mica = 2.82 (average density of muscovite), carbonate = 2.71 (calcite is assumed to be carbonate here), chlorite = 2.42, quartz = 2.62, rutile = 4.25, (clino)zoisite = 3.30, albite = 2.62, hornblende = 3.23. Because all the Fe in mineral composition analyses are expressed as FeO, the total Fe as Fe_2O_3 in bulk-rock composition are then converted into FeO by multiplying 0.89981 to compare.

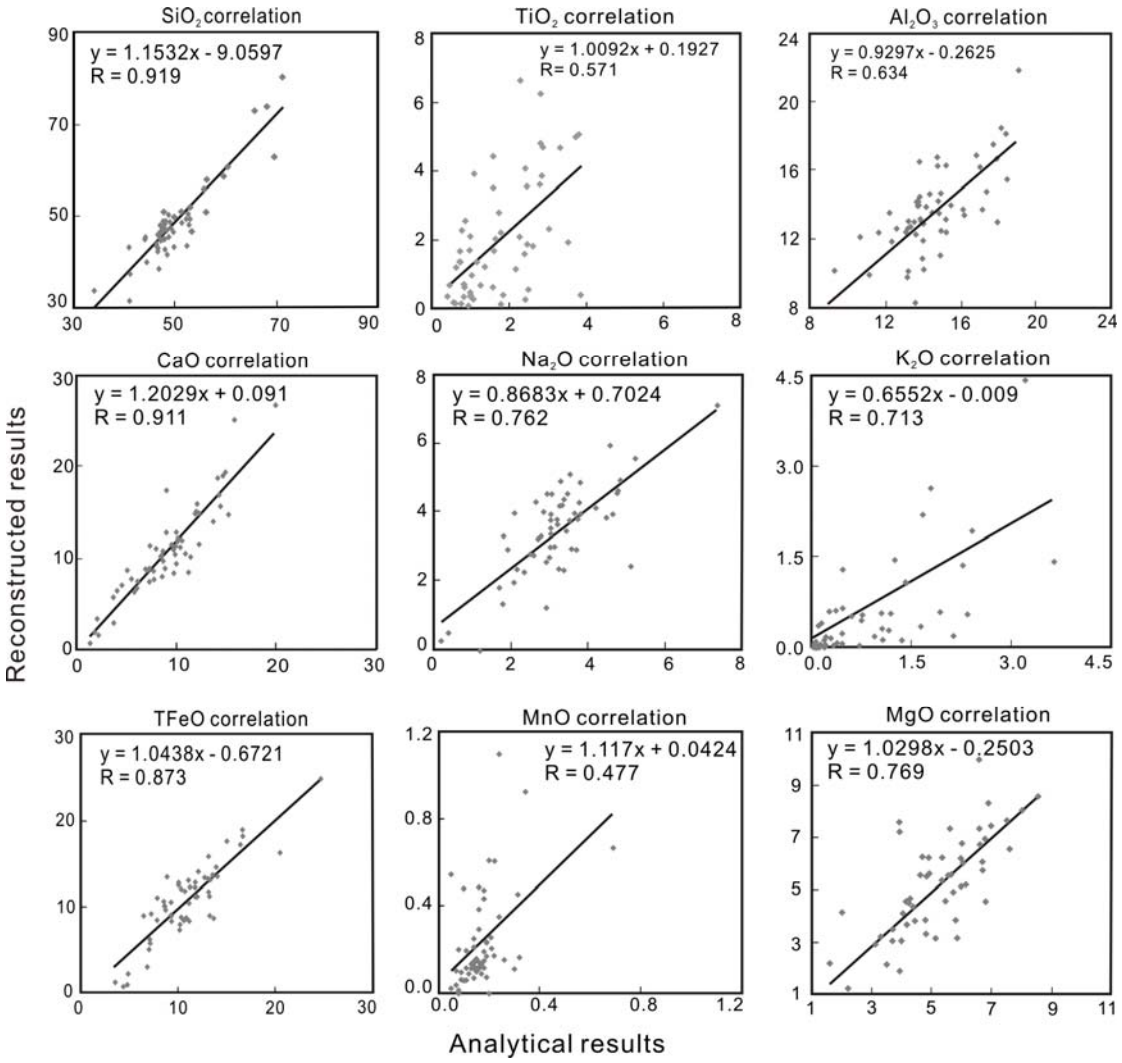

For 56 samples, the correlation coefficients (R) > 0.305 are considered statistically significant at > 99% confidence levels. Therefore, all the relationships between the reconstructed bulk-rock major element contents and the analytical data for our samples in above figures are significantly correlated. It suggests that both mineral compositional data (Table C.2) and the estimated mineral modal abundances (Table C.9) are of good quality, which is very encouraging for metamorphic rocks of multiple phases with varying mineralogy and grain sizes. Deviations from unity of the slope for TiO_2 (1.01), Al_2O_3 (0.93), MgO (1.03) and TFeO (1.04) ensure that the reconstructed compositions are within 10% uncertainties, although SiO_2 (1.15), MnO (1.12) and CaO (1.20) may be slightly overestimated. Several reasons would result in uncertainties: (1). Heterogeneous mineral compositions; (2). Heterogeneous mineral distributions; (3). Opaque minerals that have been omitted during estimations of mineral modes; (4). Tiny minerals that have not been identified under microscope. Nevertheless, the absence of systematic uncertainties for major elements, together with the significant correlations between reconstructed bulk-rock compositions and analytical data, indicate our estimated mineral modes are reliable and could be used for discussing trace element distribution/budgets in our subsequent studies.

APPENDIX D:

GEOLOGY AND GEOCHEMICAL DATA OF NORTH QILIAN MOUNTAIN

Table D.1 Summarized Geological Background for North Qilian Mountain (ONQ), China

	Low grade blueschist belt (LGB) & north ophiolite belt	High grade blueschist/eclogite belt (HGB)	Related ophiolite and arc volcanic rocks	References
Locations	Tadungou (E) & Baishuiquangou (W), along Bailang river, Jiugequan area, Sunan County, Gansu Province	Qingshuigou, Shangxiangzigou and Baishiya (or Baijingsi) from west to east, Qilian County, Qinghai Province		Song *et al.*, 2004; Lin *et al.*, 2010
Protolith	volcanic rocks	graywacke, marble, chert and basaltic rocks		Wu *et al.*, 1993; Song *et al.*, 2009a
P-T conditions	150 ~ 250 °C, 0.4 ~ 0.7 GPa	Eclogite: 340 ± 10 °C, 0.8 ± 0.1 GPa; blueschist: > 380 °C, 0.6 ~ 0.7 GPa		Wu *et al.*, 1993
		Eclogite: 500 ~ 550 °C, 18 ~ 25.6 kbar by Grt-Omp-Ph geothermobarometer		Song *et al.*, 2004
		Weakly deformed eclogite: 460 ~ 510 °C, 2.2 ~ 2.6 GPa; strongly foliated eclogite: 475 ~ 500 °C, 1.75 ~ 1.95 GPa; Grt-Omp-Ph-Gln schist: 475 ~ 540 °C, 2.15 ~ 2.6 GPa; Mg-carpholite schist (chloritoid-bearing schist): 525-530 °C, 2.45 ~ 2.5 GPa; 6 ~ 7 °C/km thermal gradient		Song *et al.*, 2007
	250 ~ 350 °C, 0.6 ~ 1.1 GPa			Song *et al.*, 2009a
	320 ~ 375 °C, 0.75 ~ 0.95 GPa			Zhang *et al.*, 2009
	Lawsonite blueschist：335 ~ 355 °C，0.8 ～ 0.95 GPa; epidote blueschist：345 ～ 375 °C，0.75 ～0.85 GPa			Lin *et al.*, 2010
Tectonic setting		subduction-accretionary complex		Wu *et al.*, 1993; Song, 1997; Zhang *et al.*, 1997

(Continued)

Table D.1 (continued)

	LGB & north ophiolite belt	HGB	Related ophiolite and arc volcanic rocks	References
Tectonic setting	Back-arc, supra-subduction zone type (vs. mature ocean spreading center; evidenced by the presence of the cumulate with banded wehrlite + gabbros and high volume of volcanic breccias and terrigenous-sedimentary rocks)	(Phengite-rich eclogites: most like E-type MORB or alkali basalts from ridges and near ridge seamounts without ruling out the possibility of an OIB protolith) + (Epidote-rich eclogites: the N- to E-type MORB group) + the gabbroic group		Song *et al.*, 2009a; Xia & Song, 2010
	REE patterns of chert: neither in the vicinity of continental margin or in the typical open ocean basin vs. a back-arc basin			Zhang *et al.*, 1997
	Middle-northern volcanic zones: backarc basin			Xia *et al.*, 2003
Age		> 460 Ma: eclogite facies; 460-440 Ma: blueschist facies/cooing ages; 400-382 Ma: greenschist facies - orogeny uplift on glaucophane and phengite ($^{39}Ar/^{40}Ar$ and K-Ar)		Wu *et al.*, 1993
		448.6 ± 1.1 Ma: phengite from blueschists - ancient Qilian Ocean closed age (Ar-Ar plateau age; Qingshuigou or Baijingsi)		Liou *et al.*, 1989
		Ar-Ar plateau age: 462.02 ± 1.33 Ma: on phengite from blueschists - cooling age shortly after peak metamorphism (QL7-2 from Baijingsi); 489.29 ± 16.24 Ma: glaucophane from blueschist - beginning of prograde metamorphism; 422.89 ± 7.07 Ma: glaucophane from blueschist – thermo-tectonic event during exhumation (QL6-5 from Wayaohe); 412.40 ± 0.94 Ma: amphibole from amphibolite – the exhumation age (QL90-87 from Yuergou)	466 ± 9 and 481 ± 18 Ma: for island-arc acid volcanic rock (two single-grain zircons U-Pb age)	Zhang *et al.*, 1997

(Continued)

Table D.1 (continued)

LGB & north ophiolite belt	HGB	Related ophiolite and arc volcanic rocks	References
Age		465.68 ± 23.18 Ma (Biandukou); 453.56 ± 4.44 Ma: mafic lavas of the ophiolite (whole rock Sm-Nd isochron age; Laohushan in the Northern Terrane, north of Baiyin), which is inconsistent with Xia and Song, 2010 and may not reliable for basaltic rocks	Xia *et al.*, 1991, 1996, 1998 from Xia *et al.*, 2003; Xia *et al.*, 1995 from Wang *et al.*, 2005
		486-445Ma: for island-arc shoshonite and basalt (whole-rock Sm-Nd and Rb-Sr isochron; Shishuigou, Yongdeng County).	Xia *et al.*, 1995 from Song *et al.*, 2004
		464.59 ± 21.89 Ma: middle volcanic zone (whole-rock Sm-Nd isochron); 469-454 Ma, 468.87 ± 4.63 Ma: southern volcanic zone (whole rock Sm-Nd isochron age) - back-arc basin lavas	Xia *et al.*, 2003
		568-533 Ma: for gabbro of ophiolite - Qilian ocean existed at least in Early Cambrian (zircon U-Pb SHRIMP)	Yang *et al.*, 2002
		550 ± 17 Ma: cumulated gabbro (zircon U-Pb SHRIMP; Yushigou)	Shi *et al.*, 2004
	453.9-442.1 Ma: on white mica from meta-pelite (Ar-Ar age; peak metamorphic age or cooling age shortly after; Qingshuigou)		Liu *et al.*, 2006
	463 ± 6 Ma (Shangxiangzigou, western) and 468 ± 13 Ma (Baijingsi, eastern): for eclogites (zircon U-Pb SHRIMP)	Silurian remnant - sea flysch formation: ancient Qilian Ocean closed at end of Ordovician Era	Song *et al.*, 2004

(Continued)

Table D.1 (continued)

	LGB & north ophiolite belt	HGB	Related ophiolite and arc volcanic rocks	References
		449-478Ma: Shangxiangzigou (QS45); 463-469Ma: Baishiya (or Baijingsi; 2Q27) – for eclogites (zircon U-Pb SHRIMP)		Song *et al.*, 2006
		489 ± 7 Ma and 477 ± 16 Ma: eclogite-facies metamorphism from lawsonite-bearing eclogitic metabasites (zircon U-Pb SHRIMP).	502 ± 16 Ma: core of igneous zircon grains from lawsonite pseudomorph-bearing eclogite with gabbroic protolith (from Baijingsi) - the formation age of Early Ordovician for some ophiolite sequences and period of oceanic crust formation	Zhang *et al.*, 2007b
			497 ± 7 Ma: gabbronorite - tectonic emplacement age of the Dongcaohe ophiolite (zircon U-Pb SHRIMP; Dongcaohe)	Tseng *et al.*, 2007
			513.0 ± 4.5 Ma: for mafic-ultramafic intrusion – Cambrian arc magmatism for the northern margin of the Qilian Block (zircon U-Pb SHRIMP; Zhamashi).	Tseng *et al.*, 2009
Age	have not been precisely dated so far	462-448 Ma: Ar-Ar ages of glaucophane and phengite from blueschist	496-554 Ma: zircon SHRIMP ages of cumulated gabbro	Song *et al.*, 2009a
	415 ± 7 Ma: phengite from lawsonite blueschist; 413 ± 5 Ma: glaucophane from epidote blueschist (Ar-Ar isochron; Baishuiquangou) - the final closed time for ancient Qilian oceanic basin, i.e., the collision time between North China Craton and Qaidam plate			Lin *et al.*, 2010
			508-480 Ma with a weighted mean age of 490 ± 5Ma: isotropic gabbro of ophiolite (zircon U-Pb SHRIMP; Tadungou around Jiugequan)	Xia & Song, 2010

See Abbreviation List for abbreviations, also for abbreviations used in the following tables.

Table D.2 Representative mineral assemblages for metamorphic rocks with different lithologies from LGB (Zhang *et al.*, 2009; Song *et al.*, 2009a) and HGB (Song *et al.*, 2007, 2009a; Cao *et al.*, 2011) of ONQ

LGB			HGB		
Lawsonite glaucophanite	Lws (porphyroblast) + Gln + Chl + Ab	Fig. 6.1a	Eclogite-facies meta-pelite	Cld + Gln + Ph ± Car; chloritoid, sometimes together with garnet, occurs as porphyroblast in the glaucophane-mica-epidote defined schistosity	Fig. 6.1c
Pumpellyite blueschist	Pmp + Gln + Chl + Ab (+ minor Lws), in which pumpellyite with glaucophane interbed defines the foliation, or occurred as veins or mineral clusters	Fig. 6.1b	Blueschist-facies meta-graywackes	Gln + Mica + Ep + Ab + Qz + Chl (+ Grt) with variable amounts of carbonate, and some are highly foliated; characterized by the high modal amounts of quartz and white micas	Fig. 6.1d
Epidosite	Ep + Qz with viable modal amounts of carbonate		Mafic eclogites and blueschists	Grt + Gln + Omp + Ep + Ph + Rt (+ Pg + Qz). Garnet occurs as porphyroblast, while epidote, omphacite and white micas make up the matrix. Retrograde overprints are common.	Fig. 6.1e, f
LGB blueschists may have not reached the equilibrium, evidenced by their fine grain size and the inheritance of magmatic clinopyroxene as well as relic volcanic textures.			Meta-chert	Qz + minor Mica (+ Grt + Gln); week foliation defined by white micas and Gln.	
Only mafic metamorphic rocks (no metamorphic rocks of sedimentary protoliths) have been found in LGB.			Marble	Ca + (minor Ph, Gln and Aeg), the latter of which can constrain a week foliation.	

Table D.3 Bulk-rock geochemical compositions of metamorphic rocks from LGB of ONQ, China

Sample	0807QL-003	0807QL-015-2	0807QL-022-1	0807QL-007-1	0807QL-007-2	0807QL-010	0807QL-011	0807QL-014	0807QL-005	0807QL-012
Lithology	Epidosite			Lws glaucophanite		Glaucophane pumpellyite schist				
weight percent (wt.%)										
SiO_2	51.98	45.91	53.24	49.88	48.41	49.68	48.03	53.67	50.56	50.04
TiO_2	1.38	1.04	0.66	1.20	1.18	1.38	1.54	0.89	1.38	1.51
Al_2O_3	12.05	12.71	16.71	15.49	16.07	14.74	14.58	13.75	13.85	15.25
TFe_2O_3*	9.88	7.98	8.55	10.51	10.49	11.05	11.64	8.98	11.58	10.11
MnO	0.15	0.14	0.14	0.16	0.16	0.18	0.16	0.20	0.16	0.15
MgO	2.54	3.83	2.03	8.30	8.38	7.35	7.38	6.75	8.80	6.82
CaO	16.66	16.14	15.15	5.45	5.86	7.81	5.88	8.73	5.10	8.74
Na_2O	0.89	4.77	0.12	4.15	3.56	4.45	5.01	4.88	4.66	4.50
K_2O	0.00	0.05	0.01	0.15	0.65	0.07	0.16	0.03	0.44	0.14
P_2O_5	0.16	0.12	0.09	0.10	0.09	0.12	0.12	0.07	0.13	0.14
LOI	3.84	7.01	2.81	4.86	5.31	3.34	5.76	2.33	3.45	3.01
Total	99.53	99.7	99.51	100.3	100.2	100.2	100.3	100.3	100.1	100.4
parts per million (ppm)										
Li	2.41	4.43	4.22	44.7	44.4	30.3	49.5	7.55	37.7	12.9
Be	1.00	0.78	0.42	0.39	0.40	0.52	0.56	0.29	0.58	0.56
Sc	31.2	30.8	23.3	31.5	30.7	38.8	37.1	31.6	39.4	35.7
V	281	222	152	296	290	267	252	202	287	241
Cr	107	97.0	187	340	348	101	111	257	133	175
Co	20.9	25.0	25.9	42.2	43.5	42.7	39.9	34.4	44.9	35.8
Ni	31.6	30.8	52.0	123	135	46.8	47.9	83.7	58.5	76.1
Cu	7.35	28.1	6.18	54.8	74.1	75.0	54.5	2.96	47.6	4.04
Zn	24.1	38.6	32.0	72.8	72.0	89.7	94.2	83.3	89.1	45.0
Ga	20.8	15.4	17.4	16.4	16.8	15.3	15.4	12.2	15.7	14.6
Ge	2.69	2.17	1.90	1.70	1.56	1.66	1.56	1.35	1.31	1.67
Rb	0.23	0.64	0.14	5.80	19.0	1.71	4.83	0.37	13.1	2.04
Sr	1266	556	776	95.5	89.5	41.2	132	39.9	33.9	42.7
Y	46.0	29.3	18.6	29.1	26.7	36.7	31.0	24.2	32.7	40.0
Zr	124	68.2	50.8	67.7	64.4	93.4	101	49.1	83.9	104
Nb	3.19	2.00	1.87	1.27	1.21	2.53	2.94	0.72	1.77	2.78
Cs	0.05	0.37	0.08	4.52	6.15	0.63	1.28	0.09	0.73	0.17
Ba	18.5	23.0	21.8	46.9	191	19.7	33.6	14.3	91.5	41.4
La	6.52	3.70	3.39	2.04	2.05	4.62	4.59	1.70	2.78	4.12
Ce	18.7	10.4	9.08	7.02	6.91	13.1	13.3	5.70	8.35	12.9
Pr	2.83	1.75	1.38	1.30	1.30	2.12	2.16	1.05	1.40	2.22
Nd	14.5	9.34	6.90	7.40	7.23	10.9	11.2	5.89	7.34	12.2
Sm	4.81	3.25	2.23	2.85	2.78	3.69	3.76	2.27	2.81	4.48
Eu	1.82	1.18	0.91	1.00	0.99	1.34	1.29	0.88	1.06	1.59
Gd	6.50	4.36	2.92	3.93	3.77	4.84	4.78	3.23	4.02	5.99
Tb	1.12	0.77	0.51	0.71	0.68	0.88	0.84	0.60	0.77	1.04
Dy	7.55	5.23	3.50	5.02	4.73	6.14	5.62	4.19	5.54	7.01
Ho	1.69	1.16	0.78	1.13	1.08	1.39	1.25	0.96	1.26	1.57
Er	4.60	3.17	2.14	3.17	2.94	3.85	3.39	2.62	3.55	4.28
Tm	0.67	0.45	0.30	0.47	0.43	0.56	0.49	0.38	0.53	0.61
Yb	4.35	2.92	2.02	3.10	2.86	3.69	3.34	2.48	3.57	4.03
Lu	0.66	0.44	0.31	0.47	0.43	0.56	0.50	0.38	0.55	0.61
Hf	3.18	2.05	1.53	1.98	1.91	2.59	2.74	1.51	2.33	2.86
Ta	0.24	0.17	0.15	0.10	0.10	0.20	0.23	0.06	0.13	0.21
Pb	4.64	3.01	1.80	1.23	1.30	1.13	1.08	0.64	0.89	0.84
Th	0.81	0.50	0.38	0.14	0.13	0.70	0.60	0.07	0.26	0.42
U	0.55	0.17	0.12	0.34	0.19	0.31	0.19	0.14	0.25	0.15
Nb/Ta	13.3	11.7	12.7	12.9	12.6	12.6	12.7	11.2	13.1	13.3
Zr/Hf	39.0	33.2	33.3	34.1	33.8	36.1	36.8	32.5	36.0	36.4

*TFe_2O_3 - total Fe as Fe_2O_3.

Table D.4 Bulk-rock compositions for rocks of basaltic protoliths from HGB of ONQ, China

Group*	Group 1			Group 2			Group 3				
Sample	0807 QL -038	0807 QL -040-1	0807 QL -041	0807 QL -056	0807 QL -068	0807 QL -059	0807 QL -053-1	0807 QL -053-2	0807 QL -057-1	0807 QL -057-2	0807 QL -072
Lithology	Blueschist			Blueschist		Eclogitic blueschist	Eclogitic blueschist				AMP
weight percent (wt.%)											
SiO_2	48.57	50.44	52.43	49.33	48.76	49.82	48.45	46.63	49.58	49.73	50.06
TiO_2	2.20	2.13	2.30	1.92	1.17	1.09	1.07	1.09	1.36	1.07	1.05
Al_2O_3	13.54	12.82	13.79	16.45	15.34	16.10	15.79	16.59	14.69	16.15	15.91
TFe_2O_3†	15.92	17.39	14.24	11.74	11.70	10.21	8.65	8.90	9.94	9.58	8.83
MnO	0.15	0.19	0.15	0.14	0.19	0.18	0.13	0.13	0.14	0.13	0.17
MgO	5.47	5.77	4.76	7.08	7.95	7.05	6.97	6.43	7.01	7.07	8.30
CaO	7.17	4.91	5.34	4.75	8.11	9.26	12.12	12.63	11.88	9.71	11.66
Na_2O	3.73	3.38	2.80	3.17	4.07	4.21	2.96	2.47	2.52	3.42	0.47
K_2O	1.20	0.78	1.59	2.67	0.27	0.21	0.42	0.72	0.18	0.86	0.81
P_2O_5	0.19	0.23	0.22	0.23	0.11	0.12	0.09	0.10	0.14	0.11	0.14
LOI	1.84	1.53	1.88	2.84	2.46	1.78	2.86	3.90	2.13	1.97	2.20
Total	99.98	99.57	99.5	100.3	100.1	100.0	99.51	99.59	99.57	99.80	99.60
parts per million (ppm)											
Li	17.8	16.4	15.8	33.1	30.3	8.87	16.2	16.4	11.1	15.9	16.0
Be	1.21	1.10	1.19	0.72	0.67	0.55	0.65	0.70	0.57	0.61	0.67
Sc	40.5	34.4	40.3	42.5	39.3	36.7	32.1	32.4	38.2	38.1	31.3
V	386	410	430	263	263	263	226	234	290	248	241
Cr	33.3	12.8	16.5	235	215	195	356	359	238	341	318
Co	40.7	37.0	36.0	45.1	45.0	41.7	38.6	38.6	42.1	40.2	36.4
Ni	35.9	53.6	54.4	92.2	65.4	77.9	120	122	84.7	97.8	119
Cu	66.8	149	203	43.9	116	104	65.9	52.4	62.4	47.8	64.4
Zn	127	131	108	99.2	66.4	110	69.8	59.0	71.2	69.5	60.6
Ga	19.8	18.9	21.3	20.6	16.5	16.9	14.7	15.6	17.2	16.1	13.1
Ge	1.54	1.32	1.31	1.58	1.53	1.38	1.29	1.33	1.36	1.40	1.34
Rb	27.1	17.7	36.0	105	7.29	4.65	13.7	19.5	4.46	18.8	38.5
Sr	950	198	261	172	231	202	143	156	172	103	310
Y	45.6	44.2	49.2	47.5	28.7	28.4	27.0	26.4	33.3	27.5	23.5
Zr	142	165	194	143	81.1	82.7	84.5	86.5	96.9	76.0	76.5
Nb	17.4	4.32	14.1	6.95	3.44	3.12	2.91	2.92	3.56	2.74	4.03
Cs	1.41	0.92	1.79	4.66	0.41	0.08	0.47	0.50	0.24	0.71	0.59
Ba	355	262	564	277	90.2	36.1	33.4	53.3	19.8	103	99.1
La	18.9	21.6	24.1	6.77	7.20	7.50	3.63	3.62	4.17	3.56	3.65
Ce	44.2	48.4	54.9	19.1	17.7	17.6	11.1	11.1	12.7	10.6	10.1
Pr	5.96	6.84	7.35	3.03	2.39	2.40	1.78	1.78	2.07	1.69	1.57
Nd	25.8	29.8	31.9	15.3	11.2	11.0	9.20	9.19	10.9	8.93	7.95
Sm	7.09	8.01	8.39	5.08	3.39	3.31	3.11	3.08	3.72	3.08	2.64
Eu	2.13	2.11	2.44	1.70	1.14	1.17	1.12	1.09	1.29	1.13	0.92
Gd	8.26	8.97	9.43	6.66	4.17	4.15	4.01	3.92	4.85	4.06	3.41
Tb	1.40	1.48	1.54	1.19	0.72	0.71	0.71	0.69	0.86	0.72	0.61
Dy	9.23	9.71	10.1	8.17	4.95	4.91	4.76	4.64	5.88	4.91	4.17
Ho	2.02	2.09	2.21	1.87	1.13	1.12	1.08	1.07	1.33	1.10	0.97
Er	5.42	5.64	6.06	5.10	3.08	3.05	2.91	2.90	3.58	2.94	2.64
Tm	0.78	0.81	0.90	0.76	0.47	0.46	0.42	0.43	0.53	0.44	0.39
Yb	5.03	5.37	5.96	4.93	3.01	2.94	2.78	2.77	3.37	2.78	2.52
Lu	0.75	0.81	0.90	0.79	0.48	0.47	0.43	0.43	0.53	0.44	0.39
Hf	4.72	5.37	6.38	3.68	2.10	2.12	2.15	2.15	2.50	1.99	1.95
Ta	0.92	0.49	1.05	0.51	0.21	0.19	0.20	0.21	0.25	0.20	0.26
Pb	28.3	10.7	13.7	23.2	6.56	7.28	0.79	0.83	1.32	1.13	10.6
Th	2.48	4.00	5.16	0.64	1.43	1.77	0.28	0.28	0.34	0.33	0.41
U	0.85	2.13	2.86	0.72	0.39	0.45	0.17	0.15	0.18	0.10	0.23
Nb/Ta	18.9	8.75	13.3	13.8	16.7	16.2	14.2	14.2	14.1	13.9	15.6
Zr/Hf	30.1	30.7	30.5	38.8	38.7	39.0	39.3	40.1	38.8	38.1	39.2

*See grouping for meta-basaltic rocks from HGB of ONQ in section 6.4.2.1. †TFe_2O_3 - total Fe as Fe_2O_3.

Table D.5 Bulk-rock compositions for representative meta-sedimentary rocks from HGB of ONQ

Lithology	Meta-graywacke			Grt-Cld-Gln-Ph schist			Meta-chert	Marble
Sample	0807QL-058	0807QL-067	0807QL-069	0807QL-048	0807QL-050-3	0807QL-050-4	0807QL-030-2	0807QL-061
weight percent (wt.%)								
SiO_2	51.47	65.09	66.22	57.85	66.61	64.68	93.14	37.27
TiO_2	1.39	0.85	0.40	0.75	0.69	0.76	0.01	< 0.01
Al_2O_3	15.42	14.90	14.88	15.34	11.78	11.80	0.62	0.30
TFe_2O_3*	11.45	5.16	4.44	7.94	6.32	6.77	4.91	4.49
MnO	0.12	0.07	0.09	0.13	0.08	0.07	0.04	0.13
MgO	2.99	2.58	1.94	6.13	5.16	5.81	0.35	2.48
CaO	8.30	1.27	4.14	2.32	2.74	3.41	0.07	30.14
Na_2O	3.62	0.74	3.75	2.47	2.05	2.50	< 0.01	0.12
K_2O	1.86	5.61	1.71	2.52	1.68	1.16	0.06	0.02
P_2O_5	0.36	0.04	0.14	0.11	0.13	0.15	0.05	0.02
LOI	2.55	3.38	1.87	4.07	2.29	2.66	0.27	24.59
Total	99.53	99.69	99.58	99.63	99.53	99.77	99.52	99.56
parts per million (ppm)								
Li	15.7	21.2	3.53	49.2	43.2	43.9	1.88	1.66
Be	1.25	1.64	1.66	2.36	1.58	1.35	0.12	0.16
Sc	27.8	15.5	11.3	24.8	18.7	19.2	2.22	4.14
V	183	89.7	74.4	146	119	134	21.7	21.9
Cr	16.4	75.1	56.2	246	381	444	1931	1814
Co	37.5	13.3	13.2	33.1	25.4	27.1	67.9	44.8
Ni	27.4	34.8	30.1	230	183	206	800	643
Cu	23.3	24.6	13.0	36.1	34.9	25.8	14.8	4.79
Zn	98.2	34.0	23.8	81.4	66.6	71.6	54.0	30.4
Ga	19.5	19.8	15.9	18.9	13.5	13.8	1.03	0.53
Ge	1.69	1.52	1.32	1.55	1.34	1.60	0.81	0.60
Rb	45.0	186	73.0	100	68.4	48.3	1.77	0.75
Sr	476	102	310	143	165	187	1.74	149
Y	41.4	25.2	21.5	25.7	24.7	24.9	1.29	0.60
Zr	163	379	180	146	139	173	1.58	3.40
Nb	8.31	16.8	11.7	10.9	9.47	10.0	0.23	0.21
Cs	1.92	4.92	2.20	6.66	4.65	2.98	0.10	0.03
Ba	466	1323	433	510	304	206	36.6	7.77
La	23.2	44.5	25.9	20.7	22.3	25.2	1.01	0.29
Ce	49.2	96.2	47.3	43.7	46.7	52.6	1.43	0.50
Pr	6.14	10.7	4.86	5.27	5.62	6.33	0.22	0.07
Nd	25.8	39.4	16.9	20.7	21.9	24.5	0.91	0.27
Sm	6.14	7.48	3.36	4.56	4.81	5.23	0.20	0.07
Eu	1.83	1.62	0.92	1.06	1.07	1.11	0.05	0.02
Gd	6.71	6.36	3.35	4.57	4.64	4.89	0.20	0.08
Tb	1.08	0.83	0.52	0.70	0.71	0.74	0.03	0.01
Dy	7.09	4.79	3.35	4.49	4.50	4.63	0.20	0.09
Ho	1.59	0.96	0.76	0.98	0.97	0.99	0.04	0.02
Er	4.30	2.48	2.17	2.73	2.62	2.70	0.12	0.06
Tm	0.64	0.35	0.35	0.41	0.39	0.41	0.02	0.01
Yb	4.11	2.27	2.37	2.71	2.56	2.68	0.12	0.06
Lu	0.65	0.38	0.39	0.43	0.39	0.42	0.02	0.01
Hf	3.92	9.54	4.19	3.87	3.71	4.38	0.05	0.03
Ta	0.51	0.82	1.17	0.79	0.71	0.76	0.02	0.01
Pb	21.8	12.3	7.86	23.4	19.1	19.3	1.15	0.65
Th	6.42	23.6	11.0	8.78	8.33	9.95	0.22	0.03
U	1.09	1.18	1.94	1.62	1.42	1.62	0.09	0.25
Nb/Ta	16.2	20.5	10.0	13.8	13.4	13.1	13.7	14.3
Zr/Hf	41.4	39.8	43.0	37.8	37.3	39.4	31.5	114

*TFe_2O_3 - total Fe as Fe_2O_3.

Table D.6 Analytical results of representative mineral major element concentrations using EPMA

Sample	0807QL-038		0807QL-043		0807QL-057-2		0807QL -015-1	0807QL -057-2	0807QL -030-1	0807QL -048-2	0807QL -050-3	0807QL -047	0807QL -030-1	0807QL -050-3	0807QL -050-4	0807QL -003		
Analyzed No.	63	64	193	197	160	165	36	164	3	86	53	10	7	46	55	15	16	17
Mineral	Grt-c	Grt-r	Tiny Grt	Tiny Grt	Grt-c	Grt-c	Aug	Omp	Gln	Gln	Gln	Pg	Ph	Ph	Ph	Ep	Ep	Ep
weight percent (wt.%)																		
SiO_2	37.66	37.02	38.44	38.31	38.32	37.81	51.51	56.81	56.62	57.91	58.09	46.69	50.89	51.56	51.64	37.31	36.96	37.37
TiO_2	0.10	0.05	0.03	-	0.12	0.04	0.53	0.08	0.07	0.05	0.01	0.09	0.13	0.19	0.18	0.19	0.03	0.05
Al_2O_3	19.14	19.55	20.69	20.53	20.24	20.50	3.02	8.96	8.88	9.02	8.49	36.72	27.41	26.99	27.06	18.76	21.85	20.88
Cr_2O_3	-	0.03	0.02	-	0.03	-	0.54	0.01	0.02	0.05	0.09	0.18	-	0.22	0.14	-	-	0.01
FeO*	30.10	31.46	25.63	25.85	26.43	26.97	5.78	5.27	12.28	8.60	9.34	1.07	3.35	2.83	2.58	15.48	12.06	13.18
MnO	2.29	1.36	4.66	5.64	0.87	0.45	0.18	0.05	0.07	0.11	0.03	-	-	0.14	0.05	-	-	0.08
MgO	1.46	1.91	4.80	4.80	2.41	2.82	15.69	8.69	9.61	12.56	12.19	0.01	3.25	3.51	3.64	0.04	-	0.01
CaO	8.99	8.40	5.90	4.87	11.59	11.48	21.06	14.51	0.47	0.77	0.81	0.25	0.01	0.01	0.00	24.27	23.67	23.95
Na_2O	0.02	0.06	0.01	-	-	0.05	0.15	6.81	6.76	6.44	6.71	5.05	0.39	0.46	0.38	-	0.06	0.04
K_2O	0.02	-	0.01	0.01	0.01	-	-	-	0.02	0.01	0.03	0.41	9.30	9.13	9.04	-	-	0.00
Total	99.79	99.87	100.2	100.0	100.0	100.1	98.46	101.2	94.83	95.51	95.80	90.51	94.73	95.03	94.71	96.05	94.68	95.57
O	12	12	12	12	12	12	6	6	23	23	23	11	11	11	11	12.5	12.5	12.5
Si	3.05	3.00	3.02	3.04	3.04	3.00	1.92	2.02	8.10	8.07	8.12	3.11	3.41	3.43	3.43	3.18	3.11	3.15
Ti	0.01	0.00	0.00	-	0.01	0.00	0.02	0.00	0.01	0.00	-	0.00	0.01	0.01	0.01	0.01	0.00	0.00
Al	1.82	1.87	1.92	1.92	1.88	1.92	0.13	0.37	1.50	1.47	1.40	2.88	2.17	2.11	2.12	1.88	2.18	2.08
Cr	-	0.00	0.00	-	0.00	-	0.02	0.00	0.00	0.00	0.01	0.01	-	0.01	0.01	-	-	0.00
Fe	2.04	2.14	1.69	1.70	1.75	1.79	0.18	0.16	1.47	1.01	1.08	0.06	0.19	0.15	0.14	1.10	0.85	0.93
Mn	0.16	0.10	0.31	0.37	0.06	0.03	0.01	0.00	0.01	0.01	0.00	-	-	0.01	0.00	-	-	0.01
Mg	0.18	0.23	0.56	0.56	0.29	0.34	0.87	0.46	2.05	2.60	2.53	0.00	0.32	0.35	0.36	0.01	-	0.00
Ca	0.78	0.73	0.49	0.41	0.98	0.97	0.84	0.55	0.07	0.12	0.12	0.02	-	-	-	2.21	2.14	2.16
Na	0.00	0.01	0.00	-	-	0.01	0.01	0.47	1.86	1.75	1.82	0.65	0.05	0.06	0.05	-	0.01	0.01
K	0.00	-	0.00	0.00	-	-	-	-	0.00	0.00	0.00	0.04	0.79	0.77	0.77	-	-	-
Total	8.04	8.08	8.01	8.01	8.01	8.06	3.99	4.03	15.07	15.05	15.09	6.77	6.93	6.91	6.90	8.38	8.29	8.33

(Continued)

Table D.6 (continued)

Sample	0807QL-058		0807QL-057-2	0807QL-007-1					0807QL-014	0807QL-071-1	0807QL-048	0807QL-014	
Analyzed No.	120	123	167	2	3	8	9	10	42	185	82	41	43
Mineral	Ep	Ep	Ep	Lws	Lws	Lws	Lws	Lws	Chl	Chl	Cld	Pmp	Pmp
weight percent (wt.%)													
SiO_2	37.46	37.52	38.21	38.98	39.55	38.83	38.99	39.14	27.85	29.04	24.85	37.47	37.55
TiO_2	-	0.06	0.07	0.59	0.05	0.67	1.06	0.70	0.05	0.03	0.04	-	0.09
Al_2O_3	21.41	21.69	26.14	29.58	29.90	28.94	29.13	29.52	17.84	19.35	38.35	23.82	22.99
Cr_2O_3	-	0.05	0.08	0.08	-	0.09	0.05	0.00	0.01	0.06	0.32	0.06	-
FeO	12.87	11.93	6.06	0.60	0.46	0.42	0.42	0.52	24.71	23.64	18.85	2.86	3.93
MnO	0.45	0.22	-	0.08	0.03	-	-	-	0.32	0.19	0.19	0.25	0.91
MgO	0.07	-	0.02	-	0.00	0.01	-	-	16.49	18.02	7.46	3.00	3.13
CaO	23.15	24.09	24.78	17.27	16.87	16.83	16.80	17.56	0.13	0.22	-	22.62	22.57
Na_2O	-	0.01	0.01	0.04	0.09	0.20	0.18	0.02	0.05	0.17	-	0.00	0.22
K_2O	-	-	0.01	0.05	0.08	0.18	0.22	0.02	0.04	0.02	0.01	0.01	0.01
Total	95.40	95.57	95.38	87.31	87.05	86.16	86.85	87.51	87.48	90.74	90.17	90.09	91.45
O	12.5	12.5	12.5	8	8	8	8	8	14	14	6	12	12
Si	3.15	3.14	3.09	2.07	2.10	2.09	2.08	2.08	2.93	2.91	1.03	3.02	3.02
Ti	-	0.00	0.01	0.02	0.00	0.03	0.04	0.03	0.00	0.00	0.00	-	0.01
Al	2.13	2.14	2.49	1.85	1.87	1.84	1.83	1.84	2.21	2.28	1.87	2.27	2.18
Cr	-	0.00	0.01	0.00	-	0.00	0.00	-	0.00	0.01	0.01	0.00	-
Fe	0.90	0.84	0.41	0.03	0.02	0.02	0.02	0.02	2.17	1.99	0.65	0.19	0.26
Mn	0.03	0.02	-	0.00	0.00	-	-	-	0.03	0.02	0.01	0.02	0.06
Mg	0.01	-	0.00	-	-	0.00	-	-	2.59	2.69	0.46	0.36	0.37
Ca	2.09	2.16	2.15	0.98	0.96	0.97	0.96	1.00	0.01	0.02	-	1.96	1.94
Na	-	0.00	0.00	0.00	0.01	0.02	0.02	0.00	0.01	0.03	-	-	0.03
K	-	-	0.00	0.00	0.01	0.01	0.01	0.00	0.00	0.00	-	0.00	-
Total	8.30	8.30	8.15	4.98	4.97	4.98	4.97	4.97	9.96	9.95	4.04	7.82	7.89

*FeO - total Fe as FeO.

Table D.7 Compositions of representative anhydrous minerals using LA-ICPMS

Analyzed No.	201003 21B034	201003 21B035	201003 17B008	201003 16A02	201003 16A026	201003 30B030	201003 29A063	2010031 5B087	201003 15B119	2010031 7B127
Sample	0807QL-015-2		0807QL -057-1	0807QL-051-2		0807Q L-067	0807Q L-072	0807QL-050-2	0807QL -050-3	0807QL -072
Mineral	Ab	Aug	Omp	Grt-m	Grt-c	Ttn in Ph	Ttn in Rt	Rt	Rt	Rt
weight percent (wt.%)										
SiO_2	68.91	50.99	53.9	38.98	38.07	29.37	29.09	< 0.37*	< 0.33	< 0.35
TiO_2	n.d.	0.44	0.03	0.07	0.08	37.28	37.75	98.25	98.18	98.63
Al_2O_3	19.43	2.68	10.0	21.05	21.56	1.94	1.65	0.002	0.003	0.01
FeO†	< 0.02	6.84	5.51	30.01	29.95	0.66	0.11	0.48	0.40	0.27
MnO	0.001	0.19	0.15	0.33	0.35	0.02	0.01	< 0.0002	< 0.0003	< 0.0002
MgO	< 0.004	15.73	8.05	2.32	2.27	0.09	0.00	0.007	0.01	0.007
CaO	0.23	20.83	13.7	7.02	7.57	30.19	30.94	< 0.06	< 0.09	< 0.13
Na_2O	11.37	0.53	7.83	0.02	0.02	0.05	0.02	0.002	< 0.003	< 0.007
K_2O	0.04	0.01	< 0.002	< 0.002	< 0.002	0.01	< 0.005	< 0.001	< 0.002	< 0.002
P_2O_5	< 0.11	< 0.04	< 0.02	< 0.06	< 0.06	0.10	< 0.11	< 0.04	< 0.03	< 0.14
Total	99.98	98.24	53.9	99.80	99.87	99.71	99.56	98.74	98.59	98.92
parts per million (ppm)										
Li	< 14.7	< 4.68	33.0	1.22	0.70	n.d.	n.d.	< 0.44	< 0.45	< 0.89
Be	< 19.6	< 6.40	0.65	< 2.92	n.d.	7.22	3.99	< 1.05	0.56	0.46
Sc	< 2.59	127	62.3	64.4	72.6	2.29	3.12	0.56	1.36	2.54
V	< 9.56	354	371	55.5	61.0	130	526	938	701	1106
Cr	< 28.3	2883	1330	120	36.6	38.4	508	1612	1939	1303
Co	< 0.95	43.1	15.2	97.2	95.0	< 0.67	0.23	< 0.10	< 0.14	< 0.12
Ni	6.90	116	17.9	< 3.40	< 3.25	2.90	n.d.	< 2.45	< 3.67	< 2.33
Cu	17.4	3.33	5.40	< 2.38	< 2.53	6.07	7.92	3.43	3.65	4.21
Zn	< 4.04	40.7	51.8	132	139	6.59	4.48	14.4	13.8	5.16
Ga	8.31	5.48	6.17	5.19	5.61	1.71	1.07	< 0.16	< 0.19	< 0.23
Ge	< 7.76	3.16	0.45	6.16	4.86	< 6.27	n.d.	< 1.28	< 1.48	< 2.33
Rb	< 0.89	< 0.36	< 0.08	< 0.09	< 0.08	< 0.42	< 0.40	< 0.06	< 0.07	< 0.12
Sr	28.7	17.4	0.99	0.04	0.03	259	21.5	4.06	4.23	2.53
Y	0.128	17.6	0.11	164	188	736	0.14	0.28	0.33	0.17
Zr	< 1.06	17.2	1.27	5.16	2.71	5.96	17.3	40.0	39.2	31.7
Nb	n.d.	< 0.04	0.02	n.d.	< 0.03	245	238	1151	1141	244
Cs	< 0.29	0.31	< 0.03	< 0.03	< 0.02	< 0.08	< 0.12	< 0.02	< 0.03	< 0.02
Ba	30.5	4.19	0.05	< 0.13	0.05	3.55	1.03	0.07	0.11	< 0.10
La	n.d.	0.29	0.003	0.12	0.03	4.08	0.17	0.002	n.d.	0.002
Ce	0.02	1.48	0.01	0.16	0.02	31.3	0.24	0.005	< 0.009	< 0.01
Pr	< 0.03	0.36	< 0.009	< 0.01	< 0.008	8.61	0.03	0.001	< 0.007	< 0.01
Nd	0.04	2.78	0.02	0.14	0.22	66.8	0.16	0.008	0.01	< 0.06
Sm	n.d.	1.51	0.02	0.21	0.08	50.5	< 0.19	< 0.04	0.007	0.02
Eu	< 0.04	0.54	0.004	0.18	0.13	18.2	0.07	0.002	0.02	n.d.
Gd	< 0.35	2.21	< 0.03	2.61	2.16	96.7	0.08	0.009	0.02	< 0.11
Tb	< 0.02	0.45	0.001	1.57	1.49	22.1	< 0.02	0.003	n.d.	< 0.01
Dy	< 0.10	3.22	0.02	22.2	22.8	166	0.03	0.01	n.d.	n.d.
Ho	< 0.02	0.68	0.005	6.23	6.99	29.6	0.01	< 0.006	0.001	0.002
Er	< 0.07	1.99	0.02	19.4	23.5	70.7	< 0.05	n.d.	0.01	n.d.
Tm	n.d.	0.30	0.004	2.76	3.27	6.22	0.01	n.d.	< 0.007	< 0.01
Yb	0.01	1.89	0.04	16.6	20.6	29.0	< 0.07	0.006	< 0.03	< 0.05
Lu	0.003	0.29	< 0.01	2.25	2.57	3.60	0.002	0.003	n.d.	n.d.
Hf	< 0.12	0.79	0.21	0.07	0.05	0.61	0.78	2.08	1.82	2.39
Ta	n.d.	< 0.01	< 0.01	0.002	0.002	21.2	12.2	88.4	74.8	12.6
Pb	< 0.08	0.20	0.06	< 0.03	< 0.02	30.3	0.67	0.08	0.15	< 0.05
Th	n.d.	< 0.02	<0.03	n.d.	0.003	1.40	< 0.03	< 0.01	0.004	< 0.02
U	n.d.	0.008	0.01	< 0.01	0.002	2.61	< 0.03	0.04	0.14	0.03

*< value: lower than detection limits. †FeO: total Fe as Fe^{2+}. These are as used in the following tables. See abbreviations used in Abbreviation List.

Table D.8 Trace element contents (in ppm) of representative hydrous minerals using LA-ICPMS

Analyzed No.	201003 29A031	201003 29A030	2010031 2A017	201003 17B093	201003 17B105	2010031 7B037	201003 15B066	201003 15B067	2010031 1B019	2010031 1B025
Sample	0807QL-007-2		0807QL -037	0807QL-069		0807QL -058	0807QL-049-1		0807QL -030-1	0807QL -031
Mineral	Lws	Lws	Ep	Ep-r	Ep-c	Ep	Ap	Ap	Gln	Gln
Li	< 12.6	< 10.3	0.37	< 0.61	< 0.62	0.41	0.54	0.06	73.6	69.6
Be	10.8	< 12.1	n.d.	n.d.	1.23	1.20	n.d.	0.05	1.28	n.d.
Sc	< 5.18	< 4.44	89.3	11.8	6.53	122	0.25	0.19	356	93.4
V	210	710	467	57.5	59.5	273	2.96	3.90	235	337
Cr	76.3	182	177	36.8	28.2	< 13.8	1.43	0.36	47.5	18.7
Co	< 0.97	0.80	0.09	0.44	0.34	0.55	0.29	0.02	45.9	45.5
Ni	< 8.66	< 5.79	1.51	< 2.11	< 2.25	< 1.05	2.28	n.d.	60.5	46.1
Cu	< 8.26	< 7.34	n.d.	< 1.31	< 2.05	3.01	2.72	9.93	4.18	4.21
Zn	< 5.27	< 7.72	3.18	1.99	< 2.00	4.68	0.45	0.39	101	119
Ga	19.1	30.5	64.6	34.2	36.5	53.6	0.03	n.d.	10.1	9.09
Ge	< 10.0	< 7.27	6.40	3.38	6.11	21.6	0.11	n.d.	3.75	< 2.32
Rb	< 0.92	< 0.55	0.10	< 0.11	< 0.12	0.07	0.03	0.0003	< 0.19	< 0.29
Sr	813	158	2216	835	675	2623	386	506	0.13	0.34
Y	71.4	35.0	177	58.3	10.9	460	43.8	54.0	< 0.05	0.07
Zr	0.21	< 0.33	4.70	2.96	1.49	31.1	0.08	0.01	< 0.50	0.46
Nb	n.d.	< 0.37	0.008	0.004	0.02	< 0.33	0.001	0.005	0.01	0.12
Cs	< 0.32	< 0.14	n.d.	< 0.02	< 0.02	< 0.02	0.002	n.d.	< 0.05	< 0.04
Ba	6.90	< 0.36	5.48	3.35	2.22	10.6	0.64	0.69	0.02	< 0.18
La	2.28	4.29	182	0.003	0.02	952	3.82	1.47	n.d.	n.d.
Ce	8.38	13.9	396	0.008	0.006	1393	5.42	4.96	n.d.	< 0.02
Pr	1.69	2.65	49.2	< 0.01	n.d.	140	1.52	0.87	< 0.02	0.008
Nd	11.8	15.1	202	0.023	0.01	564	7.63	5.74	n.d.	< 0.08
Sm	5.06	4.54	44.2	0.009	0.02	100	2.79	2.77	0.03	< 0.09
Eu	2.20	1.75	6.59	< 0.02	0.01	52.7	0.72	0.90	0.004	0.004
Gd	7.05	6.62	38.6	0.11	0.02	116	3.71	5.80	< 0.103	0.09
Tb	1.29	1.01	5.70	0.09	< 0.02	14.3	0.73	1.17	< 0.031	0.004
Dy	10.3	6.37	32.7	3.14	0.66	79.5	5.38	8.47	n.d.	0.008
Ho	2.98	1.15	6.35	1.67	0.31	14.6	1.44	1.82	0.004	0.01
Er	10.6	3.13	14.5	9.27	1.64	32.7	6.02	6.36	n.d.	0.02
Tm	1.69	0.30	1.98	1.90	0.27	3.49	0.96	0.91	< 0.01	0.008
Yb	12.5	1.92	11.3	16.2	1.83	19.3	7.17	6.70	0.01	< 0.06
Lu	2.27	0.21	1.37	2.78	0.31	2.38	1.12	1.10	n.d.	0.01
Hf	0.01	< 0.08	0.26	< 0.10	0.03	0.99	n.d.	n.d.	< 0.06	0.06
Ta	< 0.03	0.006	n.d.	0.003	< 0.02	n.d.	0.001	0.003	< 0.02	0.007
Pb	1.36	0.51	106	11.0	10.2	87.3	8.38	12.7	< 0.08	0.14
Th	< 0.03	0.07	71.8	0.003	0.003	12.2	1.20	0.04	< 0.02	< 0.03
U	0.02	< 0.03	12.0	< 0.02	< 0.03	4.06	0.04	0.21	< 0.02	< 0.03

(Continued)

Table D.8 (continued)

Analyzed No.	20100316A028	20100311B088	20100312A007	20100315B101	AUG15A27	20100312A038	20100313B053	20100311B054	20100314A006	AUG14C10	20100321B028
Sample	0807QL-051-2	0807QL-035	0807QL-036	0807QL-050-2	0807QL- 043	0807QL-038	0807QL-041	0807QL-033	0807QL-045-2	0807QL-014	0807QL-012
Mineral	Pg incl. in Gln	Pg	Pg	Ph in meta-sediment		Ph in mafic blueschist		Chl	Cld	Pmp	Pmp
Li	15.7	31.5	24.3	30.4	31.6	15.6	12.3	75.9	5.26	11.9	3.99
Be	4.59	2.67	3.37	4.06	8.18	< 2.61	5.47	0.50	0.39	0.18	< 3.95
Sc	3.23	30.4	43.5	2.54	1.43	4.72	8.42	3.13	32.0	2.69	3.23
V	82.0	354	265	274	377	590	827	220	130	481	305
Cr	180	73.8	360	1248	208	23.9	38.0	72.1	127	17.3	75.8
Co	0.77	5.98	2.05	9.87	24.5	10.6	11.2	89.2	132	43.9	17.1
Ni	7.48	7.18	7.14	91.5	347	6.86	30.3	112	63.9	152	33.0
Cu	6.43	28.8	3.91	< 2.86	< 0.27	< 2.90	< 1.63	5.08	< 2.28	< 0.30	< 3.16
Zn	5.59	20.1	5.08	45.1	75.3	68.4	55.8	303	408	81.8	23.2
Ga	37.5	28.0	36.6	99.0	207	49.7	134	18.0	43.9	29.7	29.0
Ge	< 1.98	< 3.60	< 3.41	< 1.38	0.81	< 3.44	< 3.19	2.22	4.98	3.72	< 2.25
Rb	3.43	34.2	41.7	387	367	227	196	< 0.14	< 0.31	0.18	< 0.40
Sr	337	90.8	90.5	199	172	9.72	28.84	0.16	< 0.06	6.57	5.43
Y	< 0.03	0.08	0.05	< 0.05	0.05	0.05	< 0.06	0.02	< 0.06	52.07	51.6
Zr	< 0.28	< 0.46	< 0.54	0.28	0.24	<0.43	0.20	0.20	< 1.20	0.98	< 0.30
Nb	< 0.04	< 0.06	0.05	0.39	0.88	0.64	0.14	< 0.04	< 0.07	0.00	0.01
Cs	0.17	1.12	1.28	25.9	25.9	12.3	9.60	< 0.04	< 0.10	0.10	< 0.09
Ba	51.9	207	520	1729	2968	2893	3195	0.35	0.18	1.27	4.17
La	0.002	n.d.	0.01	0.003	0.01	0.01	n.d.	n.d.	n.d.	0.03	0.18
Ce	0.006	n.d.	0.02	n.d.	< 0.02	0.003	n.d.	0.003	0.005	0.09	0.57
Pr	0.002	0.003	n.d.	n.d.	< 0.02	0.002	n.d.	n.d.	0.007	< 0.03	0.10
Nd	0.009	0.02	n.d.	n.d.	0.02	0.01	0.03	n.d.	n.d.	0.29	0.79
Sm	n.d.	n.d.	n.d.	< 0.07	< 0.12	< 0.12	n.d.	n.d.	0.02	0.41	0.82
Eu	0.008	< 0.04	0.01	< 0.02	< 0.05	0.004	0.02	n.d.	< 0.04	0.31	0.51
Gd	< 0.07	< 0.18	< 0.13	0.03	< 0.17	0.06	0.02	< 0.08	n.d.	2.09	2.46
Tb	0.003	0.005	n.d.	n.d.	0.01	0.002	n.d.	0.004	n.d.	0.65	0.68
Dy	0.01	n.d.	n.d.	n.d.	0.02	n.d.	< 0.10	0.007	0.01	7.23	5.99
Ho	0.001	0.009	0.003	< 0.01	0.004	< 0.02	0.003	n.d.	< 0.02	1.90	1.74
Er	n.d.	0.008	0.01	< 0.03	< 0.07	n.d.	n.d.	0.01	0.02	5.07	6.21
Tm	< 0.01	< 0.03	0.004	< 0.01	< 0.02	0.004	0.003	n.d.	< 0.02	0.85	0.96
Yb	0.01	< 0.13	0.02	< 0.06	< 0.13	0.01	n.d.	0.008	0.01	6.12	7.14
Lu	n.d.	< 0.02	0.02	< 0.01	n.d.	< 0.02	< 0.03	0.002	n.d.	0.87	0.97
Hf	< 0.04	0.03	n.d.	< 0.04	< 0.05	0.02	n.d.	0.007	0.01	< 0.08	0.01
Ta	< 0.01	0.003	0.01	< 0.01	< 0.01	< 0.02	0.003	0.002	< 0.02	< 0.01	0.002
Pb	8.15	2.07	6.79	31.1	40.0	0.49	1.77	< 0.04	0.04	0.31	0.28
Th	< 0.02	0.03	< 0.03	< 0.02	< 0.02	0.003	< 0.04	< 0.02	0.02	0.01	0.02
U	0.002	0.02	< 0.05	< 0.04	< 0.02	0.01	n.d.	< 0.03	0.005	< 0.01	< 0.01

Table D.9 Petrography of studied rocks from the North Qilian Mountain, China

Sample	Lithology	GPS	Mineral assemblage
Low-grade blueschist metamorphic belt, LGB			
Baishuiquangou, Jiugequan, Sunan; sampling location 1 in Fig. 2.4b			
0807QL-003	Epidosite	N38°50′58 E99°18′27	Ep (> 60%) + Qz (~ 20%) + Ca (~ 10%) + Opq (< 10%)
0807QL-005	Pumpellyite blueschist		Foliated; Gln (~ 58%) + Pmp (~ 30%) + Qz vein (5%) + Ca (2%) + Fine grains (~ 5%)
0807QL-007-1	Lawsonite glaucophanite	N38°51′01 E99°18′30	Gln (~ 55%) + Lws (~ 10%) + Fine grains (~ 35%)
0807QL-007-2	Lawsonite glaucophanite		Gln (~ 40%) + Lws (~ 10%) + Pmp (~ 4%) + Fine grains (~ 45%)
Tadungou, Jiugequan, Sunan; sampling location 1 in Fig. 2.4b			
0807QL-010	Glaucophane pumpellyite schist	N38°50′04 E99°19′20	Foliated; Pmp (~ 50%) + Gln (~ 30%) + Fine grains (~ 19%) + minor Lws
0807QL-011	Glaucophane-bearing pumpellyite schist		Foliated; Pmp (~ 65%) + Gln (~ 5%) + Ca (~ 8%) + Fine grains (~ 20%)
0807QL-012	Lawsonite-bearing pumpellyite blueschist		Foliated; Pmp (~ 30%) + Gln (~ 65%) + Lws (~ 3%)
0807QL-014	Glaucophane-bearing pumpellyite schist	N38°50′09 E99°19′22	Foliated; Pmp (~ 60%) + Gln (~ 1%) + Qz (~ 10%) + Ab (~ 5%) + Chl (< 15%) + minor Lws
0807QL-015-2	Epidosite	N38°50′16 E99°19′20	Ep (~ 40%) + Aug (~ 10%) + Pmp (~ 2%) + Ab (~ 5%) + Qz (~ 10%) + Ca (~ 25%) + Opq (< 8%)
0807QL-022-1	Epidosite		Ep (> 65%) + Qz (~ 35%) + minor Ca
High-grade blueschist/eclogites metamorphic belt, HGB			
Qingshuigou, Qilian County; sampling location 3 in Fig. 2.4b			
0807QL-030-1	Meta-graywacke	N38°18′52 E99°51′01	Foliated; Gln (~ 15%) + Qz (~ 30%) + Ca (~ 20%) + Mica (~ 7%) + Ep (~ 5%) + Chl (~ 20%) + Rt (< 3%)
0807QL-030-2	Meta-chert		Foliated; Qz (~ 96%) + Opq (~ 2.5%) + Chl (~ 1%) + Mica (~ 0.5%) + minor Gln
0807QL-031	Meta-graywacke		Foliated; Gln (~ 30%) + Mica (~ 15%) + Ep (~ 10%) + Qz (~ 25%) + Ca (~ 15%) + Chl (~ 5%; replaced Gln)
0807QL-032	Cld-Ph schist		Foliated; Cld porphyroblast (~ 15%) + Mica (> 15%) + Ca (~ 17%) + Qz (~ 45%) + Chl (< 5%; replaced Cld) + Ap
0807QL-033	Meta-graywacke		Foliated; Gln (~ 20%) + Mica (~ 5%) + Ep (~ 18%) + Qz (~ 22%) + Ca (~ 20%) + Chl (~ 15%) + Rt (< 2%)

(Continued)

Table D.9 (continued)

Sample	Lithology	GPS	Mineral assemblage
0807QL-034	Chloritoid-glaucophane schist		Foliated; Cld porphyroblast (~ 20%) + Mica (~ 15%) + Qz (~ 40%) + Chl (~ 10%) + Ca (~ 5%) + Opq (~ 8%) + Rt + Ap + Gln
0807QL-035	Meta-graywacke		Foliated; Gln (~ 20%) + Mica (~ 15%) + Ep (~ 10%) + Qz (~ 37%) + Ca (~ 6%) + Chl (~ 12%)
0807QL-036	Meta-graywacke	N38°18′52 E99°51′01	Foliated; Mica (~ 20%) + Qz (~ 35%) + Ca (~ 35%) + Chl (~ 10%); no glaucophane found
0807QL-038	Blueschist		Foliated; Grt porphyroblast (~ 5%) + Gln (~ 45%) + Ph (~ 6%) + Ep (~ 40%) + Qz (~ 4%) + Chl (~ 0.5%) + minor Rt
0807QL-040-1	Blueschist		Foliated; Grt porphyroblast (~ 8%) + Gln (~ 50%) + Ep (~ 15%) + Qz (~ 12%) + Chl (~ 6%) + Rt (~ 1%)
0807QL-041	Blueschist		Foliated; Grt porphyroblast (~ 13%) + Gln (~ 38%) + Ph (~ 20%) + Ep (~ 5%) + Qz (~ 18%) + Chl (~ 4.5%) + Rt (~ 1.5%)
Shangxiangzigou, Qilian County; sampling location 3 in Fig. 2.4b			
0807QL-058	Meta-graywacke		Gln (~ 28%) + Mica (~ 16%) + Ep (~ 44%) + Qz (~ 8%) + Chl (~ 2%) + Ap + Rt
0807QL-059	Eclogitic blueschist	N38°15′49 E99°55′04	Transition from eclogite (omphacite-rich) to blueschist (epidote-rich); Grt porphyroblast (~ 15%) + Omp (~ 10%) + Gln (~ 35%) + Epi (~ 30%) + Qz (~ 3%) + Chl (~ 2%) + Rt (replaced by Ttn) + Opq (5%; pyrite?)
0807QL-061	Marble		Ca (~ 65%) + Qz (~ 20%) + Gln (~ 3%) + Ep (~ 10%)
0807QL-065	Cld-Grt-Gln schist		Foliated; Grt porphyroblast (~ 17%) + Cld porphyroblast (~ 6%) + Gln (~ 55%) + Ep (~ 1%) + Chl (~ 8%) + Rt (~ 3%) + Qz (~ 10%) + Mica
0807QL-066-1	Quartz mica schist		Foliated; Mica (~ 14%) + Ep (~ 17%) + Qz (~ 60%) + Chl (~ 8%) + Ap + Gln
0807QL-067	Meta-graywacke	N38°16′48 E99°55′00	Foliated; Gln (~ 5%) + Mica (~ 47%) + Ep (~ 3%) + Grt (~ 4%) + Qz (~ 40%) + Rt (~ 0.5%) + Ttn (~ 0.5%)
0807QL-068	Blueschist		Grt (~ 18%) + Gln (~ 50%) + Mica (~ 1%) + Ep (~ 15%) + Ca (~ 1%) + Qz (~ 1%) + Chl (~ 2%) + Rt (2%; overprinted by Ttn)
0807QL-069	Meta-graywacke		Foliated; Grt (~ 3%) + Gln (~ 10%) + Mica (~ 10%) + Ep (~ 20%) + Qz (~ 50%) + Chl (~ 5%) + Ap
0807QL-071-1	Meta-graywacke		Foliated; Gln (~ 20%) + Mica (~ 35%) + Ep (~ 4%) + Ca (~ 10%) + Qz (~ 30%) + Chl (~ 1%)

(Continued)

Table D.9 (continued)

Sample	Rock name	GPS	Mineral assemblage
Baishiya, Qilian County; sampling location 4 in Fig. 2.4b			
0807QL-042	Meta-graywacke		Foliated; Grt (~ 15%) + Gln (~ 20%) + Mica (~ 13%) + Ep (~ 10%) + Qz (~ 30%) + Chl (~ 2%) + Ca (~ 10%) + Rt
0807QL-043	Meta-chert		Foliated; Qz (~ 83%) + Grt (~ 10%) + Mica (~ 5%) + Chl (~ 2%) + Rt (~ 0.5%) + Ap + Ca (rare)
0807QL-044-1	Grt-Cld-Gln-Ph schist		Foliated; Cld (~ 5%) + Gln (~ 10%) + Mica (~ 20%) + Ep (~ 10%) + Qz (~ 35%) + Chl (~ 5%) + Ap + Grt + Tur
0807QL-044-2	Grt-Cld-Ph schist		Foliated; Mica (~ 40%) + Ep (~ 25%) + Qz (~ 25%) + Grt (~ 1.5%) + Cld (~ 1.5%) + Gln (~ 1%) + Chl (~ 5%) + Ap (~ 2%)
0807QL-045-1	Cld-Ph schist		Foliated; Cld (~ 1.5%) + Mica (~ 25%) + Chl (~ 20%) + Ep (~ 20%) + Qz (~ 20%) + Ca (~ 10%) + rare Gln
0807QL-045-2	Grt-Cld-Gln-Ph schist		Grt (~ 8%) + Cld (~ 3%) + Mica (~ 25%) + Ep (~ 25%) + Qz (~ 20%) + Chl (~ 20%)
0807QL-045-3	Meta-graywacke		Foliated; Mica (~ 50%) + Chl (~ 18%) + Qz (~ 12%) + Ep (~ 18%) + Ca (~ 10%) + Ap (~ 2%)
0807QL-045-4	Meta-graywacke		Highly carbonated and chloritized; Mica (~ 15%) + Qz (~ 5%) + Ca (~ 20%) + Ep (~ 20%) + Chl (~ 40%)
0807QL-045-5	Meta-graywacke	N38°04′34.9 E100°32′49.5	Ca (~ 20%) + Ep (~ 20%) + Mica (~ 15%) + Qz (~ 5%) + Chl (~ 40%) + Ap
0807QL-046-1	Meta-graywacke		Foliated; Grt (~ 5%) + Ep (~ 30%) + Mica (~ 18%) + Qz (~ 15%) + Chl (~ 24%) + Ca (~ 5%) + Opq (2%; pyrite?) + Rt (~ 1%)
0807QL-046-2	Meta-graywacke		Foliated; Grt (~ 1%) + Ep (~ 20%) + Mica (~ 15%) + Qz (~ 27%) + Chl (17%) + Ca (~ 15%) + Opq (~ 5%; pyrite) + Ap
0807QL-047	Grt-Cld-Gln-Ph schist		Foliated; Grt (~ 17%) + Gln (~ 5%) + Ep (~ 30%) + Mica (~ 30%) + Qz (~ 10%) + Rt (~ 1%) + Ca (~ 3%) + Chl (~ 3%) + Ap + Cld
0807QL-048	Grt-Cld-Gln-Ph schist		Foliated; Grt (~ 10%) + Cld (~ 5%) + Gln (~ 10%) + Mica (~ 15%) + Ep (~ 25%) + Ca (~ 2%) + Qz (~ 23%) + Chl (~ 10%) + Opq + Rt
0807QL-049-1	Meta-graywacke		Foliated; Grt (~ 6%) + Gln (~ 10%) + Mica (~ 15%) + Ep (~ 20%) + Qz (~ 45%) + Ca (~ 3%) + Chl + Rt (~ 2%) + Ap
0807QL-049-2	Grt-Cld-Gln-Ph schist		Foliated; Grt (~ 8%) + Gln (~ 15%) + Mica (~ 10%) + Ep (~ 10%) + Qz (~ 50%) + Ca (~ 3%) + Chl (~ 3%) + Rt (~ 1%) + Cld + Tur
0807QL-050-2	Meta-graywacke		Foliated; Grt (~ 15%) + Gln (~ 20%) + Mica (~ 15%) + Ep (~ 10%) + Qz (~ 29%) + Ca (~ 5%) + Chl (~ 3%) + Rt (~ 3%)

(Continued)

Table D.9 (continued)

Sample	Rock name	GPS	Mineral assemblage
0807QL-050-3	Grt-Cld-Gln-Ph schist		Foliated; Grt (~ 7%) + Cld (~ 8%) + Gln (~ 20%) + Ep (~ 8%) + Mica (~ 15%) + Qz (~ 40%) + Chl (~ 1.5%) + Rt (~ 0.5%) + Ap + Tur
0807QL-050-4	Grt-Cld-Gln-Ph schist	N38°04′34.9 E100°32′49.5	Foliated; Grt (~ 7%) + Cld (~ 6%) + Gln (~ 15%) + Ep (~ 14%) + Qz (~ 50%) + Chl (~ 3%) + Ca (~ 1%) + Rt (~ 1%)
0807QL-051-1	Grt-Cld-Gln-Pg schist		Foliated; Grt (~ 15%) + Mica (~ 30%) + Gln (~ 25%) + Ep (~ 15%) + Cld (~ 5%) + Rt (~ 2%) + Chl (~ 3%) + Qz (~ 5%) + Ca
0807QL-051-2	Grt-Cld-Gln-Pg schist		Foliated; Grt (~ 15%) + Cld (~ 6%) + Gln (~ 10%) + Mica (~ 12%) + Ep (~ 45%) + Chl (~ 5%) + Qz (~ 5%)
0807QL-053-1	Eclogitic blueschist		Grt (~ 15%) + Omp (~ 25%) + Ep (~ 40%) + Ph (~ 6%) + Qz (~ 5%) + Ca (~ 3%) + Chl (~ 2%) + Act (~ 4%)
0807QL-053-2	Eclogitic blueschist		Grt (~ 15%) + Omp (~ 27%) + Ep (~ 30%) + Ph (~ 8%) + Qz (~ 5%) + Ca (~ 7%) + Chl (~ 1%) + Act (~ 5%)
0807QL-054	Meta-graywacke		Foliated; Grt (~ 10%) + Gln (~ 20%) + Mica (~ 25%) + Qz (~ 15%) + Ep (~ 25%; some are green with clear zoning) + Chl (~ 2%) + Rt (~ 2%) + Ap
0807QL-055	Meta-graywacke	N38°04′55.1 E100°33′4.4	Foliated; Ep (~ 35%) + Gln (~ 20%) + Qz (~ 10%) + Chl (~ 10%) + Ca (~ 25%)
0807QL-056	Blueschist		Foliated; Grt (~ 8%) + Gln (~ 43%) + Ph (~ 18%) + Ep (~ 20%) + Ca (~ 3%) + Qz (~ 5%) + Chl (~ 1%) + Rt (~ 2%)
0807QL-057-1	Eclogitic blueschist		Grt (~ 15%) + Omp (~ 25%) + Ep (~ 15%) + Gln (~ 25%) + Ph (~ 1%) + Qz (~ 10%) + Ca (~ 3%) + Chl (~ 3%) + Rt (~ 1%) + Ttn (~ 1%)
0807QL-057-2	Eclogitic blueschist		Grt (~ 18%) + Omp (~ 20%) + Gln (~ 30%) + Ph (? ~ 7%) + Ep (~ 20%) + Qz (~ 5%)
0807QL-072	Amphibolite	N38°14′23.1 E100°34′3.3	Grt (~ 15%) + Act (~ 45%) + Ep (~ 25%) + Qz (~ 6%) + Rt (~ 4%) + Chl (~ 5%)

REFERENCES

Ai, Y. L., Zhang, L. F., Li, X. P. & Qu, J. F. (2006). Geochemical characteristics and tectonic implications of HP-UHP eclogites and blueschists in Southwestern Tianshan, China. *Progress in Natural Science* **16**, 624 - 632.

Allègre, C. J., Hart, S. R. & Minster, J.-F. (1983). Chemical structure and evolution of the mantle and continents determined by inversion of Nd and Sr isotopic data, I. Theoretical methods. *Earth and Planetary Science Letters* **66**, 177-190.

Allen, M. B., Windley, B. F. & Chi, Z. (1993). Paleozoic Collisional Tectonics and Magmatism of the Chinese Tien-Shan, Central-Asia. *Tectonophysics* **220**, 89-115.

Als-Nielsen, J. & McMorrow, D. (2011). *Elements of modern X-ray physics*: Wiley.

Antignano, A. & Manning, C. E. (2008). Rutile solubility in H_2O, H_2O-SiO_2, and H_2O-$NaAlSi_3O_8$ fluids at 0.7-2.0 GPa and 700-1000°C: Implications for mobility of nominally insoluble elements. *Chemical Geology* **255**, 283-293.

Arculus, R. J. (1994). Aspects of magma genesis in arcs. *Lithos* **33**, 189-208.

Armstrong, R. L. (1971). Isotopic and chemical constraints on models of magma genesis in volcanic arcs. *Planetary Science Letters* **12**, 137-142.

Audétat, A. & Keppler, H. (2005). Solubility of rutile in subduction zone fluids, as determined by experiments in the hydrothermal diamond anvil cell. *Earth and Planetary Science Letters* **232**, 393-402.

Ayers, J. C. & Watson, E. B. (1993). Rutile solubility and mobility in supercritical aqueous fluids. *Contributions to Mineralogy and Petrology* **114**, 321-330.

Baier, J., Audétat, A. & Keppler, H. (2008). The origin of the negative niobium tantalum anomaly in subduction zone magmas. *Earth and Planetary Science Letters* **267**, 290-300.

Bailey, E. H. & Vala Ragnarsdottir, K. (1994). Uranium and thorium solubilities in subduction zone fluids. *Earth and Planetary Science Letters* **124**, 119-129.

Barth, M. G., McDonough, W. F. & Rudnick, R. L. (2000). Tracking the budget of Nb and Ta in the continental crust. *Chemical Geology* **165**, 197-213.

Beattie, P. (1993). Uranium-thorium disequilibria and partitioning on melting of garnet peridotite. *Nature* **363**, 63-65.

Bebout, G. E. & Nakamura, E. (2003). Record in metamorphic tourmalines of subduction-zone devolatilization and boron cycling *Geology* **31**, 407-410.

Bebout, G. E. (2007). Metamorphic chemical geodynamics of subdution zones. Earth and Planetary Science Letters 260, 373-393.

Bebout, G. E., Bebout, A. E. & Graham, C. M. (2007). Cycling of B, Li, and LILE (K, Cs, Rb, Ba, Sr) into subduction zones: SIMS evidence from micas in high-P/T metasedimentary rocks. *Chemical Geology* **239**, 284-304.

Bebout, G. E., Ryan, J. G. & Leeman, W. P. (1993). B-Be Systematics in Subduction-Related Metamorphic Rocks - Characterization of the Subducted Component. *Geochimica et Cosmochimica Acta* **57**, 2227-2237.

Becker, H., Jochum, K. P. & Carlson, R. W. (1999). Constraints from high-pressure veins in eclogites on the composition of hydrous fluids in subduction zones. *Chemical Geology* **160**, 291-308.

Becker, H., Jochum, K. P. & Carlson, R. W. (2000). Trace element fractionation during dehydration of eclogites from high-pressure terranes and the implications for element fluxes in subduction zones. *Chemical Geology* **163**, 65-99.

Beinlich, A., Klemd, R., John, T. & Gao, J. (2010). Trace-element mobilization during Ca-metasomatism along a major fluid conduit: Eclogitization of blueschist as a consequence of fluid–rock interaction. *Gechimica et Cosmochimica Acta* **74**, 1892-1922.

Ben Othman, D., White, W. M. & Patchett, J. (1989). The geochemistry of marine sediments, island arc magma genesis, and crust-mantle recycling. *Earth and Planetary Science Letters* **94**, 1-21.

Biellmann, C., Gillet, P., Guyot, F., Peyronneau, J. & Reynard, B. (1993). Experimental evidence for carbonate stability in the Earth's lower mantle. *Earth and Planetary Science Letters* **118**, 31-41.

Brandon, A. D. & Draper, D. S. (1996). Constraints on the origin of the oxidation state of mantle overlying subduction zones: An example from Simcoe, Washington, USA. *Geochimica et Cosmochimica Acta* **60**, 1739-1749.

Breeding, C. M., Ague, J. J. & Bröcker, M. (2004). Fluid-metasedimentary rock interactions in subduction-zone mélange: Implicaitions for the chemical composition of arc magmas.

Geology **32**, 1041-1044.

Brenan, J. M., Shaw, H. F., Ryerson, F. J. & Phinney, D. L. (1995). Mineral-aqueous fluid partitioning of trace elements at 900 °C and 2.0 GPa: Constraints on the trace element chemistry of mantle and deep crustal fluids. *Geochimica et Cosmochimica Acta* **59**, 3331-3350.

Bright, E. & Readey, D. W. (1987). Dissolution Kinetics of TiO_2 in HF-HCl Solutions. *Journal of the American Ceramic Society* **70**, 900-906.

Browning, P. (2005). Introduction to Plasma Physics: With Space and Laboratory Applications. *Plasma Physics and Controlled Fusion* **47**, 1109.

Brunsmann, A., Franz, G., Erzinger, J. & Landwehr, D. (2000). Zoisite- and clinozoisite-segregations in metabasites (Tauern Window, Austria) as evidence for high-pressure fluid-rock interaction. *Journal of Metamorphic Geology* **18**, 1-21.

Cao, Y., Song, S. G., Niu, Y. L., Jung, H. & Jin, Z. M. (2011). Variation of mineral composition, fabric and oxygen fugacity from massive to foliated eclogites during exhumation of subducted ocean crust in the North Qilian suture zone, NW China. *Journal of Metamorphic Geology* **29**, 699-720.

Carlson, W. D. (1989). The significance of intergranular diffusion to the mechanisms and kinetics of porphyroblast crystallization. *Contributions to Mineralogy and Petrology* **103**, 1-24.

Carlson, W. D. (2002). Scales of disequilibrium and rates of equilibration during metamorphism. *American Mineralogist* **87**, 185-204.

Cervantes, P. & Wallace, P. J. (2003). Role of H_2O in subduction-zone magmatism: New insights from melt inclusions in high-Mg basalts from central Mexico. *Geology* **31**, 235-238.

Chen, C. M., Lu, H. F., Jia, D., Cai, D. S. & Wu, S. M. (1999). Closing history of the southern Tianshan oceanic basin, western China: an oblique collisional orogeny. *Tectonophysics* **302**, 23-40.

Chopin, C. (1984). Coesite and pure pyrope in high-grade blueschists of the Western Alps: a first record and some consequences. *Contributions to Mineralogy and Petrology* **86**, 107-118.

Churikova, T., Dorendorf, F. & Wörner, G. (2001). Sources and fluids in the mantle wedge

below Kamchatka, evidence from across-arc geochemical variation. *Lithos* **42**, 1567-1593.

Currie, C. A., Beaumont, C. & Huismans, R. S. (2007). The fate of subducted sediments: A case for backarc intrusion and underplating. *Geology* **35**, 1111-1114.

Davies, J. H. & Stevenson, D. J. (1992). Physical Model of Source Region of Subduction Zone Volcanics. *Journal of Geophysical Research* **97**, 2037-2070.

de Jong, K., Wang, B., Faure, M., Shu, L., Cluzel, D., Charvet, J., Ruffet, G. & Chen, Y. (2009). New $^{40}Ar/^{39}Ar$ age constraints on the Late Palaeozoic tectonic evolution of the western Tianshan (Xinjiang, northwestern China), with emphasis on Permian fluid ingress. *International Journal of Earth Sciences* **98**, 1239-1258.

Deer, W. A., Howie, R. A. & Zussman, J. (1992). *An Introduction to the Rock-Forming Minerals*: Prentice Hall.

Dickinson, W. R. & Hatherton, T. (1967). Andesitic volcanism and seismicity around the Pacific. *Science* **157**, 801-803.

Dickinson, W. R. (1968). Circum-Pacific Andesite Types. *Journal of Geophysical Research* **73**, 2261-2269.

Dilek, Y. & Furnes, H. (2011). Ophiolite genesis and global tectonics: Geochemical and tectonic fingerprinting of ancient oceanic lithosphere. *Geological Society of America Bulletin* **123**, 387-411.

Domanik, K. J. & Holloway, J. R. (1996). The stability and composition of phengitic muscovite and associated phases from 5.5 to 11 GPa: Implications for deeply subducted sediments *Geochimica et Cosmochimica Acta* **60**, 4133-4150.

Domanik, K. J. & Holloway, J. R. (2000). Experimental synthesis and phase relations of phengitic muscovite from 6.5 to 11 GPa in a calcareous metapelite from the Dabie Mountains, China. *Lithos* **52**, 51-77.

Donnelly, K. E., Goldstein, S. L., Langmuir, C. H. & Spiegelman, M. (2004). Origin of enriched ocean ridge basalts and implications for mantle dynamics. *Earth and Planetary Science Letters* **226**, 347-366.

Dreyer, B. M., Morris, J. D. & Gill, J. B. (2010). Incorporation of Subducted Slab-derived Sediment and Fluid in Arc Magmas: B–Be–10Be–εNd Systematics of the Kurile Convergent Margin, Russia. *Journal of Petrology* **51**, 1761-1782.

Edwards, C. M. H., Morris, J. D. & Thirlwall, M. F. (1993). Separating Mantle from Slab Signatures in Arc Lavas Using B/Be and Radiogenic Isotope Systematics. *Nature* **362**, 530-533.

Eiler, J. M., Farley, K. A., Valley, J. W., Hauri, E., Craig, H., Hart, S. R. & Stolper, E. M. (1997). Oxygen isotope variations in ocean island basalt phenocrysts. *Geochimica et Cosmochimica Acta* **61**, 2281-2293.

El Korh, A., Schmidt, S. T., Ulianov, A. & Potel, S. (2009). Trace element partitioning in HP-LT metamorphic assemblages during subduction-related metamorphism, Ile de Groix, France: a detailed LA-ICPMS Study. *Journal of Petrology* **50**, 1107-1148.

Elliott, T. (2003). Tracers of the slab. *Geophysical monograph* **138**, 23-45.

Elliott, T., Plank, T., Zindler, A., White, W. & Bourdon, B. (1997). Element transport from slab to volcanic front at the Mariana arc. *Journal of Geophysical Research* **102**, 14,991-915,019.

Feineman, M. D., Ryerson, F. J., DePaolo, D. J. & Plank, T. (2007). Zoisite-aqueous fluid trace element partitioning with implications for subduction zone fluid composition. *Chemical Geology* **239**, 250-265.

Feng, Y. & He, S. (1995). Research for geology and geochemistry of several ophiolites in the North Qilian Mountains, China. *Acta Petrologica Sinica (in Chinese)* **11**, 125-146.

Feng, Y., Coleman, R. G., Tilton, G. & Xiao, X. (1989). Tectonic evolution of the West Junggar Region, Xinjiang, China. *Tectonics* **8**, 729-752.

Ferrari, L., Petrone, C. M. & Francalanci, L. (2001). Generation of oceanic-island basalt–type volcanism in the western Trans-Mexican volcanic belt by slab rollback, asthenosphere infiltration, and variable flux melting. *Geology* **29**, 507-510.

Forneris, J. F. & Holloway, J. R. (2003). Phase equilibria in subducting basaltic crust: implications for H_2O release from the slab. *Earth and Planetary Science Letters* **214**, 187-201.

Gao , J. (1997). The discovery of eclogites and its tectonic implication, Southwest Tianshan. *Chinese Science Bulletin (in Chinese)* **42**, 737-740.

Gao, J. & Klemd, R. (2000). Eclogite occurrences in the southern Tianshan high pressure belt, Xinjiang, Western China. *Gondwana Research* **3**, 33-38.

Gao, J. & Klemd, R. (2001). Primary fluids entrapped at blueschist to eclogite transition: evidence from the Tianshan meta-subduction complex in northwestern China. *Contributions to Mineralogy and Petrology* **142**, 1-14.

Gao, J. & Klemd, R. (2003). Formation of HP-LT rocks and their tectonic implications in the western Tianshan Orogen, NW China: geochemical and age constraints. *Lithos* **66**, 1-22.

Gao, J., He, G. Q., Li, M. S., Xiao, X. C., Tang, Y. Q., Wang, J. & Zhao, M. (1995). The Mineralogy, Petrology, Metamorphic Ptdt Trajectory and Exhumation Mechanism of Blueschists, South Tianshan, Northwestern China. *Tectonophysics* **250**, 151-168.

Gao, J., John, T., Klemd, R. & Xiong, X. M. (2007). Mobilization of Ti-Nb-Ta during subduction: Evidence from rutile-bearing dehydration segregations and veins hosted in eclogite, Tianshan, NW China. *Geochimica et Cosmochimica Acta* **71**, 4974-4996.

Gao, J., Klemd, R., Zhang, L., Wang, Z. & Xiao, X. (1999). P-T path of high-pressure/low-temperature rocks and tectonic implications in the western Tianshan Mountains, NW China. *Jounal of Metamorphic Geology* **17**, 621-636.

Gao, J., Li, M. S., Xiao, X. C., Tang, Y. Q. & He, G. Q. (1998). Paleozoic tectonic evolution of the Tianshan Orogen, northwestern China. *Tectonophysics* **287**, 213-231.

Gao, J., Long, L. L., Qian, Q., Huang, D. Z., Su, W. & Klemd, R. (2006). South Tianshan: a Late Paleozoic or a Triassic orogen? . *Acta Petrologica Sinica (in Chinese)* **22**, 1049-1061.

Gao, J., Long, L., Klemd, R., Qian, Q., Liu, D., Xiong, X., Su, W., Liu, W., Wang, Y. & Yang, F. (2009). Tectonic evolution of the South Tianshan orogen and adjacent regions, NW China: geochemical and age constraints of granitoid rocks. *International Journal of Earth Sciences* **98**, 1221-1238.

Gao, S., Yang, J., Zhou, L., Li, M., Hu, Z., Guo, J., Yuan, H., Gong, H., Xiao, G. & Wei, J. (2011). Age and growth of the Archean Kongling terrain, South China, with emphasis on 3.3 ga granitoid gneisses. *American Journal of Science* **311**, 153-182.

Gast, P. W. (1968). Trace element fractionation and the origin of tholeiitic and alkaline magma types. *Geochimica et Cosmochimica Acta* **32**, 1057-1086.

Gill, J. B. & Williams, R. W. (1990). Th isotope and U-series studies of subduction-related volcanic rocks. *Geochimica et Cosmochimica Acta* **54**, 1427-1442.

Gill, J. B. (1981). *Orogenic Andesites and Plate Tectonics*. Berlin, Heidelberg, New York:

Springer-Verlag.

Gill, R. (1997). *Modern analytical geochemistry: an introduction to quantitative chemical analysis techniques for earth, environmental and materials scientists*: Longman.

Grove, M., Bebout, G. E., Jacobson, C. E., Barth, A. P., Kimbrough, D. L., King, R. L., Zou, H. B., Lovera, O. M., Mahoney, B. J. & Gehrels, G. E. (2008). The Catalina Schist: Evidence for middle Cretaceous subduction erosion of southwestern North America. *Formation and Applications of the Sedimentary Record in Arc Collision Zones* **436**, 335-361.

Guillong, M., Hametner, K., Reusser, E., Wilson, S. A. & Gunther, D. (2005). Preliminary characterisation of new glass reference materials (GSA-1G, GSC-1G, GSD-1G and GSE-1G) by laser ablation-inductively coupled plasma-mass spectrometry using 193 nm, 213 nm and 266 nm wavelengths. *Geostandards and Geoanalytical Research* **29**, 315-331.

Halliday, A. N., Lee, D. C., Tommasini, S., Davies, G. R., Paslick, C. R., Fitton, J. G. & James, D. E. (1995). Incompatible Trace-Elements in Oib and Morb and Source Enrichment in the Sub-Oceanic Mantle. *Earth and Planetary Science Letters* **133**, 379-395.

Hawkesworth, C. J., Gallagher, K., Hergt, J. M. & Mcdermott, F. (1993). Mantle and Slab Contributions in Arc Magmas. *Annual Review of Earth and Planetary Sciences* **21**, 175-204.

Hawkesworth, C. J., Turner, S. P., McDermott, F., Peate, D. W. & Calsteren, P. V. (1997). U-Th isotopes in arc magmas: Implications for element transfer from the subducted crust. *Science* **276**, 551-555.

Hayden, L. A. & Manning, C. E. (2011). Rutile solubility in supercritical $NaAlSi_3O_8$-H_2O fluids. *Chemical Geology*.

Hegner, E., Klemd, R., Kröner, A., Corsini, M., Alexeiev, D. V., Iaccheri, L. M., Zack, T., Dulski, P., Xia, X. & Windley, B. F. (2010). Mineral ages and P-T conditions of Late Paleozoic high-pressure eclogite and provenance of mélange sediments from Atbashi in the south Tianshan orogen of Kyrgyzstan. *American Journal of Science* **310**, 916-950.

Hermann, J. & Rubatto, D. (2009). Accessory phase control on the trace element signature of sediment melts in subduction zones. *Chemical Geology* **265**, 512-526.

Hermann, J. (2002). Allanite: thorium and light rare earth element carrier in subducted crust. *Chemical Geology* **192**, 289-306.

Hermann, J., Spandler, C., Hack, A. & Korsakov, A. V. (2006). Aqueous fluids and hydrous

melts in high-pressure and ultra-high pressure rocks: Implications for element transfer in subduction zones. *Lithos* **92**, 399-417.

Hofmann, A. W. & Hart, S. R. (1978). An assessment of local and regional isotopic equilibrium in the mantle. *Earth and Planetary Science Letters* **38**, 44-62.

Hofmann, A. W. (1997). Mantle geochemistry: the message from oceanic volcanism. *Nature* **385**, 219-229.

Holzapfel, C., Rubie, D. C., Frost, D. J. & Langenhorst, F. (2005). Fe-Mg interdiffusion in $(Mg,Fe)SiO_3$ perovskite and lower mantle reequilibration. *Science* **309**, 1707-1710.

Ishikawa, T. & Nakamura, E. (1994). Origin of the slab component in arc lavas from across-arc variation of B and Pb isotopes. *Nature* **370**, 205-208.

Jochum, K. P., Stolz, A. J. & McOrist, G. (2000). Niobium and tantalum in carbonaceous chondrites: Constraints on the solar system and primitive mantle niobium/tantalum, zirconium/niobium, and niobium/uranium ratios. *Meteoritics & Planetary Science* **35**, 229-235.

Jochum, K. P., Willbold, M., Raczek, I., Stoll, B. & Herwig, K. (2005). Chemical characterisation of the USGS reference glasses GSA-1G, GSC-1G, GSD-1G, GSE-1G, BCR-2G, BHVO-2G and BIR-1G using EPMA, ID-TIMS, ID-ICP-MS and LA-ICP-MS. *Geostandards and Geoanalytical Research* **29**, 285-302.

John, T., Klemd, R., Gao, J. & Garbe-Schönberg, C. D. (2008). Trace-element mobilization in slabs due to non steady-state fluid-rock interaction: Constraints from an eclogite-facies transport vein in blueschist (Tianshan, China). *Lithos*, 1-24.

John, T., Scambelluri, M., Frische, M., Barnes, J. D. & Bach, W. (2011). Dehydration of subducting serpentinite: Implications for halogen mobility in subduction zones and the deep halogen cycle. *Earth and Planetary Science Letters* **308**, 65-76.

John, T., Schenk, V., Haase, K., Scherer, E. & Tembo, F. (2003). Evidence for a Neoproterozoic ocean in south-central Africa from mid-oceanic-ridge-type geochemical signatures and pressure-temperature estimates of Zambian eclogites. *Geology* **31**, 243-246.

John, T., Scherer, E. E., Haase, K. & Schenk, V. (2004). Trace element fractionation during fluid-induced eclogitization in a subducting slab: trace element and Lu-Hf-Sm-Nd isotope systematics. *Earth and Planetary Science Letters* **227**, 441-456.

Kalfoun, K., Ionov, D. & Merlet, C. (2002). HFSE residence and Nb/Ta ratios in metasomatised, rutile-bearing mantle peridotites. *Earth and Planetary Science Letters* **199**, 49-65.

Katayama, I., Nakashima, S. & Yurimoto, H. (2006). Water content in natural eclogite and implication for water transport into the deep upper mantle. *Lithos* **86**, 245-259.

Katayama, I., Parkinson, C. D., Okamoto, K., Nakajima, Y. & Maruyama, S. (2000). Supersilicic clinopyroxene and silica exsolution in UHPM eclogite and pelitic gneiss from the Kokchetav massif, Kazakhstan. *American Mineralogist* **85**, 1368-1374.

Kay, R. W., Sun, S.-S. & Lee-Hu, C.-N. (1978). Pb and Sr in volcanic rocks from the Aleutian Islands and Pribilof Islands, Alaska. *Geochimica et Cosmochimica Acta* **42**, 263-273.

Kelley, K. A., Plank, T., Farr, L., Ludden, J. & Staudigel, H. (2005). Subduction cycling of U, Th, and Pb. *Earth and Planetary Science Letters* **234**, 369-383.

Kelley, K. A., Plank, T., Grove, T. L., Stolper, E. M., Newman, S. & Hauri, E. (2006). Mantle melting as a function of water content beneath back-arc basins. *J. Geophys. Res.* **111**, B09208.

Kelley, K. A., Plank, T., Ludden, J. & Staudigel, H. (2003). Composition of altered oceanic crust at ODP Sites 801 and 1149. *Geochemistry Geophysics Geosystems* **4**.

Kendrick, M. A., Scambelluri, M., Honda, M. & Phillips, D. (2011). High abundances of noble gas and chlorine delivered to the mantle by serpentinite subduction. *Nature Geoscience* **4**, 807-812.

Keppler, H. (1996). Constraints from partitioning experiments on the composition of subduction-zone fluids. *Nature* **380**, 237-240.

Kessel, R., Schmidt, M. W., Ulmer, P. & Pettke, T. (2005). Trace element signature of subduction-zone fluids, melts and supercritical liquids at 120-180km depth. *Nature* **437**, 724-727.

King, R. L., Bebout, G. E., Kobayashi, K., Nakamura, E. & van der Klauw, S. N. G. C. (2004). Ultrahigh-pressure metabasaltic garnets as probes into deep subduction zone chemical cycling. *Geochemistry Geophysics Geosystems* **5**.

Klemd, R. (2003). Ultrahigh-pressure metamorphism in eclogites from the western Tianshan high-pressure belt (Xinjiang, western China)-Comment. *American Mineralogist* **88**, 1153-1156.

Klemme, S., Prowatke, S., Hametner, K. & Günther, D. (2005). Partitioning of trace elements between rutile and silicate melts: implications for subduction zones. *Gechimica et Cosmochimica Acta* **69**, 2361-2371.

Klimm, K., Blundy, J. D. & Green, T. H. (2008). Trace Element Partitioning and Accessory Phase Saturation during H2O-Saturated Melting of Basalt with Implications for Subduction Zone Chemical Fluxes. *Journal of Petrology* **49**, 523-553.

Kogiso, T., Tatsumi, Y. & Nakano, S. (1997). Trace element transport during dehydration processes in the subducted oceanic crust .1. Experiments and implications for the origin of ocean island basalts. *Earth and Planetary Science Letters* **148**, 193-205.

Konrad-Schmolke, M., Zack, T., O'Brien, P. J. & Jacob, D. E. (2008). Combined thermodynamic and rare earth element modelling of garnet growth during subduction: Examples from ultrahigh-pressure eclogite of the Western Gneiss Region, Norway. *Earth and Planetary Science Letters* **272**, 488-498.

Konzett, J., Frost, D. J., Proyer, A. & Ulmer, P. (2008). The Ca-Eskola component in eclogitic clinopyroxene as a function of pressure, temperature and bulk composition: an experimental study to 15 GPa with possible implications for the formation of oriented SiO2-inclusions in omphacite. *Contrib. Mineral Petrol* **155**, 215-228.

Kuno, H. (1959). Origin of Cenozoic petrographic provinces of Japan and surrounding areas. *Bulletin of Volcanology* **20**, 37-76.

Langmuir, D. (1978). Uranium solution-mineral equilibria at low temperatures with applications to sedimentary ore deposits. *Gechimica et Cosmochimica Acta* **42**, 547-569.

LaTourrette, T. Z., Kennedy, A. K. & Wasserburg, G. J. (1993). Thorium-Uranium Fractionation by Garnet: Evidence for a Deep Source and Rapid Rise of Oceanic Basalts. *Science* **261**, 739-742.

Lavis, S. (2005). Recycling in subduction zones: Evidence from eclogites and blueschist of NW China. Cardiff University, 1-245.

Leake, B. E., Woolley, A.R., Arps, C.E.S., Birch, W.D., Gilbert, M.C., Grice, J.D., Hawthorne, F.C., Kato, A., Kisch, H.J., Krivovichev, V.G., Linthout, K., Laird, J., Mandarino, J.A., Maresch, W.V., Nickel, E.H., Rock, N.M.S., Schumacher, J.C., Smith, D.C., Stephenson, N.C.N., Ungaretti, L., Whittaker, E.J.W., and Youshi, G. (1997). Nomenclature of amphiboles: Report of the subcommittee on amphiboles of the International Mineralogical

Association, Commission on new minerals and mineral names. *American Mineralogist* **82**, 1019-1037.

Lee, C. T. A., Brandon, A. D. & Norman, M. (2003). Vanadium in peridotites as a proxy for paleo-fO(2) during partial melting: Prospects, limitations, and implications. *Geochimica et Cosmochimica Acta* **67**, 3045-3064.

Lee, C. T. A., Leeman, W. P., Canil, D. & Li, Z. X. A. (2005). Similar V/Sc systematics in MORB and arc basalts: Implications for the oxygen fugacities of their mantle source regions. *Journal of Petrology* **46**, 2313-2336.

Lin, Y., Zhang, L., Ji, J., Wang, Q. & Song, S. (2010). $^{40}Ar/^{39}Ar$ isochron ages of lawsonite blueschists from Jiuquan in the northern Qilian Mountain, NW China, and their tectonic implications. *Chinese Science Bulletin* **55**, 2021-2027.

Liou, J. G., Graham, S. A., Maruyama, S., Wang, X., Xiao, X., Carroll, A. R., Chu, J., Feng, Y., Hendrix, M. S., Liang, Y. H., McKnight, C. L., Tang, Y., Wang, Z. X., Zhao, M. & Zhu, B. (1989). Proterozoic blueschist belt in western China: Best documented Precambrian blueschists in the world. *Geology* **17**, 1127-1131.

Liou, J. G., Tsujimori, T., Zhang, R. Y., Katayama, I. & Maruyama, S. (2004). Global UHP Metamorphism and Continental Subduction/Collision: The Himalayan Model. *International Geology Review* **46**, 1-27.

Liou, J. G., Wang, X., Coleman, R. G., Zhang, Z. M. & Maruyama, S. (1989). Blueschists in major suture zones of China. *Tectonics* **8**, 609-619.

Litasov, K. D., Kagi, H., Shatskiy, A., Ohtani, E., Lakshtanov, D. L., Bass, J. D. & Ito, E. (2007). High hydrogen solubility in Al-rich stishovite and water transport in the lower mantle. *Earth and Planetary Science Letters* **262**, 620-634.

Liu, J., Bohlen, S. R. & Ernst, W. G. (1996). Stability of hydrous phases in subducting oceanic crust. *Earth and Planetary Science Letters* **143**, 161-171.

Liu, Y. S., Hu, Z. C., Gao, S., Günther, D., Xu, J., Gao, C. G. & Chen, H. H. (2008). In situ analysis of major and trace elements of anhydrous minerals by LA-ICP-MS without applying an internal standard. *Chemical Geology* **257**, 34-43.

Liu, Y., Liu, X. M., Hu, Z. C., Diwu, C. R., Yuan, H. L. & Gao, S. (2007). Evaluation of accuracy and long-term stability of determination of 37 trace elements in geological samples

by ICP-MS. *Acta Petrologica Sinica (in Chinese with English abstract)* **23**, 1203-1210.

Liu, Y.-J., Neubauer, F., Genser, J., Takasu, A., Ge, X.-H. & Handler, R. (2006). $^{40}Ar/^{39}Ar$ ages of blueschist facies pelitic schists from Qingshuigou in the Northern Qilian Mountains, western China. *Island Arc* **15**, 187-198.

Long, L. L., Gao, J., Klemd, R., Beier, C., Qian, Q., Zhang, X., Wang, J. B. & Jiang, T. (2011). Geochemical and geochronological studies of granitoid rocks from the Western Tianshan Orogen: Implications for continental growth in the southwestern Central Asian Orogenic Belt. *Lithos* **126**, 321-340.

Long, L. L., Gao, J., Xiong, X. M. & Qian, Q. (2006). Geochemical Characteristics and Chronologic Study on Ophiolites from Kule Lake, South Tianshan. *Acta Petrologica Sinica (in Chinese)* **22**, 65-73.

Lü, Z., Zhang, L. F., Du, J. X. & Bucher, K. (2008). Coesite inlusions in garnet from eclogitic rocks in western Tianshan, northwest China: Convincing proof of UHP metamorphism. *American Mineralogist* **93**, 1845-1850.

Lü, Z., Zhang, L. F., Du, J. X. & Bucher, K. (2009). Petrology of coesite-bearing eclogite from Habutengsu Valley, western Tianshan, NW China and its tectonometamorphic implication. *Journal of Metamorphic Geology* **27**, 773-787.

Lü, Z., Zhang, L., Du, J., Yang, X., Tian, Z. & Xia, B. (2012). Petrology of HP metamorphic veins in coesite-bearing eclogite from western Tianshan, China: Fluid processes and elemental mobility during exhumation in a cold subduction zone. *Lithos* **136–139**, 168-186.

Lucassen, F., Dulski, P., Abart, R., Franz, G., Rhede, D. & Romer, R. L. (2010). Redistribution of HFSE elements during rutile replacement by titanite. *Contributions to Mineralogy and Petrology* **160**, 279-295.

Lucassen, F., Franz, G., Dulski, P., Romer, R. L. & Rhede, D. (2011). Element and Sr isotope signatures of titanite as indicator of variable fluid composition in hydrated eclogite. *Lithos* **121**, 12-24.

Luth, R. W. (2001). Experimental determination of the reation aragonite+magnesite=dolomite at 5 to 9 GPa. *Contribuions to Mineralogy and Petrology* **141**, 222-232.

Manning, C. E. (2004). The chemistry of subduction-zone fluids. *Earth and Planetary Science Letters* **223**, 1-16.

Manning, C. E., Wilke, M., Schmidt, C. & Cauzid, J. (2008). Rutile solubility in albite-H_2O and $Na_2Si_3O_7$-H_2O at high temperatures and pressures by in-situ synchrotron radiation micro-XRF. *Earth and Planetary Science Letters* **272**, 730-737.

Marschall, H. R., Pogge von Strandmann, P. A. E., Seitz, H.-M., Elliott, T. & Niu, Y. (2007). The lithium isotopic composition of orogenic eclogites and deep subducted slabs. *Earth and Planetary Science Letters* **262**, 563-580.

Martin, L. A. J., Wood, B. J., Turner, S. & Rushmer, T. (2011). Experimental Measurements of Trace Element Partitioning Between Lawsonite, Zoisite and Fluid and their Implication for the Composition of Arc Magmas. *Journal of Petrology* **52**, 1049-1075.

Maruyama, S., Masago, H., Katayama, I., Iwase, Y., Toriumi, M., Omori, S. & Aoki, K. (2010). A new perspective on metamorphism and metamorphic belts. *Gondwana Research* **18**, 106-137.

Maulana, A., Ellis, D. J. & Christy, A. G. (2010). Petrology, geochemistry and tectonic evolution of the south Sulawesi basement rocks, Indonesia. *Proceedings of the Indonesian Petroleum Association, IPA10-G-192*.

McCulloch, M. T. & Gamble, J. A. (1991). Geochemical and geodynamicai constraints on subduction. *Earth and Planetary Science Letters* **102**, 358-374.

Melzer, S. & Wunder, B. (2000). Island-arc basalt alkali ratios: Constraints from phengite-fluid partitioning experiments. *Geology* **28**, 583-586.

Meng, Q.-R. & Zhang, G.-W. (2000). Geologic framework and tectonic evolution of the Qinling orogen, central China. *Tectonophysics* **323**, 183-196.

Meschede, M. (1986). A method of discriminating between different types of mid-ocean ridge basalts and continental tholeiites with the Nb-Zr-Y diagram. *Chemical Geology* **56**, 207-218.

Mibe, K., Kawamoto, T., Matsukage, K. N., Fei, Y. & Ono, S. (2011). Slab melting versus slab dehydration in subduction-zone magmatism. *Proceedings of the National Academy of Sciences* **108**, 8177-8182.

Mibe, K., Yoshino, T., Ono, S., Yasuda, A. & Fujii, T. (2003). Connectivity of aqueous fluid in eclogite and its implications for fluid migration in the Earth's interior. *Journal of Geophysical Research* **108**, 2295.

Moriguti, T. & Nakamura, E. (1998). Across-arc variation of Li isotopes in lavas and

implications for crust/mantle recycling at subduction zones. *Earth and Planetary Science Letters* **163**, 167-174.

Morimoto, N. (1988). Nomenclature of pyroxenes. *Mineralogy and Petrology* **39**, 55-76.

Morris, J. D. & Hart, S. R. (1983). Isotopic and Incompatible Element Constraints on the Genesis of Island-Arc Volcanics from Cold Bay and Amak Island, Aleutians, and Implications for Mantle Structure. *Geochimica et Cosmochimica Acta* **47**, 2015-2030.

Morris, J. D. & Ryan, J. G. (2003). 2.11 - Subduction Zone Processes and Implications for Changing Composition of the Upper and Lower Mantle. In: Editors-in-Chief: Heinrich, D. H. & Karl, K. T. (eds.) *Treatise on Geochemistry*. Oxford: Pergamon, 451-470.

Morris, J. D. & Ryan, J. G. (2003). Subduction zone processes and implications for changing composition of the upper and lower mantle. In: Carlson, R. W. (ed.) *Treatise on Geochemistry*: Elsevier, 451-470.

Münker, C., Pfänder, J. A., Weyer, S., Büchl, A., Kleine, T. & Mezger, K. (2003). Evolution of Planetary Cores and the Earth-Moon System from Nb/Ta Systematics. *Science* **301**, 84-87.

Nagasaki, A. & Enami, M. (1998). Sr-bearing zoisite and epidote in ultra-high pressure (UHP) metamorphic rocks from the Su-Lu province, eastern China: An important Sr reservoir under UHP conditions. *American Mineralogist* **83**, 240-247.

Nakano, T. & Nakamura, E. (2001). Boron isotope geochemistry of metasedimentary rocks and tourmalines in a subduction zone metamorphic suite. *Physics of the Earth and Planetary Interiors* **127**, 233-252.

Niu, Y. (2012). Earth processes cause Zr-Hf and Nb-Ta fractionations, but why and how? *RSC Advances*.

Niu, Y. L. & Batiza, R. (1997). Extreme mantle source heterogeneities beneath the northern East Pacific Rise N trace element evidence from near-ridge seamounts. *Proc. 30th IntOl. Geol. Congr.* **Part 15**, 109-120.

Niu, Y. L. & Batiza, R. (1997). Trace element evidence from seamounts for recycled oceanic crust in the Eastern Pacific mantle. *Earth and Planetary Science Letters* **148**, 471-483.

Niu, Y. L. & Lesher, C. M. (1991). Hydrothermal Alteration of Mafic Metavolcanic Rocks and Genesis of Fe-Zn-Cu Sulfide Deposits, Stone Hill District, Alabama. *Economic Geology and the Bulletin of the Society of Economic Geologists* **86**, 983-1001.

Niu, Y. L. & O'Hara, M. J. (2003). Origin of ocean island basalts: A new perspective from petrology, geochemistry, and mineral physics considerations. *Journal of Geophysical Research* **108**, ECV5.1-ECV5.19.

Niu, Y. L. (2004). Bulk-rock major and trace element compositions of abyssal peridotites: Implications for mantle melting, melt extraction and post-melting processes beneath mid-ocean ridges. *Journal of Petrology* **45**, 2423-2458.

Niu, Y. L. (2005). Generation and evolution of basaltic magmas: some basic concepts and a new view on the origin of Mesozoic-Cenozoic basaltic volcanism in Eastern China. *Geological Journal of China Universities* **11**, 9-46.

Niu, Y. L. (2009). Some basic concepts and problems on the petrogenesis of intra-plate ocean island basalts. *Chinese Science Bulletin* **54**, 4148-4160.

Niu, Y. L., Regelous, M., Wendt, I. J., Batiza, R. & O'Hara, M. J. (2002). Geochemistry of near-EPR seamounts: importance of source vs. process and the origin of enriched mantle component. *Earth and Planetary Science Letters* **199**, 327-345.

Noll Jr, P. D., Newsom, H. E., Leeman, W. P. & Ryan, J. G. (1996). The role of hydrothermal fluids in the production of subduction zone magmas: Evidence from siderophile and chalcophile trace elements and boron. *Geochimica et Cosmochimica Acta* **60**, 587-611.

O' Nions, R. K., Evensen, N. M. & Hamilton, P. J. (1979). Geochemical modelling of mantle differentiation and crustal growth. *Journal of Geophysical Research* **84**, 6091-6101.

Page, F. Z., Essene, E. J. & Mukasa, S. B. (2005). Quartz exsolution in clinopyroxene is not proof of ultrahigh pressures: Evidence from eclogites from the Eastern Blue Ridge, Southern Appalachians, U.S.A. *American Mineralogist* **90**, 1092-1099.

Parkinson, C. D., Miyazaki, K., Wakita, K., Barber, A. J. & Carswell, D. A. (1998). An overview and tectonic synthesis of the pre-Tertiary very-high-pressure metamorphic and associated rocks of Java, Sulawesi and Kalimantan, Indonesia. *Island Arc* **7**, 184-200.

Pawley, A. R. & Holloway, J. R. (1993). Water Sources for Subduction Zone Volcanism: New Experimental Constraints *Science* **260**, 664-667.

Pawley, A. R. (1994). The pressure and temperature stability limits of lawsonite-implications for H_2O recycling in subduction zones. *Contributions to Mineralogy and Petrology* **118**, 99-108.

Peacock, S. M. & Wang, K. L. (1999). Seismic consequences of warm versus cool subduction

metamorphism: Examples from southwest and northeast Japan. *Science* **286**, 937-939.

Peacock, S. M. (1990). Fluid processes in subduction zone. *Science* **248**, 329-337.

Peacock, S. M. (1993). The importance of blueschist-eclogite dehydration reactions in subducting oceanic crust. *Geological Society of America Bulletin* **105**, 684-694.

Pearce, J. A. & Cann, J. R. (1973). Tectonic setting of basic volcanic rocks determined using trace element analyzes. *Earth and Planetary Science Letters* **19**, 290-300.

Pearce, J. A. & Wyman, D. A. (1996). A user's guide to basalt discrimination diagrams. *Trace element geochemistry of volcanic rocks: Applications for massive sulphide exploration*: Geological Association Canada, Short Course Notes, 79-113.

Pearce, J. A. (2008). Geochemical fingerprinting of oceanic basalts with applications to ophiolite classification and the search for Archean oceanic crust. *Lithos* **100**, 14-48.

Pfänder, J. A., Münker, C., Stracke, A. & Mezger, K. (2007). Nb/Ta and Zr/Hf in ocean island basalts - Implications for crust-mantle differentiation and the fate of Niobium. *Earth and Planetary Science Letters* **254**, 158-172.

Philippot, P. & Selverstone, J. (1991). Trace-element-rich brines in eclogitic veins: implications for fluid composition and transport during subduction. *Contributions to Mineralogy and Petrology* **106**, 417-430.

Philippot, P. (1993). Fluid-melt-rock interaction in mafic eclogites and coesite-bearing metasediments: Constraints on volatile recycling during subduction. *Chemical Geology* **108**, 93-112.

Pilchin, A. (2005). The role of serpentinization in exhumation of high- to ultra-high-pressure metamorphic rocks. *Earth and Planetary Science Letters* **237**, 815-828.

Pilet, S., Baker, M. B. & Stolper, E. M. (2008). Metasomatized lithosphere and the origin of alkaline lavas. *Science* **320**, 916-919.

Plank, T. & Langmuir, C. H. (1993). Tracing trace elements from sediment input to volcanic output at subduction zones. *Nature* **362**, 739-743.

Plank, T. & Langmuir, C. H. (1998). The chemical composition of subducting sediment and its consequences for the crust and mantle. *Chemical Geology* **145**, 325-394.

Poli, S. & Schmidt, M. W. (1995). H_2O transport and release in subduction zones: Experimental

constraints on basaltic and andesitic systems. *Journal of Geophysical Research* **100**, 22299-22314.

Poli, S. & Schmidt, M. W. (1997). The high-pressure stability of hydrous phases in orogenic belts: an experimental approach on eclogite-forming processes. *Tectonophysics* **273**, 169-184.

Poli, S. & Schmidt, M. W. (1998). The high-pressure stability of zoisite and phase relationships of zoisite-bearing assemblages. *Contributions to Mineralogy and Petrology* **130**, 162-175.

Poli, S. & Schmidt, M. W. (2002). Petrology of subducted slabs. *Annual Review Earth Planet Science* **30**, 207-235.

Qian, Q., Gao, J., Klemd, R., He, G., Song, B., Liu, D. & Xu, R. (2009). Early Paleozoic tectonic evolution of the Chinese South Tianshan Orogen: constraints from SHRIMP zircon U–Pb geochronology and geochemistry of basaltic and dioritic rocks from Xiate, NW China. *International Journal of Earth Sciences* **98**, 551-569.

Rapp, J. F., Klemme, S., Butler, I. B. & Harley, S. L. (2010). Extremely high solubility of rutile in chloride and fluoride-bearing metamorphic fluids: An experimental investigation. *Geology* **38**, 323-326.

Rapp, R. P., Irifune, T., Shimizu, N., Nishiyama, N., Norman, M. D. & Inoue, T. (2008). Subduction recycling of continental sediments and the origin of geochemically enriched reservoirs in the deep mantle. *Earth and Planetary Science Letters* **271**, 14-23.

Rebay, G., Powell, R. & Diener, J. F. A. (2010). Calculated phase equilibria for a MORB composition in a P-T range, 450-650°C and 18–28 kbar: the stability of eclogite. *Journal of Metamorphic Geology* **28**, 635-645.

Regelous, M., Gamble, J. A. & Turner, S. P. (2010). Mechanism and timing of Pb transport from subducted oceanic crust and sediment to the mantle source of arc lavas *Chemical Geology* **273**, 46-54.

Ringwood, A. E. (1974). The petrological evolution of island arc systems. *Journal of the Geological Society* **130**, 183-204.

Roggensack, K., Hervig, R. L., McKnight, S. B. & Williams, S. N. (1997). Explosive basaltic volcanism from Cerro Negro Volcano: Influence of volatiles on eruptive style. *Science* **277**, 1639-1642.

Rubatto, D. & Hermann, J. (2003). Zircon formation during fluid circulation in eclogites (Monviso, Western Alps): Implications for Zr and Hf budget in subduction zones. *Geochimica et Cosmochimica Acta* **67**, 2173-2187.

Rubatto, D. & Hermann, J. (2007). Experimental zircon/melt and zircon/garnet trace element partitioning and implications for the geochronology of crustal rocks. *Chemical Geology* **241**, 38-61.

Rudnick, R. L., Barth, M., Horn, I. & McDonough, W. F. (2000). Rutile-bearing refractory eclogites: Missing link between continents and depleted mantle. *Science* **287**, 278-281.

Rudnick, R. L., Gao, S., Ling, W.-l., Liu, Y.-s. & McDonough, W. F. (2004). Petrology and geochemistry of spinel peridotite xenoliths from Hannuoba and Qixia, North China craton. *Lithos* **77**, 609-637.

Ryan, J. G. & Langmuir, C. H. (1993). The Systematics of Boron Abundances in Young Volcanic-Rocks. *Geochimica et Cosmochimica Acta* **57**, 1489-1498.

Ryan, J. G., Morris, J., Tera, F., Leeman, W. P. & Tsvetkov, A. (1995). Cross-Arc Geochemical Variations in the Kurile Arc as a Function of Slab Depth. *Science* **270**, 625-627.

Sato, K. & Katsura, T. (2001). Experimental investigation on dolomite dissociation into aragonite+magnesite up to 8.5 GPa. *Earth and Planetary Science Letters* **184**, 529-534.

Scambelluri, M., Fiebig, J., Malaspina, N., Muntener, O. & Pettke, T. (2004). Serpentinite subduction: Implications for fluid processes and trace-element recycling. *International Geology Review* **46**, 595-618.

Scambelluri, M., Piccardo, G. B., Philippot, P., Robbiano, A. & Negretti, L. (1997). High salinity fluid inclusions formed from recycled seawater in deeply subducted alpine serpentinite. *Earth and Planetary Science Letters* **148**, 485-499.

Schiano, P., Clocchiatti, R., Shimizu, N., Maury, R. C., Jochum, K. P. & Hofmann, A. W. (1995). Hydrous, Silica-Rich Melts in the Sub-Arc Mantle and Their Relationship with Erupted Arc Lavas. *Nature* **377**, 595-600.

Schmidt, A., Weyer, S., John, T. & Brey, G. P. (2009). HFSE systematics of rutile-bearing eclogites: New insights into subduction zone processes and implications for the earth's HFSE budget. *Geochimica et Cosmochimica Acta* **73**, 455-468.

Schmidt, M. W. & Poli, S. (1994). The stability of lawsonite and zoisite at high pressures:

experiments in CASH to 92 kbar and implications for the presence of hydrous phases in subducted lithosphere. *Earth and Planetary Science Letters* **124**, 105-118.

Schmidt, M. W. & Poli, S. (1998). Experimentally based water budgets for dehydrating slabs and consequences for arc magma generation. *Earth and Planetary Science Letters* **163**, 361-379.

Schmidt, M. W. & Poli, S. (2003). Generation of mobile components during subduction of oceanic crust. In: Rudnick, R. L. (ed.) *Treatise on Geochemistry*. New York: Elsevier, 567-591.

Schmidt, M. W. (1995). Lawsonite: Upper pressure stability and formation of higher density hydrous phases. *American Mineralogist* **80**, 1286-1292.

Schmidt, M. W., Dardon, A., Chazot, G. & Vannucci, R. (2004b). The dependence of Nb and Ta rutile-melt partitioning on melt composition and Nb/Ta fractionation during subduction process. *Earth and Planetary Science Letters* **226**, 415-432.

Schmidt, M. W., Vielzeuf, D. & Auzanneau, E. (2004a). Melting and dissolution of subducting crust at high pressures: the key role of white mica. *Earth and Planetary Science Letters* **228**, 65-84.

Selverstone, J., Franz, G., Thomas, S. & Getty, S. (1992). Fluid variability in 2 GPa eclogites as an indicator of fluid behavior during subduction. *Contributions to Mineralogy and Petrology* **112**, 341-357.

Şengör, A. M. C., Natalin, B. A. & Burtman, V. S. (1993). Evolution of the Altaid Tectonic Collage and Paleozoic Crustal Growth in Eurasia. *Nature* **364**, 299-307.

Shannon, R. (1976). Revised effective ionic radii and systematic studies of interatomic distances in halides and chalcogenides. *Acta Crystallographica Section A* **32**, 751-767.

Shi, R., Yang, J., Wu, C. & Wooden, J. (2004). First SHRIMP dating for the formation of the late Sinian Yushigou Ophiolite, North Qilian Mountains. *Acta Geologica Sinica (in Chinese with English abstract)* **78**, 649-657.

Shi, Y., Lu, H., Jia, D., Cai, D., Wu, S., Chen, C., Howell, D. G. & Valin, Z. C. (1994). Paleozoic plate-tectonic evolution of the Tarim and western Tianshan regions, western China. *International Geology Review* **36**, 1058-1066.

Sisson, T. W. & Layne, G. D. (1993). H_2O in basalt and basaltic andesite glass inclusions from

four subduction-related volcanoes. *Earth and Planetary Science Letters* **117**, 619-635.

Smit, M. A., Bröcker, M. & Scherer, E. E. (2008). Aragonite and magnesite in eclogites from the Jæren nappe, SW Norway: disequilibrium in the system $CaCO_3$–$MgCO_3$ and petrological implications. *Journal of Metamorphic Geology* **26**, 959-979.

Smith, D. C. (1984). Coesite in Clinopyroxene in the Caledonides and Its Implications for Geodynamics. *Nature* **310**, 641-644.

Smyth, J. R. (1980). Cation vacancies and the crystal chemistry of breakdown reactions in kimberlitic omphacites. *American Mineralogist* **65**, 1185-1191.

Song, S. (1997). Tectonic evolution of subductive complex belts in the north Qilian mountains. *Advance in Earth Sciences* **12**, 351-365.

Song, S., Zhang, L., Niu, Y., Song, B., Zhang, G. & Wang, Q. (2004). Zircon U-Pb SHRIMP ages of eclogites from the North Qilian Mountains in NW China and their tectonic implication. *Chinese Science Bulletin* **49**, 848-852.

Song, S. G., Zhang, L. F., Niu, Y. L., Su, L., Song, B. & Liu, D. Y. (2006). Evolution from oceanic subduction to continental collision: A case study from the Northern Tibetan Plateau based on geochemical and geochronological data. *Jounal of Petrology* **47**, 435-455.

Song, S. G., Zhang, L. F., Niu, Y., Wei, C. J., Liou, J. G. & Shu, G. M. (2007). Eclogite and carpholite-bearing metasedimentary rocks in the North Qilian suture zone, NW China: implications for Early Palaeozoic cold oceanic subduction and water transport into mantle. *Journal of Metamorphic Geology* **25**, 547-563.

Song, S.. (2009). High-pressure metamorphic rocks in the North Qilian oceanic subduction zone, China: A review. *Geological Bulletin of China (in Chinese with English abstract)* **28**, 1769-1778.

Song, S., Niu, Y., Zhang, L., Wei, C., Liou, J. G. & Su, L. (2009a). Tectonic evolution of early Paleozoic HP metamorphic rocks in the North Qilian Mountains, NW China: New perspectives. *Journal of Asian Earth Sciences* **35**, 334-353.

Song, S. G., Su, L., Niu, Y. L., Lai, Y. & Zhang, L. F. (2009b). CH_4 inclusions in orogenic harzburgite: Evidence for reduced slab fluids and implication for redox melting in mantle wedge. *Geochimica et Cosmochimica Acta* **73**, 1737-1754.

Song, S., Niu, Y., Su, L. & Xia, X. (2012). Tectonics of the North Qilian orogen, NW China. *Gondwana Research* **in press**.

Sorensen, S. S. (1991). Petrogenetic significance of zoned allanite in garnet amphibolites from a paleo-subduction zone: Catalina Schist, southern California. *American Mineralogist* **76**, 589-601.

Sorensen, S. S., Grossman, J. N. & Perfit, M. R. (1997). Phengite-hosted LILE enrichment in eclogite and related rocks: Implications for fluid-mediated mass transfer in subduction zones and arc magma genesis. *Journal of Petrology* **38**, 3-34.

Spandler, C. & Hermann, J. (2006). High-pressure veins in eclogite from New Caledonia and their significance for fluid migration in subduction zones. *Lithos* **89**, 135-153.

Spandler, C., Hermann, J., Arculus, R. & Mavrogenes, J. (2003). Redistribution of trace elements during prograde metamorphism from lawsonite blueschist to eclogite facies; implications for deep subduction-zone processes. *Contributions to Mineralogy and Petrology* **146**, 205-222.

Spandler, C., Hermann, J., Arculus, R. & Mavrogenes, J. (2004). Geochemical heterogeneity and element mobility in deeply subducted oceanic crust; insights from high-pressure mafic rocks from New Caledonia. *Chemical Geology* **206**, 21-42.

Stalder, R., Foley, S. F., Brey, G. P. & Horn, I. (1998). Mineral aqueous fluid partitioning of trace elements at 900-1200 degrees C and 3.0-5.7 GPa: New experimental data for garnet, clinopyroxene, and rutile, and implications for mantle metasomatism. *Geochimica et Cosmochimica Acta* **62**, 1781-1801.

Staudigel, H., Davies, G. R., Hart, S. R., Marchant, K. M. & Smith, B. M. (1995). Large scale isotopic Sr, Nd and O isotopic anatomy of altered oceanic crust: DSDP/ODP sites 417/418. *Earth and Planetary Science Letters* **130**, 169-185.

Stern, R. J., Kohut, E., Bloomer, S. H., Leybourne, M., Fouch, M. & Vervoort, J. (2006). Subduction factory processes beneath the Guguan cross-chain, Mariana Arc: no role for sediments, are serpentinites important? *Contributions to Mineralogy and Petrology* **151**, 202-221.

Stolper, E. & Newman, S. (1994). The Role of Water in the Petrogenesis of Mariana Trough Magmas. *Earth and Planetary Science Letters* **121**, 293-325.

Sturrock, P. A. (1994). Plasma physics. an introduction to the theory of astrophysical, geophysical, and laboratory plasmas. *Cambridge, UK: Cambridge University Press,*| *c1994* **1**.

Su, W., Gao, J., Klemd, R., Li, J.-L., Zhang, X., Li, X.-H., Chen, N.-S. & Zhang, L. (2010). U–Pb zircon geochronology of Tianshan eclogites in NW China: implication for the collision between the Yili and Tarim blocks of the southwestern Altaids. *European Journal of Mineralogy* **22**, 473-478.

Sun, S. S., McDonough, W.F. (1989). Chemical and isotopic systematic in ocean basalt: Implication for mantle composition and processes. **Magmatism in the ocean Basins**, 313-345.

Sun, S.-s. & McDonough, W. F. (1989). Chemical and isotopic systematics of oceanic basalts: implications for mantle composition and processes. *Geological Society, London, Special Publications* **42**, 313-345.

Syracuse, E. M. & Abers, G. A. (2006). Global compilation of variations in slab depth beneath arc volcanoes and implications. *Geochem. Geophys. Geosyst.* **7**, Q05017.

Tamura, Y., Tani, K., Chang, Q., Shukuno, H., Kawabata, H., Ishizuka, O. & Fiske, R. S. (2007). Wet and Dry Basalt Magma Evolution at Torishima Volcano, Izu–Bonin Arc, Japan: the Possible Role of Phengite in the Downgoing Slab. *Journal of Petrology* **48**, 1999-2031.

Tanaka, S. & Inoue, T. (1980). Be-10 Evidence for Geochemical Events in the North Pacific during the Pliocene. *Earth and Planetary Science Letters* **49**, 34-38.

Tatsumi, Y. & Eggins, S. (1995). *Subduction Zone Magmatism*. Cambridge: Blackwell.

Tatsumi, Y. & Kogiso, T. (1997). Trace element transport during dehydration processes in the subducted oceanic crust: 2. Origin of chemical and physical characteristics in arc magmatism. *Earth and Planetary Science Letters* **148**, 207-221.

Tatsumi, Y. & Kogiso, T. (2003). The subduction factory: its role in the evolution of the Earth's crust and mantle. In: Larter, R. D. & Leat, P. T. (eds.) *Intra-Oceanic Subduction Systems: Tectonic and Magmatic Processes*. London: Geological Society, London, Special Publication, 55-80.

Tatsumi, Y. (1986). Formation of the volcanic front in subduction zones. *Geophysical Research Letters* **13**, 717-720.

Tatsumi, Y., Hamilton, D. L. & Nesbitt, R. W. (1986). Chemical characteristics of fluid phase from a subducted lithosphere and origin of arc magmas: evidence from high-pressure experiments and natural rocks. *Journal of Volcanology and Geothermal Research* **29**, 293-309.

Taylor, R. N., Nesbitt, R. W., Vidal, P., Harmon, R. S., Auvray, B. & Croudace, I. W. (1994). Mineralogy, Chemistry, and Genesis of the Boninite Series Volcanics, Chichijima, Bonin Islands, Japan. *Journal of Petrology* **35**, 577-617.

Tera, F., Brown, L., Morris, J. & Sacks, I. S. (1986). Sediment incorporation in island-arc magmas: Inferences from ^{10}Be. *Geochimica et Cosmochimica Acta* **50**, 535-550.

Thompson, A. B. (1992). Water in the Earth's upper mantle. *Nature* **358**, 295-302.

Tommasini, S., Heumann, A., Avanzinelli, R. & Francalanci, L. (2007). The fate of high-angle dipping slabs in the subduction factory: An integrated trace element and radiogenic isotope (U, Th, Sr, Nd, Pb) study of Stromboli volcano, Aeolian Arc, Italy. *Journal of Petrology* **48**, 2407-2430.

Tribuzio, R., Messiga, B., Vannucci, R. & Bottazzi, P. (1996). Rare earth element redistribution during high-pressure–low-temperature metamorphism in ophiolitic Fe-gabbros (Liguria, northwestern Italy): Implications for light REE mobility in subduction zones. *Geology* **24**, 711-714.

Tropper, P. & Manning, C. (2005). Very low solubility of rutile in H_2O at high pressure and temperature, and its implications for Ti mobility in subduction zones. *American Mineralogist* **90**, 502-505.

Tseng, C. Y., Yang, H. J., Yang, H. Y., Liu, D. Y., Tsai, C. L., Wu, H. Q. & Zuo, G. C. (2007). The Dongcaohe ophiolite from the North Qilian Mountains: A fossil oceanic crust of the Paleo-Qilian ocean. *Chinese Science Bulletin* **52**, 2390-2401.

Tseng, C.-Y., Zuo, G.-C., Yang, H.-J., Yang, H.-Y., Tung, K.-A., Liu, D.-Y. & Wu, H.-Q. (2009). Occurrence of Alaskan-type mafic-ultramafic intrusions in the North Qilian Mountains, northwest China: Evidence of Cambrian arc magmatism on the Qilian Block. *Island Arc* **18**, 526-549.

Tsujimori, T., Sisson, V. B., Liou, J. G., Harlow, G. E. & Sorensen, S. S. (2006). Very-low-temperature record of the subduction process: a review of worldwide lawsonite eclogites. *Lithos* **92**, 609-624.

Turner, S. & Hawkesworth, C. (1997). Constraints on Flux Rates and Mantle Dynamics Beneath Island Arcs from Tonga-Kermadec Lava Geochemistry. *Nature* **389**, 568-573.

Turner, S. T. & Foden, J. F. (2001). U, Th and Ra disequilibria, Sr, Nd and Pb isotope and trace element variations in Sunda arc lavas: predominance of a subducted sediment component. *Contributions to Mineralogy and Petrology* **142**, 43-57.

Turner, S., Hawkesworth, C., van Calsteren, P., Heath, E., Macdonald, R. & Black, S. (1996). U-series isotopes and destructive plate margin magma genesis in the Lesser Antilles. *Earth and Planetary Science Letters* **142**, 191-207.

Ulmer, P. (2001). Partial melting in the mantle wedge — the role of H2O in the genesis of mantle-derived 'arc-related' magmas. *Physics of the Earth and Planetary Interiors* **127**, 215-232.

Usui, T., Kobayashi, K., Nakamura, E. & Helmstaedt, H. (2007). Trace element fractionation in deep subduction zones inferred from a lawsonite-eclogite xenolith from the Colorado Plateau. *Chemical Geology* **239**, 336-351.

Van Baalen, M. R. (1993). Titanium mobility in metamorphic systems: a review. *Chemical Geology* **110**, 233-249.

van der Straaten, F., Schenk, V., John, T. & Gao, J. (2008). Blueschist-facies rehydration of eclogites (Tian Shan, NW-China): Implications for fluid-rock interaction in the subduction channel. *Chemical Geology* **255**, 195-219.

van Keken, P. E., Hacker, B. R., Syracuse, E. M. & Abers, G. A. (2011). Subduction factory: 4. Depth-dependent flux of H_2O from subducting slabs worldwide. *J. Geophys. Res.* **116**, B01401.

Van Orman, J. A., Grove, T. L. & Shimizu, N. (2002). Diffusive fractionation of trace elements during production and transport of melt in Earth's upper mantle. *Earth and Planetary Science Letters* **198**, 93-112.

Van Orman, J. A., Saal, A. E., Bourdon, B. & Hauri, E. H. (2006). Diffusive fractionation of U-series radionuclides during mantle melting and shallow-level melt-cumulate interacion. *Geochimica et Cosmochimica Acta* **70**, 4797-4812.

Vidal, P., Dupuy, C., Maury, R. & Richard, M. (1989). Mantle metasomatism above subduction zones: Trace-element and radiogenic isotope characteristics of peridotite xenoliths from

Batan Island (Philippines). *Geology* **17**, 1115-1118.

Volkova, N. I. & Budanov, V. I. (1999). Geochemical discrimination of metabasalt rocks of the Fan-Karategin transitional blueschist/greenschist belt, South Tianshan, Tajikistan: seamount volcanism and accretionary tectonics. *Lithos* **47**, 201-216.

Wade, J. & Wood, B. J. (2001). The Earth's 'missing' niobium may be in the core. *Nature* **409**, 75-78.

Walker, J. A., Patino, L. C., Carr, M. J. & Feigenson, M. D. (2001). Slab control over HFSE depletions in central Nicaragua. *Earth and Planetary Science Letters* **192**, 533-543.

Walker, J., Roggensack, K., Patino, L., Cameron, B. & Matías, O. (2003). The water and trace element contents of melt inclusions across an active subduction zone. *Contributions to Mineralogy and Petrology* **146**, 62-77.

Wallace, P. J. (2005). Volatiles in subduction zone magmas: concentrations and fluxes based on melt inclusion and volcanic gas data. *Journal of Volcanology and Geothermal Research* **140**, 217-240.

Wang, C. Y., Zhang, Q., Qian, Q. & Zhou, M. F. (2005). Geochemistry of the Early Paleozoic Baiyin volcanic rocks (NW China): Implications for the tectonic evolution of the North Qilian Orogenic Belt. *Journal of Geology* **113**, 83-94.

Wang, C., Liu, L., Luo, J., Che, Z., Teng, Z., Cao, X. & Zhang, J. (2007). Late Paleozoic post-collisional magmatism in the southwestern Tianshan orogenic belt, take the Baleigong pluton in the Kokshal region as an example. *Acta Petrologica Sinica* **23**, 1830-1840.

Weaver, B. L. (1991). The origin of ocean island end-member compositions: trace element and isotopic constraints. *Earth and Planetary Science Letters* **104**, 381-397.

White, W. M. & Patchett, J. (1984). Hf-Nd-Sr isotopes and incompatible element abundances in island arcs: implications for magma origins and crust-mantle evolution. *Earth and Planetary Science Letters* **67**, 167-185.

White, W. M. (1985). Sources of oceanic basalts: Radiogenic isotopic evidence. *Geology* **13**, 115-118.

Whitney, D. L. & Evans, B. W. (2010). Abbreviations for names of rock-forming minerals. *American Mineralogist* **95**, 185-187.

Willbold, M. & Stracke, A. (2006). Trace element composition of mantle end-members: Implications for recycling of oceanic and upper and lower continental crust. *Geochemistry Geophysics Geosystems* **7**.

Winchester, J. A. & Floyd, P. A. (1977). Geochemical discrimination of different magma series and their differentiation products using immobile elements. *Chemical Geology* **20**, 325-343.

Wood, B. J., Bryndzia, L. T. & Johnson, K. E. (1990). Mantle Oxidation-State and Its Relationship to Tectonic Environment and Fluid Speciation. *Science* **248**, 337-345.

Woodhead, J. D., Hergt, J. M., Davidson, J. P. & Eggins, S. M. (2001). Hafnium isotope evidence for 'conservative' element mobility during subduction zone processes. *Earth and Planetary Science Letters* **192**, 331-346.

Wu, H. Q., Feng, Y. M. & Song, S. G. (1993). Metamorphism and deformation of blueschist belts and their tectonic implications, North Qilian Mountains, China. *Jounal of Metamorphic Geologist* **11**, 523-536.

Wyllie, P. J. & Sekine, T. (1982). The formation of mantle phlogopite in subduction zone hybridization. *Contributions to Mineralogy and Petrology* **79**, 375-380.

Wyllie, P. J. (1988). Magma genesis, plate tectonics, and chemical differentiation of the Earth. *Review of Geophysics* **26**, 370-404.

Xia, L. Q., Xia, Z. C. & Peng, L. G. (1991). Determination of magmatie nature of Ordovician island-arc volcanic series in the Shihuigou area in the Northern Qilian Mountains. *Acta Petrologica et Mineralogica* **10**, 1-10.

Xia, L. Q., Xia, Z. C. & Xu, X. Y. (1995). Dynamics of tectono-volcano-magmatic evolution from North Qilian Mountains, China. *Northwest Geoscience* **16**, 1-28.

Xia, L. Q., Xia, Z. C. & Xu, X. Y. (1996). *Petrogenesis of marine volcanic rocks from Northern Qilian Mountains*. Beijing: Geological Publishing House.

Xia, L. Q., Xia, Z. C. & Xu, X. Y. (1998). Early Palaeozoic mid-ocean ridge-ocean island and back-arc basin volcanism in the North Qilian Mountains. *Acta Geologica Sinica* **72**, 301-312.

Xia, L. Q., Xia, Z. C. & Xu, X. Y. (2003). Magmagenesis in the Ordovician backarc basins of the northern Qilian Mountains, China. *Geological Society of Ameirca Bulletin* **115**, 1510-1522.

Xia, X. H. & Song, S. G. (2010). Forming age and tectono-petrogenises of the Jiugequan ophiolite in the North Qilian Mountain, NW China. *Chinese Science Bulletin* **55**, 1899-1907.

Xia, X., Song, S. & Niu, Y. (2011). Tholeiite–Boninite terrane in the North Qilian suture zone: Implications for subduction initiation and back-arc basin development. *Chemical Geology*.

Xiao, W. J., Windley, B. F., Yong, Y., Yan, Z., Yuan, C., Liu, C. Z. & Li, J. L. (2009). Early Paleozoic to Devonian multiple-accretionary model for the Qilian Shan, NW China. *Journal of Asian Earth Science* **35**, 323-333.

Xiao, Y., Lavis, S., Niu, Y., Pearce, J. A., Li, H., Wang, H. & Davidson, J. (2012). Trace element transport during subduction-zone ultrahigh pressure metamorphism: Evidence from Western Tianshan, China. *Geological Society of America Bulletin* **in press**.

Yakubchuk, A. (2004). Architecture and mineral deposit settings of the Altaid orogenic collage: a revised model. *Journal of Asian Earth Sciences* **23**, 761-779.

Yang, J., Xu, Z., Zhang, J., Song, S., Wu, C., Shi, R., Li, H. & Maurice, B. (2002). Early Palaeozoic North Qaidam UHP metamorphic belt on the north-eastern Tibetan plateau and a paired subduction model. *Terra Nova* **14**, 397-404.

Yiou, F. & Raisbeck, G. M. (1972). Half-Life of ^{10}Be. *Physical Review Letters* **29**, 372-375.

You, C. F., Castillo, P. R., Gieskes, J. M., Chan, L. H. & Spivack, A. J. (1996). Trace element behavior in hydrothermal experiments: Implications for fluid processes at shallow depths in subduction zones. *Earth and Planetary Science Letters* **140**, 41-52.

Zack, T. & John, T. (2007). An evaluation of reactive fluid flow and trace element mobility in subducting slabs. *Chemical Geology* **239**, 199-216.

Zack, T., Rivers, T. & Foley, S. F. (2001). Cs-Rb-Ba systematics in phengite and amphibole: an assessment of fluid mobility at 2.0GPa in eclogites from Trescolmen, Central Alps. *Contributions to Mineralogy and Petrology* **140**, 651-669.

Zack, T., Tomascak, P. B., Rudnick, R. L., Dalpé, C. & McDonough, W. F. (2003). Extremely light Li in orogenic eclogites: The role of isotope fractionation during dehydration in subducted oceanic crust. *Earth and Planetary Science Letters* **208**, 279-290.

Zhang, J. X. & Meng, F. C. (2006). Lawsonite-bearing eclogites in the north Qilian and north Altyn Tagh：Evidence for cold subduction of oceanic crust. *Chinese Science Bulletin* **51**, 1238—1244.

Zhang, J. X., Xu, Z. Q., Chen, W. & Xu, H. F. (1997). A tentative discussion on the ages of the subduction–accretionary complex/volcanic arcs in the middle sector of North Qilian Mountain. *Acta Petrologica et Mineralogica* **16**, 112-119.

Zhang, L. F., Ai, Y. L., Li, X. P., Rubatto, D., Song, B., Williams, S., Song, S. G., Ellis, D. & Liou, J. G. (2007a). Triassic collision of western Tianshan orogenic belt, China: Evidence from SHRIMP U-Pb dating of zircon from HP/UHP eclogitic rocks. *Lithos* **96**, 266-280.

Zhang, J. X., Meng, F. C. & Wan, Y. S. (2007b). A cold Early Palaeozoic subduction zone in the North Qilian Mountains, NW China: Petrological and U-Pb geochronological constraints. *Journal of Metamorphic Geology* **25**, 285-304.

Zhang, L. F., Ellis, D. J. & Jiang, W. B. (2002a). Ultrahigh-pressure metamorphism in western Tianshan, China: Part I. Evidence from inclusions of coesite pseudomorphs in garnet and from quartz exsolution lamellae in omphacite in eclogites. *American Mineralogist* **87**, 853-860.

Zhang, L. F., Ellis, D. J., Williams, S. & Jiang, W. B. (2002b). Ultra-high pressure metamorphism in western Tianshan, China: Part II. Evidence from magnesite in eclogite. *American Mineralogist* **87**, 861-866.

Zhang, L. F., Ellis, D. J., Arculus, R. J., Jiang, W. & Wei, C. (2003a). 'Forbidden zone' subduction of sediments to 150km depth – the reaction of dolomite to magesite + aragonite in the UHPM metapelites from western Tianshan, China. *Journal of Metamorphic Geology* **21**, 523-529.

Zhang, L. F., Ellis, D. J., Williams, S. & Jiang, W. B. (2003b). Ultrahigh- pressure metamorphism in elogites from the western Tianshan, China-Reply. *American Mineralogist* **88**, 1157-1160.

Zhang, L. F., Song, S. G., Liou, J. G., Ai, Y. L. & Li, X. P. (2005). Relict coesite exsolution in omphacite from Western Tianshan eclogites, China. *American Mineralogist* **90**, 181-186.

Zhang, L. F., Wang, Q. & Song, S. G. (2009). Lawsonite blueschist in Northern Qilian, NW China: P–T pseudosections and petrologic implications. *Journal of Asian Earth Science* **35**, 354-366.

Zhang, Q., Xu, Z., Chen, W. & Xu, H. (1997). A tentative discussion on the ages of the subductionaccretionary complex/volcanic arcs in the middle sector of north Qilian mountain. *Acta Petrologica et Mineralogica (in Chinese with English abstract)* **16**, 112-119.

Zindler, A. & Hart, S. (1986). Chemical Geodynamics. *Annual Review Earth Planet Science* **14**, 493-571.